University of California
Santa Barbara

Black Holes and Holography: Insights and Applications

A dissertation submitted in partial satisfaction
of the requirements for the degree

Doctor of Philosophy
in
Physics

by

Jason Wien

Committee in charge:

Professor Donald Marolf, Chair
Professor Gary Horowitz
Professor David Stuart

December 2017

The Dissertation of Jason Wien is approved.

Professor Gary Horowitz

Professor David Stuart

Professor Donald Marolf, Committee Chair

November 2017

Black Holes and Holography:

Insights and Applications

by

Jason Wien

Acknowledgements

I am fortunate to have been supported by a network of friends, family, peers, collaborators, and mentors throughout my time in graduate school. This dissertation could not have been completed without the support of this strong community, for which I am incredibly thankful.

First, I would like to thank my advisor, Don Marolf, for his tireless mentorship and guidance. He taught me the art of careful research guided by experience and intuition, and he patiently pointed me in the right direction any of the numerous times I found myself off course. The skills he helped me develop will help me through both my career and life in general.

Thank you to the numerous professors who have be invaluable in my education. Thank you to Gary Horowitz, David Stuart, David Berenstein, Dave Morrison, Steve Giddings, Joe Polchinski, Nathaniel Craig, Mark Srednicki, and Andreas Ludwig for imparting physics wisdom both through numerous class lectures as well as informal discussions.

I had the pleasure of collaborating with Max Rota, Will Donnelly and Ben Michel for parts of this dissertation. Thank you for helping to broaden my research perspective. Additionally, thank you to Will Kelly, Sebastian Fischetti, Netta Englehardt, Gavin Hartnett, Eric Mefford, Henry Maxfield, Alex Miller, Jason Weinberg, Benson Way, and anyone else whose office I stumbled in to, deep in a calculation and looking for help.

Thank you to my community of peers who helped me through late night problem sets and provided friendship and support during my time here. Thank you to Mickey, Ryan, Chai, Alex, Milind, Matt, Sky, Megan, Giulia, Brianna, Zicao, Seth, Alex, Gabriel, and Timothy. Thank you especially to Alex Miller for keeping the high energy theory journal club running strong.

Thank you to my parents, Mike and Nannette Wien, for cultivating my curiosity from a young age, and to my brother Andrew for trying to distract me from doing physics all the time. Thank you to my brother Brian for teaching me the beauty of every moment. Thank you to my great aunt and uncle, Anita and Byron Wien, for being long supporters of and investors in my education and intellectual growth. I would especially like to thank my grandfather, Robert Earle Wien, for instilling in me a drive to wonder at the world. Thank you for that visit to Fermilab all those years ago.

Finally, I would like to thank my life partner Elyse. You have been a source of emotional and intellectual support throughout this journey, keeping my brain sharp and my heart open. Truly we connect on every dimension, and no one understands me just as well as you do. I look forward to the rest of our lives together.

This work was supported in part by the U.S. National Science Foundation under grant numbers PHY12-05500 and PHY15-04541, by the Simons foundation, and by funds from the University of California.

Curriculum Vitæ

Jason Wien

Education

2017	Ph.D. in Physics (Expected), University of California, Santa Barbara.
2016	M.A. in Physics, University of California, Santa Barbara.
2014	M.Sc. in Physics, University of Waterloo
2013	B.A. in Physics and Mathematics, Harvard Univeristy

Publications

1. J. Wien, *Numerical Methods for Handlebody Phases*, [arXiv:1711.02711].
2. D. Marolf and J. Wien, *The Torus Operator in Holography*, [arXiv:1708.03048].
3. D. Marolf, M. Rota, and J. Wien, *Handlebody phases and the polyhedrality of the holographic entropy cone*, *JHEP* **1710** (2017) 069, [arXiv:1705.10736].
4. W. Donnelly, D. Marolf, B. Michel, and J. Wien, *Living on the Edge: A Toy Model for Holographic Reconstruction of Algebras with Centers*, *JHEP* **1704** (2017) 093, [arXiv:1611.05841].
5. D. Marolf and J. Wien, *Adiabatic corrections to holographic entanglement in thermofield doubles and confining ground states*, *JHEP* **1609** (2016) 058, [arXiv:1605.02803].
6. D. Marolf and J. Wien, *Holographic confinement in inhomogeneous backgrounds* , *JHEP* **1608** (2016) 015, [arXiv:1605.02804].
7. J. Wien, *A Holographic Approach to Spacetime Entanglement* (Master's Thesis), [arXiv:1408.6005].
8. M. Headrick, R. Myers, and J. Wien, *Holographic Holes and Differential Entropy*, *JHEP* **1410** (2014) 149, [arXiv:1408.4770].

Abstract

Black Holes and Holography:

Insights and Applications

by

Jason Wien

This dissertation focuses on the role classical black hole spacetimes play in the AdS/CFT correspondence. We begin by introducing some of the puzzles surrounding black holes, and we review their connection to strongly correlated CFT states through holography. Additionally, we detail numerical methods for constructing black hole states of non-trivial topology in three dimensions and evaluating their actions.

In part I we focus on using black hole spacetimes to derive insights into holography and quantum gravity. Using numerical methods, we study a class of non-local operators in the CFT, defined via a path integral over a torus with two punctures. In particular, we are interested in determining the spectrum of such operators at various points in moduli space. In the dual gravitational theory, such an operator might be used to construct black hole spacetimes with arbitrarily high topology behind the horizon. We present evidence suggesting this fails, and along the way encounter a puzzle related to the positivity of these operators. The resolution of this puzzle lies in developing technology to better catalogue the relevant gravitational phases.

Additionally, we use multi-boundary wormhole spacetimes to investigate the constraints on the subregion entanglement entropies of holographic states. We find tension with previously claimed properties of these constraints, namely that they define a polyhedral cone in the space of entanglement entropies. These results either suggest the possible existence of further unknown constraints, or the need for a more complicated

construction procedure to realize the extremal states.

In part II we focus on the holographic description of CFT states via black hole spacetimes, focusing on spacetimes perturbatively constructed from the planar AdS-Schwarzschild metric. First, we consider corrections to properties of confining ground states of holographic CFTs as we introduce spatial curvature. Next, we compute shifts in vacuum entanglement entropy in a thermal state with a locally varying temperature as well as similar shifts in the confining ground states with spatial curvature.

Contents

Chapter 1

Introduction

Black holes are one of the most enchanting aspects of the known universe, providing inspiration for countless science fiction stories while remaining a puzzle to physicists as to their exact nature. These mysterious objects follow directly from Einstein's theory of General Relativity [1], and in fact they are as essential to the theory as a mass on a spring is to Newtonian mechanics.

General Relativity describes how massive objects warp and stretch the fabric of space and time itself, and how objects travel through such a warped universe. These two notions are linked through Einstein's equations, which relate the curvature of a spacetime encoded in the tensor $G_{\mu\nu}$ with the matter and energy content encoded in the stress tensor $T_{\mu\nu}$:

$$G_{\mu\nu} = \frac{8\pi G_N}{c^4} T_{\mu\nu} \,. \tag{1.1}$$

These equations were elegantly summarized by John Wheeler as, "Matter tells space how to curve; space tells matter how to move."

A black hole is a region of space that is warped so strongly that nothing can escape it, not even light. Anyone or anything that enters a black hole is ultimately doomed to

be torn apart by the extreme gravitational forces within. These forces become infinitely large inside of the black hole, where the solution has a singularity, and so some theory other than General Relativity must become relevant in the interior. The prototypical black hole solution of Einstein's equations, the Schwarzschild solution [2], was derived just one year after Einstein developed his theory, although physicists did not understand it to be a black hole until decades later. In the present day, black holes provide a rich theoretical testing ground for how to go beyond the limits of General Relativity due to their singular nature and unique causal structure.

One could hope the Schwarzschild singularity arises because the solution assumes perfect spherical symmetry, and real black holes wouldn't be plagued by this theoretical oddity; however, it was shown in 1965 that any black hole in a spacetime satisfying a set of generic conditions would contain a singularity [3]. In this way, singularities are a fundamental feature of General Relativity, rather than a finely tuned pathology.

Furthermore, black holes are thought to be ubiquitous in our universe, with one sitting right at the center of our galaxy [4]. Recently the LIGO collaboration has reported multiple observations of gravitational waves emitted from the coalescence of two black holes, with waveforms consistent with that predicted by General Relativity [5, 6, 7]. Indeed, black holes seem to be a robust feature of our universe, even though our theoretical understanding of them is incomplete.

Despite this incompleteness, black holes have a rich theoretical description as objects with temperature, mass, angular momentum, and charge. Their dynamics are elegantly described by the four laws of black hole mechanics [8], standing in direct analogy to the four laws of thermodynamics. This description hints at a deeper connection between black holes and real thermodynamic objects, a connection made more explicit in the 1970s by the works of Stephen Hawking and Jacob Bekenstein [9, 10, 11, 12]. This characterization of black holes as thermodynamic objects revealed a beautiful theoretical

structure built in to General Relativity, but also laid bare some of its inconsistencies.

An essential ingredient of this formulation is the Bekenstein-Hawking formula for the entropy of a black hole:

$$S_{\mathrm{BH}} = \frac{A}{4G_N\hbar}\,, \tag{1.2}$$

where A is the area of the event horizon of the black hole [10, 11]. Treating a black hole as a thermodynamic object, this formula for the entropy follows from general arguments involving the partition function. However, it remains a mystery to derive this entropy in a statistical mechanical way in terms of counting the number of microstates corresponding to the black hole macrostate. Such a counting requires an underlying theory of quantum gravity, and a derivation of this formula is an important benchmark for such a theory. Indeed a major success of string theory has been to provide this microscopic explanation [13].

Additionally, it is puzzling that the entropy scales with the area of the black hole, rather than the volume as it does for most thermodynamic systems. In some sense this formula suggests that gravity is "holographic," meaning the degrees of freedom in the interior of region are somehow encoded on its boundary. This notion later was explicitly realized through the AdS/CFT correspondence [14, 15, 16], and this general idea of holography fuels much modern research in quantum gravity, providing a window into understanding how these puzzles might be resolved.

The AdS/CFT correspondence originated from the conjecture that a particular type of string theory defined in Anti-de Sitter space (AdS) is dual to a particular type of conformal field theory (CFT). More specifically, Juan Maldacena in 1997 motivated that Type IIB string theory on $\mathrm{AdS}_5 \times S_5$ should be dual to $\mathcal{N} = 4$ Super Yang-Mills in four dimensions [14]. In many cases we can consider only the AdS sector of the string

theory, in which case this duality relates a four dimensional quantum field theory to a five dimensional string theory. Furthermore, inserting sources in the CFT corresponds to changing the asymptotically AdS boundary conditions, and so as a cartoon one can think of the CFT as repackaging the quantum gravitational theory in terms of degrees of freedom on its boundary. In this way, Maldacena's original conjecture provides a description of a theory of quantum gravity in terms of a holographic duality.

This idea of holography is thought to apply more generally to theories of quantum gravity as explained in various reviews [17, 18, 19, 20]. The correspondence more generally can be stated at the level of partition functions:

$$\mathcal{Z}_{CFT} = \mathcal{Z}_{\text{QG}} \,. \tag{1.3}$$

On the left hand side is the partition function of some conformal field theory defined on a d dimensional manifold X. On the right hand side is the partition function of a dual quantum gravitational theory with asymptotic boundary conditions $\partial M = X$. Through this relation, the kinematics and dynamics in one theory has a corresponding description on the other side.

In most cases, the quantum gravity partition function is either unknown or intractable, and so it is convenient to consider the strong coupling and large number of flavors limit of the CFT. In this limit, the dual gravitational theory reduces to Einstein gravity with asymptotically AdS boundary conditions and some auxiliary fields that depend on the details of the original quantum gravitational theory. For the purposes of this dissertation, we will work exclusively in this limit and turn off all the auxiliary fields, restricting to the so called "universal sector" that does not depend on the specific details of the underlying theory quantum gravity. With these assumptions the duality is

summarized by

$$\mathcal{Z}_{CFT} = \mathcal{Z}_{\rm EH} \ , \tag{1.4}$$

where the right hand side is the partition function for pure Einstein gravity with no matter fields[1], i.e. $\int \mathcal{D}g\, e^{-S_{\rm EH}[g]}$. The limit of a large number of flavors in the CFT corresponds to the limit $G_N \to 0$ in the gravitational theory, and as the Einstein-Hilbert action scales like $1/G_N$, the partition function on the gravity side is often evaluated using a saddle point approximation. For the rest of this dissertation, we set $c = \hbar = k_B = 1$, but leave G_N explicit in order to make this limit more explicit.

This dissertation focuses on various classical black hole spacetimes and the role they play in holography. The AdS/CFT correspondence relates these spacetimes to highly correlated (thermal) states in the CFT and provides the basis for a symbiotic relationship between the two. On one side of the relationship, the previously mentioned puzzles associated with black holes should have conceptually clear resolutions in terms of the language of the CFT. For example, there should be a microscopic accounting of the black hole entropy formula in terms of states in the CFT. Going in the other direction, holography can be used to translate difficult computations involving strongly coupled CFTs into simpler calculations in Einstein gravity. In this dissertation, we explore both aspects of this symbiosis.

The material in this dissertation is organized as follows. In §1.1 below, we review the simplest example of the correspondence between a CFT state and a black hole, namely the duality between the thermofield double state and the AdS-Schwarzschild solution [21]. Finding the gravitational dual of a CFT state defined via a path integral amounts to solving for the dominant saddle point of the Einstein-Hilbert action with the correct

[1]Note that the Gibbons-Hawking-York boundary term must also be included.

boundary conditions, and so we first explain this example in order to make the material in the rest of the dissertation more accessible.

We begin in section 2, where we detail the numerical techniques used in this dissertation to study black hole spacetimes with non-trivial topology behind the horizon in two spatial dimensions plus time. Constructing these spacetimes involves numerical methods for solving non-linear differential equations using the finite element method, as well as mathematical methods for uniformizing Riemann surfaces. We include a *Mathematica* package for doing these computations, and we provide a simple example to demonstrate its use. The reader more interested in the applications of these methods to physical questions can skip this section without loss of narrative.

In part I, we construct classical black hole spacetimes of non-trivial topology and use them to try and gain insights into holography and quantum gravity in general. First in chapter 3 we consider a class of non-local CFT operators defined via a path integral over a torus with two punctures. One might use these operators to naturally construct gravitational states of high topology. Using numerical methods to compute the relevant bulk saddles, we study the action of such operators on the vacuum state as well as the associated projector onto the highest eigenvalue state. Along the way, we are confronted with an apparent contradiction in our arguments with no clear resolution, motivating further study.

Next, in chapter 4 we try to characterize the set of states in a CFT which have gravitational duals through the holographic entropy cone. This cone consists of the subregion entanglement entropies realizable by holographic CFT states, and for n subregions has dimension $2^n - 1$. It was previously claimed that this cone is polyhedral, and we evaluate this claim by searching for the holographic dual of states at the vertices of the cone. Such dual states are naturally constructed as multi-boundary wormholes, and thus black holes play an essential role in these insights.

In part II, we focus on applications of holography to CFT states with gravitational duals described by black holes. In particular, in chapter 5 we study confinement in gauge theory through corresponding calculations in spacetimes related to black hole spacetimes. This program was initiated by Witten [22], and we study how various quantities change as we perturbatively add boundary curvature.

An important tool for studying strongly correlated CFT states is entanglement entropy, and in chapter 6 we use holography to study entanglement entropy in thermal CFT states and confining states on curved backgrounds. These states are dual to black hole-like spacetimes, and we use the Ryu-Takayanagi formula to compute the entanglement entropy holographically [23, 24].

We conclude with a short summary and an outlook.

1.1 Preamble: From black holes to thermal states

The simplest example of the holographic connection between black holes and CFTs is the correspondence between the Euclidean AdS-Schwarzschild black hole and the thermofield double (TFD) state in the CFT [21]. In this section, we review the argument that these states are related by a holographic duality. First we introduce each state individually, then we explain how they are linked through the AdS/CFT correspondence.

In Euclidean signature, the metric for the AdS-Schwarzschild black hole in $d+1$ dimensions is given by

$$ds^2 = f(r)d\tau^2 + \frac{dr^2}{f(r)} + r^2 d\Omega_{d-1}\,, \qquad f(r) = 1 + \frac{r^2}{\ell^2} - \frac{r_+^d}{r^{d-2}}\left(\frac{1}{r_+^2} + \frac{1}{\ell^2}\right)\,, \tag{1.5}$$

where $d\Omega_{d-1}$ is the metric on the $d-1$ dimensional sphere, ℓ is the AdS radius, and r_+ is the location of the event horizon. Note that $f(r_+) = 0$, and so the g_{tt} component of

the metric vanishes and the g_{rr} component blows up at $r = r_+$. This behavior seems to signal that the spacetime becomes singular at the event horizon, but in Lorentzian signature we can remove this singularity through a coordinate transformation. As we explain below, in order to perform the analogous transformation in Euclidean signature we need to identify $\tau \sim \tau + \beta$ where β is the inverse temperature of the black hole

$$\beta = \frac{4\pi\ell^2 r_+}{d\, r_+^2 + (d-2)\ell^2}\,. \tag{1.6}$$

In Lorentzian signature, we can choose a coordinate system so that the AdS-Schwarzschild metric near the horizon has the form

$$ds^2 = -\xi^2\kappa^2 dt^2 + d\xi^2 + \cdots\,, \tag{1.7}$$

where the horizon is at $\xi = 0$, κ is the surface gravity of the horizon, and the dots signify terms that are finite as $\xi \to 0$. Further transforming to $X = \xi\cosh\kappa t$ and $T = \xi\sinh\kappa t$ yields the metric

$$ds^2 = -dT^2 + dX^2 + \cdots\,, \tag{1.8}$$

which is perfectly regular at $\xi = 0$. In Euclidean signature however, the near horizon metric has the form

$$ds^2 = \xi^2\kappa^2 d\tau^2 + d\xi^2 + \cdots\,, \tag{1.9}$$

and so the appropriate coordinate transformation is $X = \xi\cos\kappa\tau$ and $Y = \xi\sin\kappa\tau$. In order for this transformation to be well defined, we must identify $\tau \sim \tau + 2\pi/\kappa$. We can similarly derive that $\kappa = 2\pi/\beta$, where β is defined in eq. (1.6). This means that in

order to preserve regularity in the Euclidean solution, we must make the identification $\tau \sim \tau + \beta$ for a fixed β.

The main result of the above derivation is that in Euclidean signature, the AdS-Schwarzschild black hole has periodically identified time. As asymptotically AdS spacetimes have a boundary at asymptotic infinity, the boundary of AdS-Schwarzschild is given by $S^1 \times S^{d-1}$, where the first S^1 corresponds to Euclidean time. Collapsing the S^{d-1} directions into a single S^1, we can draw this spacetime as a filled in torus as shown in figure 1.1.

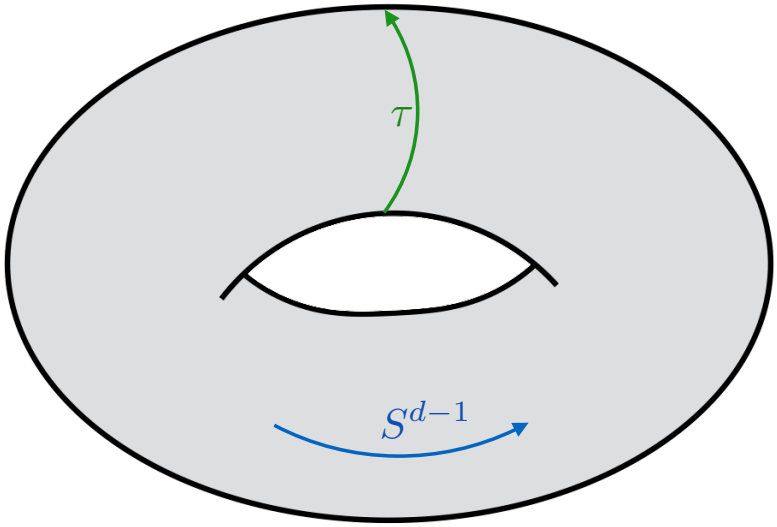

Figure 1.1: A cartoon of the Euclidean AdS-Schwarzschild spacetime, represented by a filled in torus. The filled-in direction corresponds to the r direction of the spacetime in the range $r \in [r_+, \infty)$. Note that in this picture the τ direction is contractible, as by eq. (1.5) this direction pinches off to zero size at $r = r_+$. However the S^{d-1} directions are non-contractible, as they remain finite size at $r = r_+$.

This spacetime has a CFT dual given by the thermofield double state, which we can think of as a maximally entangled state of two CFTs. Formally we can define this state as the path integral over a cylinder of length $\beta/2$ with two cuts (more precisely the space $[0, \beta/2] \times S^{d-1}$), with each cut corresponding to a CFT defined on an S^{d-1}. Imposing boundary conditions on each cut computes the inner product of the TFD state with the

state imposed on the boundaries. In particular, the TFD wavefunction is

$$\langle \phi_1, \phi_2 | \text{TFD} \rangle = \int_{\phi(\text{CFT}_1)=\phi_1,\ \phi(\text{CFT}_2)=\phi_2} \mathcal{D}\phi\, e^{-S_E[\phi]} \quad , \tag{1.10}$$

where S_E is the Euclidean action for the CFT and we have set $\hbar = 1$. Pictorally we represent this path integral definition of the TFD state in figure 1.2.

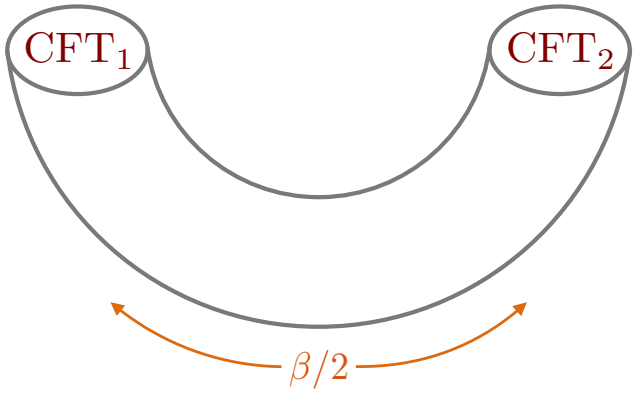

Figure 1.2: A pictoral representation of the path integral definition of the TFD state.

We can gain better understanding of this state by taking the partial trace of the density matrix $|\text{TFD}\rangle \langle \text{TFD}|$ over the degrees of freedom in one of the CFTs. First, we can construct the density matrix by taking two copies of the path integral drawn in fig. 1.2. Tracing over CFT_2 corresponds to integrating over all boundary conditions $\phi(\text{CFT}_2)$. As the path integral integrates over all fields ϕ, this is equivalent to sewing the two path integrals along CFT_2, and we are left with a path integral over a cylinder of length β as shown in figure 1.3. As well known from the Suzuki-Trotter decomposition, a path integral over a Euclidean time interval corresponds to a thermal state. Therefore we have

$$\text{Tr}_{\text{CFT}_2} |\text{TFD}\rangle \langle \text{TFD}| = e^{-\beta H} \,, \tag{1.11}$$

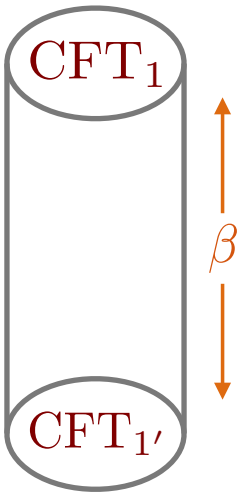

Figure 1.3: The TFD density matrix reduced to a single CFT.

where H is the Hamiltonian for a single copy of the CFT. In this way, we see that $|\text{TFD}\rangle$ is a purification of the thermal CFT state with inverse temperature β. Reversing the path integral manipulations in bra-ket language we see that that the TFD state is constructed through the standard doubling trick for purifications, and so we can write

$$|\text{TFD}\rangle = \sum_n e^{-\beta E_n/2} |n\rangle |n\rangle \ , \tag{1.12}$$

where $|n\rangle$ is an energy eigenstate of the CFT Hamiltonian with eigenvalue E_n. Hence, this state is referred to as the thermofield double state.

We can now link together the TFD state and the AdS black hole through holography. From the equivalence of the partition functions in eq. (1.4), the gravitational dual of the TFD state is characterized by the path integral over metrics with boundary given by $[0, \beta/2] \times S^{d-1}$, or a cylinder of length $\beta/2$. Working in the limit $G_N \to 0$, we can perform the gravitational path integral by a saddle point approximation. Therefore, we need to find solutions of Einstein's equations with the required boundary conditions, then choose the solution with least action.

One such solution is half the AdS-Schwarzschild black hole with inverse temperature β. As discussed previously, the boundary of this spacetime is the $S^1 \times S^{d-1}$ where the length of the S^1 on the boundary is given by β. Cutting this spacetime in half along a fixed τ slice gives a solution with boundary $[0, \beta/2] \times S^{d-1}$. From fig. 1.1, we see that this cut corresponds to cutting the torus along the plane of the page. The constant τ slice consists of two boundaries connected through the bulk, which we draw a cartoon of in fig. 1.4. The bulk state prepared by our path integral is thus a semi-classical state[2] that

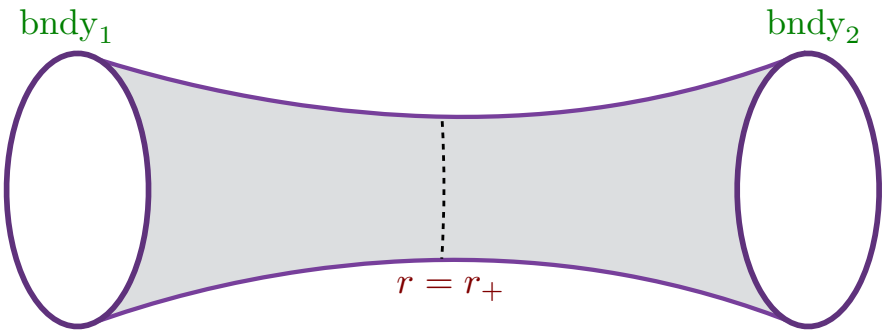

Figure 1.4: The constant τ slice of half the AdS black hole. Two boundaries are connected through the bulk wormhole.

is strongly peaked on classical solutions that are close to this two boundary wormhole geometry at time τ. Note that an observer on one boundary sees a black hole with inverse temperature β, which exactly matches the temperature of the thermal CFT state on a single boundary. In this way, holography makes explicit the treatment of black holes as thermodynamic objects.

However, in order for the thermal CFT state to be dual to the above black hole state, the bulk solution just described needs to be the dominant saddle in the path integral. But there is another solution of Einstein's equations matching these boundary conditions, namely Euclidean AdS$_{d+1}$ with periodically identified Euclidean time, with which it must

[2]Note this saddle point approximation is equivalent to the WKB approximation of the semi-classical wavefunction, in which the probability density is peaked on classical trajectories with quantum corrections suppressed by order G_N. See [25] for more details.

compete. The action for each solution is infinite due to the infinite spatial extent of AdS, but by subtracting "counter-terms" that depend only on the boundary conditions (and which are the same for both saddles) we can renormalize the action to find

$$S^{\text{ren}}[\text{AdS}] = 0 \qquad S^{\text{ren}}[\text{BH}] = \frac{\pi^2 \beta r_+^2}{8 G_N \ell^2} \left(\ell^2 - r_+^2\right) . \tag{1.13}$$

Said differently, $S[\text{BH}] - S[\text{AdS}] = S^{\text{ren}}[\text{BH}] - S^{\text{ren}}[\text{AdS}] = \frac{\pi^2 \beta r_+^2}{8 G_N \ell^2} \left(\ell^2 - r_+^2\right)$ is finite and well defined. As long as $r_+ > \ell$ the black hole solution has lower Euclidean action and is the dominant saddle. From eq. (1.6) we see that large r_+ corresponds to small β, i.e. high temperatures. So at high temperatures the thermal CFT state and the AdS black hole are holographic duals.

This duality has many applications. For example, the phase transition at $r_+ = \ell$ has been used to try and understand the confinement/deconfinement phase transition in QCD [22]. In chapters 5 and 6 we investigate questions related to this program. Additionally, one can construct generalizations of this example to link together entangled states of multiple copies of the CFT with multiboundary wormholes as in [26, 27]. In chapters 3 and 4 we explore further applications of these generalizations.

1.2 Permissions and Attributions

1. The content of chapter 3 is the result of a collaboration with Donald Marolf [28].

2. The content of chapter 4 is the result of a collaboration with Donald Marolf and Massimiliano Rota, and has previously appeared in the Journal of High Energy Physics (JHEP) [29]. It is reproduced here with the permission of the International School of Advanced Studdies (SISSA), Trieste, Italy. `http://jhep.sissa.it/jhep/help/JHEP/CR_OA.pdf`.

3. The content of chapter 5 is the result of a collaboration with Donald Marolf, and has previously appeared in the Journal of High Energy Physics (JHEP) [30]. It is reproduced here with the permission of the International School of Advanced Studdies (SISSA), Trieste, Italy. `http://jhep.sissa.it/jhep/help/JHEP/CR_OA.pdf`.

4. The content of chapter 6 is the result of a collaboration with Donald Marolf, and has previously appeared in the Journal of High Energy Physics (JHEP) [31]. It is reproduced here with the permission of the International School of Advanced Studdies (SISSA), Trieste, Italy. `http://jhep.sissa.it/jhep/help/JHEP/CR_OA.pdf`.

Chapter 2

Numerical Methods

In this section we review some of the tools used in chapters 3 and 4 to study handlebody solutions of Einstein's equations. These techniques include the finite element method (FEM) for numerically solving differential equations as well as the mathematical framework of Schottky uniformization for characterizing Riemann surfaces. The focus will be on useful formulas for implementing these calculations, and as such we have attached a *Mathematica* package to the electronic version of this dissertation that implements many of these tools. Readers interested in physical insights should skip to the next section.

First, we review the aspects of finite element methods used in this dissertation. Next, we give a rough overview of Schottky uniformization, focusing on explicitly writing down a uniformization for a given Riemann surface that describes a desired handlebody phase. We additionally give explicit formulas for computing the regularized action of these phases reduced by certain symmetries, which we conveniently encode in the attached *Mathematica* package. Finally, we give a simple example to illustrate the concepts and techniques described.

Note that in chapters 5 and 6 we use pseudo-spectral methods for solving differential equations of a single variable. These methods are well reviewed in [32, 33], and so we

leave this material out of this section.

2.1 Finite Element Methods

Finite element methods are numerical methods for solving differential equations which involve discretizing the domain with a set of finite "elements" [34, 35]. We will restrict our attention exclusively to equations in two dimensions of the form

$$\nabla^2 u(x,y) + f(x,y)u(x,y) = g(x,y)\,. \tag{2.1}$$

In order to solve this equation, we will discretize our solution space and convert this equation into a finite dimensional matrix equation, which we can then easily solve by algebraic methods.

2.1.1 Discretization of the domain

First, we discretize the domain D with a mesh made up of triangular elements. We will use elements with six nodes: one on each vertex and one on the midpoint of each edge. An example of a valid triangulation for a domain used in chapter 3 is shown in figure 2.1. The meshes used in this dissertation were generated using *Mathematica*'s built-in `ToElementMesh` function. Note that for numerical convenience, we approximate curved boundaries of D by a large number of straight segments. We can estimate the error introduced by computing the length of ∂D using the mesh and comparing it to the true value. The error introduced by this approximation can easily be made smaller by including more nodes on the boundary, and we always choose a sufficient number of nodes so that this error is always sub-leading.

Given a valid mesh, we can define our solution space as the Sobolev space of piecewise

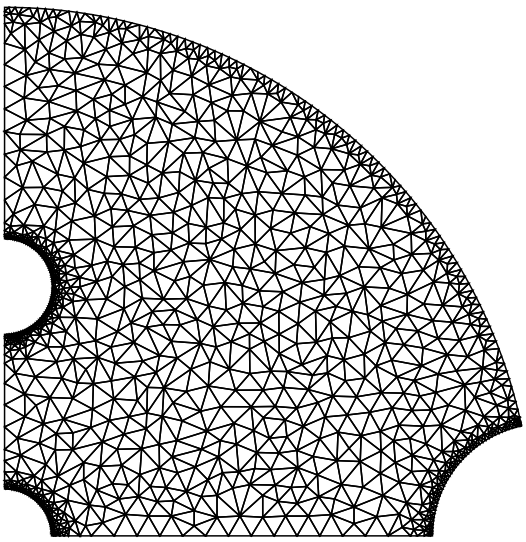

Figure 2.1: An example FEM mesh used in this dissertation.

continuous second-order polyomials spanned by the set of functions ψ_i on D such that $\psi_i(n_j) = \delta_{ij}$. That is, we parameterize our solution space with a basis of second order polynomials such that ψ_i is one on node n_i and vanishes on all other nodes. In this way we can approximate any function as

$$u \approx \sum_{i=1}^{N} u_i \psi_i \,, \tag{2.2}$$

where $u_i = u(n_i)$ and N is the number of nodes in the mesh. We can improve this approximation by increasing the number of elements in the mesh.

Note that ψ_i is non-vanishing only on the set of elements containing n_i. In the discussion below and in the attached code, we refer to such a set as the "neighborhood" of n_i, and we can simplify some of the computations by restricting only to the appropriate neighborhood. We plot an example ψ_i and highlight its associated neighborhood in figure 2.2.

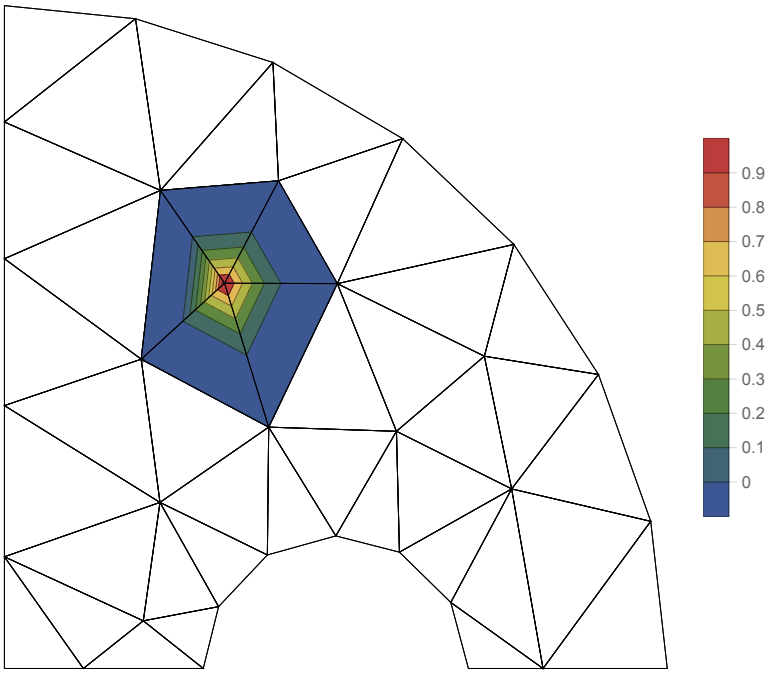

Figure 2.2: A contour plot of ψ_i for a particular n_i and FEM mesh. Note that ψ_i is 1 on n_i, 0 on $n_j \neq n_i$, and non-vanishing only in the highlighted neighborhood $\mathscr{N}_i$.

2.1.2 Solving the differential equation

To convert the equation (2.1) to a matrix equation, we can integrate both sides against an arbitrary ψ_i.

$$\int_D \nabla^2 u \, \psi_i + \int_D f \, u \, \psi_i = \int_D g \, \psi_i \, . \tag{2.3}$$

Integrating by parts gives the equation

$$\int_{\partial D} \nabla_n u \, \psi_i - \int_D \nabla u \cdot \nabla \psi_i + \int_D f \, u \, \psi_i = \int_D g \, \psi_i \, . \tag{2.4}$$

Finally we can use the approximation eq. (2.2) to convert this equation into a matrix equation:

$$\sum_{j=1}^{N} u_j \left[\int_{\partial D} \psi_i \nabla_n \psi_j\right] - \sum_{j=1}^{N} u_j \left[\int_D \nabla\psi_i \cdot \nabla\psi_j\right] + \sum_{j=1}^{N} u_j f_j \left[\int_D \psi_i\psi_j\right] = \sum_{j=1}^{N} g_j \left[\int_D \psi_i\psi_j\right] . \tag{2.5}$$

This equation is a bit ugly, but we can clean it up by introducing the following notation:

$$M_{ij} = \int_D \psi_i\psi_j \qquad W_{ij} = \int_D \nabla\psi_i \cdot \nabla\psi_j \qquad K_{ij} = \int_{\partial D} \psi_i \nabla_n \psi_j \tag{2.6}$$

where M and W are often called the "mass" and "stiffness" matrices respectively. Note that K_{ij} is non-zero only when both n_i and n_j are on the boundary.[1] With these definitions we can write our equation as

$$\begin{aligned} \sum_{j=1}^{N} K_{ij}u_j - \sum_{j=1}^{N} W_{ij}u_j + \sum_{j,k=1}^{N} M_{ij}(f_j\delta_{kj})u_k &= \sum_{j=1}^{N} M_{ij}g_j \\ \sum_{j=1}^{N} \left[K_{ij} - W_{ij} + \sum_{k=1}^{N} M_{ik}(f_k\delta_{kj})\right] u_j &= \sum_{j=1}^{N} M_{ij}g_j \,, \end{aligned} \tag{2.7}$$

which now takes the form of a matrix equation $A \cdot \vec{u} = \vec{b}$. We can easily solve this equation using the `LinearSolve` function in *Mathematica*, after appropriately enforcing the boundary conditions.

In this dissertation, we exclusively use boundary conditions which can be converted into a Neumann-type form. That is, we only consider cases where we can rewrite K_{ij}

[1] Additionally it is often possible to rewrite K_{ij} in a simpler manner using the boundary conditions. We do so in the applications of FEM to this dissertation and later in this section.

using the boundary conditions $\nabla_n u = f$ in the manner

$$\sum_{j=1}^{N} K_{ij} u_j = \int_{\partial D} \psi_i \nabla_n u = \int_{\partial D} \psi_i f = \sum_{j=1}^{N} \int_{\partial D} \psi_i \psi_j f_j \,. \tag{2.8}$$

In this way, we have converted the term K_{ij} in our matrix equation into a source term given by $\sum_{j=1}^{N} C_{ij} f_j$ where

$$C_{ij} = \int_{\partial D} \psi_i \psi_j \,. \tag{2.9}$$

This new source term enforces the appropriate boundary conditions, and so no further modifications need to be made to eq. (2.7) to ensure the solution obeys them. The modified equation is given by

$$\sum_{j=1}^{N} \left[-W_{ij} + \sum_{k=1}^{N} M_{ik} (f_k \delta_{kj}) \right] u_j = \sum_{j=1}^{N} \left[M_{ij} g_j - C_{ij} f_j \right] \,. \tag{2.10}$$

2.1.3 Computation of matrix elements

In practice, we can compute the matrices M, W, and C by deriving an analytic formula based on a unit "reference element" R with vertices at $(0,0)$, $(0,1)$, and $(1,0)$ as drawn in figure 2.3. Note that as ψ_i is non-vanishing only in the neighborhood of n_i (denoted by $\mathscr{N}_i$) we can write

$$M_{ij} = \int_D \psi_i \psi_j = \int_{\mathscr{N}_i \cap \mathscr{N}_j} \psi_i \psi_j = \sum_{E \in \mathscr{N}_i \cap \mathscr{N}_j} \int_E \psi_i \psi_j \,. \tag{2.11}$$

Therefore we can decompose M_{ij} (and similarly W_{ij} and C_{ij}) as a sum of integrals over elements in $\mathscr{N}_i \cap \mathscr{N}_j$. It will be useful then to derive analytic formulas for the following

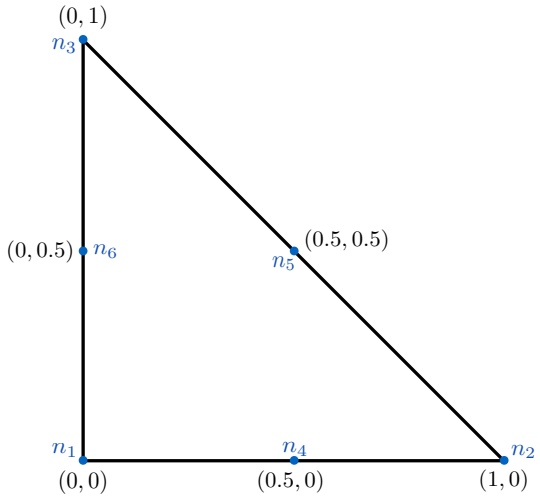

Figure 2.3: The unit reference element with nodes labeled.

integrals over an arbitrary element E specified by the coordinates of its vertices:

$$m_{ij} = \int_E \psi_i \psi_j \qquad w_{ij} = \int_E \nabla\psi_i \cdot \nabla\psi_j \qquad c_{ij}(s) = \int_s \psi_i \psi_j \,, \tag{2.12}$$

where E is assumed to contain nodes n_i and n_j and s is a particular boundary segment of E. First we can compute the value of these integrals on the unit reference element, then transform to an arbitrary element E using an appropriate change of coordinates.[2] Quantities associated with the reference element we denote by a superscript R.

First we can write ψ_i for the reference element:

$$\begin{aligned} &\psi_1^{(R)} = (x+y-1)(2x+2y-1)\,, \quad \psi_2^{(R)} = x(2x-1)\,, \quad \psi_3^{(R)} = y(2y-1)\,, \\ &\psi_4^{(R)} = 4x(1-x-y)\,, \qquad\qquad \psi_5^{(R)} = 4xy\,, \qquad\qquad \psi_6^{(R)} = 4y(1-x-y)\,. \end{aligned} \tag{2.13}$$

One can easily see that these functions are second order polynomials that satisfy $\psi_i(n_j) = \delta_{ij}$ as required. Additionally, given these expressions we can analytically compute the 36

[2]One can also compute these integrals using Gaussian quadrature rules as in [36], but we choose to eliminate the need to compute any analytic derivatives of the ψ_i.

matrix elements of $m_{ij}^{(R)}$, $w_{ij}^{(R)}$, and each of the three $c_{ij}^{(R)}(s)$.

To transform from the reference element to an arbitrary element with nodes $n_i = (x_i, y_i)$, we can perform the coordinate transformation

$$\begin{pmatrix} x' \\ y' \end{pmatrix} = \begin{pmatrix} x_2 - x_1 & x_3 - x_1 \\ y_2 - y_1 & y_3 - y_1 \end{pmatrix} \begin{pmatrix} x \\ y \end{pmatrix} + \begin{pmatrix} x_1 \\ y_1 \end{pmatrix} . \tag{2.14}$$

Using the standard change of basis formulas for integrals and derivatives, we can derive analytic expressions for the matrix elements as functions of the vertices (x_i, y_i) of E:

$$m_{ij} = |J| \begin{bmatrix} \frac{1}{60} & -\frac{1}{360} & -\frac{1}{360} & 0 & -\frac{1}{90} & 0 \\ -\frac{1}{360} & \frac{1}{60} & -\frac{1}{360} & 0 & 0 & -\frac{1}{90} \\ -\frac{1}{360} & -\frac{1}{360} & \frac{1}{60} & -\frac{1}{90} & 0 & 0 \\ 0 & 0 & -\frac{1}{90} & \frac{4}{45} & \frac{2}{45} & \frac{2}{45} \\ -\frac{1}{90} & 0 & 0 & \frac{2}{45} & \frac{4}{45} & \frac{2}{45} \\ 0 & -\frac{1}{90} & 0 & \frac{2}{45} & \frac{2}{45} & \frac{4}{45} \end{bmatrix}$$

$$w_{ij} = \frac{1}{6|J|} \begin{bmatrix} 3\,\chi_{23} & \xi_3 & \xi_2 & -4\,\xi_3 & 0 & -4\,\xi_2 \\ \xi_3 & 3\,\chi_{13} & \xi_1 & -4\,\xi_3 & -4\,\xi_1 & 0 \\ \xi_2 & \xi_1 & 3\,\chi_{12} & 0 & -4\,\xi_1 & -4\,\xi_2 \\ -4\,\xi_3 & -4\,\xi_3 & 0 & 4\,(\chi_{12}+\chi_{13}+\chi_{23}) & -8\,\xi_2 & -8\,\xi_1 \\ 0 & -4\,\xi_1 & -4\,\xi_1 & -8\,\xi_2 & 4\,(\chi_{12}+\chi_{13}+\chi_{23}) & -8\,\xi_3 \\ -4\,\xi_2 & 0 & -4\,\xi_2 & -8\,\xi_1 & -8\,\xi_3 & 4\,(\chi_{12}+\chi_{13}+\chi_{23}) \end{bmatrix} , \tag{2.15}$$

where we have used the notations

$$|J| = |\,(x_3 - x_2)\,y_1 + (x_1 - x_3)\,y_2 + (x_2 - x_1)\,y_3|$$

$$\xi_1 = (x_1 - x_2)(x_1 - x_3) + (y_1 - y_2)(y_1 - y_3)$$

$$\xi_2 = (x_2 - x_1)(x_2 - x_3) + (y_2 - y_1)(y_2 - y_3)$$

$$\begin{aligned}
\xi_3 &= (x_3 - x_1)(x_3 - x_2) + (y_3 - y_1)(y_3 - y_2) \\
\chi_{12} &= (x_1 - x_2)^2 + (y_1 - y_2)^2 \\
\chi_{23} &= (x_2 - x_3)^2 + (y_2 - y_3)^2 \\
\chi_{13} &= (x_1 - x_3)^2 + (y_1 - y_3)^2 \,.
\end{aligned} \tag{2.16}$$

For $c_{ij}^{(s)}$ we can write the matrix elements as

$$\begin{aligned}
c_{a_s a_s}^{(s)} &= c_{b_s b_s}^{(s)} = 2/15|s| \\
c_{a_s d_s}^{(s)} &= c_{b_s d_s}^{(s)} = 1/15|s| \\
c_{a_s b_s}^{(s)} &= -1/30|s| \\
c_{d_s d_s}^{(s)} &= 8/15|s| \,,
\end{aligned} \tag{2.17}$$

where all matrix elements not implied by $i \leftrightarrow j$ symmetry vanish and segment s extends between nodes a_s and b_s with midpoint d_s, and $|s|$ is the Euclidean length of segment s. Using these formulas provides an efficient way to compute M_{ij}, W_{ij}, and C_{ij} and, then numerically solve a given differential equation in terms of the matrix equation eq. (2.10).

2.2 Handlebody Phases

All solutions of vacuum Einstein's equations with negative cosmological constant in 2+1 dimensions are quotients of AdS_3. These solutions provide a rich set of spacetimes for probing holography, as we are able to construct geometries with non-trivial topology simply by taking quotients. In this dissertation, these geometries arise as the gravitational duals of CFT states in two dimensions defined via a Euclidean path integrals. For a state defined as a path integral over a genus g Riemann surface X, the associated gravitational

path integral with boundary conditions $\partial M = X$ has a set of Euclidean saddles which we can characterize by specifying a set of g cycles on the boundary to be made contractible in the bulk. We refer to these saddles as handlebody phases, which have been extensively studied in [37, 38, 39, 40, 41, 36], and which are the focus of this section.

In this section, we review methods for constructing these handlebody phases and evaluating their actions. We focus on practical tools and formulas for doing computations, and we refer the reader to §3.3 and the various references for more details on the rich mathematical theory underlying these methods. In particular, we will show how to compute the regularized Einstein Hilbert action in the conformal frame where $R_{\text{bndy}} = -2/\ell^2$, and we will set $\ell = 1$.

2.2.1 Schottky Uniformization

We can construct a convenient representation of a handlebody phase, called a Schottky uniformization, by starting with the boundary Riemann surface X of genus g. To specify a handlebody phase, we need to choose a set of g independent and non-intersecting cycles to be made contractible in the bulk. For example, given a basis $\{\alpha_i, \beta_j\}$ of the homotopy group of X such that $\alpha_i \beta_j = \delta_{ij}$ and $\prod_i \alpha_i^{-1} \beta_i^{-1} \alpha_i \beta_i = 1$, we can choose the set of g cycles $\{\alpha_i\}$, the cycles $\{\beta_i\}$, or any set of cycles given by the image of $\{\alpha_i\}$ under an element of the mapping class group.

Having chosen a set of g cycles, we now cut open the Riemann surface along each cycle and label each side of the cut C_i and C_i'. The resulting surface is a Riemann sphere punctured by $2g$ circles that come in pairs. We can project this sphere into the complex plane, resulting in a Schottky domain for X. It is often useful to make sure that certain reflection and rotational symmetries of X are preserved along the way, although it is sometimes not possible to preserve all such symmetries (see §3.5 for an

example). Alternatively, one can begin with $2g$ circles in the complex plane and then reverse engineer the corresponding surface X and handlebody phase, although we found this process to be more difficult in practice.[3]

The region in $\mathbb{C}$ exterior to all the C_i and C_i' can be taken as a fundamental domain D for the surface X. As C_i and C_i' are the same cycle on X, we can recover X from the Schottky uniformization by taking the quotient by the subgroup of Möbius transformations $\langle L_i \rangle$, where each L_i maps the interior of C_i to the exterior of C_i'.

The Schottky domain resulting from this construction describes a bulk phase in which the initial cycles chosen on the boundary are contractible in the bulk. If we consider the half-plane model of $\mathbb{H}^3$ with the complex plane as its boundary,[4] we can extend the identifications on the boundary into the bulk along geodesic hemispheres. That is, the quotient group acts in the bulk by identifying the hemispheres anchored on C_i and C_i'. In this way, the cycles homologous to C_i on the boundary are contractible in the bulk, as they may be lifted off the boundary along the corresponding hemisphere and shrunk down to a point. The dual cycles running between C_i and C_i' remain non-contractible. Therefore, we have successfully described the handlebody phase with the requisite boundary cycles contractible in the bulk.

One way to characterize a handlebody phase is by the topology of a particular slice through the bulk, often corresponding to a moment of time-reflection symmetry. When this slice is fixed by a reflection symmetry of the boundary X, we can compute the topology using the following formula:

$$g_{\text{slice}} = \frac{1}{2}(n - b + 1)\,, \tag{2.18}$$

[3]There is an additional complication that sometimes the symmetries of X act in a non-trivial way on the Schottky uniformization, so determining the bulk geometry on a particular symmetry slice of the boundary can be difficult.

[4]We remind the reader that Euclidean AdS_3 is $\mathbb{H}^3$ or three dimensional hyperbolic space.

where b is the number of disconnected boundaries of the slice and n is the number of pairs of circles that lie on the slice. Note that the assumption of reflection symmetry ensures that either both circles of a pair lie on the slice or neither do. For example, a slice intersecting 2 pairs of circles that divides the boundary into 3 disconnected circles has no topology in the interior, and so this slice describes a simple three boundary wormhole.

To compare the gravitational action between different phases, we must numerically solve for a standard conformal frame on the boundary and regularize the action. Additionally, we must be sure to compare phases with the same boundary X, and so we will need to compute the moduli of the boundary for each phase, and match the moduli between phases. This process is computationally intensive, but we may sometimes use a heuristic to get a rough understanding of the phase diagram.

In general the phase with minimal action will be the one in which the total length of the boundary cycles made contractible is minimized.[5] Note that for many phases there is not a unique choice of g cycles that yield that phase, and so when applying the heuristic one must choose the choice of g cycles that yields the minimal action. We can summarize this heuristic simply as: *"Shorter cycles are more likely to pinch off than longer cycles"*. While this heuristic does not hold exactly (in fact we can construct cases where it fails), it is true approximately in the sense that as boundary cycles get longer the phase in which they are contractible becomes more subdominant. In this way, this heuristic is a useful shortcut for determining the general structure of the phase diagram.

2.2.2 The boundary metric

In order to fully specify the boundary Riemann surface X and the corresponding handlebody phase, along with the set of contractible cycles we need to additionally specify the $3g-3$ moduli of the boundary. In the cases we consider, some of the moduli

[5]Note that we have fixed the conformal frame of the boundary to be $R_{\text{bndy}} = -2$.

are fixed by symmetry, while others are computed by evaluating the lengths of certain geodesics on the boundary. Therefore, we need to specify a boundary metric before we can fully match a Schottky uniformization with its Riemann surface X. As detailed in [40], to properly renormalize the gravitational action, we should choose a conformal frame on the boundary in which $R_{\text{bndy}} = -2$. As all metrics in 2d are conformally flat, we can write in general

$$ds^2 = e^{2\phi(w)}|dw|^2\,, \tag{2.19}$$

where $\phi(w)$ is an arbitrary function for which we will solve. The regularity of the metric under the quotient by the L_i imposes the following boundary conditions on ∂D:

$$\phi(L_i(w)) = \phi(w) - \frac{1}{2}\log|L_i'(w)|^2\,. \tag{2.20}$$

Additionally, the requirement $R_{\text{bndy}} = -2$ yields the Liouville equation for ϕ:

$$\nabla^2\phi = e^{2\phi}\,. \tag{2.21}$$

In all cases we consider, the circles C_i and C_i' are fixed point sets of a symmetry of D given by inversion through some circle in the complex plane. Using polar coordinates (r_I, θ_I) centered on the circle of inversion with radius R_I, invariance of the metric under this symmetry requires that

$$\phi(R_I^2/r_I, \theta_I) = \phi(r_I, \theta_I) + \log(r_I^2/R_I^2)\,. \tag{2.22}$$

Differentiating with respect to the unit normal $\hat{r}_I$ we find

$$\partial_{r_I}\phi(R_I^2/r_I,\theta) = -\frac{r_I^2}{R_I^2}\left(\partial_{r_I}\phi(r_I,\theta_I) + \frac{2}{r_I}\right). \tag{2.23}$$

Evaluating this equation on $r_I = R_I$ we have the simple formula that on C_I

$$\partial_{R_I}\phi|_{C_I} = -\frac{1}{R_I}. \tag{2.24}$$

In fact, we can show that when C_i and $C_{i'}$ are related by an involution symmetry, this equation also holds on C_i and $C_{i'}$. First, we consider C and C' as concentric circles centered at the origin with radii λ and $1/\lambda$ respectively with $\lambda > 1$, and $L(w) = w/\lambda^2$. The domain D is the region between the circles[6]. From the boundary conditions eq. (2.20) we have

$$\frac{1}{\lambda^2}\partial_r\phi(1/\lambda) = \partial_r\phi(\lambda). \tag{2.25}$$

Additionally, C and C' are related by inversion through the unit circle, and so by eq. (2.23) we have

$$\partial_r\phi(1/\lambda) = -\lambda^2\left(\partial_r\phi(\lambda) + \frac{2}{\lambda}\right). \tag{2.26}$$

Solving these two equations and noting $\nabla_n = \pm\partial_r$ for C and C' respectively we have

$$\nabla_n\phi|_C = -\frac{1}{\lambda} \qquad \nabla_n\phi|_{C'} = \lambda. \tag{2.27}$$

[6]Note that the "outside" of C is the region including the origin.

Or in general we have

$$\nabla_n \phi|_{C_i} = \frac{\sigma}{R_i}\,, \tag{2.28}$$

where $\sigma_i = \pm 1$ for D outside or inside of C_i respectively and R_i is the radius of C_i.

To show that the condition eq. (2.28) holds whenever C_i and $C_{i'}$ are related by an involution symmetry, we can perform a Möbius transformation to move the unit circle to the appropriate circle of involution. Let the appropriate transformation be given by

$$w' = \frac{a\,w + b}{c\,w + d}\,. \tag{2.29}$$

Under this transformation we have

$$\vec{\nabla}' \left(\phi(w') - \frac{1}{2} \log \left| \frac{bc - ad}{(a - c\,w')^2} \right|^2 \right) = J^{-1} \cdot \vec{\nabla} \phi(w)\,, \tag{2.30}$$

where J is the Jacobian of the transformation eq. (2.29). As on C and C' we know $\vec{\nabla}\phi(w)$ from eq. (2.27) and we can compute J, we can solve this equation for $\vec{\nabla}'\phi(w')$. Taking the inner product with the normal vector on the image of C and C' under the coordinate transformation yields eq. (2.28).

We can now solve eq. (2.21) using the Newton-Raphson algorithm and the finite element methods described in the previous section. First, we write $\phi = \phi_{(n)} + \delta\phi_{(n)}$ and expand the Liouville to first order in $\delta\phi_{(n)}$:

$$\nabla^2 \delta\phi_{(n)} - 2e^{2\phi_{(n)}} \delta\phi_{(n)} = -\left(\nabla^2 \phi_{(n)} - e^{2\phi_{(n)}} \right)\,. \tag{2.31}$$

With the assumption that all C_i and $C_{i'}$ are related by a $\mathbb{Z}_2$ symmetry of the domain, we can rewrite the boundary conditions eq. (2.20) as Neumann-type conditions eq. (2.28).

In the manner discussed in the previous section, we can enforce these boundary conditions by introducing a source term in the integral form of our differential equation:[7]

$$-\int_D \nabla\psi\cdot\nabla\delta\phi_{(n)} - 2\int_D \psi\, e^{2\phi_{(n)}}\,\delta\phi_{(n)} = \int_D \nabla\psi\cdot\nabla\phi_{(n)} + \int_D \psi\, e^{2\phi_{(n)}} + \sum_i \frac{1}{R_i}\int_{\partial D_i}\psi\, d\theta_i\,. \tag{2.32}$$

This equation is now in the form to apply the formulas from the previous section.

Further, we can often use the symmetries of the Schottky uniformization to reduce D down to a reduced domain $\tilde{D}$. In all cases we consider, we use at least one reflection symmetry to reduce D, and without loss of generality we can choose for this reflection symmetry to act as inversion through the unit circle. Therefore, we choose to always work with a finite domain $\tilde{D}$. Note that the boundary conditions on the unit circle are fixed by eq. (2.24), and are accounted for by the final term in eq. (2.32).

Using FEM to discretize this equation, we then can solve the appropriate matrix equation for $\delta\phi_{(n)}$. Then, we update our solution to $\phi_{(n+1)} = \phi_{(n)} + \delta\phi_{(n)}$ and solve a similar equation for $\delta\phi_{(n)}$. Starting with an initial seed of $\phi_{(0)} = 0$, we repeat this process until $||\delta\phi_{(n+1)}||_\infty < 10^{-10}$ or another desired accuracy.

Given the solution for ϕ, we can use the metric to numerically compute the lengths of all segments of $\partial\tilde{D}$. However, to compute the lengths of geodesics that do not make up $\partial\tilde{D}$ we must use a different method. We note that the region $\tilde{D}$ with $R_{\text{bndy}} = -2$ can be represented as a region in $\mathbb{H}^2$, and so if we can construct this region we can use the known analytic properties of $\mathbb{H}^2$ to compute the lengths of geodesics. Given a region $\tilde{D}$ with boundary segments $\partial\tilde{D}_i$ given by geodesics that meet at right angles,[8] we can construct a corresponding region in $\mathbb{H}^2$ by the following algorithm. First, we start with

[7]Note that in the last term the orientation σ_i is absorbed into the orientation of $d\theta_i$ in the manner described in the next section.

[8]This condition will be guaranteed by our symmetry requirements.

an arbitrary geodesic segment of length $|\partial\tilde{D}_1|$. Next, we solve for the geodesic in $\mathbb{H}^2$ that intersects it orthogonally, and we follow that geodesic for length $|\partial\tilde{D}_2|$. We continue this process until we have represented all boundary segments and form a closed region. Using this region in $\mathbb{H}^2$, we can now solve for the lengths of geodesics using well known formulas. In this way, we can compute all the remaining moduli of the boundary X.

2.2.3 The bulk action

We can now compute the Einstein-Hilbert action for the associated handlebody phase. In terms of the field ϕ it was shown in [36] that the regularized action is given by

$$I = -\frac{c}{24\pi}\left[I_{\mathrm{TZ}}[\phi] - A - 4\pi(g-1)(1-\log 4\rho_0^2)\right] , \tag{2.33}$$

where A is the area of the boundary, $c = 3/2G_N$ is the central charge of the dual CFT, and ρ_0 is the radius of the sphere for which the partition function is one, and we set $\rho_0 = 1$. Additionally defining R_i to be the radius of C_i and Δ_i as the distance between the center of C_i and the point $w_\infty^{(i)}$ mapped to ∞ by L_i, we have,

$$I_{TZ}[\phi] = \int_D d^2w \left((\nabla\phi)^2 + e^{2\phi}\right) + \sum_i \left(\int_{C_i} 4\phi\, d\theta_\infty^{(i)} - 4\pi \log\left|R_i^2 - \Delta_i^2\right|\right) , \tag{2.34}$$

where $\theta_\infty^{(i)}$ is the angle measured from the point $w_\infty^{(i)}$. In the rest of this section, we use our assumption of symmetries to simplify this action and derive useful formulas.

First, we note that on shell we have the relation

$$A = \int_D d^2w\, e^{2\phi} \tag{2.35}$$

and therefore the term A in eq. (2.33) cancels part of the integration in eq. (2.34).

Further, we can reduce the remaining ntegral over D to integrations over $\tilde{D}$ using the various inversion and reflection symmetries. Using the relation eq. (2.23) we have

$$\int_D d^2w\,(\nabla\phi)^2 = 2\int_{\tilde{D}} d^2w\left[(\nabla\phi)^2 + \frac{2}{r_I}\partial_{r_I}\phi + \frac{2}{r_I^2}\right]. \tag{2.36}$$

In practice, we only use reflections and inversion through the unit circle to reduce the Schottky domain.[9] We can think of a reflection as the limit of an inversion where $r_I \to \infty$, and so we see that there are no additional terms generated by this reduction (i.e. we can simply integrate over half the domain and multiply by a factor of 2). Therefore reducing the domain by a product of s reflections and an inversion through the unit circle yields

$$\begin{aligned}\int_D d^2w\,(\nabla\phi)^2 &= 2^{s+1}\left[\int_{\tilde{D}} d^2w\,(\nabla\phi)^2 + \int_{\tilde{D}} d^2w\left(\frac{2}{r}\partial_r\phi + \frac{2}{r^2}\right)\right] \\ &= 2^{s+1}\int_{\tilde{D}} d^2w\,(\nabla\phi)^2 + 2^{s+2}\int_{\partial\tilde{D}}\phi\,d\theta + 2^{s+2}\int_{\partial\tilde{D}}\log r\,d\theta\,.\end{aligned} \tag{2.37}$$

We can additionally integrate by parts to get

$$\int_D d^2w\,(\nabla\phi)^2 = -2^{s+1}\int_{\tilde{D}} d^2w\phi\nabla^2\phi + 2^{s+1}\int_{\partial\tilde{D}}\phi\nabla_n\phi + 2^{s+2}\int_{\partial\tilde{D}}\phi\,d\theta + 2^{s+2}\int_{\partial\tilde{D}}\log r\,d\theta\,, \tag{2.38}$$

which we can further simplify using the equations of motion $\nabla^2\phi = e^{2\phi}$.

Note that with our assumptions the boundary of $\tilde{D}$ consists of lines through the origin, the unit circle U, and some portion of the circles C_i, C_i', and so we write $\partial\tilde{D} = \{\partial D_i\}$. It is thus convenient to write the integrals over $\partial\tilde{D}$ above as integrals over these lines and circles. All the integrals over the lines through the origin vanish due to either $d\theta$ or

[9]Note that for some domains we consider inversion through the unit circle is not a symmetry, but the product of this inversion with a reflection is a symmetry. The discussion that follows also applies to this case.

$\vec{\nabla}_n\phi$ vanishing, and so we are left with the integral over circles. Denoting $\mathscr{I}[\partial D_i]$ the contribution to the action from boundary segment ∂D_i, we can write the action as

$$-\frac{24\pi}{c}I = -4\pi(g-1)(1-\log 4) - 2\int_{\tilde{D}} \phi\, e^{2\phi}\, d^2w + \sum_i \mathscr{I}\left[\partial D_i\right] , \tag{2.39}$$

where $\mathscr{I}[\partial D_i]$ includes possible contributions coming from eq. (2.34). We now compute this contribution for each type of boundary segment. The following subsection is rather technical, and should be thought of as a compendium of useful formulas. The reader more interested in the overall narrative should skip to the example in §2.4.

2.2.4 Boundary circle contributions

For simplicity, in this section we only compute the contribution reduced over inversion through the unit circle (or the product of this inversion and a reflection). Reducing over more reflections is straightforward and simply multiplies certain terms by factors of 2. Throughout this section, we leave the sign inherited through the orientation of ∂D implicit, i.e. we have

$$\int_{C_i} d\theta_0^{(i)} = \pm\, 2\pi \tag{2.40}$$

where we choose the positive or negative sign when D lies inside or outside C_i respectively.

As previously mentioned, when ∂D_i is a line the contribution $\mathscr{I}[\partial D_i]$ vanishes. For the unit circle U, we only have the contribution from eq. (2.38):

$$\mathscr{I}[U] = 2\int_U \phi\nabla_n\phi\, d\theta + 4\int_U \phi\, d\theta\,, \tag{2.41}$$

as the $\log r$ term vanishes on U. We can use eq. (2.24) to rewrite the normal derivative

and we have

$$\mathscr{I}[U] = 2\int_U \phi \, d\theta \,. \tag{2.42}$$

The rest of the boundary segments are made up of parts or all of C_i and C_i'. There are multiple cases depending on the positions of these circles, and we go through all of them in detail. Note that we only consider cases in which the domain can be reduced by at least inversion through the unit circle, and additionally in which C_i and C_i' are the fixed point set of a symmetry of the domain.

In the simplest case, only one of C_i or C_i' is included in $\partial\tilde{D}$ and this circle does not intersect U. Without loss of generality, we can choose C_i to be included in $\partial\tilde{D}$, so we have contributions to $\mathscr{I}[C_i]$ from eq. (2.38) and from the final summation in eq. (2.34). Using the boundary conditions eq. (2.28) we have

$$\mathscr{I}[C_i] = -2\int_{C_i} \phi \, d\theta_0^{(i)} + 4\int_{C_i} \phi \, d\theta + 4\int_{C_i} \log r d\theta + 4\int_{C_i} d\theta_\infty^{(i)} - 4\pi \log|R_i^2 - \Delta_i^2| \,, \tag{2.43}$$

where $\theta_0^{(i)}$ is the angular coordinate measured from the center of C_i. Additionally, one can show

$$\int_{C_i} \log r d\theta = \pi \log\left(1 - R_i^2/X_i^2\right) \,, \tag{2.44}$$

for $X_i > R_i$ where X_i is the Euclidean distance of the center of C_i from the origin. Putting everything together we have

$$\mathscr{I}[C_i] = 2\int_{C_i} \phi \, \left(2d\theta + 2d\theta_\infty^{(i)} - d\theta_0^{(i)}\right) + 4\pi \log \frac{1 - R_i^2/X_i^2}{|R_i^2 - \Delta_i^2|} \,. \tag{2.45}$$

Further, numerically it is only convenient to integrate over $d\theta_0^{(i)}$, and so we can introduce Jacobian factors to transform $d\theta$ and $d\theta_\infty^{(i)}$. In general integrating on C_i over an angle ξ measured from a point along the axis connecting the origin and X_i introduces the factor[10]

$$\frac{d\xi}{d\theta_0^{(i)}} = \frac{R_i(R_i - d\cos\theta_0^{(i)})}{d^2 - 2\,d\,R_i\cos\theta_0^{(i)} + R_i^2}\,, \tag{2.46}$$

where d is the signed distance between X_i and the point. For example, applying this formula to θ we have $d = -X_i$ and

$$\frac{d\theta}{d\theta_0^{(i)}} = \frac{R_i(R_i + X_i\cos\theta_0^{(i)})}{X_i^2 + 2\,X_i\,R_i\cos\theta_0^{(i)} + R_i^2}\,. \tag{2.47}$$

In the second case, we assume both C_i and $C_{i'}$ are fully contained in $\partial\tilde{D}$. By the symmetry assumptions, there must be a conjugate pair $C_{\bar{i}}$, $C_{\bar{i}'}$ related by inversion through the unit circle. Therefore we must account for the contribution from this pair as well. Following similar arguments and using the transformation of ϕ under the inversion (with details given in §4.A) we have

$$\begin{aligned}\mathscr{I}[C_i] + \mathscr{I}[C_i'] =& 2\int_{C_i}\phi\,(2d\theta + 2d\theta_\infty^{(i)} - d\theta_0^{(i)}) + 4\int_{C_i}(\phi + 2\log|w|)\frac{d\theta_\infty^{(\bar{i})}}{d\theta_0^{(\bar{i})}}\frac{d\theta_0^{(\bar{i})}}{d\theta_0^{(i)}}d\theta_0^{(i)} \\ &+ 2\int_{C_{i'}}\phi\,(2d\theta - d\theta_0^{(i')}) + 4\pi\log\frac{(1 - R_i^2/X_i^2)(1 - R_{i'}^2/X_{i'}^2)}{|R_i^2 - \Delta_i^2|\,\big|R_{\bar{i}}^2 - \Delta_{\bar{i}}^2\big|}\,.\end{aligned} \tag{2.48}$$

We can similarly introduce Jacobian factors of the form eq. (2.46) to numerically evaluate these integrals. The Jacobian for transforming the integral on $C_{(\bar{i})}$ to one on $C_{(i)}$ can be

[10]Note using the signed Jacobian factor is more convenient numerically as a built-in way to keep track of possible orientation reversal.

worked out geometrically as

$$\frac{d\theta_0^{(\bar{i})}}{d\theta_0^{(i)}} = \frac{R_i^2 - X_i^2}{X_i^2 + 2\,X_i\,R_i\cos\theta_0^{(i)} + R_i^2}\,. \tag{2.49}$$

Finally, we have to consider the cases in which C_i and C_i' intersect the unit circle. First, we consider when C_i is mapped to itself under inversion through the unit circle. In this case the analytic formulas were worked out in [36] and we have

$$\mathscr{I}[C_i] + \mathscr{I}[C_i'] = 2\int_{\tilde{C}_i} \phi\, d\theta_0^{(i)} + 2\int_{\tilde{C}_i'} \phi\, d\theta_0^{(i')} - 8\pi\log R_i + 8\int_0^{2\arctan R_i} \frac{x}{\sin x} dx\,, \tag{2.50}$$

where $\tilde{C}_i$ refers to the part of C_i that is part of $\partial\tilde{D}$ and similarly for $\tilde{C}_i'$.

Additionally, we can consider the case when inversion through the unit circle is not a symmetry, but the product of this inversion and a reflection is a symmetry. In this case, the part of C_i outside of $\tilde{D}$ gets mapped to the part of $C_{i'}$ inside $\tilde{D}$, and so we must include the appropriate Jacobian factor for inversion as in eq. (2.49), with an extra minus sign to account for the reversal of orientation.

$$\begin{aligned}\mathscr{I}[C_i] + \mathscr{I}[C_i'] =& 2\int_{\tilde{C}_i} \phi\,(2d\theta + 2d\theta_\infty^{(i)} - d\theta_0^{(i)}) + 4\int_{\tilde{C}_i} \log|w|\, d\theta \\ &+ 2\int_{\tilde{C}_{i'}} \phi\,(2d\theta - d\theta_0^{(i')}) + 4\int_{\tilde{C}_{i'}} \log|w|\, d\theta \\ &+ 4\int_{\tilde{C}_{i'}} (\phi + 2\log|w|)\frac{d\theta_\infty^{(i)}}{d\theta_0^{(i)}}\frac{d\theta_0^{(i)}}{d\theta_0^{(i')}} d\theta_0^{(i')} - 4\pi\log\left|R_i^2 - \Delta_i^2\right|.\end{aligned} \tag{2.51}$$

All of the above formulas are included in the attached *Mathematica* package, providing a convenient set of tools to study these phases.

2.3 A *Mathematica* package

In this section, we document the usage of the attached *Mathematica* package for computing the action and moduli of a handlebody phase. There are two packages included; *FEMfine.m* implements general finite element methods for numerically solving differential equations, and *handlebodies.m* provides a framework for solving for the handlebody geometry.

To load the packages, make sure both files are included in the same directory as the working notebook and execute

```
SetDirectory[NotebookDirectory[]];
<<``handlebodies.m'';
```

The *FEMfine* package is automatically loaded as part of *handlebodies*.

To solve for a handlebody, one must first specify the circles C_i and C_i' in the domain and the symmetries. There are five allowed circle types, as documented in figure 2.4, categorized according to the symmetry that C_i and C_i' are the fixed point set under. Inversion in the unit circle must be a symmetry of the domain, and one can additionally speicfy reflection across the x axis or y axis as symmetries. This framework allows one to construct all of the handlebody phases considered in this dissertation, and additionally one can construct a large set of handlebodies for general application.

In the *handlebodies* package, one can specify the handlebody via the following code:

```
InitializeHandlebody[]
AddCircle[{c1, r1, t1}]
AddCircle[{c2, r2, t2}]
...
AddSymmetry[``x'']
AddSymmetry[``y'']
```

where $c = \{c_x, c_y\}$ is the center of each circle, r is the radius, and t is the type. The function `IntializeHandlebody[]` resets the list of circles and symmetries, and sets the mesh

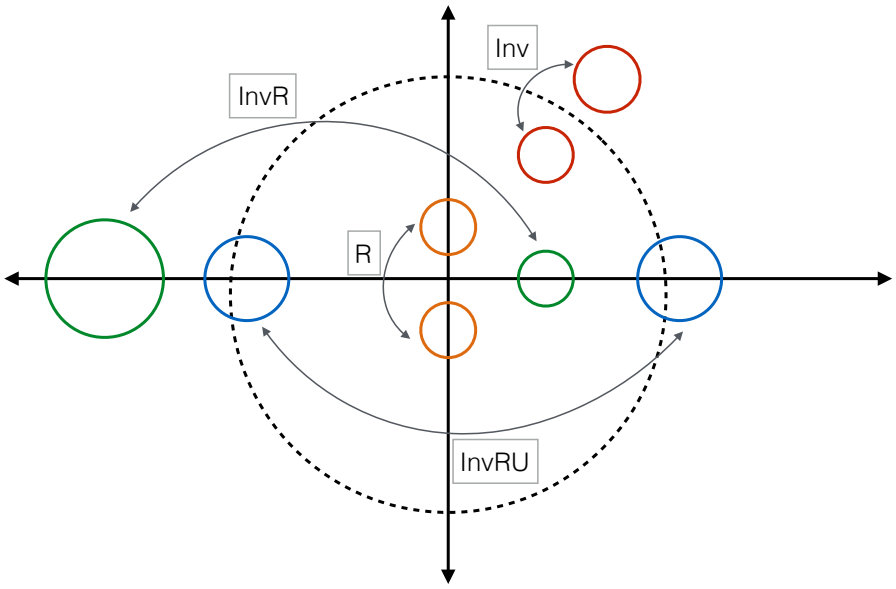

Figure 2.4: Illustration of the allowed circle types according to the symmetries that exchange C_i and C_i' as follows. "R": a reflection across $\hat{x}$ or $\hat{y}$. "Inv:" inversion through the unit circle. "InvR:" product of a reflection and inversion through the unit circle. "InvRU:" circles which are InvR and also intersect the unit circle. "RU" (not pictured): circles exchaged by reflection and also intersect the unit circle, and additionally must be fixed under inversion through unit circle.

generation parameters in *Mathematica*'s `ToElementMesh` function as "MaxCellMeasure"→ 0.005 and "AccuracyGoal"→ 4. To increase the quality of the mesh, one can change the values of these parameters by resetting the variables `mcm` and `ag` to the desired values after the handlebody is initialized.

Once the handlebody is specified, the executing the command `SolveHandlebody[name]` computes a set of quantities and stores them as `name[''Attribute'']`. If no variable `name` is specified the attributes are stored as `Handlebody[''Attribute'']`. The full list of quantities computed can be seen in the package documentation, and a few relevant ones are listed below.

- `name[''genus'']`: Genus of boundary Riemann surface
- `name[''mesh'']`: Finite element mesh used to discretize domain D

- `name[``CError'']`: Estimation of numerical error due to discretization by mesh
- `name[``AError'']`: Estimation of numerical error from computation of area compared to the area determined from the genus by the Gauss-Bonnet theorem
- `name[``BoundaryLengths'']`: List of the length of each boundary segment ∂D_i compute using the solution for the metric in the order {circle segments, x segments, y segments} with the order for the circle segments given by the order they were added, with the unit circle first.
- `name[``Action'']`: The Einstein-Hilbert action for the handlebody

One can read off various moduli of the Riemann surface in the list of boundary segment lengths, and additionally one can use this list to construct the analogous region in $\mathbb{H}^2$ to compute the rest of the moduli.

Additionally, one must match moduli between different phases to determine the dominant phase for given boundary conditions. The `NM` function and `GradSearch` function are included as part of *handlebodies* as convenient ways to match moduli using Newton's method and a gradient search method respectively. The documentation for these functions can also be read off from the package.

2.4 An example

As an example, we can use the *handlebodies* package and the methods outlined in this section to study the toroidal geon phase originally studied in [36]. First, we choose boundary conditions given by a genus 2 Riemann surface drawn in figure 2.5 with three $\mathbb{Z}_2$ symmetries. This Riemann surface has a two dimensional moduli space leftover after imposing these symmetries.

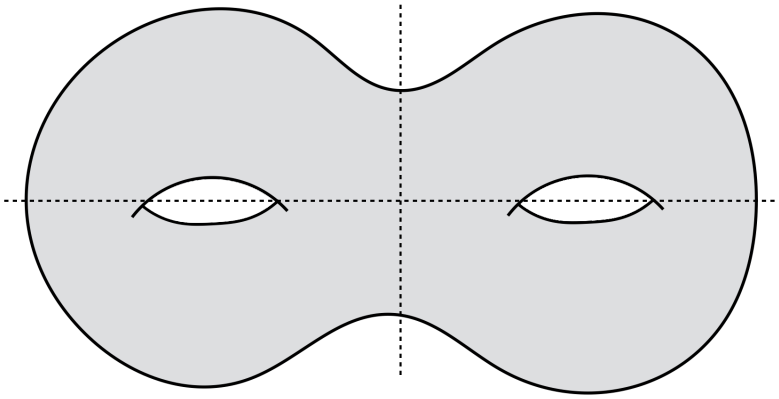

Figure 2.5: Boundary Riemann surface with three $\mathbb{Z}_2$ symmetries given by reflection in each dashed line and the plane of the page.

In order to specify a handlebody phase, we choose two independent cycles to make contractible in the bulk. There are three distinct choices that respect the $\mathbb{Z}_2$ symmetries of the boundary. Letting the α cycles go around the handles (red in fig 2.6a) and the β cycles go around the holes (orange in fig 2.6a), the phases are defined by choosing $\{\alpha_1, \alpha_2\}$ contractible, choosing $\{\beta_1, \beta_2\}$, or choosing $\{\alpha_1 - \alpha_2, \beta_1 + \beta_2\}$. Each of these choices results in a different handlebody phase.

We choose to study the phase in which $\{\alpha_1 - \alpha_2, \beta_1 + \beta_2\}$ are contractible. These cycles are drawn in blue and green on figure 2.6a respectively. To study this phase we must first cut the Riemann surface apart along theses cycles and project it into the complex plane. First, cutting the Riemann surface along $\alpha_1 - \alpha_2$ yields a square torus with two punctures related by a reflection symmetry. Next, we can cut this torus along its β cycle (i.e. $\beta_1 + \beta_2$) to yield the Riemann sphere with four punctures, where the punctures are identified by orthogonal reflection symmetries. Projecting this sphere into the plane gives the Schottky domain drawn in figure 2.6b. Reflection about the $\hat{x}$ and $\hat{y}$ axis identify each pair of C_i, C_i', and inversion in the unit circle leaves the domain unchanged. Additionally, we can identify the cycles α_1 and β_1 in this domain as the fixed point sets under the relevant symmetries.

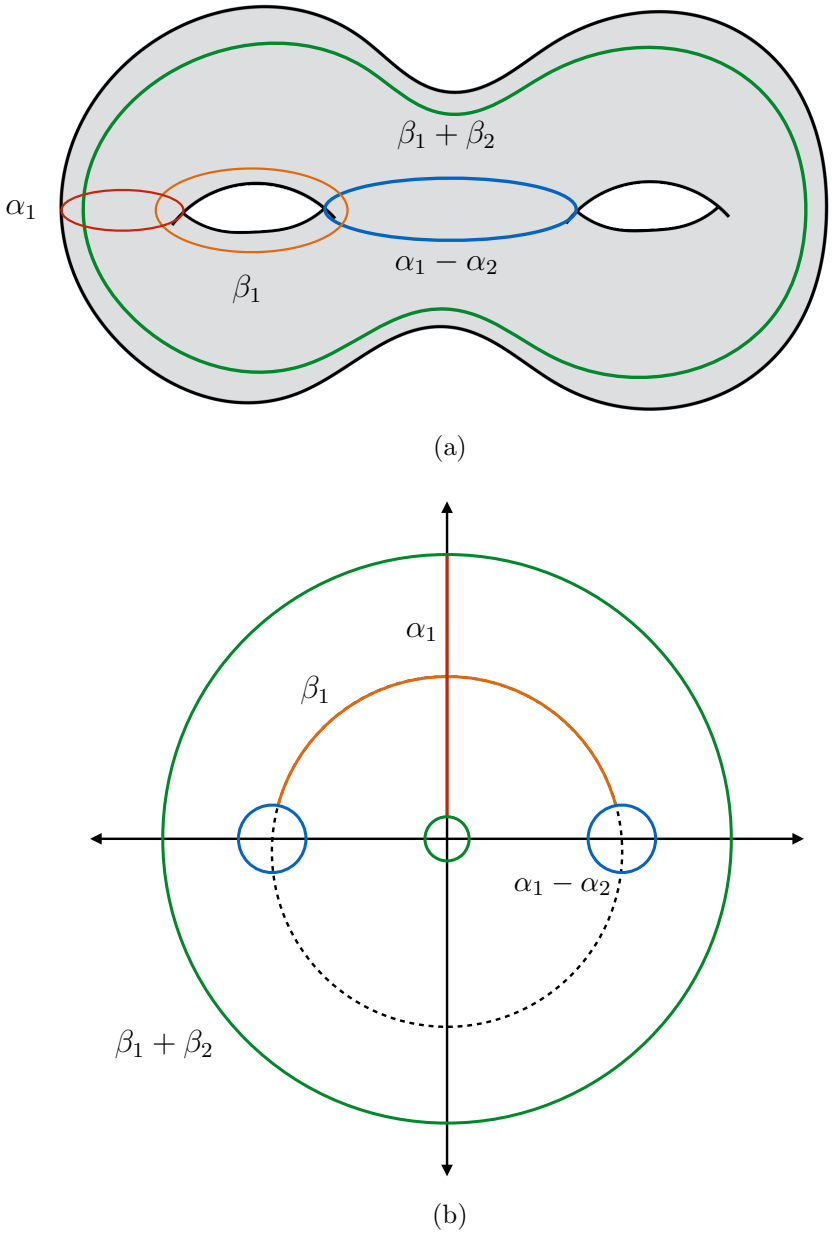

Figure 2.6: (a) Cycles labeled on the boundary Riemann surface. (b) The Schottky uniformization of this Riemann surface used to compute the toroidal geon phase.

We can characterize the bulk geometry of this handlebody by considering the geometry of a particular time slice. Consider the slice given by the fixed point set of reflection across the vertical line in fig 2.5. This symmetry fixes the $\hat{x}$ axis of the Schottky domain in fig 2.6b, and the topology of this slice is determined by eq. (2.18). The slice has 2 pairs

of circles, and the boundary consists of a single segment, giving a topology of $g_{\text{slice}} = 1$. Therefore, in this phase this bulk time slice has geometry given by a single boundary wormhole with a genus one surface behind the horizon. As in [28] we refer to this phase as the toroidal geon.

Note that we could have chosen a different time slice to characterize the bulk geometry. A potential source of confusion is that doing so does not change the handlebody phase, but rather simply the bulk slice we are using to characterize it. If we had chosen either of the two remaining slices fixed by $\mathbb{Z}_2$ symmetries we would have resulted in a geometry with three boundaries– with two of the boundaries connected by a wormhole, and the third a copy of the Poincaré disk. In each of these cases it is important to take the entire fixed point set of the reflection symmetry as the boundary. For example, if we considered the fixed point set of the reflection across the horizontal line in fig. 2.5 the boundary slice consists not only of the $\hat{y}$ axis but also of the cycle $\alpha_1 - \alpha_2$. This statement is clear in fig. 2.6a but more sublte in fig. 2.6b.

Having specified the phase, we can now compute its action and moduli using the *handlebodies* package. We can construct a general such phase via the following code:

```
InitializeHandlebody[]

AddCircle[{{0, 0}, r, ‘‘Inv’’}]
AddCircle[{{Sec[a], 0}, Tan[a], ‘‘RU’’}]

AddSymmetry[‘‘x’’]; AddSymmetry[‘‘y’’];

SolveHandlebody[geon]
```

A sample mesh used for this phase is shown in figure 2.7. Evaluating this code for different values of r and a computes the action of this phase at various points in moduli space. To parameterize the moduli space, we can use $|\alpha_1|$ and $|\beta_1|$, which after reducing the Schottky domain by the three $\mathbb{Z}_2$ symmetries correspond to boundary segments ∂D_i.

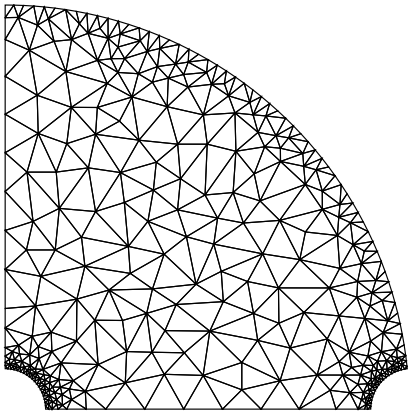

Figure 2.7: A mesh used to compute the toroidal geon phase.

In figure 2.8 we show a contour plot of the action in this moduli space.

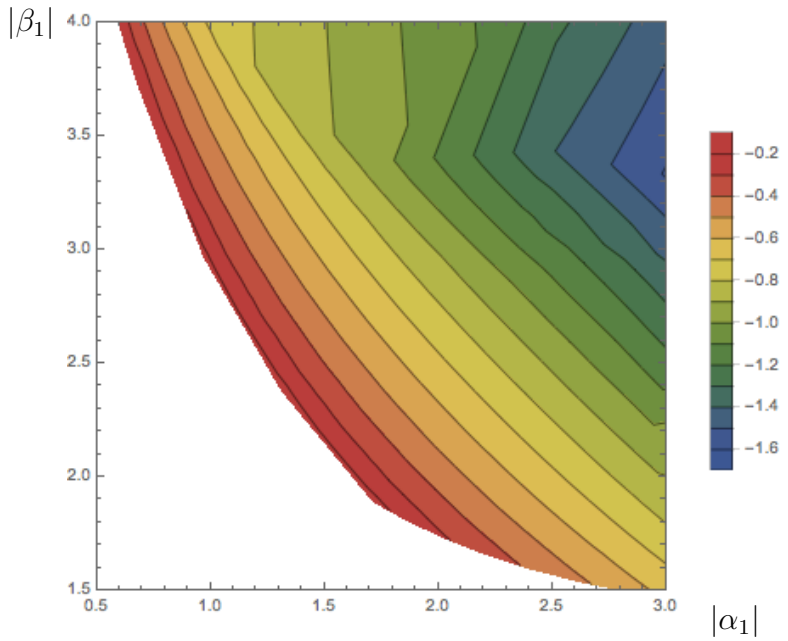

Figure 2.8: The action I/c for the toroid geon as a function of moduli. We see the action decreases as $|\alpha_1|$ and $|\beta_1|$ increase.

Part I

Insights

Chapter 3

The Torus Operator and Holography

3.1 Introduction

The Euclidean time-evolution operator $e^{-\beta H}$ is a central object in quantum field theory (QFT). We focus on conformal field theories in $d = 2$ spacetime dimensions so that the matrix elements of $e^{-\beta H}$ are given by Euclidean path integrals over a cylinder of height β and radius r_0, with the latter chosen to agree with the radius of the circle on which the QFT is defined. We thus refer to $e^{-\beta H}$ as the cylinder operator $C(\beta) = e^{-\beta H}$ below. Interesting properties of this operator include the ground state of $\beta H = -\ln C(\beta)$, the partition function $\mathcal{Z} = \mathrm{Tr}\,(C(\beta))$, the gap between the ground state and the first excited state, and other properties of the spectrum.

We restrict our attention to holographic CFTs; i.e., to families of CFTs that have a bulk AdS_3 dual in the limit of large central charge c. For such theories the AdS_3 analogue of the Hawking-Page phase-transition [42] is associated with the fact that the above-mentioned gap is of order 1 at large c, while above some energy threshold H has a black-hole-like density of states with entropy $S = 2\pi\sqrt{E\,\ell\,c/3}$.

The goal of the present work is to study the effect of adding topology to the above

path integrals. In partiuclar, we investigate CFT operators $\mathcal{T}$ defined by Euclidean path integrals over some twice-punctured torus $\mathscr{T}$ as drawn in figure 3.1. We wish to understand how such properties depend on the moduli of $\mathscr{T}$, though we suppress these moduli from our notation. For simplicity we impose three $\mathbb{Z}_2$ symmetries on $\mathscr{T}$ which act on figure 3.1 by reflecting the page front-to-back, top-to-bottom, and right-to-left across the vertical dashed line. This reduces the dimension of the moduli space to two. Furthermore, by cutting the path integral along the dashed vertical line in figure 3.1, one sees that the reflection exchanging the two resulting pieces implies that $\mathcal{T} = A^\dagger A$ for the operator A that maps our CFT Hilbert space $\mathcal{H}$ to $\mathcal{H} \otimes \mathcal{H}$ as defined by the path integral over the right piece. It follows that $\mathcal{T}$ is manifestly non-negative and we may define the corresponding "Hamiltonian" $K := -\log \mathcal{T}$. The largest eigenvalue of $\mathcal{T}$ corresponds to the ground state of K. We call this state $|0\rangle_K$ and often refer to it simply as the torus operator ground state. We also refer to eigenvalues of K as "K-energies."

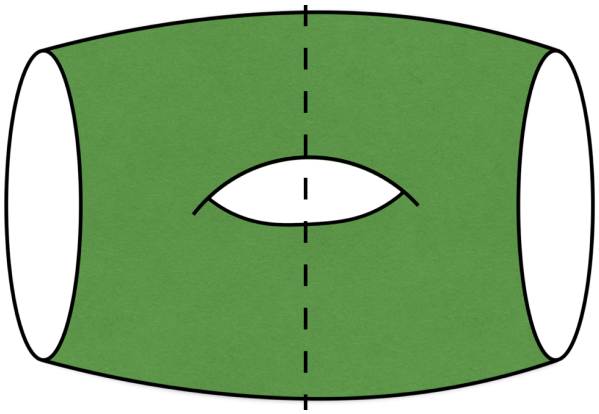

Figure 3.1: The surface $\mathscr{T}$ used to define the torus operator $\mathcal{T}$. The surface has three $\mathbb{Z}_2$ symmetries, acting on the page by reflecting front-to-back, right-to-left across the vertical dashed line, and top-to-bottom. Cutting the path integral along the plane defined by the normal to the page and the vertical axis (dashed line) decomposes $\mathcal{T}$ into the product $A^\dagger A$ where A maps our CFT Hilbert space $\mathcal{H}$ to $\mathcal{H} \otimes \mathcal{H}$.

A closely related problem was recently considered in [36], which studied path integrals over tori with a single puncture in holographic CFTs. To understand the precise

connection, recall that the CFT vacuum $|0\rangle$ is given by the Euclidean path integral over a disk. The state $\mathcal{T}|0\rangle$ is thus computed by sewing a disk into the right-hand puncture of the twice-punctured torus $\mathscr{T}$. The result is a once-punctured torus $\overline{\mathscr{T}}$, which is conformally equivalent to the once-punctured tori studied in [36]. In particular, we show in appendix 3.A below that our $\mathbb{Z}_2$ symmetries do not significantly restrict the resulting moduli space.

Now, as we review in greater detail in appendix 3.A, ref. [36] identified two phases in the moduli space of $\overline{\mathscr{T}}$. In the first phase, the bulk dual of $\mathcal{T}|0\rangle$ is empty AdS_3 with $O(1)$ excitations for the bulk quantum fields. But in the second phase the bulk dual of $\mathcal{T}|0\rangle$ contains a black hole with one asymptotic region and a (punctured) torus inside the horizon; see figure 3.2. Such spacetimes are known as toroidal geons. This raises the question of whether $\mathcal{T}$ might have other black-hole-like properties when the bulk dual of $\mathcal{T}\,|0\rangle$ is a toroidal geon. Indeed, we will show in section 3.4.2 that this transition also implies a phase transition for the ground state $|0_K\rangle$ of $K = -\log \mathcal{T}$. While the actual properties of $|0_K\rangle$ remain unclear in the toroidal geon case, it is natural to ask if $|0_K\rangle$ might also be dual to a bulk black hole, what the internal topology of that black hole might be, and whether the density of states for $\mathcal{T}$ might become black-hole-like near $|0_K\rangle$ with $S = O(c)$ for large c. Such a density of states would be high enough that we would then refer to it as a "gapless" or "continuous" spectrum.

We begin in section 3.2 by discussing how the above issues are related to properties of the partition functions $\mathrm{Tr}(\mathcal{T}^n)$. Much of our work will analyze such partition functions using the dual AdS_3 system by further developing the techniques described in [40, 41, 36]. We therefore review the construction of the relevant (handlebody) bulk solutions in §3.3, along with the computation of the associated bulk actions. We also discuss a heuristic for understanding which phase dominates a given path integral. Using such techniques to study $\mathrm{Tr}(\mathcal{T}^n)$ in §3.4 then leads to a puzzle: although $\mathcal{T} = A^\dagger A$ is manifestly non-

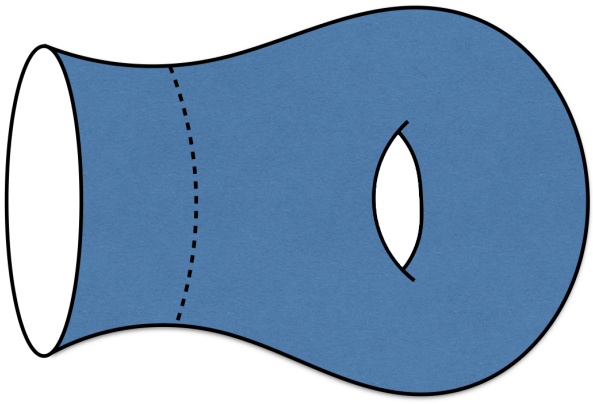

Figure 3.2: A cartoon of the $t = 0$ surface for the toroidal geon state. The geometry consists of a single asymptotically AdS boundary separated from a genus one surface by a black hole horizon (dashed line).

negative, the most tractable phases – and in particular those directly associated with the phases studied in [36] – suggest $\mathcal{T}$ to have negative eigenvalues. In §3.5 we then consider the action of $\mathcal{T}$ on states containing black holes with toroidal interiors. We close with some discussion of possible resolutions in §3.6. Further technicalities related to our use of results from [36] appear in appendix 3.A, and comments on numerical errors are relegated to appendix 3.B.

3.2 Gaps, ground states, and traces

As mentioned above, a key question of interest is the density of K-eigenstates near the torus ground state $|0_K\rangle$. In particular, we wish to distinguish between the case where K has a gap Δ that does not vanish at large c and the case where $\Delta \to 0$ as $c \to \infty$. We will probe this issue in section 3.4 by studying $\mathrm{Tr}(\mathcal{T}^n)$ for large n. This trace is computed by evaluating the path integral over a Riemann surface consisting of n copies of $\mathcal{T}$ glued together along the seams. As shown in figure 3.3, the result is a Riemann surface of genus $n + 1$ with an $n-$fold "replica symmetry" acting by a $2\pi/n$ rotation.

In particular, as explained in more detail in section 3.3, we will further translate

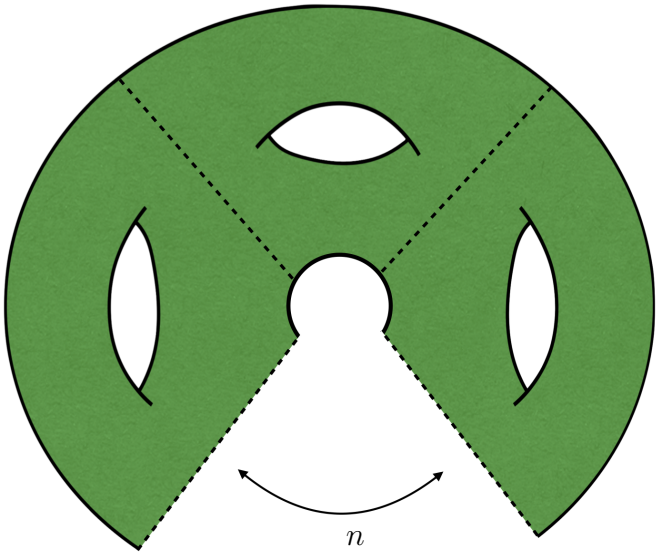

Figure 3.3: Partition function of genus $n+1$ that computes $\mathrm{Tr}(\mathcal{T}^n)$ in the CFT.

$\mathrm{Tr}(\mathcal{T}^n)$ into a bulk Euclidean path integral. For the 2d CFTs on which we focus, taking the limit of large central charge c corresponds to taking $G_N = \frac{3\ell}{2c} \to 0$ with fixed AdS scale ℓ. In this limit we may evaluate the gravitational partition function via the saddle point approximation using only the dominant bulk solution (dom.):

$$-\log \mathrm{Tr}(\mathcal{T}^n) = S_{\mathrm{EH}}[g_{\mathrm{dom.}}]\,. \tag{3.1}$$

In the rest of this section we describe how studying (3.1) can both determine the value of Δ and characterize the ground state $|0_K\rangle$.

3.2.1 Gapped or Gapless?

To understand how properties of Δ relate to properties of the dominant bulk saddle, let us first suppose that Δ does not vanish at large c. Then for large n we have

$$\mathrm{Tr}(\mathcal{T}^n) = e^{-\lambda_0 n}\left(1 + O(e^{-\Delta n})\right) \tag{3.2}$$

where λ_0 is the smallest eigenvalue of K. Since exponential corrections as in (3.2) correspond to $O(c^0)$ effects in the bulk (for $\Delta = O(c^0)$) or sub-dominant bulk solutions (for $\Delta = O(c)$), for such cases there should be an n_0 of order 1 such that the leading-order gravitational action of the dominant bulk solution becomes precisely linear for $n > n_0$. We refer to this behavior as "gapped," and in this case we can write for $n > n_0$

$$-\ln \mathrm{Tr}\,(\mathcal{T}^n) \sim n\lambda_0 + O(e^{-\Delta n}) \cdots . \tag{3.3}$$

On the other hand, if Δ vanishes as $c \to \infty$ then the corrections in (3.2) can be neglected only for $n \gtrsim 1/\Delta$. For Δ vanishing as a power of c this should result from perturbative corrections in the bulk. It is difficult to imagine how this could be the case, so we instead focus on the case where the density-of-states becomes black-hole like and the gap is exponentially small (with $-\ln \Delta = O(c)$). The resulting near-continuum of low energy states means that evaluating the trace requires us to sum over all the states in the associated band:

$$\mathrm{Tr}\,(\mathcal{T}^n) = \sum_{k=0}^{\infty} e^{-n(\lambda_0 + g(k) e^{-c\,\hat{s}})}\,, \tag{3.4}$$

where we have taken the spectrum of excitations above the ground state $k = 0$ to be $g(k)e^{-c\,\hat{s}}$; i.e. to leading order the density of states is $s = c\,\hat{s}$ for some constant $\hat{s}$ with further $O(1)$ details determined by $g(k)$.

To understand the implications for a bulk dual, recall that in a theory with c degrees of freedom it is natural to expect the number of states at each k to scale like the volume k^{c-1} of a $(k-1)-$sphere so that $g(k) \sim k^{1/c}$ at large c, or more generally that $g(k) \sim k^{1/(\alpha c)}$ for some α of order 1. For small $ne^{-c\,\hat{s}}$ we can then approximate the sum in (3.4) by an

integral to find

$$-\ln \mathrm{Tr}\,(\mathcal{T}^n) \sim n\lambda_0 + \alpha\, c \log(n) + O(1) \cdots . \tag{3.5}$$

Note that since the bulk saddle-point approximation is valid only for asymptotically large c, in this approximation c is always taken large relative to n and we may use (3.5) no matter how large n may be, as λ_0 also scales with c. The gravitational action of the dominant bulk saddle should thus also be given by (3.5) at large n; i.e., it is never precisely linear in n, but only becomes approximately linear as $n \to \infty$. We refer to this behavior as "gapless."

3.2.2 Characterizing the ground state

Whether gapped or gapless, for large n the operator $\mathcal{T}^n$ approximates $e^{-n\lambda_0}$ times the projector $|0_K\rangle\langle 0_K|$. At least for even n, the analogous statement also holds for $\mathcal{T}^{n/2}$. Note that this operator is defined by path integrals over an $n/2$-torus with two punctures. Indeed, sewing together two copies of this Riemann surface along the two pairs of punctures gives the partition function $\mathcal{Z}(n) = \mathrm{Tr}(\mathcal{T}^n)$. Reversing this logic, we see that $\mathcal{T}^{n/2}$ is obtained by cutting open the path integral for $\mathcal{Z}(n)$ along a pair of circles C_1, C_2.

Now, it is well known that cutting open a partition function path integral yields a state. For n even, let $|\psi_{\mathcal{T},n/2}\rangle$ be the state defined in this way by cutting $\mathcal{Z}(n)$ along the above two circles (C_1, C_2). The relation between $\mathcal{T}^{n/2}$ and $|\psi_{\mathcal{T},n/2}\rangle$ is described by the time-reversal operator $\mathbb{T}$. While time-reversal is often described as an anti-linear operator on the Hilbert space, it may be equivalently characterized as a map from ket-vectors $\langle\alpha|$ to bra-vectors $|\mathbb{T}\alpha\rangle$. We shall use the latter description. As a result we may use $\mathbb{T}$ to recode the information in any operator $\mathcal{O}$ as a state on two copies of the system.

Choosing a basis $\{|i\rangle\}$, we may write this recoding in the form

$$|\psi_{\mathcal{O}}\rangle = \mathbb{T}\mathcal{O} = \mathbb{T}\sum_{i,j}|i\rangle\mathcal{O}_{ij}\langle j| := \sum_{i,j}\mathcal{O}_{ij}(|i\rangle\otimes|\mathbb{T}j\rangle), \tag{3.6}$$

where we have defined $\mathbb{T}$ on $|i\rangle\langle j|$ to act trivially on the ket-vector and to map $\langle j|$ into $|\mathbb{T}j\rangle$. When $\mathbb{T}$ is a symmetry of the system, it commutes with the Hamiltonian and we may choose a basis of energy eigenstates $\{|E\rangle\}$ such that $|\mathbb{T}E\rangle = |E\rangle$. Equation (3.6) then gives the well-known relation between the cylinder operator $C(\beta/2) = e^{-\beta H/2}$ and the thermofield double state $|TFD(\beta)\rangle$ at temperature $1/\beta$:

$$|\psi_{C(\beta/2)}\rangle = \mathbb{T}e^{-\beta H/2} = \sum_{E} e^{-\beta E/2}(|E\rangle\otimes|E\rangle) = |TFD(\beta)\rangle. \tag{3.7}$$

In the same way, we have

$$|\psi_{\mathcal{T},n/2}\rangle = \mathbb{T}\mathcal{T}^{n/2}. \tag{3.8}$$

Due to the analogy between (3.7) and (3.8), we refer to the latter as a thermofield-double-like state.

In [21], Maldacena studied the bulk dual of $|\psi_{C(\beta/2)}\rangle = |TFD(\beta)\rangle$ by cutting open the corresponding bulk path integral. We will do the same below for the TFD-like states $|\psi_{\mathcal{T},n/2}\rangle$. Now, at large enough n, the operator $\mathcal{T}^{n/2}$ approaches $e^{-n\lambda_0/2}|0_K\rangle\langle 0_K|$, so (choosing an appropriate phase for $|0_K\rangle$) we find

$$|\psi_{\mathcal{T},n/2}\rangle = \mathbb{T}\mathcal{T}^{n/2} = e^{-n\lambda_0/2}\left(|0_K\rangle|0_K\rangle + O(e^{-n\Delta/2})\right). \tag{3.9}$$

And as discussed above, for Δ of order 1 or larger at large c, the bulk semi-classical approximation will not capture the exponentially small corrections. So above some n_0, the state defined by cutting open the bulk path integral for $\mathcal{Z}(n)$ should be a product

state proportional to two copies of $|0_K\rangle$. One thus expects to find a disconnected pair of bulk spacetimes analogous to the pair of empty AdS_3 spacetimes dual to the thermofield double $|\psi_{C(\beta/2)}\rangle = TFD(\beta)\rangle$ at temperatures lower than the AdS_3 version [21] of the Hawking-Page transition[1].

On the other hand, much as in our discussion above, for a black-hole-like density of states the semiclassical limit cannot access large enough n to see the corrections in (3.9) become small. At any n it will thus characterize $|\psi_{\mathcal{T},n/2}\rangle$ as a highly entangled state. The amount $S(n)$ of such entanglement then quantifies the density of states and should take on values typical of a bulk black hole for each n, with $S(n) \to 0$ as $n \to \infty$. In such cases, the bulk dual of $|\psi_{\mathcal{T},n/2}\rangle$ should be a connected wormhole-like spacetime having two asymptotic regions, and where the corresponding entanglement wedges meet at a Hubeny-Rangamani-Takayanagi (HRT) surface [43] of area $4GS(n)$. Topological censorship theorems [44] then imply that this wormhole lies inside a black hole.

As $n \to \infty$, the area of this HRT surface shrinks to zero and the spacetime approximately splits into two parts, each of which should again be closely related to the bulk dual of $|0_K\rangle$. In particular, the topology of the bulk dual to $|0_K\rangle$ can be determined in this way.

3.3 Handlebody Phases

We now review the use of bulk handlebodies to compute partition functions $Z[X]$ for $d = 2$ holographic CFTs on Riemann surfaces X. That the CFT is holographic means

[1] As in [21], our Euclidean bulk saddles will all be invariant under a (Euclidean) time-reversal symmetry that fixes a bulk surface we call $t = 0$. In the bulk semi-classical approximation, cutting open the path integral at $t = 0$ amounts to using the induced metric at $t = 0$ as initial data to construct a Lorentz-signature spacetime that is similarly invariant under time-reversal. In particular, the resulting spacetime has vanishing extrinsic curvature at $t = 0$.

[15, 16] that we have,

$$\mathcal{Z}_{\rm CFT} = \mathcal{Z}_{\rm grav.}\,, \tag{3.10}$$

where $\mathcal{Z}_{\rm grav.} = \int \mathcal{D}g\, e^{-S_{EH}[g]}$ and S_{EH} is the Einstein-Hilbert action with Newton constant G_N and negative cosmological constant.[2]

The gravitational path integral is over Asymptotically Locally Anti-de Sitter (AlAdS) Euclidean bulk manifolds M that satisfy the boundary condition $\partial M = X$, where ∂M is the conformal boundary of M. All solutions of this theory are quotients of global AdS_3, even if the solution features non-trivial topology and/or multiple boundary regions. An interesting class of bulk solutions are the so-called handlebodies, described by choosing an appropriate set of cycles on the Euclidean boundary to be contractible in the bulk. As above, we consider boundary conditions in Euclidean signature given by a compact Riemann surface X, where X has at least one reflection symmetry, which we will call time-reflection. The bulk surface Σ invariant under this reflection will be called the $t = 0$ surface. We leave implicit any analytic continuation to Lorentzian signature.

For a given boundary Riemann surface X of genus g, we can choose a basis $\{\alpha_i, \beta_j\}$ of cycles[3] for the homotopy group $\pi_1(X)$, such that $\alpha_i \cap \beta_j = \delta_{ij}$ and

$$\prod_{i=1}^{g} \alpha_i^{-1}\beta_i^{-1}\alpha_i\beta_i = 1\,. \tag{3.11}$$

[2]For exact equality, $\mathcal{Z}_{\rm grav.}$ should be the full quantum gravity partition function including other fields, strings, higher derivative corrections, etc. But we will largely restrict attention below to the so-called universal sector in which the bulk is described by $S_{EH}[g]$ alone at leading order in large central charge c. As discussed in [45], for known holographic dualities involving AdS_3, instabilities involving "long strings" often imply that the dominant bulk solution does not in fact lie in the universal sector. But at least when large black holes are present, we may expect the associated temperature to remove such instabilities in much the same way as the mass deformations described in [46]. We therefore ignore such instabilities until §3.6.

[3]Throughout this paper we use the term "cycle" to mean not only an element of $\pi_1(X)$ but in fact a particular curve in X belonging to the associated equivalence class.

Given a such basis, we can define a bulk manifold with boundary X by declaring the cycles $\{\alpha_i\}$ to be contractible in the bulk while the cycles $\{\beta_i\}$ remain non-contractible. To be explicit, we take the smallest normal subgroup Γ of $\pi_1(X)$ generated by the α_i and define the bulk to have homotopy group $\pi_1(M) \coloneqq \pi_1(X)/\Gamma$; see [47, 48] for further discussion of these Schottky groups. It is known that all such $\pi_1(M)$ can be embedded in the group of AdS_3 isometries so that we may construct M as the quotient $AdS_3/\pi_1(M)$.

In this way, each possible basis for the boundary Riemann surface X defines a handlebody geometry with boundary X, and we refer to these bulk solutions as the set of handlebody phases. While they are not the only solutions for a particular set of boundary conditions, it has been conjectured that the non-handlebody solutions are always subdominant [49], and indeed certain non-handlebody solutions are known to be forbidden by AdS/CFT [46].

We wish to compute the Euclidean gravitational path integral using a saddle point approximation, so for each boundary X we need to find the bulk phase with least action. It is often assumed that phases which break the symmetry of the boundary are subdominant to the ones which preserve the symmetry, and for simplicity we will often focus on bulk manifolds with fundamental groups $\pi_1(M)$ which preserve the symmetries of $\pi_1(X)$. We will use a normalization in which the action for certain non-handlebody solutions vanishes, and we will see explicitly that the dominant action is always negative for the subspace of moduli space considered.

We can generate a large class of phases by the following algorithm. For simplicity we work with the homology group, and therefore we might miss phases with the same bulk homology but different bulk homotopy. However, we do not expect this restriction to affect our main results. First, we embed X into $\mathbb{R}^3$ and choose a standard basis in which the α cycles go around the "handles" and the β cycles go around the "holes" as shown in Figure 3.4. This phase is referred to as the "naive handlebody," as it corresponds to

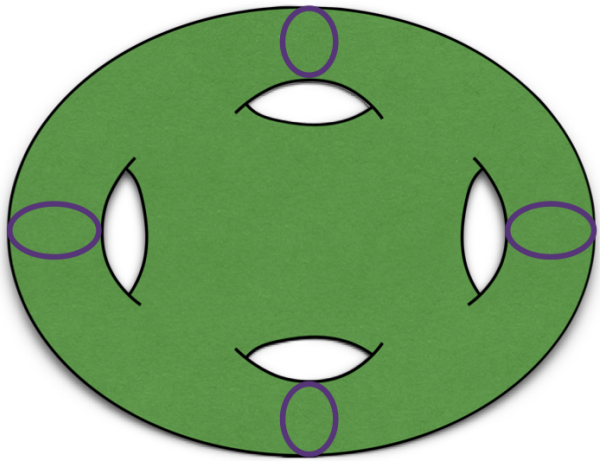

Figure 3.4: The naive handlebody phase for a genus 4 boundary with the α cycles drawn in purple. The four β cycles are not drawn but each circle one of the four holes.

filling in the bulk manifold with a solid handlebody as suggested by the picture. We then construct new phases by considering the image of these cycles under an arbitrary element M of the mapping class group and choosing the cycles $M(\{\alpha\})$ to be contractible in the bulk. Note that this procedure can generate phases that break symmetries of X. One might expect such phases to be subdominant, though this is not always the case.

Some of the resulting phases were originally described in [37, 38], with their application to holography described in [39]. A more systematic treatment in terms of Schottky uniformization and a recipe for computing their actions were then derived in [40, 41]. Numerical techniques for evaluating these actions and matching moduli between phases were later introduced in [36]. The remainder of this section reviews these techniques for use in §3.4 and §3.5.

3.3.1 Schottky Uniformization

All solutions of Einstein's equation in 2+1 dimensions with negative cosmological constant can be constructed by taking a quotient of Euclidean AdS_3 by some subset of

the symmetry group $\mathrm{PSL}(2,\mathbb{C})$. In the half-space representation of Euclidean AdS_3, the quotient operations act to identify pairs of hemispheres anchored to the boundary. If we think of the boundary as the complex plane $\mathbb{C}$, then on the boundary the identifications are given by Möbius transformations which identify pairs of circles. We can thus specify a particular bulk quotient by describing these pairs of boundary circles, with the quotient extending into the bulk by acting on hemispheres anchored to each such boundary circle. Any connected part of the bulk region that remains after these hemispheres are removed can serve as a fundamental domain for the quotient handlebody.

Representing a Riemann surface in terms of pairs of circles identified on $\mathbb{C}$ is known as a Schottky uniformization. In general, this uniformization is not unique. More explicitly, we think of $\mathbb{C}\cup\{\infty\}$ as the Riemann sphere and consider the domain defined by removing $2g$ non-intersecting closed disks. The boundaries of these disks are $2g$ circles, which we group into g pairs (C_i, C_i'). Further let the Möbius transformation L_i map the interior of C_i (defined by the embedding in $\mathbb{C}$) to the exterior of C_i'.

As defined, each L_i is a loxodromic transformation, meaning that it is conjugate to the transformation $w \mapsto q_i^2 w$ for some $q_i \in \mathbb{C}$ with $0 < |q_i| < 1$. Taking the quotient by the group generated by $\{L_i\}$ defines a Riemann surface of genus g with a fundamental domain D given by the region exterior to all of the circles. Each transformation L_i is associated with three complex free parameters, while we are free to choose overall normalizations which fix three of these $3g$ parameters. The space of surfaces described in this manner is thus $\mathbb{C}^{3g-3}$, which matches the moduli space of a genus g Riemann surface. In fact, the Koebe retrosection theorem [50] tells us that all compact Riemann surfaces can be described in this way.

To connect the choice of Schottky uniformization for the boundary Riemann surface to the choice of bulk handlebody phase, note that the circles C_i on the boundary are contractible in the bulk since each C_i can be shrunk to a point by contracting the cycle

along the corresponding bulk hemisphere. As a result, to construct a bulk in which $\{\alpha_i\}$ are contractible, we need only find a Schottky uniformization with $C_i = \alpha_i$.

The cycles β_i that are dual to α_i remain non-contractible, as these are the cycles that run from C_i to C_i' on the boundary. Each such cycle is associated with the transformation L_i, and any non-contractible bulk cycle given by a product of β_i can be associated with some L which is correspondingly a product of the L_i. Additionally, for any non-contractible cycle there is a unique geodesic representative of the associated homotopy class. Since all loxodromic L have $\mathrm{Tr}\, L > 2$, as shown in [51] the length of this geodesic is

$$\ell(L) = 2\cosh^{-1}\frac{\mathrm{Tr}\, L}{2}\,. \tag{3.12}$$

This technology provides a useful way to understand the bulk topology and compute the lengths of various horizons and geodesics.

Given a Schottky representation of a boundary Riemann surface, the topology of the "$t = 0$" bulk slice can be determined as follows. Suppose n of the g pairs of circles $\{C_i, C_i'\}$ lie on the boundary $t = 0$ slice.[4] Additionally, suppose these identifications create b disjoint boundary circles at $t = 0$. The number of holes in the bulk $t = 0$ slice is then given by

$$g_{t=0} = \frac{n - b + 1}{2}\,. \tag{3.13}$$

This formula follows from an analog of the "doubling" construction $X = 2Y$ as pointed out in [41], using only the subset of identifications that act on the $t = 0$ slice. As the boundary identifications are extended into the bulk along hemispheres, the quotient

[4]Since the bulk $t = 0$ surface is invariant under a reflection symmetry of the boundary, if C_i lies on the boundary slice then so must C_i'.

of the bulk $t = 0$ slice is determined precisely by the identifications which act on the intersection of this slice with the boundary.

To construct a Schottky domain for a particular bulk handlebody, however, it is more convenient to reverse this procedure. Given a handlebody phase described by cycles $\{\alpha_i\}$ on X to be made contractible in the bulk, we can construct a Schottky uniformization as follows. First, for each i cut along the geodesics homologous to α_i, calling each side of the cut C_i and C_i'. Cutting the Riemann surface in this manner defines a sphere with $2g$ punctures. Next, project this punctured sphere into the plane $\mathbb{C}$. The resulting circles and maps L_i identifying C_i and C_i' are precisely the ingredients needed for Schottky uniformization. In §3.4 and §3.5 we provide some explicit examples; further examples can be found in [36, 29].

Finally, in comparing different handlebody phases with the same boundary conditions we must be sure that the moduli of the two boundary Riemann surfaces agree. Determining the moduli of a Riemann surface from its Schottky representation requires defining a boundary conformal frame in which to compute cycle lengths. While some of the moduli are fixed by symmetry, others must be fixed by computing the lengths of certain cycles. In practice this moduli matching problem is the most difficult part of constructing a phase diagram for higher genus partition functions. However, there is a useful heuristic which can sometimes be used as a shortcut.

From the numerical results of [36, 29] and results presented in §3.4 and §3.5, one observes that the action tends to be a monotonic function of the sum of the lengths of boundary cycles chosen to be contractible. When this sum is large the action tends to be more positive, and when this sum is small the action tends to be more negative. We therefore posit the heuristic that for a particular Riemann surface X, the phase which dominates the partition function is the one in which the sum of contractible cycle lengths is minimized, or simply "small boundary cycles like to pinch off." We will use

this heuristic to try to gain some intuition for the results in §3.4 and §3.5, and we will also test the heuristic against numerical computations of the actions.

One caveat in applying this heuristic is that for a given bulk phase there may be multiple choices of contractible boundary cycles one can use to define it, and so in applying the heuristic one needs to consider the choice with minimal total length. While this heuristic is known not to be exact (for example it fails near the AdS/toroidal geon phase boundary in [36]), it is still useful for building intuition about which phase dominates a given partition function. Moreover, in many cases there is a symmetry relating two bulk phases at a particular point in moduli space; see e.g. the example in appendix A.3 of [26]. At the symmetry point there is a choice of basis in which the action and the total length of contractible cycles are equal in each phase. Moving away from this point as the total length of contractible cycles decreases, the action typically becomes more negative, and if for the dual phase the total length of contractible cycles increases then the heuristic is exact.

3.3.2 The Boundary Metric and Bulk Action

Ultimately we will be interested in comparing the actions of different handlebody phases in order to determine the dominant semi-classical bulk geometry. We must therefore regulate the action by choosing a particular conformal frame. We do so by choosing the boundary to have constant Ricci scalar $R_{\text{bndy}} = -2$ in AdS units.

Using coordinates $w = x + iy$, we can write the boundary metric as

$$ds^2_{\text{bndy}} = e^{2\phi}|dw|^2\,, \tag{3.14}$$

where regularity of the metric under the quotient by L_i requires

$$\phi(L_i(w)) = \phi(w) - \frac{1}{2}\log|L_i'(w)|^2 \ . \tag{3.15}$$

The requirement $R_{\text{bndy}} = -2$ is equivalent to choosing ϕ to satisfy the Liouville equation

$$\nabla^2\phi = 4\partial_w\partial_{\bar{w}}\phi = (\partial_x^2 + \partial_y^2)\phi = e^{2\phi}\,, \tag{3.16}$$

subject to the boundary conditions (3.15). In this way, the problem of finding the boundary conformal frame is reduced to solving the scalar field equation (3.16) on the Schottky domain D with boundary conditions (3.15). We will do so in §3.4 and §3.5 using the numerical methods described in [36] and reviewed in the next subsection.

As shown in [40], with this choice of conformal frame the evaluation of the Einstein-Hilbert action for a particular solution can be written in terms of the Takhtajan-Zograf action [48] for the scalar field ϕ:

$$I = -\frac{c}{24\pi}\left[I_{\text{TZ}}[\phi] - A - 4\pi(g-1)(1-\log 4R_0^2)\right]\ , \tag{3.17}$$

where A is the area of the boundary and R_0 is the radius of the sphere for which the partition function is one. We will set $R_0 = 1$ in the results section. As explained in [36], if we define R_k to be the radius of C_k and Δ_k as the distance between the center of C_k and the point $w_\infty^{(k)}$ mapped to ∞ by L_k, this action reduces to

$$I_{TZ}[\phi] = \int_D d^2w\left((\nabla\phi)^2 + e^{2\phi}\right) + \sum_k\left(\int_{C_k} 4\phi\, d\theta_\infty^{(k)} - 4\pi\log\left|R_k^2 - \Delta_k^2\right|\right)\ , \tag{3.18}$$

where $\theta_\infty^{(k)}$ is the angle measured from the point $w_\infty^{(k)}$. If we can further reduce D by some set of symmetries, this action can take an even simpler form as shown in [36, 29]. As

in [29], we introduce Jacobian factors to turn all of the integrals over $\theta_\infty^{(k)}$ into numeric integrals over $\theta_0^{(k)}$, i.e. about the center of each circle.

3.3.3 Numerical Methods

Equation (3.16) on the Schottky domain D with boundary conditions (3.15) is generally difficult to solve analytically. Following [36], we thus proceed numerically using finite element methods and the Newton-Raphson algorithm. See [34, 35] for introductions to finite element methods.

In all cases of interest, we may write the boundary of our domain as $\partial D = \bigcup_i \partial D_i$ where ∂D_i is an arc[5] of a circle with radius R_i, where each ∂D_i is the fixed point set of some involution or reflection symmetry of D. As shown in appendix A of [36], we can then use the boundary conditions (3.15) to find

$$\nabla_n \phi|_{\partial D_i} = -\frac{1}{R_i}\,. \tag{3.19}$$

To solve (3.16) using the Newton-Raphson algorithm, we first write $\phi = \phi_{(n)} + \delta\phi_{(n)}$ and solve a linearized equation for $\delta\phi_{(n)}$. We then set $\phi_{(n+1)} = \phi_{(n)} + \delta\phi_{(n)}$ and similarly solve a linearized equation for $\delta\phi_{(n+1)}$. We repeat this process until $||\delta\phi_{(n+1)}||_\infty < 10^{-10}$.

At stage n in the Newton-Raphson algorithm, we can integrate the linearized equation against a test function ψ, and integrating by parts to incorporate the reduced boundary conditions (3.19) we have the following equation for $\delta\phi_{(n)}$:

$$-\int_D \nabla\psi\cdot\nabla\delta\phi_{(n)} - 2\int_D \psi\, e^{2\phi_{(n)}}\,\delta\phi_{(n)} = \int_D \nabla\psi\cdot\nabla\phi_{(n)} + \int_D \psi\, e^{2\phi_{(n)}} + \sum_i \frac{\sigma_i}{R_i}\int_{\partial D_i}\psi\, d\theta_i\,, \tag{3.20}$$

[5]Straight line segments are "arcs" of infinite-radius circles.

where $\sigma_i = \pm 1$ when the orientation of ∂D_i as part of ∂D is counter-clockwise or clockwise respectively. With an initial seed of $\phi_{(0)} = 0$, we can now use this equation and standard finite element techniques to solve for ϕ.

To match moduli between different phases, we need to compute the lengths of various geodesics on the boundary. In the case where a geodesic is fixed by a symmetry of the domain D, we can explicitly compute its length by numerically integrating the boundary metric over the appropriate curve. However, in some cases the domain D breaks some of the symmetries of X (even though the handlebody solution does not), and in practice it is difficult to numerically solve for the associated geodesic.

However, we can instead compute the boundary geodesic lengths by mapping the domain D to a subset of the Poincaré disk. We do so using the numerical solution for ϕ to compute the length of each boundary segment ∂D_i. By symmetry each ∂D_i is a geodesic that orthogonally intersects the adjacent segment ∂D_j. Knowing that the metric has been chosen so that $R_{\text{bndy}} = -2$, we can then construct a region in the Poincaré disk bounded by orthogonally-intersecting geodesic segments of the same lengths. The geometry of this region must then exactly match the geometry of D. Since the length of any geodesic segment in the Poincaré disk can be computed using a simple analytic formula, we can use this correspondence to easily compute geodesic length in our domain D.

3.4 Computing $\mathbf{Tr}(\mathcal{T}^n)$

We now use the technology of section 3.3 to compute $\text{Tr}(\mathcal{T}^n)$ and to study the associated TFD-like states $\mathbb{T}\mathcal{T}^{n/2}$ obtained by cutting open the corresponding path integral. As explained in section 3.2, characterizing the large n bulk duals of these states would tell us if $\mathcal{T}$ is gapped or gapless, and would also give the bulk dual of the ground state

$|0_K\rangle$.

Since any Riemann surface X is associated with an infinite number of bulk handlebody saddles, it will not be possible to study them all in detail. Indeed, even classifying the full set of possible phases is an onerous task. We will therefore proceed pragmatically, beginning in section 3.4.1 with bulk handlebodies that preserve the boundary replica symmetry. We then note in section 3.4.2 that the results of [36] imply that at least one phase breaking this replica symmetry has lower action, though the positivity of $\mathcal{T}$ forbids that particular phase from being the most dominant. This raises a puzzle, as other natural alternatives for the most dominant phase also suffer from the same issue.

3.4.1 Replica Symmetric Phases

We first consider phases which explicitly preserve the replica symmetry.[6] To catalog such phases we can restrict our attention to the fundamental unit $\mathcal{T}$ drawn in figure 3.5. We consider four distinct phases of this partition function, divided into two

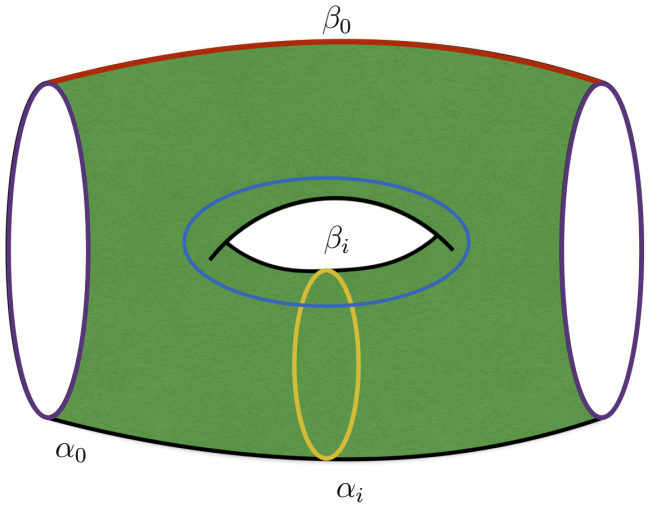

Figure 3.5: The fundamental unit $\mathcal{T}$ with cycles labeled. Only $1/n^{\text{th}}$ of β_0 is drawn.

[6]That is, we study phases whose Schottky domains respect the replica symmetry. There are more complicated phases that preserve replica symmetry, even though the symmetry is broken by the Schottky representation.

classes. The first class are called AdS phases, given by the choice of $\{\alpha_0, \alpha_1, \cdots, \alpha_n\}$ or $\{\alpha_0, \beta_1, \cdots, \beta_n\}$ contractible. In both of these phases, if any of the n choices of cycles α_0 is contractible, then the image of α_0 under $\frac{2\pi}{n}k$ rotation is also contractible. As a result, each α_0 cycle (purple in figure 3.5) bounds a slice of the bulk with vanishing extrinsic curvature and the geometry of the Poincaré disk. This is the Lorentzian-signature initial data for global AdS_3, so the bulk geometry for $\mathcal{T}^{n/2}$ (with even n) is just a pair of global AdS_3 geometries. We refer to such saddles as AdS phases for the TFD-like state.

When α_0 is contractible we can use a trick described in [36] to build phases for higher genus Riemann surfaces from lower genus phases. The boundary conditions on ϕ allow us to glue together Schottky domains along contractible geodesics, and we can glue together n copies of the unit $\mathcal{T}$ along the contractible geodesics α_0. In the bulk, this gluing occurs along the associated hemispheres (which have vanishing extrinsic curvature). In this way, when α_0 is contractible the action is given by n times the action for one of the units. The action for such AdS phases is exactly linear in n, and so these are gapped phases. If the operator $\mathcal{T}$ is gapped we would expect a phase of this general sort to dominate for large n, though there remains the possibility that the fundamental unit of the dominant phase could be larger than $\mathcal{T}$. Note that in defining the action of a fundamental unit we are free to include a Gibbons-Hawking boundary term $\frac{1}{8\pi G_N}\int K$ at any finite boundary (e.g., on the plane passing through an α_0 cycle at either end of figure 3.5). Since the extrinsic curvature vanishes on such boundaries, this boundary term does not affect the numerical value of the action.

The Schottky domains used to represent the above AdS phases are shown in figure 3.6. In each of these domains we include the cycles $\tilde{\beta}_0$ and $\tilde{\alpha}_i$, which are the images of β_0 and α_i under reflection across the horizontal line of symmetry in figure 3.5. Each domain has four free real parameters, which are reduced to two by imposing $|\tilde{\beta}_0| = |\beta_0|$ and $|\tilde{\alpha}_i| = |\alpha_i|$.

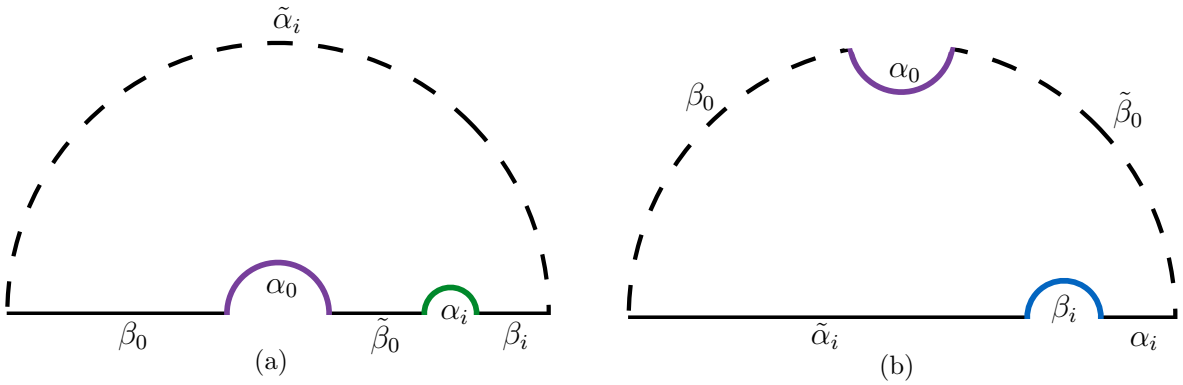

Figure 3.6: One quarter of the Schottky domains used to construct the two AdS phases, reduced by the reflection symmetries in the x-axis and the inversion symmetry through the unit circle (dashed). Various boundary cycles are labeled in each phase. (a) AdS phase with $\{\alpha_0, \alpha_i\}$ contractible. (b) AdS phase with $\{\alpha_0, \beta_i\}$ contractible.

The second class of phases we call BTZ phases, given by the choice of $\{\beta_0, \beta_1, \cdots, \beta_n\}$ or $\{\beta_0, \alpha_1, \cdots, \alpha_n\}$ contractible.[7] In these phases the moment of time symmetry in the bulk looks like a BTZ wormhole, and the action does not have a simple dependence on n. The trick we used to paste together AdS phases does not work, as these phases cannot be constructed by pasting together lower genus units along contractible geodesics. We thus expect the BTZ phases to be gapless.

Instead, we take advantage of the replica symmetry to further reduce the Schottky domain. The reduced domains for these phases are shown in figure 3.7, with the replica symmetry acting by a $2\pi/n$ rotation about the origin.

In practice, we find that it becomes difficult to numerically generate a mesh and solve the requisite differential equations for ϕ for $n > 4$. Instead we notice that given a solution ϕ_n for the metric for a particular BTZ phase at replica number n, the solution ϕ_{n+1} can be approximated as $\phi_{n+1}(w) = \phi_n(w^{n/(n+1)})$. The function $\phi_{n+1}(w)$ is a solution with the correct boundary conditions up to corrections $O(1/n)$. Under this transformation the line $\theta = \pi/n$ is mapped to $\theta = \pi/(n+1)$, effectively turning the $n-$fold replica symmetry into

[7]Note that there is another phase given by $\{\tilde{\beta}_0, \tilde{\alpha}_i\}$ contractible, but this phase will have exactly equal action by the symmetry.

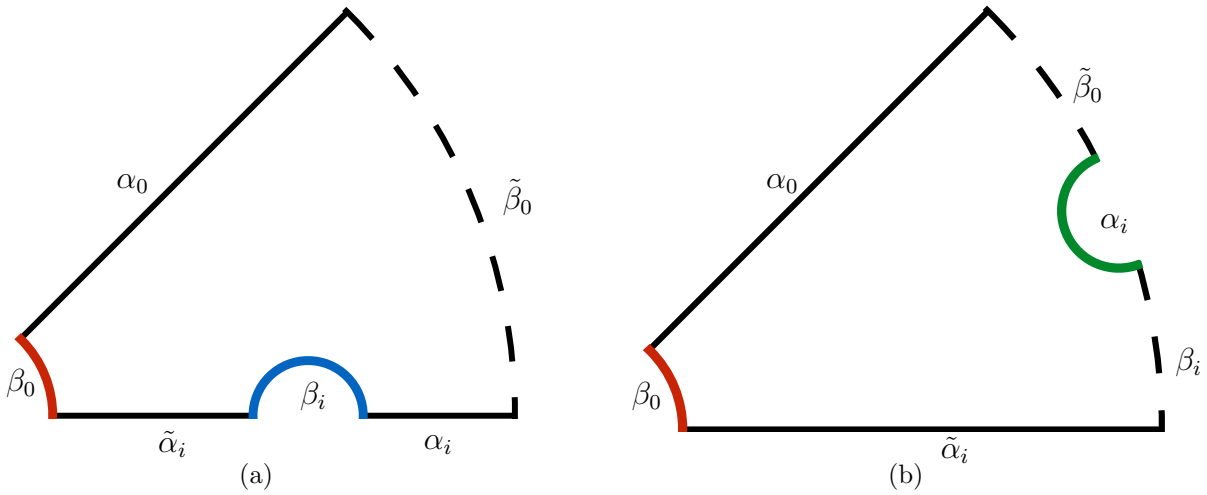

Figure 3.7: A slice of the Schottky domains used to construct the two BTZ phases, reduced by the reflection symmetry in the x-axis, $2\pi/n$ rotational symmetry about the origin, and the inversion symmetry through the unit circle (dashed). Various boundary cycles are labeled in each phase. (a) BTZ phase with $\{\beta_0, \beta_i\}$ contractible. (b) BTZ phase with $\{\beta_0, \alpha_i\}$ contractible.

$(n+1)-$fold replica symmetry. Extending this idea, we can exactly solve for $\phi_2(w)$ then approximate all higher solutions as $\phi_n(w) = \phi_2(w^{2/n})$. This approximation introduces some error into the computation of the action and moduli, and we can estimate this error by explicitly comparing it to the exact solution for $n = 4$. We find that in the region of interest the error is between 0.1% and 5% with most errors around 1%.

In comparing the phases, we first note that our heuristic predicts an AdS phase to dominate at finite n. As we increase n, the length of the cycle β_0 is proportional to n by replica symmetry, while the lengths of α_0, β_i, and α_i stay fixed. Therefore as we increase n, the sum of lengths $\{\alpha_0, \beta_1, \cdots, \beta_n\}$ will become smaller than $\{\beta_0, \beta_1, \cdots, \beta_n\}$, and the sum of lengths $\{\alpha_0, \alpha_1, \cdots, \alpha_n\}$ will become smaller than $\{\beta_0, \alpha_1, \cdots, \alpha_n\}$. So at some finite n, our heuristic predicts an AdS phase to dominate; thus for $n > n_{\text{BTZ}}$ we have the

TFD-like state

$$\mathbb{T}\mathcal{T}^{n/2} \sim |\text{AdS}\rangle\,|\text{AdS}\rangle\ , \tag{3.21}$$

so that $|0\rangle_K = |\text{AdS}\rangle$. The maximum replica number n_{BTZ} at which a BTZ phase dominates is a function of the moduli. Figure 3.8 shows n_{BTZ} at various points in the two dimensional moduli space, computed numerically using the technology described in the previous subsection. Consistent with this plot, we expect there to be a corresponding

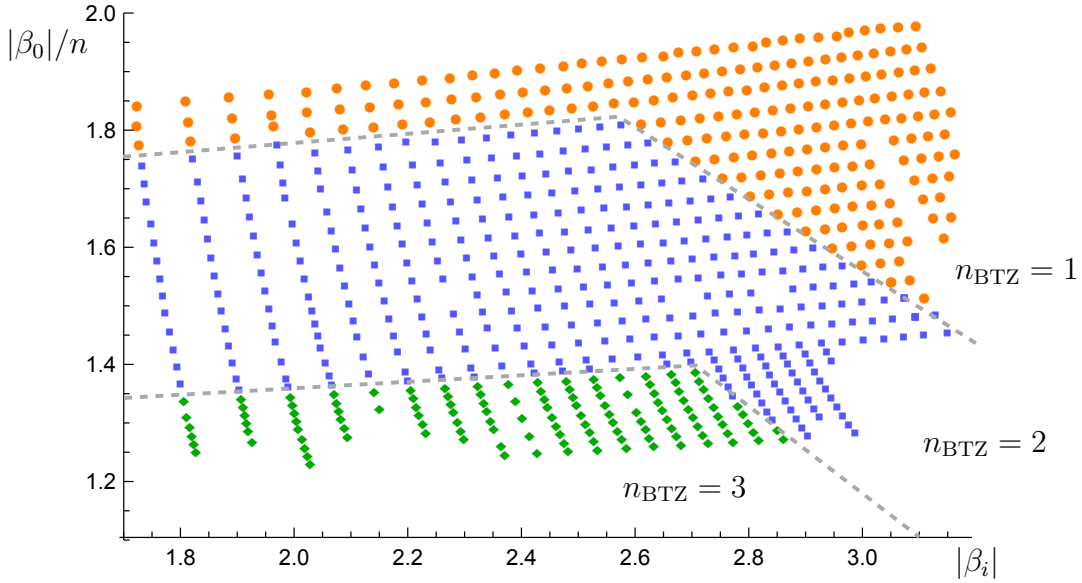

Figure 3.8: Numerical computation of n_{BTZ} for different values of the moduli. Suggested phase boundaries are drawn by hand in dashed grey, each consisting of two linear segments. The kink corresponds to a transition in dominance between two distinct AdS phases.

region of moduli space for any n_{BTZ}, with the area of the region decreasing for large n_{BTZ}. In this way, taken by themselves the above results suggest that the torus operator is gapped for any choice of moduli.

We can understand this behavior by comparing $\mathcal{T}$ to the cylinder operator. Taking the cylinder to have circumference $2\pi\ell$ and length β, the BTZ phase dominates

when $\beta n < 2\pi\ell$. In this case the region of moduli with a particular n_{BTZ} is given by $2\pi\ell/(n_{\mathrm{BTZ}}+1) < \beta < 2\pi\ell/n_{\mathrm{BTZ}}$. We can make n_{BTZ} as large as we like by choosing the moduli appropriately, but the volume occupied decreases with increasing n_{BTZ}. The torus operator shows a similar behavior, consistent with the conclusion that it too is gapped.

It is illustrative to compare these results with the values of n_{BTZ} predicted by our heuristic, which we denote $\hat{n}_{\mathrm{BTZ}}$. In figure 3.9, we plot the value of $\hat{n}_{\mathrm{BTZ}}$ predicted by the heuristic along with the boundaries previously drawn for n_{BTZ} in figure 3.8 as determined by the computation of the action. We see that the heuristic is accurate up

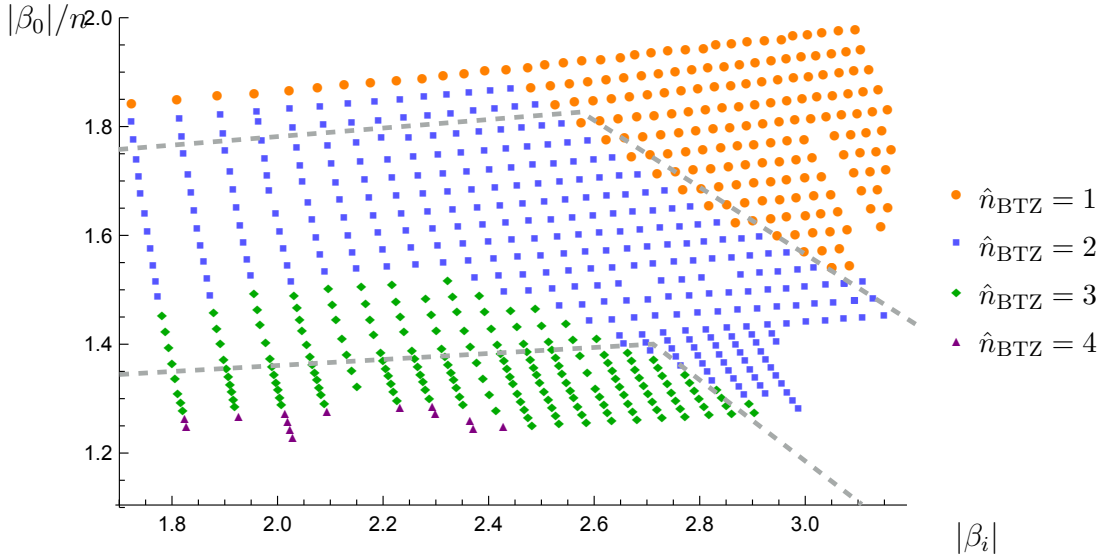

Figure 3.9: Heuristic estimation of $\hat{n}_{\mathrm{BTZ}}$ for different values of the moduli. We compare these values to the previously determined regions for n_{BTZ} by drawing the dashed boundaries from figure 3.8.

to some order one offset, in that the corresponding boundaries have the right qualitative structure but differ from the true boundaries by an order one distance in this space. However, around $|\beta_i| \sim 2.2$, for the boundary between $\hat{n}_{BTZ} = 2$ and $\hat{n}_{BTZ} = 3$ this offset becomes comparable to the (vertical) width of the $\hat{n}_{BTZ} = 2$ region. Note that our heuristic predicts an $\hat{n}_{\mathrm{BTZ}} = 4$ region and so we expect that if we were able to push the

numerics further we would expect to see this region in figure 3.8 as well.

3.4.2 Gapped Replica Symmetry Breaking Phases

We have thus far restricted our analysis to a particular class of phases which explicitly preserve replica symmetry. We now consider the possibility that replica symmetry is broken at large n, perhaps in some mild way. But since the above phases have a total cycle length that scales with n, our heuristic suggests that we focus on phases where the total cycle length grows at a similar rate or more slowly. And based on the results above, it is natural to begin with a study of gapped such phases. We postpone discussion of gapless symmetry breaking phases until §3.6.

One possibility is that the $\mathbb{Z}_n$ replica symmetry is broken to $\mathbb{Z}_{n/k}$, i.e. the phase consists of repeating blocks formed from $\mathcal{T}^k$ units. As in the previous section, our heuristic suggests that gapped phases will dominate at large n. Given some set of k cycles $\{\gamma_i\}$ contained in $\mathcal{T}^k$ which are made contractible in a replica symmetry breaking phase, at large n the total length of $\{n/k \times \gamma_i, \beta_0\}$ will always be larger than that of $\{n/k \times \gamma_i, \alpha_0\}$, as the length of β_i grows with n while the length of α_0 is constant. So we still expect gapped phases to dominate above some n.[8]

For simplicity let us assume the $\mathbb{Z}_n$ replica symmetry to be broken to $\mathbb{Z}_{n/2}$ by a bulk phase built from $n/2$ fundamental units, each corresponding to $\mathcal{T}^2$. We consider a phase in which the cycles $\{\alpha_0, \alpha_i - \alpha_{i+1}, \beta_i + \beta_{i+1}\}$ are contractible as drawn in figure 3.10. We have reason to suspect that there might be a region of moduli space where this phase might dominate over the AdS phases, as this problem is similar to that studied in [36] for a genus two Riemann surface. In our language, they computed a path integral for $\langle 0|\mathcal{T}^2|0\rangle$ and found that the above phase dominates for appropriately chosen moduli.

[8]It is possible to break the replica symmetry to $\mathbb{Z}_{n/k}$ in such a way that choosing $\{\gamma_i\}$ and α_0 to be contractible is inconsistent; the gapless phase described in §3.6 below is an example. In such cases, our heuristic could be consistent with a gapless phase dominating at large n.

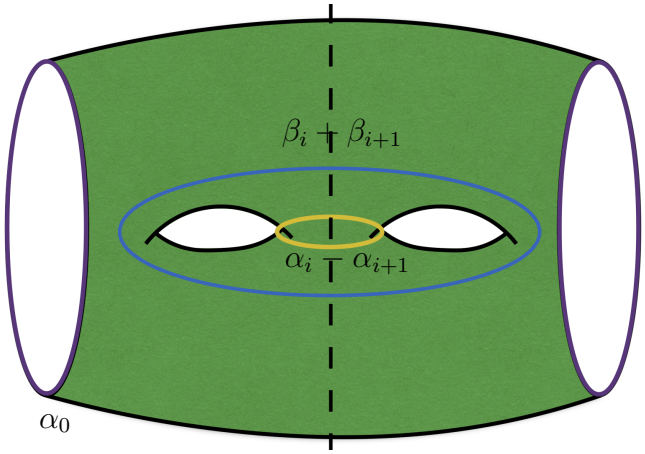

Figure 3.10: The fundamental unit $\mathcal{T}^2$ with cycles that are contractible in the phase of interest labeled.

As described in [36] and reviewed in appendix 3.A, the CFT state $\mathcal{T}|0\rangle$ is then dual to toroidal geon.[9] Our calculation differs only by the addition of the punctures on either side of figure 3.10. In particular, appendix 3.A shows that one can indeed find moduli where $\mathscr{T}$ has the $\mathbb{Z}_2$ discrete symmetries we require and the bulk dual of the path integral over $\overline{\mathscr{T}}$ is dominated by the toroidal geon.

Computing the action for this phase explicitly is beyond the scope of the present work, but we can sharpen the above argument to show that there is indeed a region of moduli space where it must dominate over the AdS phases considered in §3.4.1. Let us start with the bulk region $\mathcal{M}$ defined by figure 3.10. Recall that this $\mathcal{M}$ is constructed by cutting a replica-symmetric bulk solution $n\mathcal{M}$ along surfaces that separate the various replica copies. Since the full $n\mathcal{M}$ has a reflection symmetry across each such surface, the extrinsic curvature of these surfaces must vanish. We may thus glue half of a Poincaré ball to each surface. On the boundary, this is the same gluing construction used in

[9] To gain intuition for this result, note that contractibility of $\beta_i + \beta_{i+1}$ indicated by figure 3.10 implies that we can deform the cycle β_i through the bulk until it becomes the cycle $-\beta_{i+1}$. Thinking of the left half of figure 3.10 as bulk Euclidean time negative infinity and the right half as bulk Euclidean time positive infinity, such a deformation must pass through $t = 0$. But the cycle β_i is not required to be contractible on its own (and is shown to be non-contractible by the Schottky analysis in appendix 3.A) so the $t = 0$ slice must contain a non-contractible cycle.

section 3.1 to construct $\overline{\mathscr{T}}$ from $\mathscr{T}$, though we have now used it twice (i.e. once on each boundary).

The AlAdS boundary is now a compact Riemann surface without boundary and with genus 2. In our language, the bulk is then a phase of $\langle 0|\mathcal{T}^2|0\rangle$. The only issue is that the boundary metric on hemispherical endcaps has constant positive curvature, so that the solution is not presented in our standard conformal frame and in fact the boundary Ricci curvature is discontinuous. Nevertheless, comparison with [36] shows that the resulting bulk manifold is precisely their Euclidean toroidal geon, and one can perform a conformal transformation to make $R_{\text{bndy}} = -2$ everywhere. In appendix 3.A we show how to tune the moduli of $\mathcal{T}$ so that resulting bulk is in the toroidal geon phase.

We may repeat this gluing construction in any AdS phase from section 3.4.1. This results in precisely the set of AdS phases from [36]. Furthermore, the difference in actions between any two phases of $\langle 0|\mathcal{T}^2|0\rangle$ is invariant under conformal transformations and, moreover, in the frame with discontinuous R_{bndy} the contributions of the Poincaré hemispheres clearly cancel when comparing any two phases of $\langle 0|\mathcal{T}^2|0\rangle$ just described. Therefore, for moduli of $\mathcal{T}$ identified in appendix 3.A where $\langle 0|\mathcal{T}^2|0\rangle$ is in the toroidal geon phase, we know that there is a corresponding region where the action of figure 3.10 is smaller than that of two copies of figure 3.5 in either AdS phase from §3.4.1. For such moduli, the phase described by figure 3.10 will dominate over the AdS phases from §3.4.1 for all n.

Let us now consider the implications of the phase described by figure 3.10 for the TFD-like state $\mathbb{T}\mathcal{T}^{n/2}$. For n that are multiples of four, taking the moment of time symmetry to lie between two $\mathcal{T}^2$ blocks (i.e., passing through an α_0 cycle on either the left or right side of figure 3.10) we find the above saddles to again give an AdS phase. However if we put the moment of time symmetry so that it cuts through a $\mathcal{T}^2$ block along the dashed line in figure 3.10, the bulk $t = 0$ surface looks like two disconnected toroidal

geons, i.e., referring to the toroidal geon as $|1\rangle_{\rm BH}$, we have TFD $\sim |1\rangle_{\rm BH} \otimes |1\rangle_{\rm BH}$. By the full replica symmetry of the partition function, both of these configurations must have the same gravitational action, and the TFD-like state $\mathbb{T}\mathcal{T}^{n/2}$ is thus a superposition of the two. On the other hand, for n congruent to 2 mod 4, by similar arguments we find an equal superposition of $|1\rangle_{\rm BH} \otimes |{\rm AdS}\rangle$ and $|{\rm AdS}\rangle \otimes |1\rangle_{\rm BH}$. So if the phase described by figure 3.10 dominates we have

$$\mathbb{T}\mathcal{T}^{n/2} \sim \begin{cases} \frac{1}{2}\,|{\rm AdS}\rangle\,|{\rm AdS}\rangle + \frac{1}{2}\,|1\rangle_{\rm BH}\,|1\rangle_{\rm BH} & n \equiv 0 \bmod 4 \\ \\ \frac{1}{2}\,|1\rangle_{\rm BH}\,|{\rm AdS}\rangle + \frac{1}{2}\,|{\rm AdS}\rangle\,|1\rangle_{\rm BH} & n \equiv 2 \bmod 4 \end{cases}, \tag{3.22}$$

where the $\sim$ denotes leading behavior at large c up to normalization. The gravitational action in this phase is still linear in n, and its dominance at large n would again imply that $\mathcal{T}$ is gapped.

However, the $\mathbb{Z}_2$ symmetry associated with reflections of figure 3.10 across the vertical dashed line implies that $\mathcal{T} = A^\dagger A$ where A is the operator from one copy of the CFT Hilbert space $\mathcal{H}$ to $\mathcal{H} \otimes \mathcal{H}$ defined by the path integral over the right half of figure 3.10. Thus $\mathcal{T}$ is non-negative, and so is $\mathcal{T}^{n/2}$ for even n. Note that while we have suppressed details of the moduli and the order c^0 state of bulk quantum fields in (3.22), these will have some definite values in the phase described and so cannot resolve the problem. We conclude that the phase associated with figure 3.10 cannot be the most dominant. Instead, some new phase must become relevant.

Considering phases that repeat more complicated blocks (e.g. based on $\mathcal{T}^4$) appears to lead to similar problems. However, one possible resolution within the class of gapped

phases is that there are additional bulk saddles which, taken by themselves would give

$$\mathbb{T}\mathcal{T}^{n/2} \sim \begin{cases} \frac{1}{2}\left|1\right\rangle_{\rm BH}\left|{\rm AdS}\right\rangle + \frac{1}{2}\left|{\rm AdS}\right\rangle\left|1\right\rangle_{\rm BH} & n \equiv 0 \bmod 4 \\ \\ \frac{1}{2}\left|{\rm AdS}\right\rangle\left|{\rm AdS}\right\rangle + \frac{1}{2}\left|1\right\rangle_{\rm BH}\left|1\right\rangle_{\rm BH} & n \equiv 2 \bmod 4 \end{cases} , \tag{3.23}$$

at each n, and which turn out to be related to the phases above by an unexpected symmetry so that their actions are precisely equal to those just discussed. In that case, we should sum the contributions (3.22) and (3.23) with equal weight to give

$$\mathbb{T}\mathcal{T}^{n/2} = \frac{1}{2}\left(\left|{\rm AdS}\right\rangle + \left|1\right\rangle_{\rm BH}\right)\left(\left|{\rm AdS}\right\rangle + \left|1\right\rangle_{\rm BH}\right) , \tag{3.24}$$

for all n. Interpreting (3.24) as an operator, $\mathcal{T}^{n/2}$ is the projector onto the pure state $\frac{1}{\sqrt{2}}\left(\left|{\rm AdS}\right\rangle + \left|1\right\rangle_{\rm BH}\right)$ and is manifestly positive. The torus ground state $\left|0\right\rangle_K$ would then be an equal superposition of empty AdS and the toroidal geon.

Other possible resolutions involve gapless phases. Indeed, it might seem most natural to explore the hypothesis that the state $\mathcal{T}^n|0\rangle$ has topology of order n (at least for $n \ll c$). This would require a ground state $\left|0\right\rangle_K$ with topology of order c and, in the semiclassical bulk limit $c \to \infty$, the action would not be precisely linear at large n and so cannot be gapped.

It is an interesting question then to determine if acting with $\mathcal{T}$ on $|0\rangle$ can generate states of high topology. Indeed, if these states exist, then one could make similar cutting and pasting arguments that there are symmetry breaking phases of higher topology that dominate the path integral which computes $\mathrm{Tr}(\mathcal{T}^n)$. For this reason, we postpone our consideration of gapless symmetry-breaking phases until after studying the states $\mathcal{T}^2|0\rangle$ in §3.5. We will return to this topic during the final discussion in §3.6.

3.5 Single Boundary States

We now consider the action of $\mathcal{T}$ on both gloabl AdS and toroidal geon states. In the context of the previous section, we seek to understand if states of high topology can dominate the path integrals considered. Explicitly, we investigate whether $\mathcal{T}^k |0\rangle$ can be dual to a black hole with genus $g = 2$ behind the horizon. We fail to find a region of moduli space where this is the case, leading to the conjecture that this always fails above genus $g = 1$. Indeed, there also appear to be regions of moduli space where the bulk remains empty global AdS for all k.

3.5.1 Definitions and Phases

To study the state $\mathcal{T}^2 |0\rangle$, we consider the partition function defined by the path integral over the genus $g = 4$ Riemann surface drawn in figure 3.11 and having the three $\mathbb{Z}_2$ symmetries described in the caption. In particular, we study the part of the genus-4

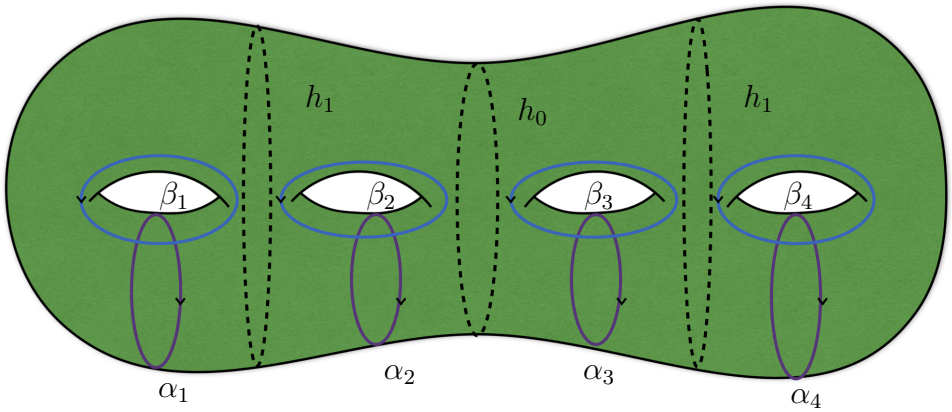

Figure 3.11: Our genus four Riemann surface with α cycles in purple and β cycles in blue. There are three reflection symmetries along the horizontal and vertical axes, as well as in the plane of the page.

moduli space where the vertical $\mathbb{Z}_2$ reflection leaves fixed the geodesics associated with β_i. We remark that this is quite different from the part of the $g = 4$ moduli space shown in figure 3.4, and that it is figure 3.4 rather than figure 3.11 which is relevant in the high

temperature limit described in [27]. Despite our negative results associated with figure 3.11 below, we strongly expect phase where the space behind the horizon has genus 2 to dominate in such a high-temperature limit.

Returning to figure 3.11, cutting the path integral along an initial time-slice given by the middle dashed black line h_0 defines the state $\mathcal{T}_1\mathcal{T}_2\,|0\rangle$ given by two torus operators acting on the vacuum. This problem has a 4-dimensional moduli space, as each torus operator has a two dimensional moduli space associated with it. Considering this generalization allows us to sidestep the need to study in detail the maps between various conformal frames that would arise in a direct computation of $\mathcal{T}^2|0\rangle$. While this comes at the cost of both increasing the dimension of moduli space and being unsure of which 2d slice describes $\mathcal{T}^2|0\rangle$, it turns out to be sufficient for our purposes below.

In general, the above initial time-slice for the corresponding bulk state can have genus $0, 1$, or 2, with many possible phases for each genus. Below, we consider the subspace of moduli space preserving our $\mathbb{Z}_2$ symmetries and study whether a bulk state with a genus 2 initial time slice can dominate in any region of this subspace. We consider six different phases, chosen as the most numerically tractable among those determined by the algorithm described in §3.3. At $t = 0$, three of the phases have genus 0, two have genus 1, and one has genus 2. As a shorthand, we refer to the associated three-dimensional bulk solutions as having genus 0, 1, and 2 respectively.

The three genus 0 phases 0_a, 0_b, 0_c are respectively defined by choosing the sets of cycles $\{\alpha_1, \alpha_{12}, \alpha_{34}, \alpha_4\}$, $\{\beta_1, \beta_2, \beta_3, \beta_4\}$, or $\{\alpha_1, \beta_2, \beta_3, \alpha_4\}$ to be contractible.[10] The corresponding Schottky domains are shown in figure 3.12. For each phase we can numerically compute the lengths of all the labeled boundary geodesics fixed by symmetry and choose parameters so as to match them to those of the genus 2 phase described below. Note that the bulk surface associated with the h_0 cycle (i.e., the surface invariant under

[10]For simplicity of notation we define $\alpha_{ij} \equiv \alpha_i - \alpha_j$ and $\beta_{ij\cdots k} \equiv \beta_i + \beta_j + \cdots + \beta_k$.

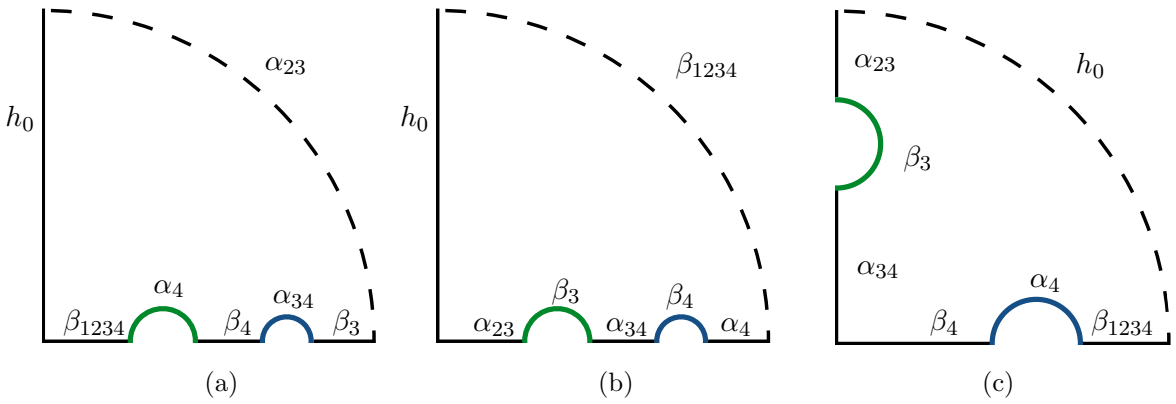

Figure 3.12: One eighth of the Schottky domain used to construct the three genus 0 phases $(0_a, 0_b, 0_c)$ reduced by the reflection symmetries in the x-axis and y-axis and the inversion symmetry through the unit circle (dashed). Various boundary cycles are labeled in each phase. (a) $\{\alpha_1, \alpha_{12}, \alpha_{34}, \alpha_4\}$ contractible. (b) $\{\beta_1, \beta_2, \beta_3, \beta_4\}$ contractible. c) $\{\alpha_1, \beta_2, \beta_3, \alpha_4\}$ contractible.

the right/left $\mathbb{Z}_2$ reflection symmetry of figure 3.11) has genus zero by (3.13).

The two genus 1 phases $1_a, 1_b$ are respectively defined by choosing the set of cycles $\{\alpha_{12}, \alpha_{34}, \alpha_{23}, \beta_{1234}\}$ or the set $\{\beta_1, \beta_4, \alpha_{23}, \beta_{1234}\}$ to be contractible. The Schottky domains are depicted in figure 3.13. Again, for each phase we can numerically compute the lengths of all the labeled boundary geodesics fixed by symmetry, and choose parameters so as to match them to those of the genus 2 phase. Note that the genus of the time-slice associated with the h_0 cycle is now 1 by (3.13).

Finally, we choose the genus 2 phase to have contractible cycles $\{\alpha_{14}, \alpha_{23}, \beta_{23}, \beta_{1234}\}$. However, for computational reasons it is more convenient to use the basis $\{\alpha_{23}, \beta_{1234}, \alpha_{14} + \beta_{1234}, \alpha_{23} + \beta_{23}\}$, which gives the same bulk phase.

Constructing the Schottky domain is difficult as the domain turns out not to preserve the full set of symmetries of this phase. We thus use the following procedure to keep track of all the boundary geodesics and symmetries. First, we cut the boundary Riemann surface along h_0, keeping only the right hand side, and then cut along β_3 and β_4. The result is the surface drawn in figure 3.14a. Next, following the procedure described in

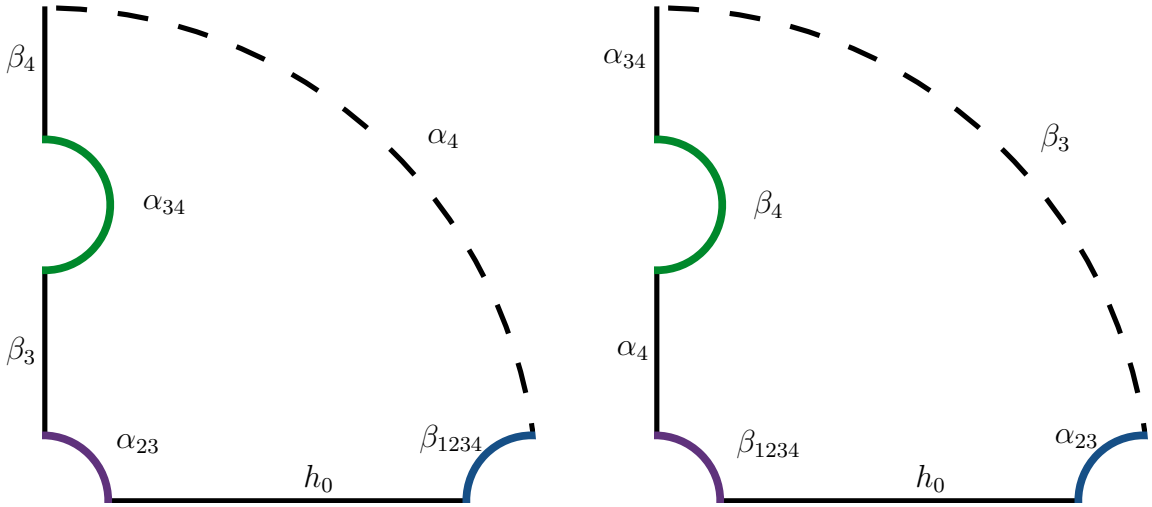

Figure 3.13: One eighth of the Schottky domain used to construct the two genus 1 phases $(1_a, 1_b)$ reduced by the reflection symmetries in the x-axis and y-axis and the inversion symmetry through the unit circle (dashed). Various boundary cycles are labeled in each phase. (a) $\{\alpha_{12}, \alpha_{34}, \alpha_{23}, \beta_{1234}\}$ contractible. (b) $\{\beta_1, \beta_4, \alpha_{23}, \beta_{1234}\}$ contractible.

§3.3 we cut along the contractible cycles $\{\alpha_{23}, \beta_{1234}, \alpha_{14} + \beta_{1234}, \alpha_{23} + \beta_{23}\}$. Note that while this choice of cycles respects the three $\mathbb{Z}_2$ symmetries of the boundary Riemann surface, when we choose representative cycles for $\alpha_{14} + \beta_{1234}$ and $\alpha_{23} + \beta_{23}$ we break two $\mathbb{Z}_2$ symmetries[11] given by reflection in the $x-$axis and $y-$axis in figure 3.14a. However, the product of these symmetries is preserved, and the cycles $\alpha_{14} + \beta_{1234}$ and $\alpha_{23} + \beta_{23}$ are fixed point sets of this product. When we glue everything back together along the cycles β_3 and β_4 to construct the Schottky domain, we thus maintain the requirement that the contractible cycles are fixed point sets of a symmetry. In the Schottky domain of figure 3.14b this symmetry is the product of reflection about the $y-$axis and inversion through the unit circle.

Finally, we can use this Schottky domain to solve for the metric ϕ as described in

[11] One could hope that there exists a basis where we can preserve all of the symmetries, but we find this not to be the case.

§3.3. In order to compute the lengths of geodesics on the boundary, we use the trick described at the end of §3.3 involving mapping to a subset of the Poincaré disk, where the lengths of the boundary segments are determined by the numerical solution for ϕ.

For the three genus 0 phases and the two genus 1 phases, the Schottky domain is defined by four free real parameters, consistent with a four dimensional moduli space for two torus operators with the required symmetries. For the genus 2 phase our Schottky representation breaks two of the symmetries so a priori we have an 8 dimensional parameter space. Carefully tracking the symmetries gives the condition $b_2 - b_1 = b_4 - b_3$ and that the two blue arcs in figure 3.14b have equal length. In the Poincaré disk we can also compute the lengths of the images of the cycles $\alpha_{23} + \beta_{23}$ and $\alpha_{14} + \beta_{1234}$ under reflection across the $x-$axis of figure 3.14a. The requirement that the lengths of these cycles be equal to the lengths of their inverse images gives two more conditions. Imposing these symmetry conditions numerically then reduces the parameter space to four dimensions, recovering the same moduli space considered for genus 0 and genus 1.

3.5.2 Results

We would like to find a region of moduli space where the genus 2 phase dominates. While we do not study all of the possible lower genus phases, the numerical evidence below suggests that the genus 2 phase never dominates even within the phases we study. Indeed, to exclude the genus 2 phase it turns out to suffice to consider only the genus 0_c phase (with contractible cycles $\{\alpha_1, \beta_2, \beta_3, \alpha_4\}$) and the two genus 1 phases.

Our first step was to perform a coarse gradient search in the full four dimensional moduli space to try to minimize the quantity $I_2 - I_{\text{dom.}}$, i.e. the difference in action between the genus 2 phase and the dominant phase within the set of phases described above. This search identified a region of moduli space which we now study in more

detail. For numerical convenience, we parameterize the moduli space using the radii ρ_i of the circles C_i in the Schottky domain for the genus 2 phase (figure 3.14b), with ρ_i computed using the flat space metric. These parameters $\{\rho_1, \rho_2, \rho_3, \rho_4\}$ are respectively related to the lengths of the cycles $\{\alpha_{23}, \beta_{1234}, \alpha_{14} + \beta_{1234}, \alpha_{23} + \beta_{23}\}$, with the precise relation determined by the conformal frame ϕ.

Let us next explore four 1-dimensional trajectories through moduli space each given by varying one of the ρ_i while holding the others fixed. We choose parameters so that these curves lie in the region of moduli space identified by the gradient search above. The results in figure 3.15 show that the phase 0_b dominates along all 4 trajectories, though at the right end of figure 3.15b we appear to begin to approach a transition to where the 1_b phase should dominate.

However, studying the 0_b phase turns out to be computationally intensive in this region. It is thus useful to observe that figure 3.15 also shows the computational-more-convenient phases 0_c, 1_a, and 1_b to dominate over the genus 2 phase. Indeed, these phases appear to capture much of the structure of our full set of phases as the actions of the other genus 0 phases differ from those of $0_c, 1_a, 1_b$ by amounts that are roughly constant along all 4 curves. We shall return to this constant-offset phenomenon below.

Note that a close study of figure 3.15 also suggests that the action difference $(I_2 - I_{0_c})$ increases as either ρ_3 or ρ_4 decrease, and that $(I_2 - I_{1_b})$ and $(I_2 - I_{1_a})$ respectively increase as ρ_3 and ρ_4 increase. It thus appears that – at least in the ρ_3, ρ_4 directions – we are near a local minimum of the quantity

$$\Delta I_{\text{sub.}} = I_2 - \min\left[I_{0_c}, I_{1_a}, I_{1_b}\right] . \tag{3.25}$$

Similarly, as ρ_1 and ρ_2 increase we find that $(I_2 - I_{0_c})$ increases. However as ρ_1 and ρ_2 decrease, all 3 actions I_2, I_{1_a}, and I_{1_b} decrease with $\Delta I_{\text{sub.}}$ appearing to approach a

constant. This latter behavior is consistent with what one expects as the lengths of cycles parameterized by ρ_1 and ρ_2 tend to zero. As shown in [36], in phases where a cycle of small boundary length ℓ is contractible in the bulk, the action diverges as

$$I \sim -\frac{c}{6}\frac{\pi^2}{\ell} + O(\ell^0)\,. \tag{3.26}$$

So as ρ_1 and ρ_2 become small, we expect the phases in which α_{23} and β_{1234} are contractible to have actions that diverge to negative infinity. However, the order one behavior depends on the details of the phase so that the difference in action between two such phases naturally approaches a constant. Figures 3.15a and 3.15b are qualitatively consistent with this behavior, in that the phases whose actions decrease as ρ_1 and ρ_2 become smaller are precisely those in which a contractible cycle pinches off.

In summary, figure 3.15 suggests we are close to a local minimum of $\Delta I_{\text{sub.}}$ up to possible flat directions associated with approaching the boundary of moduli space. To confirm this behavior, we now choose a reference point $\hat{\rho} = (0.0285, 0.009, 0.1785, 0.1905)$ such that $I_{0_c} = I_{1_a} = I_{1_b}$ and explore in more detail how $\Delta I_{\text{sub.}}$ varies near $\hat{\rho}$. Figure 3.16 displays the value of $\Delta I_{\text{sub.}}$ in two 2-dimensional slices of moduli space through $\hat{\rho}$. Figure 3.16a varies (ρ_3, ρ_4) with (ρ_1, ρ_2) fixed to match $\hat{\rho}$, while 3.16b varies (ρ_1, ρ_2) at fixed (ρ_3, ρ_4). The data is consistent with the above expectations, indicating a robust local minimum in the (ρ_3, ρ_4)-plane while in the (ρ_1, ρ_2)-plane $\Delta I_{\text{sub.}}$ either increases or remains roughly constant as one moves away from $\hat{\rho}$.

Finally, to investigate the flat directions further we compute the action of relevant phases as a function of the length of a pinching cycle along two one-dimensional curves through $\hat{\rho}$ by varying either ρ_1 or ρ_2 while holding the other three ρ_i fixed at $\hat{\rho}_i$. The results are displayed in figure 3.17 and compared with a fit to the function $-A\frac{\pi^2}{6}\frac{c}{\ell} + k$ inspired by (3.26). In 3.17a we use the range $1.73 < |\alpha_{23}| < 2.39$ and find the best fit to

have $A = 1.090$ for I_2 and $A = 1.096$ for I_{1_a}. The difference between these two best-fit values for A is consistent with our estimated 1% numerical error. However, both differ by 10% from the expected value $A = 1$. Since we study the range $\ell \sim 2$ where ℓ is not particularly small, we expect that this discrepancy is due to not probing sufficiently far into the asymptotic regime. In practice, it is numerically difficult to compute the action for smaller α_{23}. Similar comments apply to figure 3.17b where we use the range $1.65 < |\beta_{1234}| < 1.97$ to find best-fit parameters $A = 1.091$ for I_2 and $A = 1.077$ for I_{1_a}. We take the agreement shown in figure 3.17 to support the above interpretation of figure 3.16 as implying that $\Delta I_{\text{sub.}}$ will remain essentially constant up to the edges of moduli space at $\rho_1 = 0$, $\rho_2 = 0$, and thus that the genus 2 phase does not dominate anywhere in moduli space.

It is interesting to compare the results presented in figure 3.16 with our heuristic based on the total length of contractible cycles. Denoting this total length in a particular phase by $\mathscr{L}$, figure 3.18 plots the quantity,

$$\Delta\mathscr{L} = \mathscr{L}_2 - \min[\mathscr{L}_{0_c}, \mathscr{L}_{1_a}, \mathscr{L}_{1_b}] \tag{3.27}$$

in the neighborhood of $\hat{\rho}$. The heuristic suggests that $\Delta I_{\text{sub.}}$ is smaller (i.e., that the genus 2 phase is less sub-dominant) at small $\Delta\mathscr{L}$, so figures 3.16 and 3.18 should be similar. This is certainly the case at the qualitative level, though – as seen in other cases – there are quantitative differences. In particular, while $\Delta\mathscr{L}$ has a local minimum close to that of $\Delta I_{\text{sub.}}$, it clearly differs from $\hat{\rho}$.

In evaluating our claim that the dominant phase always has genus 0 or 1, one should of course ask whether there might be another genus 2 phase that is more dominant than the one considered here. We have no proof that such phases do not exist, though we have found no natural candidates. For example, we excluded the phase $\{\alpha_1 - \alpha_3, \alpha_2 -$

$\alpha_4, \beta_1 + \beta_3, \beta_2 + \beta_4\}$ from our analysis because it breaks a symmetry of the boundary Riemann surface by introducing a twist through the bulk. On the other hand, in light of the replica symmetry breaking phases for $\mathrm{Tr}(\mathcal{T}^n)$, it remains possible that this symmetry breaking phase does in fact dominate. It would be interesting to investigate this further in the future.

Bearing in mind this caveat, the above numerical evidence nevertheless suggests that – depending on the choice of moduli – $\mathcal{T}^2 |0\rangle$ can take be either of the form $|\mathrm{AdS}\rangle$ or $|1\rangle_{\mathrm{BH}}$, but that there are no moduli for which it is dual to bulk solutions with higher topology. If so, the same must hold for $\mathcal{T}^k |0\rangle$.

3.6 Discussion

The results presented in §3.4 and §3.5 set up a puzzle with no clear resolution. In §3.4 we presented arguments that if a replica symmetry preserving phase dominates the path integral computing $\mathrm{Tr}(\mathcal{T}^n)$ for all moduli, then for at least some large n we would have

$$\mathcal{T}^{n/2} \sim |\mathrm{AdS}\rangle \langle \mathrm{AdS}| \tag{3.28}$$

and therefore $|0\rangle_K = |\mathrm{AdS}\rangle$. But (3.28) is inconsistent with the calculations in §3.5 and [36] showing that, in certain regions of moduli space, applying $\mathcal{T}$ to AdS states could produce states described by toroidal geons. It thus seems that replica symmetry breaking phases must dominate the path integral for such moduli.

On the other hand, if the $\mathbb{Z}_n$ replica symmetry is broken, then acting with appropriate elements of $\mathbb{Z}_n$ would produce distinct saddles with equal action. In parallel with the

discussion of §3.4.2, if a simple gapped such phase dominates we may then expect to find

$$\mathcal{T}^{n/2} \sim |\phi\rangle \langle\psi| + |\psi\rangle \langle\phi| \tag{3.29}$$

for $|\phi\rangle$, $|\psi\rangle$ orthogonal states of differing bulk topology. But $\mathcal{T}^{n/2}$ would have a negative eigenvalue corresponding to the eigenstate $\frac{1}{\sqrt{2}}(|\phi\rangle - |\psi\rangle)$. We expect that similar issues also arise for more complicated replica-symmetry breaking gapped phases.

However, §3.4.2 noted that this issue would be resolved if there are additional phases for $\mathrm{Tr}(\mathcal{T}^n)$ which, taken by themselves would give

$$\mathcal{T}^{n/2} \sim |\phi\rangle\langle\phi| + |\psi\rangle\langle\psi|\,, \tag{3.30}$$

for the above n, and which somehow turn out to be related to those found thus far above by an unexpected symmetry so that their actions are precisely equal to those just discussed. In that case, we would sum the contributions (3.29) and (3.30) with equal weight to give

$$\mathcal{T}^{n/2} = \frac{1}{2}\left(|\phi\rangle + |\psi\rangle\right)\left(\langle\phi| + \langle\psi|\right)\,, \tag{3.31}$$

the manifestly-positive projector onto $\frac{1}{\sqrt{2}}(|\phi\rangle + |\psi\rangle)$. If (3.31) holds for all large n, the torus ground state $|0\rangle_K$ is then an equal superposition of two different bulk topologies. Unfortunately, this would alsorequire a similar unexpected new phase for the state $\mathcal{T}^2|0\rangle$ studied in §3.5, or else a fine-tuning that makes the state $\mathcal{T}|0\rangle$ have just the right moduli so that $\mathcal{T}^2|0\rangle$ lies precisely on the phase boundary at which an AdS and toroidal geon phase exchange dominance. It would be interesting to investigate both possibilities further in the future.

Other possible resolutions involve gapless phases. As mentioned at the end of §3.4.2,

one option might be for the state $\mathcal{T}^n|0\rangle$ to have genus of order n (at least for $n \ll c$). But, with the caveat that we leave for the future any investigation of genus-2 phases that spontaneously break symmetries of the boundary, our direct studies of $\mathcal{T}^2|0\rangle$ in §3.5 found no evidence that this is the case and instead suggest that $\mathcal{T}^n|0\rangle$ has at most genus 1.

We thus turn to gapless phases where the topology on a $t = 0$ surface remains of order 1 at large n. Consider for example the phase defined for $n \geq 6$ with contractible cycles given by $\alpha_i - \alpha_{i+3}$ and $\beta_i + \beta_{i+3}$ for odd i, the cycles $\alpha_i - \alpha_{i-3}$ and $\beta_i + \beta_{i-3}$ for even i, and the cycle β_0. We show a depiction of this phase for $n = 8$ and $n = 10$ in figure 3.19. In particular, the contractibility of β_0 means that any $t = 0$ surface is a connected wormhole with two boundaries. As a result, just as for the the BTZ phases of §3.4.1, the bulk solutions for large n cannot be obtained by cutting and pasting those for small n. The action should thus be only asymptotically linear in n and the phase should be gapless.

A study of figure 3.19 shows that such $t = 0$ surfaces have genus 2, 3, or 4. For example, take a $t = 0$ surface given by the vertical dashed grey line. For $n = 8$, the resulting TFD-like state is a genus 2 wormhole that is symmetric under reflection across the horizontal dashed line, with the symmetry acting to exchange the two boundaries and the two bulk handles. Rotating these dashed lines by $\pi/4$ gives a TFD-like state described by a genus 4 wormhole with a similar symmetry. For $n = 10$, the resulting TFD-like state is a genus 3 wormhole that breaks the symmetry of the Riemann surface associated with reflections through the horizontal dashed line. A cartoon of the $t = 0$ geometry is depicted in figure 3.20; it is *not* symmetric under right-to-left reflections. Rotating these dashed lines by $\pi/5$ gives the same $t = 0$ geometry, but with the two boundaries exchanged. We thus refer to this phase below as the $2, 3, 4$-handled wormhole. Note that we use the term wormhole to indicate that two distinct boundaries are connected through the bulk, while

we have consistently used the term geon to describe solutions with a single boundary but with non-trivial topology behind a horizon.

As argued previously for the BTZ phases of §3.4.1, we expect the (log) conformal factors associated with a Schottky description to satisfy the approximate scaling $\phi_{n+2}(w) = \phi_n(w^{\frac{n}{n+2}})$. And as before, this scaling should result in the length of some bulk cycle on the $t = 0$ surface shrinking like $1/n$. So if this phase dominates the state $\mathcal{T}^{n/2}$ on $\mathcal{H} \otimes \mathcal{H}$ will be entangled, with the entropy on each copy of the CFT also scaling like $1/n$. In particular, as discussed previously, in the limit $n \to \infty$ it becomes effectively pure on each side, with the would-be entangling surface turning into the infinite throat of an $M = 0$ BTZ black hole. In particular, for $n \equiv 2 \bmod 4$ any $t = 0$ surface fails to be symmetric under exchange of the two boundaries. We thus expect the shrinking cycle to separate a genus-2 geon from a toroidal geon; i.e., we expect the shrinking cycle to be the one drawn as a dashed line in fig. 3.20. At large n (and again interpreting $\mathcal{T}^{n/2}$ as an operator) we thus find

$$\mathcal{T}^{n/2} \sim \begin{cases} \frac{1}{2}\left(|1\rangle_{\rm BH}\langle 1|_{\rm BH} + |2\rangle_{\rm BH}\langle 2|_{\rm BH}\right) & n \equiv 0 \bmod 4 \\ \\ \frac{1}{2}\left(|1\rangle_{\rm BH}\langle 2|_{\rm BH} + \frac{1}{2}|2\rangle_{\rm BH}\langle 1|_{\rm BH}\right) & n \equiv 2 \bmod 4 \end{cases}, \tag{3.32}$$

so that $\mathcal{T}$ again has a negative eigenvalue just as in our discussion of gapped phases.

Indeed, it seems unlikely that the above phase will dominate at large n over the gapped replica symmetry breaking phase of figure 3.10. In order for it to do so and to respect our heuristic, we must have

$$|\alpha_i - \alpha_{i+3}| + |\beta_i + \beta_{i+3}| < |\alpha_i - \alpha_{i+1}| + |\beta_i + \beta_{i+1}|\,. \tag{3.33}$$

While we have not shown this to be impossible, it would be surprising if cycles stretching

between replicas i and $i+3$ were shorter than cycles that connect nearest neighbors. So in the end the $2,3,4$-wormhole phase seems unlikely to be relevant at large n.

It thus appears that additional phases not yet studied must become important at large n. It remains interesting to determine whether these are new gapped (or gapless) phases that lead to a ground state of indefinite topology as suggested above, phases that spontaneously break symmetries as mentioned at the end of §3.5, or merely other – perhaps more complicated – phases that we were not considered here. In the latter category one might also consider phases that do not lie in the universal sector, and which are thus not described by pure gravity in the bulk. In particular, one can ask whether considering condensates of long strings [46] might somehow resolve our puzzle.

In addition to the study of new phases, it would be useful to study in detail the map on the genus-4 moduli space associated with passing between the $R_{bndy} = -2$ conformal frame and the conformal frame in which $\mathcal{T}^2|0\rangle$ is described by an $R_{bndy} = -2$ twice-punctured genus 2 surface (representing the $\mathcal{T}^2$ with geodesic boundaries) attached to a positive-curvature hemisphere. This conformal frame was used briefly in §3.4.2 to argue that there is a region of moduli space in which the replica-symmetry breaking phase from figure 3.10 dominates over those studied in §3.4.1. A study of this map would allow a more precise understanding of $\mathcal{T}^2|0\rangle$, and also of $\mathcal{T}^k|0\rangle$ for higher k. In a different direction, it would be interesting to extract a log term of the form shown in (3.5) from the bulk action of a gapless phase at large replica number n, or to better understand the relationship between the 'total cycle length heuristic' and the actual bulk action. While we took some steps toward the latter in figures 3.8 and 3.18, we leave further investigation for future work.

3.A Phase Space of $\mathcal{T}\,|0\rangle$

In this appendix we compute the gravitational dual of $\mathcal{T}\,|0\rangle$ in the $\mathbb{Z}_2$ symmetric subspace of the moduli space of $\mathcal{T}$ considered in this paper. We show that restricting to this two dimensional subspace does not significantly restrict the phase space of states of $\mathcal{T}\,|0\rangle$. That is, by varying the moduli of $\mathcal{T}$, one is able to construct states that are dual to pure AdS or states that are dual to toroidal geons of a wide range of moduli.

Our strategy will be to start with a representation of $\mathcal{T}^2$ as the path integral over two copies of $\mathscr{T}$ glued together. We will use this representation to compute the moduli of $\mathcal{T}$ as lengths of cycles on $\mathscr{T}$ in the appropriate conformal frame. To compute the inner product $\langle 0|\mathcal{T}^2|0\rangle$, we glue hemispheres on to the two cuts in the path integral over $\mathscr{T}^2$. The resulting path integral is now one over two copies of a once punctured torus $\overline{\mathscr{T}}$ glued together along the puncture. This path integral is now of the type considered in [36], and we can compute the semi-classical gravitational approximation of $\mathcal{T}\,|0\rangle$ from the saddle points in the usual way.

Consider a Schottky uniformization of $\mathscr{T}^2$ in the conformal frame $R_{\text{bndy}} = -2$ as shown in figure 3.21. In this conformal frame, we can compute the moduli of $\mathcal{T}$ by evaluating the length of various boundary cycles as labeled in the figure. We choose to parameterize the $\mathbb{Z}_2$ symmetric moduli space by $|\alpha_0|$ and $|\beta_1|$.

Gluing hemispheres on to the boundaries of $\mathscr{T}^2$ can be achieved by filling in the purple circles α_0 in the Schottky domain of figure 3.21. The resulting domain is a representation of the surface $\overline{\mathscr{T}}^2$ used to compute the norm of the state $\mathcal{T}\,|0\rangle$, with the moduli of $\mathcal{T}$ computed by the original Schottky domain. We draw the surface $\overline{\mathscr{T}}^2$ and its Schottky uniformization in figure 3.22. The semi-classical gravitational dual of this state is given by the geometry on the surface fixed by the $\mathbb{Z}_2$ symmetry exchanging the two halves of $\overline{\mathscr{T}}$. In this way, we can map out the phase space of states $\mathcal{T}\,|0\rangle$ in terms of the moduli

of $\mathcal{T}$.

The domain constructed in this manner is a representation of a pure AdS phase of $\mathcal{T}\,|0\rangle$. The moment of time symmetry on which we define the state is given by the dashed cycle in figure 3.22. In the associated Schottky domain, this cycle is contractible in the bulk, as it can be lifted off the boundary and shrunk to a point without intersecting the geodesic hemispheres that are identified by the Schottky group. Alternatively, we can use the formula (3.13), with $n = 0$ and $b = 1$ giving $g_{t=0} = 0$.

To compute the semi-classical gravitational dual of this state, we match the moduli of $\overline{\mathscr{T}}^2$ to the Schottky uniformizations corresponding to the remaining pure AdS phase and the toroidal geon phase. The remaining pure AdS phase can be described by the Schottky domain in figure 3.22b, with the interpretation of the α and β cycles flipped. To describe the toroidal geon phase, we can use the Schottky domain in figure 3.23. In this case, the relevant $t = 0$ slice is given by the horizontal axis of the Schottky domain. This slice is broken into $b = 1$ boundary segments and intersects $n = 2$ pairs of circles given $g_{t=0} = 1$. Therefore, this domain is a representation of the toroidal geon phase. To gain intuition for this result, note that contractibility of $\beta_1 + \beta_2$ implies that we can deform the cycle β_1 through the bulk until it becomes the cycle $-\beta_2$. Thinking of the left half of figure 3.22a as bulk Euclidean time negative infinity and the right half as bulk Euclidean time positive infinity, such a deformation must pass through $t = 0$. But the cycle β_1 is non-contractible, so the $t = 0$ slice must contain a non-contractible cycle.

Comparing the actions of these phases, we can determine the dominant saddle and the semi-classical description of $\mathcal{T}\,|0\rangle$. We display the difference in action between the toriodal geon phase and the dominant phase $\frac{1}{c}(I_{\text{TG}} - I_{\text{dom.}})$ in figure 3.24. When the toroidal geon phase is dominant this quantity vanishes. In the region where the toriodal geon phase dominates, we compute the length the horizon and the lengths of the cycles of the bulk torus. We find a minimal horizon size matching [36] and a range of internal

cycles, leading us to conclude the moduli space of states is not signficantly restricted by imposing the $\mathbb{Z}_2$ symmetries of $\mathcal{T}$.

3.B Estimation of Numerical Error

In this appendix we discuss some sources of numerical error. First there is the discretization error from using finite element methods to solve for ϕ. We can estimate this error as in [36] by computing the area of the Riemann surface and comparing it to the Gauss Bonnet theorem. That is, we have

$$A(g) = 4\pi(g-1) \tag{3.34}$$

in AdS units. We define $\epsilon_A = |1 - A/A(g)|$ as an estimate for this error. For domains where the geodesic lengths are computed in the Schottky representation (and not the Poincaré disk), we report this value as the overall error.

Further, we perform numeric integration over the boundary circles by adding up the function values on the mesh nodes coinciding with a particular circle. In order to do so, we must set a tolerance for considering a point on the boundary circle, which introduces some numerical error. We can estimate this error by computing the length of a boundary segment using a flat metric and compare it to the analytic formula for the length of the arc of the corresponding circle. The tolerance is chosen to minimize the percent error of each boundary circle. We denote the maximum of all of these errors ϵ_C.

Additionally, we estimate the propagation of these uncertainties in computing the geodesic lengths in the Poincaré disk. To estimate this error, we construct the corresponding domain in the Poincaré disk for boundary segment lengths $\ell_0(1 + \max(\epsilon_A, \epsilon_A))$, where ℓ_0 is the segment length as computed by the numerical solution ϕ. The maximum

change in geodesic lengths by using different lengths of boundary segments estimates this error ϵ_G. When $\epsilon_G > 0.05$ we find the moduli matching algorithms tend not to converge, and so we take this as a cutoff of numerical error. The overall error is taken to be $\epsilon = \max(\epsilon_A, \epsilon_C, \epsilon_G)$ which is ϵ_G. We find ϵ_G tends to be 1-2 orders of magnitude larger than ϵ_A or ϵ_C, and for future work this suggests a way to reduce errors even further.

Finally, in matching moduli between phases, we only require them to match up to a certain threshold. That is we require the percentage difference between two matching moduli to be less than $\max(\epsilon_G, 3 \times 10^{-3})$.

The error ϵ_A can be reduced simply by using more lattice points to discretize the domain. To reduce ϵ_C we must include more boundary points as well as choose the tolerance accordingly. In figure 3.25 we display ϵ_A for a representative genus 2 phase from §3.5 as a function of the number of points.

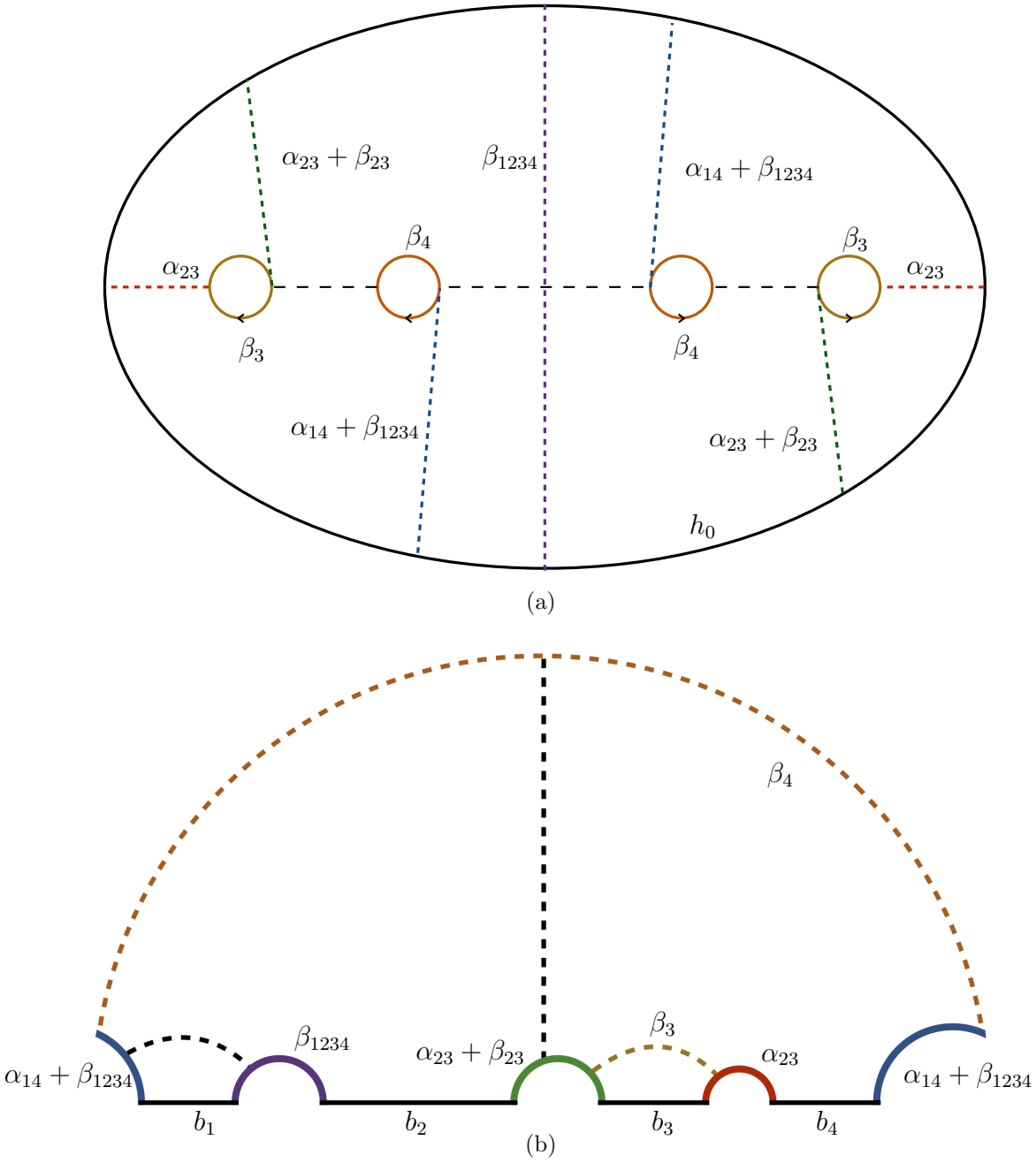

Figure 3.14: (a) One half of the flattened Riemann surface. The surface has been cut along the cycles β_3 and β_4 along the fixed point set of reflection across the vertical purple dashed line. (b) One fourth of the genus 2 Schottky domain, reduced by two symmetries. The two symmetries of the plane are reflection about the $x-$axis (labeled h_0) and the product of the reflection about the $y-$axis (dashed black) and inversion through the unit circle (labeled β_4). The boundary cycle h_0 is broken into four segments b_i.

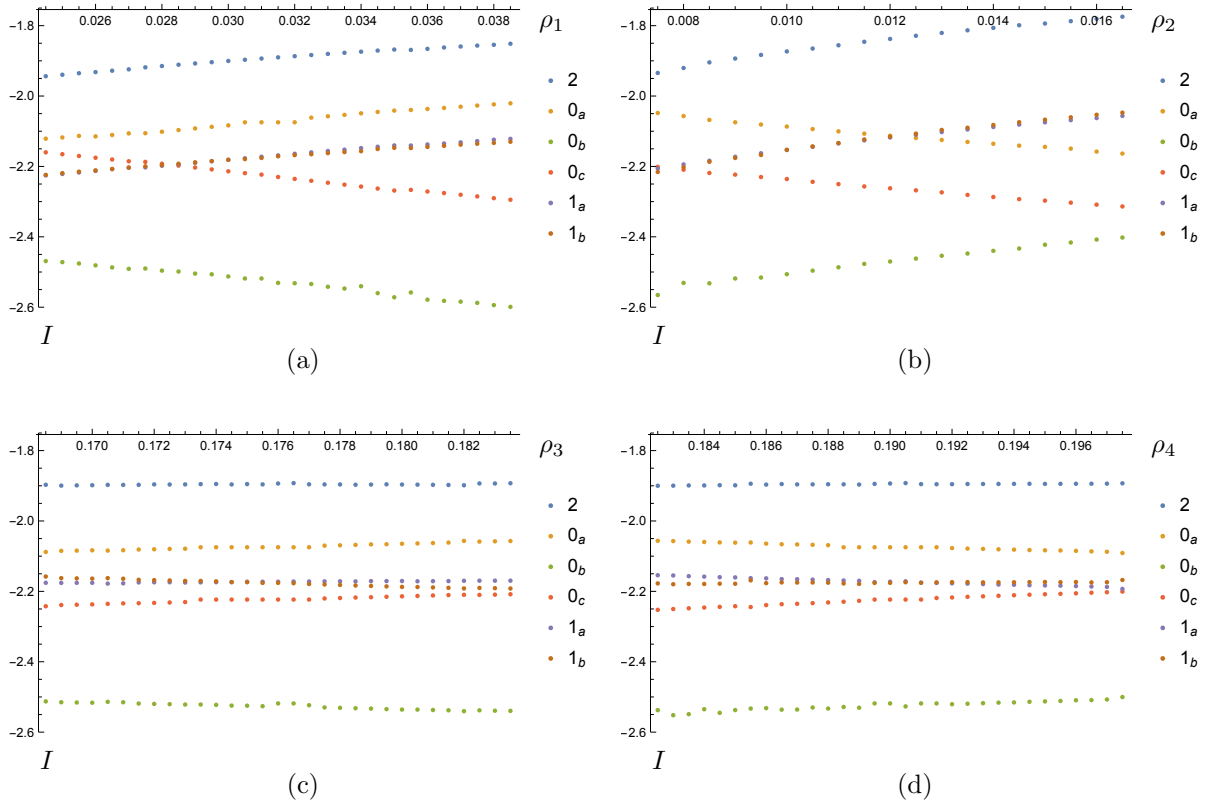

Figure 3.15: The action for all six phases along four paths through the region of moduli space picked out by the coarse gradient search. Each phase is labeled by genus with a subscript corresponding to the labels in figures 3.12 and 3.13. The numerical errors are less than 1% in the sense of Appendix A. This level of error is consistent with what may appear to be stray points along the curves.

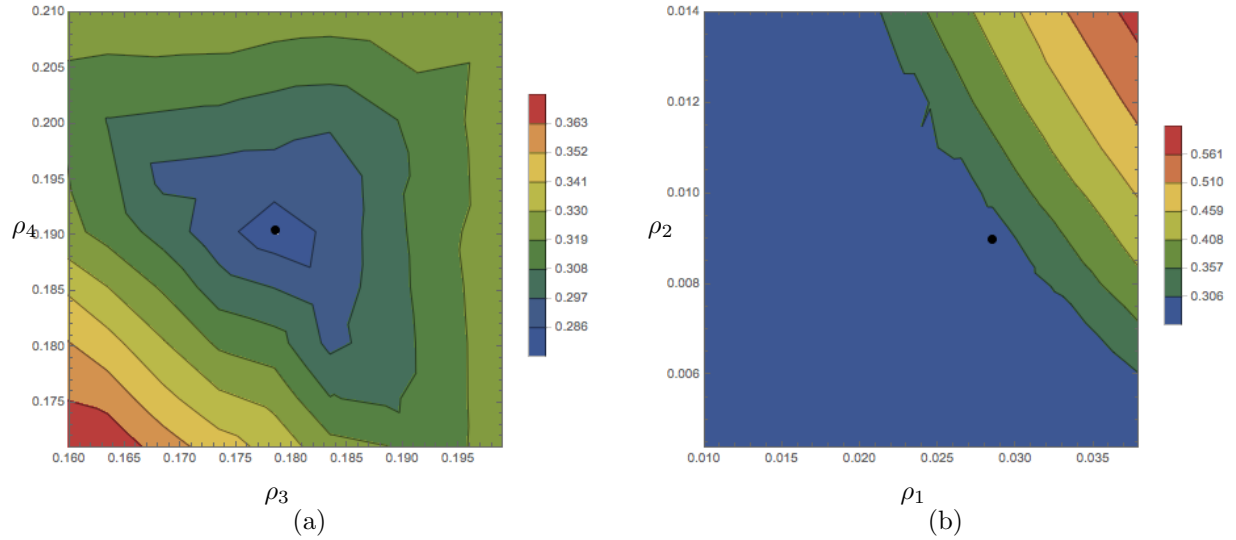

Figure 3.16: Two 2-dimensional slices of the four dimensional moduli space through $\hat{\rho}$ (black dot in each figure). ρ_1, ρ_2 are fixed at left, with $\rho_3, \rho)_4$ fixed at right. Numerical errors are less than 1% in the sense of appendix A. This level of error is consistent with some of the jagged features of the contours, though the existence of a local minima is robust to such errors. (a) ρ_1, ρ_2 fixed. (b) ρ_3, ρ_4 fixed.

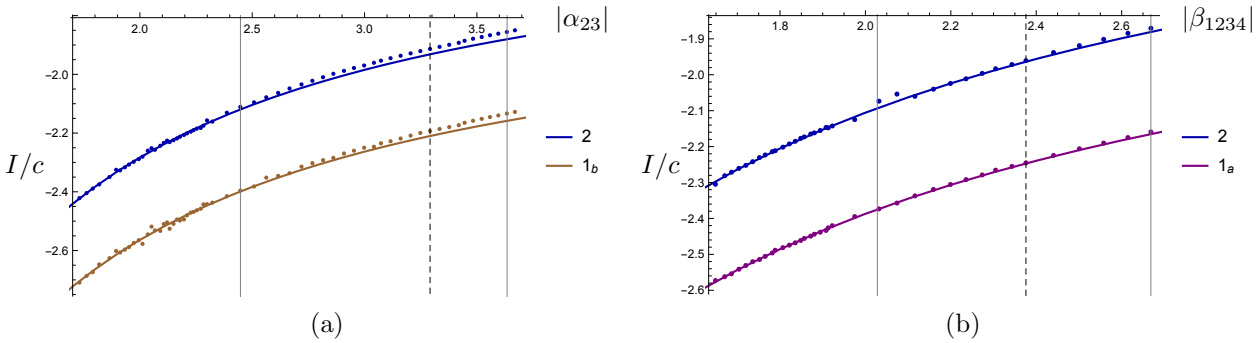

Figure 3.17: A study of the pinching limits along the plateau in figure 3.16((b) comparing I/c for the indicated phases (dots) to the form $-A\frac{\pi^2}{6}\frac{c}{\ell} + k$ inspired by eq. (3.26). The solid curve shows this function for best-fit values of A, k. Vertical lines indicate $\hat{\rho}$ and the boundaries of figure 3.16. ((a) ρ_2, ρ_3, ρ_4 are fixed to match $\hat{\rho}$ while ρ_1 varies; $A_{\text{best fit}} = 1.090, 1.096$ for I_2, I_{1_1} over the range $1.73 < |\alpha_{23}| < 2.39$. ((b) ρ_1, ρ_3, ρ_4 are fixed to match $\hat{\rho}$ while ρ_2 varies; $A_{\text{best fit}} = 1.091, 1.077$ for I_2, I_{1_a} over the range $1.65 < |\beta_{1234}| < 1.97$. (a) $\rho_1 \to 0$ plateau. (b) $\rho_2 \to 0$ plateau.

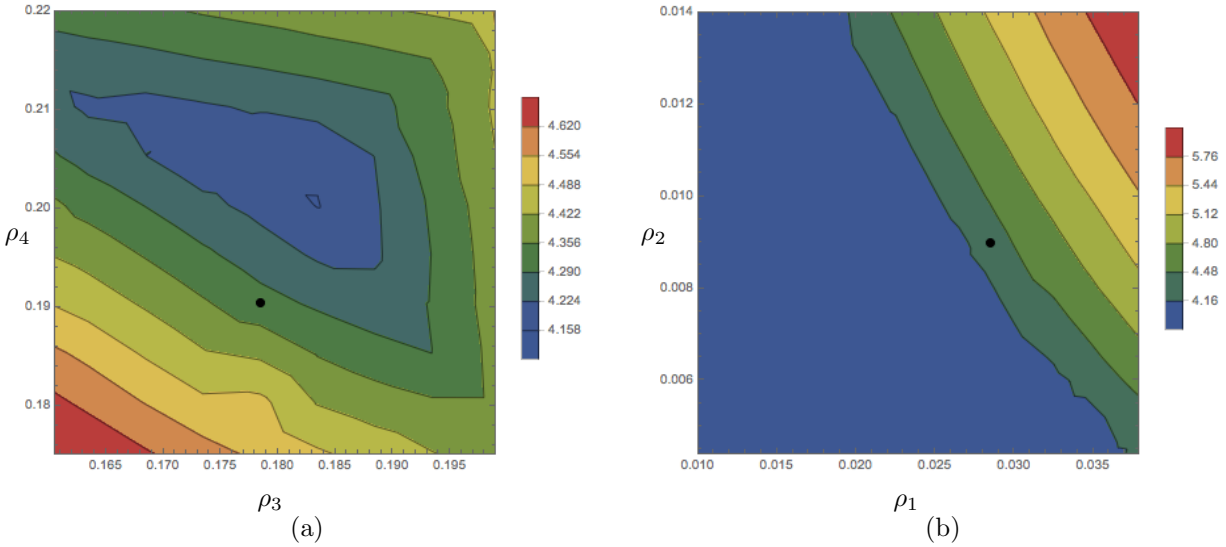

(a) (b)

Figure 3.18: The quantity $\Delta\mathscr{L}$ in the neighborhood of $\hat{\rho}$ (black dot). (a) ρ_1, ρ_2 fixed. (b) ρ_3, ρ_4 fixed.

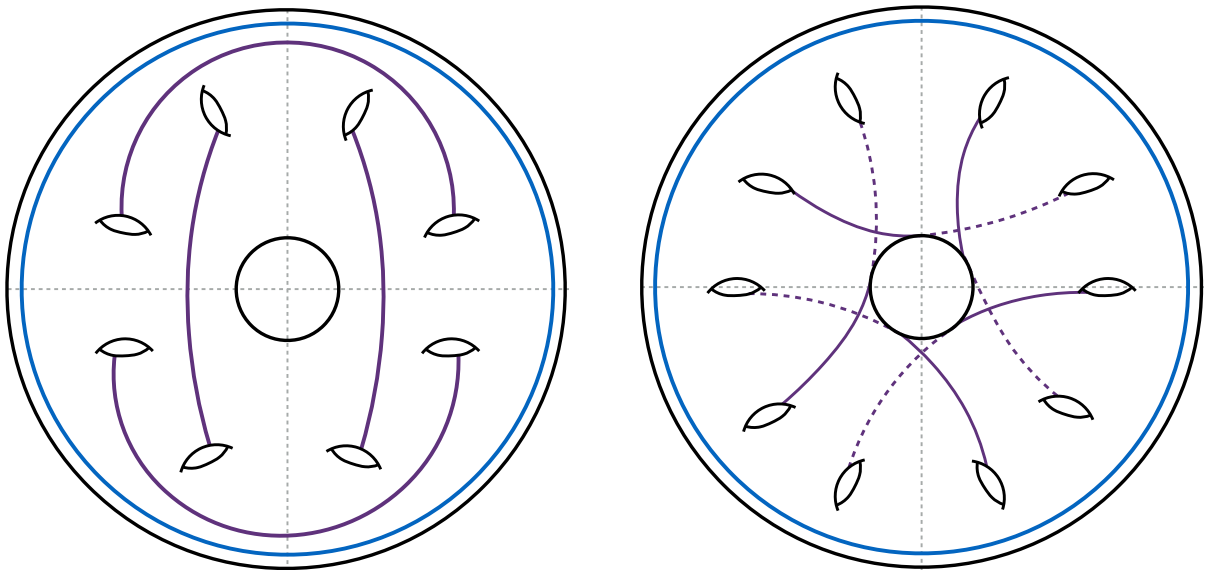

(a) (b)

Figure 3.19: A gapless phase for (a) $n = 8$ and (b) $n = 10$. The purple lines joining two holes i, j indicate the pair of cycles $\alpha_i - \alpha_j$ and $\beta_i + \beta_j$ are contractible. Relevant reflection symmetries of the boundary are drawn in dashed grey. Both dashed lines on the left and the vertical dashed lin on the right are possible $t = 0$ surfaces that can contribute to $\mathcal{T}^{n/2}$ thought of as a state on $\mathcal{H} \otimes \mathcal{H}$. In contrast, the horizontal dashed line on the right gives a 4-boundary $t = 0$ surface.

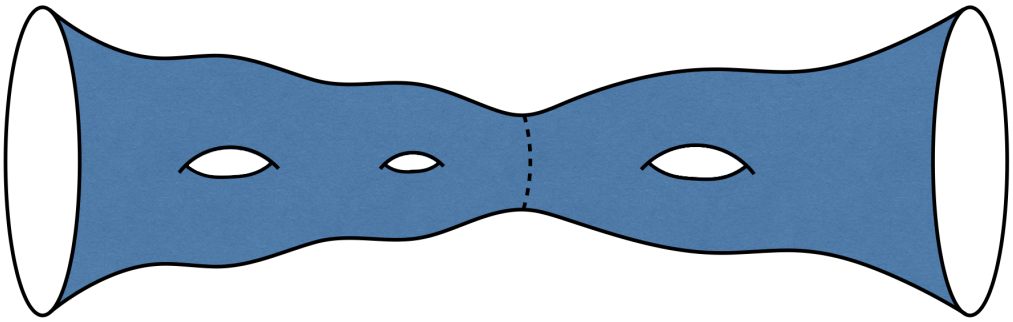

Figure 3.20: A cartoon of the 3-handled wormhole, with a candidate minimal extremal surface drawn in dashed black.

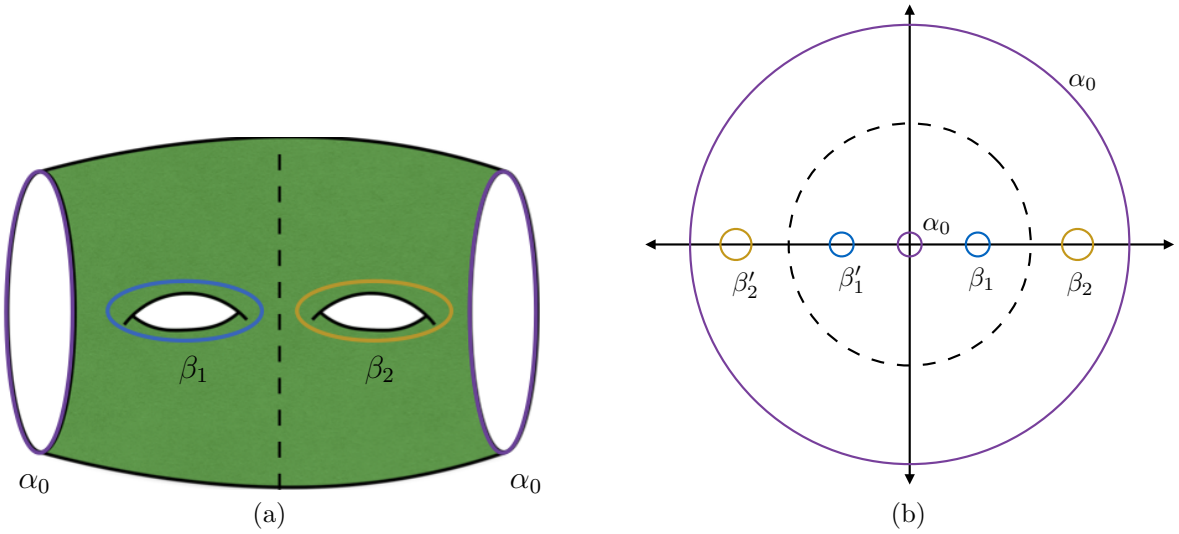

Figure 3.21: The $\mathbb{Z}_2$ symmetric surface and Schottky domain used to compute the moduli of $\mathcal{T}^2$. Note that $|\beta_1| = |\beta_2|$ by the reflection symmetry across the dashed cycle. (a) The surface $\mathscr{T}^2$ with moduli labeled. (b) The associated Schottky domain.

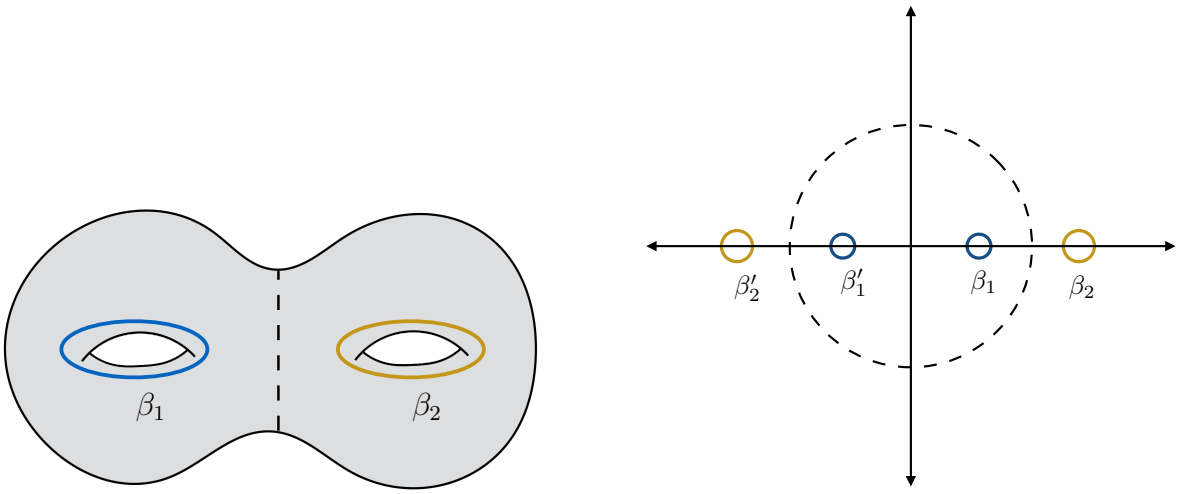

(a) (b)

Figure 3.22: The $\mathbb{Z}_2$ symmetric surface and Schottky domain used to compute $\langle 0|\mathcal{T}^2|0\rangle$. The handlebody represented by the Schottky domain is a pure AdS phase. (a) The surface $\overline{\mathscr{T}}^2$. (b) The Schottky domain for a pure AdS phase.

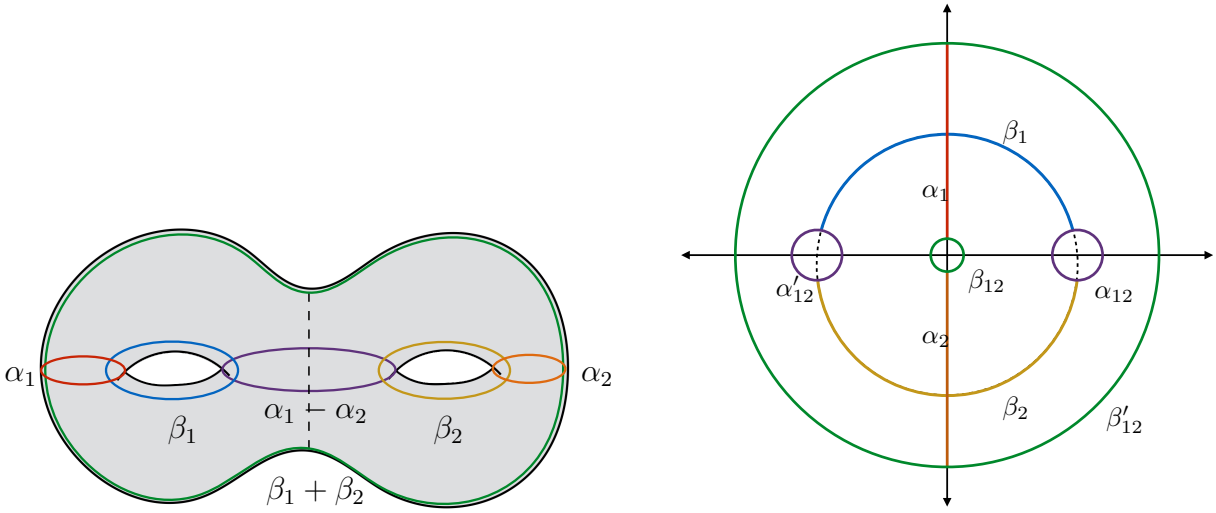

(a) (b)

Figure 3.23: The uniformization of the surface $\mathscr{T}^2$ used to represent the toroidal geon phase. The contractible cycles are given by $\alpha_{12} = \alpha_1 - \alpha_2$ and $\beta_{12} = \beta_1 + \beta_2$. To construct the Schottky domain, we cut along these cycles and identify each side of the cut as C_i and C_i'. (a) Labeled cycles on $\mathscr{T}^2$. (b) The Schottky domain for the toroidal geon.

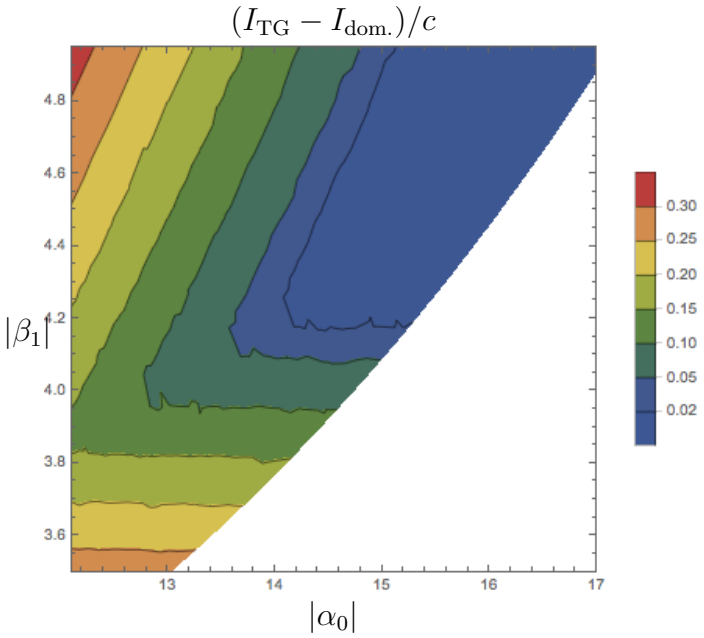

Figure 3.24: Phase diagram for $\mathcal{T}|0\rangle$. In the blue region $I_{\mathrm{TG}} - I_{\mathrm{dom.}}$ vanishes and the toroidal geon phase is dominant. Outside of this region an AdS phase is dominant. In the white region we have no data, as it is numerically difficult to probe.

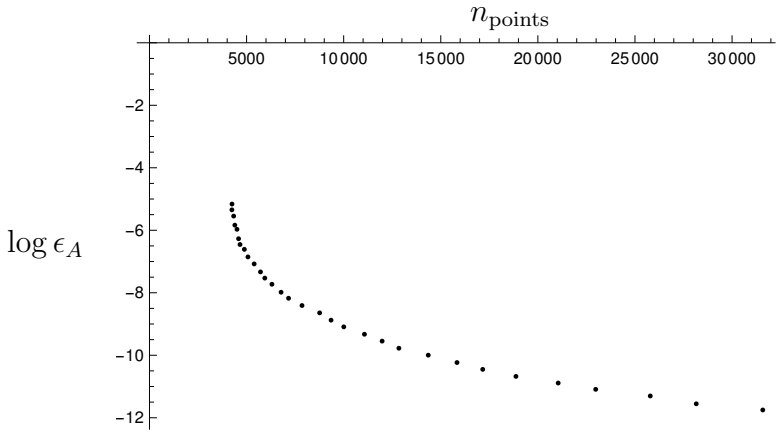

Figure 3.25: Estimation of ϵ_A as a function of number of lattice points n_{points}.

Chapter 4

The Holographic Entropy Cone

4.1 Introduction

Since the original proposal by Ryu and Takayanagi [23] for the calculation of entanglement entropy in holographic field theories, the inequalities implied by the "RT formula" have been a subject of active investigations. It was already noted in [24] that *subadditivity* ($\mathcal{SA}$) of the von Neumann entropy is satisfied by the prescription, while the celebrated proof [52] of the more restrictive *strong subadditivity* ($\mathcal{SSA}$) served as a further important check. The saturation of $\mathcal{SA}$ was later associated to a phase transition of mutual information in [53] and the saturation of the Araki-Lieb inequality ($\mathcal{AL}$) to the entanglement plateaux phenomenon [54].

While all the previous inequalities were already known from quantum mechanics (they are in fact satisfied by any quantum state), the first purely "holographic" inequality was found in [55] and dubbed *monogamy of mutual information* ($\mathcal{MMI}$).[1] This inequality is not satisfied by all quantum states and provides a new constraint on the family of states which admit a classical geometric dual. It is then interesting to ask whether the

[1] See [56, 57, 58] for more details.

RT formula implies additional constraints for a fixed (but arbitrary) number of regions in a holographic CFT. The systematic study of this problem was initiated in [59], which proved that no new inequalities exist for three or four regions and found new ones for five.[2]

In principle, for a fixed number of regions in the dual field theory, the set of entropy inequalities which are satisfied by holographic states could be rather complicated. For example, there could be an infinite number of them or they could be nonlinear. Instead, an important result of [59] was the proof that not only the number of inequalities implied by the RT prescription is finite for any number of regions, but all inequalities are in fact linear and with integer coefficients.

For an arbitrary system of inequalities it is useful to consider a geometric representation where the set of solutions is a region bounded by the corresponding hypersurfaces. For the inequalities implied by RT this is then a rational polyhedron in the space of entropies, in fact a cone, which has an equivalent description in terms of its extremal rays. Any ray inside the cone (or on its boundary) can be obtained from a (conical) linear combination of them.

Motivated by holography one then tries to construct geometries that realize the extremal rays and to show that such geometries are in fact dual to some field theory state. This would prove that the region of entropy space corresponding to states of holographic CFTs with classical bulk duals is a rational polyhedron. The present work focuses on this last statement and argues that the proof of [59] was not conclusive. This naturally raises the question of whether there are any additional entropic constraints on holographic states not implied by Ryu-Takayanagi in the manner of [59].

We will focus on three dimensional bulk geometries with a moment of time symmetry,

[2]In addition, [59] also proved a new family of inequalities for any odd number of regions. The inequality for 3 regions coincides with $\mathcal{MMI}$.

such that the time slice is in general a disjoint union of Riemann surfaces with boundaries. This can be obtained by slicing the full three dimensional Euclidean solution, which is a handlebody obtained by filling in the boundary Riemann surface [40, 39]. Different fillings will correspond to different phases of the bulk geometry [26]. One can then evaluate the Euclidean action for the different phases to determine which one is the dominant saddle. Via the AdS/CFT dictionary this will give an approximation to the corresponding state in the dual field theory. On the other hand, if the bulk solution is not the dominant saddle, one cannot immediately conclude that this geometry is dual to a field theory state.

This is the argument which we will employ in the following to challenge the conclusion that the entropy cone of holographic CFTs is polyhedral. We will evaluate numerically the Euclidean action for the particular geometries corresponding to some of the extremal rays of the cone in the $N = 3$ and $N = 4$ cases and provide evidence suggesting that these are never dominant. While it remains possible that such geometries may nevertheless be related to CFT states by more complicated constructions, such an analysis is beyond the scope of this work.

The structure of the paper is as follows. In §4.2 we review the definition of [59] and introduce a new one to make a clear distinction between a notion of the cone which is purely geometric, and one that is instead more specific to holographic states dual to classical geometries. In §4.3 we evaluate the Euclidean actions for the geometries that realize some of the extremal rays of the $N = 3, 4$ cones. We summarize our conclusions in §4.4 and comment on some open questions.

4.2 Entropy cones

In this section we first review the definition of the *quantum entropy cone* for arbitrary quantum systems, and the definition given in [59] for the holographic context. We warn the reader that we will change terminology from the one used in [59]. What we will call the *metric entropy cone* is precisely the construction of [59], instead we reserve the name *RT (or HRT) cone* for a different object that we will define in §4.2.3. The conceptual distinction between the two constructions, and the question of whether they do or do not coincide, is the main motivation for the calculation that we will present in §4.3.

4.2.1 The Quantum Entropy Cone ($\mathcal{QC}_N$)

Consider a multipartite quantum system associated to a Hilbert space $\mathcal{H}_1 \otimes ... \otimes \mathcal{H}_{N+1}$. For a given pure state we trace out the degrees of freedom in $\mathcal{H}_{N+1}$ to obtain an $N-$partite mixed state ρ_N. Then we compute the entropy of each of the N individual subsystems of ρ_N, all the pairs, triplets and so on, up to the entropy of the union of all parties (the entropy of ρ_N) and we arrange these numbers into a vector in "entropy space" $\mathbb{R}^{2^N-1}$. Consider now the set of all such vectors obtained from all possible initial pure states in all possible Hilbert spaces with the previously mentioned tensor product structure. The subset of etntropy space so obtained has the structure of a convex cone and is known as the *quantum entropy cone* ($\mathcal{QC}_N$).

For $N = 2, 3$ the cones are known to be polyhedral and they are then specified by a finite number of linear inequalities. Any polyhedral cone can equivalently be described by the list of its *extremal rays* since any vector inside the cone or on its boundary can be obtained from a conical combination of them.[3]

To clarify the construction, and for the purpose of the later discussion, let us review

[3] A conical combination is a linear combination with non-negative coefficients.

the examples of the cones $\mathcal{QC}_2$ and $\mathcal{QC}_3$. In the $N = 2$ case the inequalities that determine the quantum cone are simply subadditivity ($\mathcal{SA}$) and Araki-Lieb ($\mathcal{AL}$)

$$\begin{aligned} \mathcal{SA}: &\qquad S_A + S_B \geq S_{AB}\,, \\ \mathcal{AL}: &\qquad S_A + S_{AB} \geq S_B\,. \end{aligned} \tag{4.1}$$

Note that even if the two inequalities are physically equivalent, in the sense that one implies the other, both are necessary for the construction of the cone because they correspond to different facets. For the same reason one should also include both versions of $\mathcal{AL}$ obtained by swapping A and B. The extremal rays are

$$(S_A, S_B, S_{AB}) \in \{(1,0,1),(0,1,1),(1,1,0)\}\,, \tag{4.2}$$

corresponding to obvious quantum states. These rays are actually equivalent since they are mapped to each other by permutations of the subsystems. Here we list all of them just for clarity, in the following we will only focus on inequivalent rays.

To obtain the $N = 3$ cone we can imagine that we first build a "candidate cone" obtained from all possible versions of the $N = 2$ inequalities for three subsystems A, B, C. We then cut away parts of this cone by slicing along the hyperplanes corresponding to all new, genuinely 3−partite, inequalities.[4] These are strong subadditivity ($\mathcal{SSA}$) and weak monotonicity ($\mathcal{WM}$)[5]

$$\begin{aligned} \mathcal{SSA}: &\qquad S_{AB} + S_{BC} \geq S_B + S_{ABC}\,, \\ \mathcal{WM}: &\qquad S_{AB} + S_{BC} \geq S_A + S_C\,. \end{aligned} \tag{4.3}$$

[4]For example for $\mathcal{SA}$ one also has $S_A + S_C \geq S_{AC}$, $S_A + S_{BC} \geq S_{ABC}$ and various permutations. However this description is redundant and some of the inequalities can be removed.

[5]Again the two inequalities are equivalent but both should be considered.

The extremal rays are then, up to permutations

$$(S_A, S_B, S_C, S_{AB}, S_{AC}, S_{BC}, S_{ABC}) \in$$
$$\{(1,1,0,0,1,1,0), (1,1,1,2,2,2,1), (1,1,1,1,1,1,1)\}\,. \tag{4.4}$$

The first ray simply corresponds to a Bell pair for AB, the second is a four-qutrit stabilizer state and the last one is a GHZ state of four qubits.[6]

For $N \geq 4$ new inequalities are known, but the full structure of the cones is not known. However, they are conjectured to be non-polyhedral [60].

4.2.2 The Metric Entropy Cone ($\mathcal{MC}_N$)

Having introduced the general concept of the quantum entropy cone we can now define, following [59], an analogous object for areas of minimal surfaces in a geometric set-up inspired by holography. Consider an arbitrary $d+1$ dimensional manifold with $(N+1)$ boundaries $\mathcal{M}_{N+1}$, with a metric which is asymptotically AdS_{d+1} approaching the boundaries. Since we are restricting to the RT prescription, rather than the more general HRT [43], we will also assume that the metric has a time reflection symmetry at $t=0$ and consider the d dimensional manifold $\widetilde{\mathcal{M}}_{N+1}$ corresponding to the $t=0$ slice of $\mathcal{M}_{N+1}$. We are interested in the area of minimal surfaces homologous to regions specified on the boundaries of $\widetilde{\mathcal{M}}_{N+1}$. In this set-up it is natural to think that such a geometry is dual to a pure state of a tensor product of $N+1$ CFTs living on the boundaries, but for the moment we do not make this assumption. The *metric entropy cone*($\mathcal{MC}_N$) is then defined as the region in the space of "area vectors" $\mathbb{R}^{2^N-1}$ spanned by varying the topology and the metric of $\mathcal{M}_{d+1}$, as well as the choice of the N subregions. This is

[6]The expressions of the states realizing the second and third extremal rays are $\sum_{i,j=0}^{2}|i,j,i+j,i+2j\rangle$ and $|0000\rangle + |1111\rangle$ respectively (up to a normalization factor).

precisely the definition of [59] for the "holographic entropy cone".

For the case $N = 2$, it follows from the "RT proof" of $\mathcal{SA}$, and from the fact that one can construct a geometry that realizes the extremal rays (a two boundary wormhole), that $\mathcal{QC}_2 \equiv \mathcal{MC}_2$. We will focus on the more interesting cases $N = 3, 4$. To construct the metric entropy cone for $N = 3$ one should include monogamy of mutual information ($\mathcal{MMI}$) to the list of inequalities[7]

$$\mathcal{MMI}: \qquad S_{AB} + S_{AC} + S_{BC} \geq S_A + S_B + S_C + S_{ABC}\,. \tag{4.5}$$

The list of extremal rays is then updated to

$$(S_A, S_B, S_C, S_{AB}, S_{AC}, S_{BC}, S_{ABC}) \in \{(1,1,0,0,1,1,0), (1,1,1,2,2,2,1)\}\,. \tag{4.6}$$

Comparing (4.6) with (4.4) one sees that the net effect of including $\mathcal{MMI}$ simply is the removal of the ray corresponding to the GHZ state. Geometrically, the first extremal ray in (4.4) is realized by the disjoint union of a two boundary wormhole and two copies of empty AdS. The second ray is instead a 4-boundary wormhole which we will study in §4.3.3.

In the $N = 4$ case it has already been shown in [59] that there are no new inequalities implied by the RT formula. To see that this is the case one starts again with all the previous inequalities for fewer parties and consider all possible versions for the $4-$partite case. From this list of inequalities one can then construct a cone, which is a "candidate" for $\mathcal{MC}_4$, and can extract its extremal rays. The result is

$$(S_A, S_B, S_C, S_D, S_{AB}, S_{AC}, S_{AD}, S_{BC}, S_{BD}, S_{CD}, S_{ABC}, S_{ABD}, S_{ACD}, S_{BCD}, S_{ABCD})$$

[7]Interestingly $\mathcal{SSA}$ can be removed from the list. The reason is that it is redundant as it can be obtained from $\mathcal{MMI}$ and $\mathcal{SA}$.

$$\in \{(0,0,0,1,0,0,1,0,1,1,0,1,1,1,1),(0,1,1,1,1,1,1,2,2,2,2,2,2,1,1),$$
$$(1,1,1,1,2,2,2,2,2,2,3,3,3,3,2)\}\,. \tag{4.7}$$

The first two rays are again inheritated from those of the previous cones. The last one instead is again a multiboundary geometry which we will investigate in §4.3.2. Since any extremal ray of this candidate cone can in fact be realized by some geometry, it follows from convexity that any other ray inside the cone can also be realized geometrically. This proves that for four regions there cannot be new RT inequalities and that the candidate previously constructed is in fact $\mathcal{MC}_4$. For $N > 4$ the metric entropy cones are not known, but it was proved in [59] that they are all polyhedral. Furthermore, it was proved in [61] that $\mathcal{MC}_N \subseteq \mathcal{QC}_N$ for all N, also justifying the usage of the word "entropy".

4.2.3 The Ryu-Takayanagi Cone ($\mathcal{RTC}_N$)

The construction presented in the previous section was completely geometric and although it was motivated by holography it did not really require it. However, since we are interested in the set of constraints imposed by the RT formula on the space of CFT states with classical bulk duals, we want to be able to interpret the "areas" which appeared in the metric entropy cone as von Neumann entropies of regions in field theory.[8] For this to be true one needs to further constraint the allowed geometries for which one computes areas and impose that such geometries are in fact dual to some CFT state. We then define the *Ryu-Takayanagi cone ($\mathcal{RTC}_N$)* as the cone spanned by all holographic states, for an arbitrary number of CFTs and all possible choices of the N regions. This is a convex cone, since given any two rays it contains any conical combination of them, obtained by rescaling the metric and taking the tensor product of the corresponding two

[8] In these work we only consider the leading contribution to the entropy in the large N limit.

states.[9]

From the previous definitions, and the result of [61], it follows that for any N

$$\mathcal{RTC}_N \subseteq \mathcal{MC}_N \subseteq \mathcal{QC}_N \,. \tag{4.8}$$

The case $N = 2$ is trivial since all the cones coincide, while for $N \geq 3$ the second inclusion in (4.8) is strict as a consequence of $\mathcal{MMI}$. On the other hand the question of whether the first inclusion in (4.8) is strict is the focus of the next section (for $N = 3, 4$).

4.3 Constructing holographic geometries for the extremal rays

In this section we explore the relation between the previously defined metric entropy and RT cones in the particular cases of $N = 3$ and $N = 4$. To prove that the RT cone coincides with the metric entropy cone, one needs to find holographic CFT states dual to the geometries that realize the extremal rays of the metric entropy cone. Since the metric entropy cone was defined for the RT formula (instead of HRT) we restrict to spacetimes with a time reflection symmetry. We focus on three dimensional gravity such that all possible solutions of Einstein's equations are locally AdS_3 and can be obtained by its quotients. The $t = 0$ slice of the full spacetime will then be a Riemann surface Σ_{N+1} with $N + 1$ boundaries. Finally, following [59], we assume that the N boundary regions for which we compute areas of RT surfaces are entire boundaries.

The solutions we are interested in are then multiboundary wormholes with $N + 1$ asymptotic boundaries with a set of constraints on the size of the horizons and all internal

[9] As for the metric entropy cone, we restrict attention to geometries with a moment of time symmetry, although one could similarly define a more general HRT cone.

cycles such that the geometries correspond to extremal rays of the metric entropy cone. We seek to find states in the tensor product of $N + 1$ CFTs which are dual to such wormholes and can be obtained from a bulk Euclidean path integral via the Hartle-Hawking construction. For both the $N = 3$ and $N = 4$ cases we fail to find CFT states that meet all the requirements.

4.3.1 Handlebody solutions

A particularly interesting class of Euclidean solutions of three dimensional Einstein gravity with negative cosmological constant are the so-called handlebody solutions, which can be thought as compact Riemann surfaces "filled in" with hyperbolic space. While these are not the only solutions for a particular set of boundary conditions, it has been conjectured that the non-handlebody solutions are always sub-dominant [49]. Our numerics confirm this explicitly in certain contexts (see §4.A for more details).

As first proposed in [40, 41] (see also [39]), one can interpret such a solution for $t_E \in (-\infty, 0)$ as a saddle point of the bulk Euclidean path integral. However, for a given compact Riemann surface, different handlebodies can be obtained by different fillings and correspond to different phases [26]. If this saddle is the one with least action then by the Hartle-Hawking construction it provides the bulk state at $t = 0$ and via holography an approximation to the dual CFT state computed by the field theory path integral. For our purposes we must then check that the correct phase dominates in the region of moduli space where the entanglement entropies satisfy the relations determined by the extremal ray. Recently developed techniques [36] allow us to study these solutions numerically even in the case of three or more boundaries. While evaluating the action for these geometries is involved, numerical evidence from our work and [36] suggests that a useful heuristic is that filling in the bulk along smaller boundary cycles costs less action

than filling along larger boundary cycles. A related effect is that geometries with small internal bulk cycles tend to be subdominant in the path integral. This provides a coarse way to understand which phase dominates at a given point in moduli space.

An arbitrary handlebody solution can be obtained as a quotient of three dimensional hyperbolic space $\mathbb{H}^3$ (i.e. Euclidean AdS_3). A particular quotient can be specified by its action on the boundary Riemann surface, with the action extended into the bulk by geodesics. Explicitly, to construct a quotient of $\mathbb{H}^3$ with a genus g Riemann surface its the boundary, one chooses g pairs of non-intersecting circles C_k, C'_k which divide the Riemann sphere into a region "inside" and "outside." The set of Möbius transformations L_k mapping $C_k \mapsto C'_k$ are then used to define the particular quotient of $\mathbb{H}^3$, with the action in the bulk defined by an extension along geodesics. The Riemann sphere projected onto $\mathbb{R}^2$ with the specifications of a given set of circles is referred to as a Schottky domain D (see [40, 39] for more details).

In practice, it is difficult to determine the handlebody corresponding to a particular quotient of the Riemann sphere. Instead it is more convenient to construct a Schottky domain for a particular Riemann surface by choosing g cycles on the boundary to be made contractible in the bulk.[10] Cutting the Riemann surface along these g cycles gives a Riemann sphere with g sets of circles identified, which can then be projected into the plane to define the Schottky domain. Determining the moduli of the Riemann surface corresponding to a particular domain is done numerically for $g > 1$, and we must solve this moduli matching problem to compare solutions with given boundary conditions.

In order to compare the actions for different solutions, we must first choose a conformal frame on the boundary. The standard choice is $R_{\text{bndy}} = -2$. As shown in [40], if we

[10] One way to classify the possibilities is to first construct a basis of cycles $\{\alpha_i, \beta_i\}$ such that $\alpha_i \cap \beta_j = \delta_{ij}$. Letting the cycles $\{\alpha_i\}$ be contractible in the bulk defines a particular handlebody solution. One can then act on this basis with an element of the mapping class group and choose the resulting α cycles to be contractible. Acting with all elements of the mapping class group generates a set of handlebody phases for a given boundary surface.

write the boundary metric as

$$ds^2 = e^{2\phi(w,\bar{w})} dw d\bar{w} \,. \tag{4.9}$$

then this choice of conformal frame corresponds to the solution of the Liouville equation with an additional non-trivial condition

$$\nabla^2 \phi = e^{2\phi} \quad , \text{ with} \quad \phi(L_i(w)) = \phi(w) - \frac{1}{2} \log |L_i'(w)|^2 \,. \tag{4.10}$$

We will use the numerical methods described in [36] to solve this differential equation for a given domain.

Additionally, as shown in [40], the evaluation of the Einstein-Hilbert action for a particular solution can be written in terms of the Takhtajan-Zograf action [48] for the scalar field ϕ. As explained in [36], if we define R_k to be the radius of C_k and Δ_k as the distance between the center of C_k and the point $w_\infty^{(k)}$ mapped to ∞ by L_k, this action reduces to

$$I_{TZ}[\phi] = \int_D d^2 w \left((\nabla \phi)^2 + e^{2\phi} \right) + \sum_k \left(\int_{C_k} 4\phi \, d\theta_\infty^{(k)} - 4\pi \log \left| R_k^2 - \Delta_k^2 \right| \right) \,. \tag{4.11}$$

where $\theta_\infty^{(k)}$ is the angle measured from the point $w_\infty^{(k)}$. More details on the numerical evaluation of this action can be found in §4.A.

Finally, we will have to impose on a handlebody solution a set of constraints which guarantee that the entanglement entropies of entire boundaries (and their unions) match the values of a particular extremal ray of the metric entropy cone. Since the RT formula relates such entropies to geodesic lengths, we need to relate these geodesics lengths to the quotient which defines a particular handlebody. This can be done using the results

of [51], which showed that the length of a geodesic in the homology class corresponding to the action of a Möbius transformation L is given by

$$\ell(L) = \cosh^{-1}\left[\frac{\mathrm{Tr}L}{2}\right] . \tag{4.12}$$

In the next sections we will use all of this technology to evaluate the on-shell action for the solutions corresponding to the desired extremal rays of the $N = 3, 4$ metric entropy cones.

4.3.2 Four party extremal rays

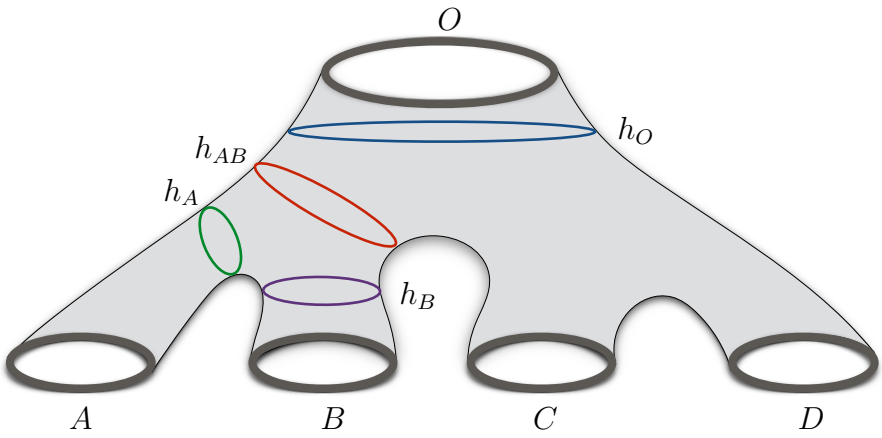

Figure 4.1: The geometry (at $t = 0$) corresponding to the four party extremal ray of interest. The sizes of the horizons and the internal cycles are fixed in order to obtain the correct entropies, see the main text.

The extremal rays of $\mathcal{MC}_4$ where listed in (4.13). The first two rays are inherited from the three party cone $\mathcal{MC}_3$ and we will ignore them, we will briefly comment on the three party case in the next section. Here instead we focus on the only new extremal ray

$$\begin{aligned}&(S_A, S_B, S_C, S_D, S_{AB}, S_{AC}, S_{AD}, S_{BC}, S_{BD}, S_{CD}, S_{ABC}, S_{ABD}, S_{ACD}, S_{BCD}, S_{ABCD})\\ &= (1, 1, 1, 1, 2, 2, 2, 2, 2, 2, 3, 3, 3, 3, 2) .\end{aligned} \tag{4.13}$$

As already shown in [59], this ray can be realized by the multiboundary wormhole geometry drawn in Fig. 4.1, with the following conditions on the horizon lengths

$$l = |h_A| = |h_B| = |h_C| = |h_D| = \frac{1}{2}|h_O|\,. \tag{4.14}$$

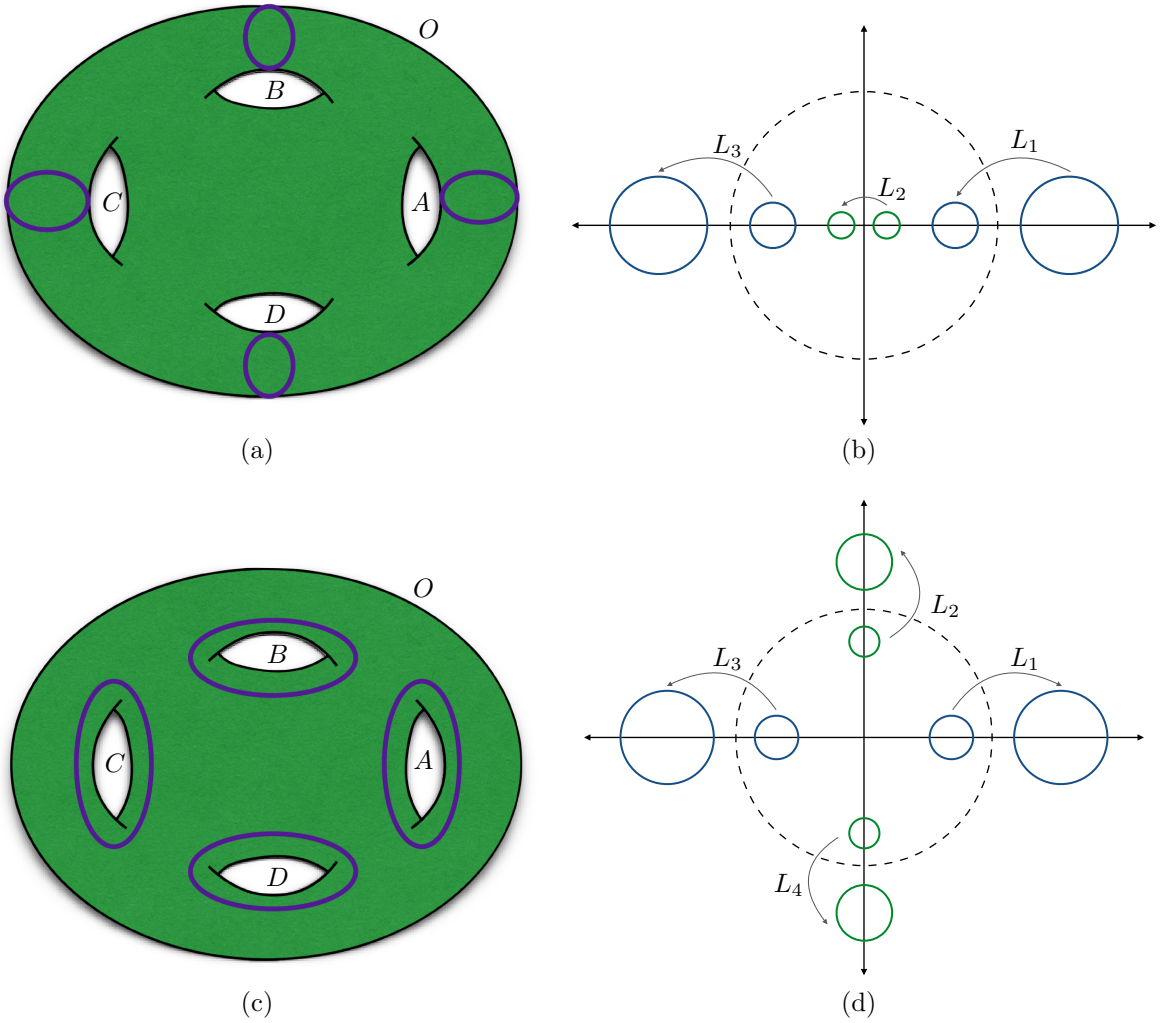

Figure 4.2: The choices of contractible cycles corresponding to the connected and disconnected phases and the corresponding Schottky domains. (a) The connected phase. (b) The associated Schottky domain, with two further circles not drawn, but implied by requiring inversion symmetry across the dashed circle. (c) The disconnected phase. (d) The associated Schottky domain.

and with the additional constraint that for any internal cycle γ homologous to a union of n of the four boundaries one has

$$|\gamma| \geq nl\,. \tag{4.15}$$

For example we should impose $|h_{AB}| \geq 2l$.

We wish to evaluate the Euclidean action for this solution, which we refer to as the *connected phase*, and compare it to the action evaluated for a solution where the surface of time-reflection symmetry in the bulk does not connect any pair of boundaries

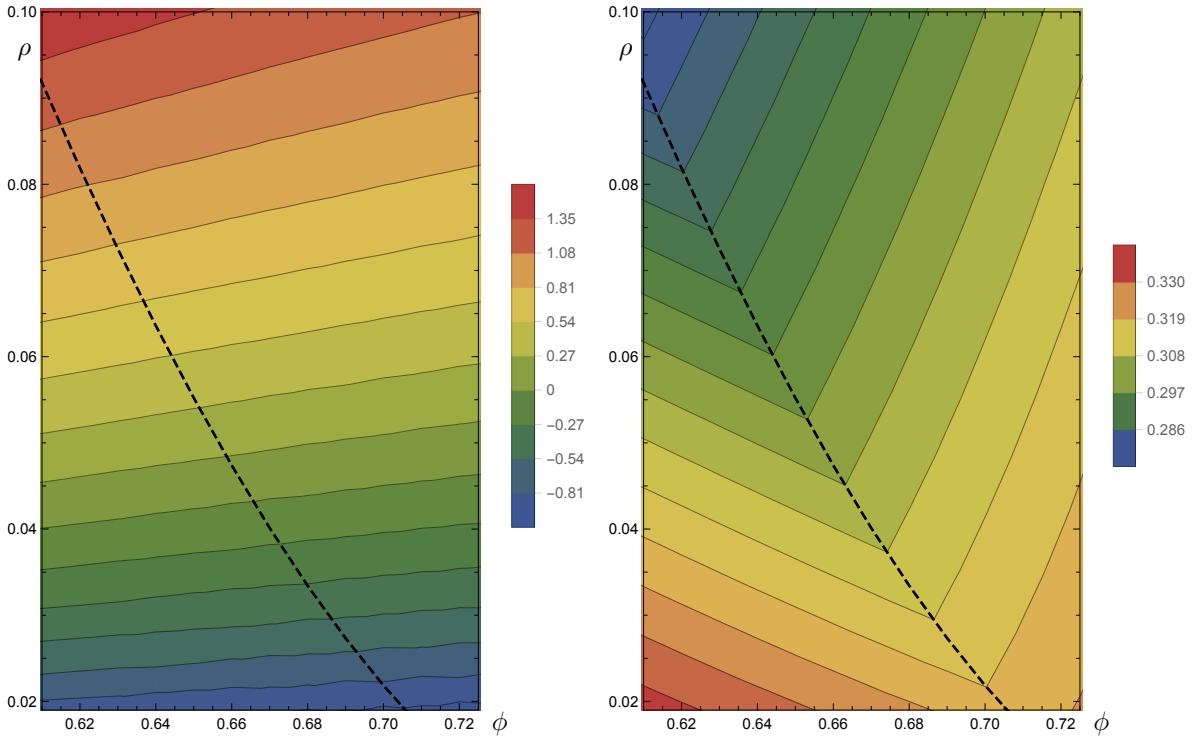

Figure 4.3: Comparison of the actions for the connected and disconnected phases in the symmetric configuration. The parameters (ϕ, ρ) are the angular position and size of C_1 on the Riemann sphere. The dashed line corresponds to the particular configuration with an additional $\pi/2$ rotational symmetry about the axis orthogonal to the plane of the page in Fig. 4.2a and Fig. 4.2c (see also Fig. 4.4). (a) $I_{\text{con}} - I_{\text{dis}}$. (b) $\max_\gamma(1 - \frac{|\gamma|}{nl})$.

(which we will simply call the *disconnected phase*).[11] If the connected phase is the one that minimizes the action then as explained earlier we can conclude that in the limit of small bulk Newton constant G (and thus large CFT central charge c) it is in fact dual to a field theory state. As anticipated, we will find evidence that this is not the case. The constraints (4.15) require that the cycles homologous to single boundaries are small compared to the other internal cycles. Intuitively then, the action favors the disconnected phase, where the wormhole "pinches off" and these cycles become contractible in the bulk.

The wormhole geometry of Fig. 4.1 can be obtained starting from a closed Riemann surface of genus $g = 4$. Different handlebody solutions with the same boundary correspond to different choices for the cycles which are contractible in the bulk. The choice that gives the connected phase is shown in Fig. 4.2a and the corresponding Schottky domain in Fig. 4.2b. In the case of the disconnected phase (see Fig. 4.2c and Fig. 4.2d), the bulk time slice consists of five disconnected copies of $\mathbb{H}^2$; the mutual information between boundaries vanishes and the constraints (4.14) are not satisfied.

We want to compare the action for these two phases in various regions of the moduli space for the associated genus-4 Riemann surface. We focus on a subspace defined by imposing three $\mathbb{Z}_2$ symmetries corresponding (for Fig. 4.2a and Fig. 4.2c) to reflections in the plane of the page and across both the horizontal and vertical axes. In both phases considered, the contractible cycles are homotopic to curves that are fixed by a subset of these symmetries. Combined with the constraints (4.14), these conditions reduce the moduli space to two real dimensions. In Fig. 4.3a we plot the difference between disconnected (I_{dis}) and connected (I_{con}) actions and in Fig. 4.3b we show $\max_\gamma(1 - \frac{|\gamma|}{nl})$; i.e. the maximal violation of the constraints (4.15). As announced before, one can clearly see that the constraints are violated when the connected phase has smaller action (bluer

[11] While in principle there are multiple phases where the surface of time reflection symmetry in the bulk is disconnected, for our analysis it is sufficient to focus only on this particular phase.

regions of Fig. 4.3b). Indeed, the region displayed in Fig. 4.3b contains no points where the constraints are all satisfied.

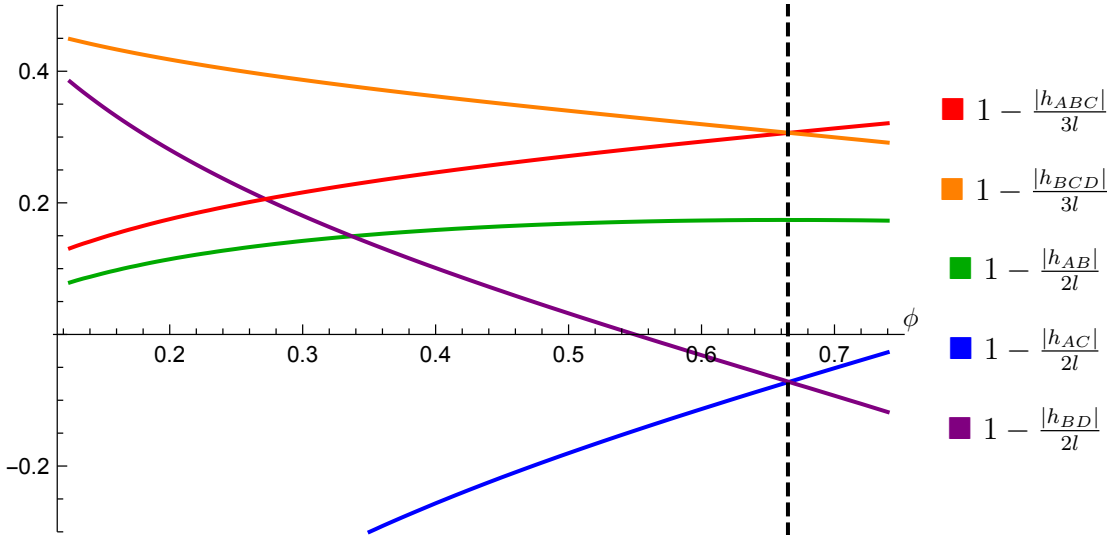

Figure 4.4: The constraints (4.15) in the subspace where the connected and disconnected actions are equal. The dashed line indicates the point with the additional $\pi/2$ rotational symmetry discussed above.

Now the particular region of moduli space studied in Fig. 4.3 was chosen in an ad hoc way for numerical convenience. To perform a more targeted analysis, we restrict attention to the 1-dimensional subspace of moduli space where the connected and disconnected actions are equal. We can then search along this curve for a point where the constraints (4.15) are satisfied. Though we have no rigorous proof, it is natural to presume that it is easier to satisfy the constraints along this line than in the region where the connected phase dominates strongly. The plot shown in Fig. 4.4 suggests that no such point exists. Toward the left, the h_{BD} and h_{BCD} cycles become too small, while the h_{ABC}, h_{AB}, and h_{AC} cycles become too small toward the right.

Note that the minimal violation of the constraints happen at the point in moduli space (dashed vertical line in Fig. 4.4) where there is an additional $\pi/2$ rotational symmetry in the Riemann surface. This observation suggests that even if we were to look outside

of the two dimensional subspace of moduli space that we have considered thus far, i.e. even if we consider regions of moduli space with less symmetry, we will still be unable to make the desired extremal ray dominate our path integral.

As a check we have also considered a different two dimensional subspace corresponding to the Riemann surface drawn in Fig. 4.5a. As before, we can study the one dimensional subspace where the connected and disconnected actions are equal. The results for the various constraints on the cycle lengths are shown in Fig. 4.6, one can see that there is no region where they are all satisfied simultaneously.

4.3.3 Three party extremal ray

We briefly comment on the case of $\mathcal{RTC}_3$. In this case the extremal ray of interest is

$$(S_A, S_B, S_C, S_{AB}, S_{AC}, S_{BC}, S_{ABC}) = (1, 1, 1, 2, 2, 2, 1)\,. \tag{4.16}$$

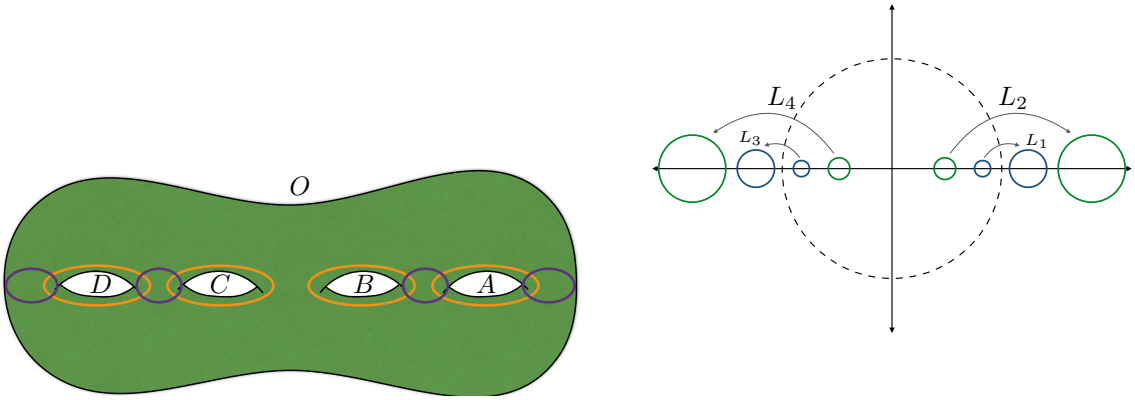

(a) (b)

Figure 4.5: In this case the two phases differ only in moduli and have the same Schottky domain. (a) The alternative Riemann surface with the two choices of contractible cycles. (b) The Schottky domain for both sets of cycles.

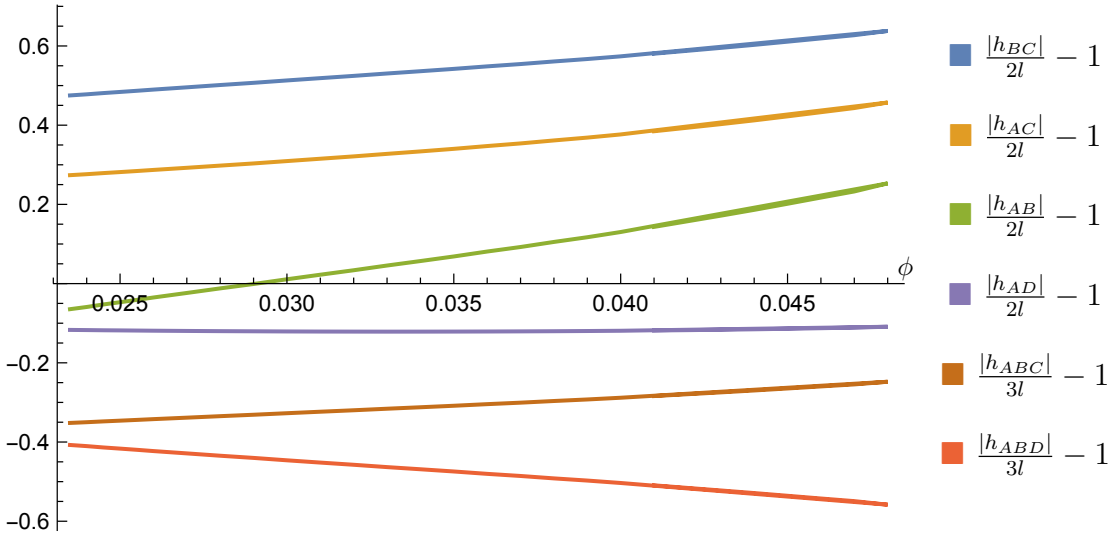

Figure 4.6: The constraints (4.15) for the alternative handlebody (Fig. 4.5a) in the subspace where the connected and disconnected actions are equal.

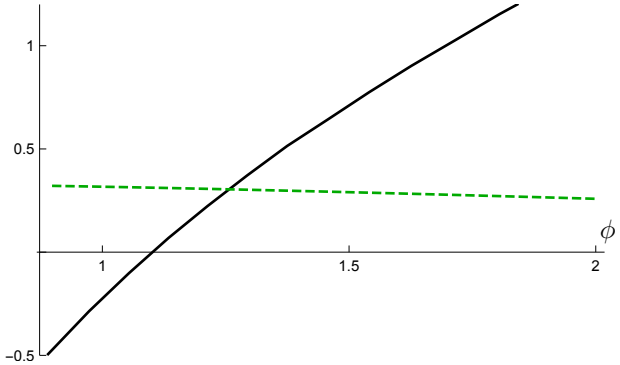

Figure 4.7: Results for the highly symmetric three genus Riemann surface. The black (solid) line is $I_{\text{con}} - I_{\text{dis}}$, the green (dashed) one $1 - \frac{|h_{AB}|}{2l}$.

For the one-dimensional subspace of moduli space where the Riemann surface has three holes arranged in a circle, and an extra $2\pi/3$ rotational symmetry, the results are shown in Fig. 4.7. They suggest in this case as well that there might not be a CFT state dual to the particular multiboundary geometry considered to realize the desired extremal ray. Although our argument is far from conclusive in proving that the RT cone for three parties is not polyhedral, it is interesting to contrast the result with the quantum mechanical case, where for three parties the cone is known to be polyhedral.

4.4 Discussion

Our findings show that the argument of [59] for the polyhedrality of the RT cones $\mathcal{RTC}_3$ and $\mathcal{RTC}_4$ was not conclusive. While [59] showed the polyhedrality of the metric entropy cones $\mathcal{MC}_3$ and $\mathcal{MC}_4$, if one further requires that the geometries realizing the extremal rays of the cones are dual to CFT states it is not clear whether these rays can be realized holographically. We have also noted that, the wormhole solutions suggested in [59] may fail to satisfy this requirements since they do not correspond to the dominant saddle points of the natural bulk Euclidean path integral in any region of moduli space. We have not ruled out the possibility that they might dominate in other more complicated path integrals, but this seems unlikely. For $\mathcal{RTC}_N$ with larger N the situation is even less clear. While [59] proved that the metric entropy cone is polyhedral for any N, without the full list of RT inequalities it is obviously not possible to construct the extremal rays and explore whether they have holographic duals.

Though our results are suggestive, they are not conclusive with regard to the polyhedrality of $\mathcal{RTC}_3$ and $\mathcal{RTC}_4$. For example, there could be other bulk solutions dual to CFT states that realize the same extremal rays. As noticed in [59], restricting spin structures can remove otherwise-dominant saddles and perhaps allow the desired saddle to dominate. However, for theories with a fixed number F of bulk Fermion fields this seems unlikely for large enough N. For example, for $F = 1$ there is no spin structure that guarantees connectivity beyond $N = 2$. If there are holographic bulk theories with arbitrarily large F, one could use them to show equality of the metric entropy and HRT cones. However, it is currently unknown whether such theories exist.

Alternatively, it might be that one can in some sense subtract off the part of the CFT state corresponding to the dominant phase to leave a CFT state dual to the subdominant phase. Indeed, one naively expects that the state defined by our path integral admits a

semi-classical expansion of the form

$$|\psi\rangle = \sum_{\substack{\text{saddles } n \\ \text{corrections } m}} e^{-S_n/2} c^{-m/2} |g_n, m\rangle, \tag{4.17}$$

in terms of the central charge c. Here $|g_n, m\rangle$ is a state that includes perturbative quantum corrections about the background geometry g_n corresponding to the nth saddle. Since each geometry g_n that appears in our sum is also associated with a more natural path integral to which it should contribute, one expects that a suitable linear combination of these states (acted upon by appropriate CFT operators to bring into alignment the states of the bulk quantum fields) will feature a leading term proportional to the part $|\tilde{g}, 0\rangle$ associated with the desired geometry (e.g. Fig. 4.1).

However, there are many details to be analyzed in fleshing out this more complicated approach to constructing CFT states dual to geometries like the one in Fig. 4.1. One should thus be open to the possibility that it fails and that the RT cone is in fact not polyhedral. While by construction it is certainly true that the RT cone is a subset of the metric entropy cone, it could be that (at least for some N) it is in fact a proper subset. This would mean that there should be other entropy inequalities, possibly non-linear, that by the same argument of [59] could not be proved by usual "cutting and pasting" procedures using the RT formula.

Finally, we remind the reader that all our discussion, as well as that in [59], was based on the RT prescription and only applies to spacetimes with a moment of time symmetry. In dynamical situations one should instead use the HRT prescription [43]. While $\mathcal{SSA}$ and $\mathcal{MMI}$ have been proved also in this more general situations [62], and by construction the metric entropy cone based on RT has to be a subset of the one based on HRT, it is not clear at present whether the polyhedrality proof of [59] extends to the dynamical case, nor it is known if the new inequalities for $N = 5$ found by [59] still hold.

We see these as interesting open questions for future investigations.

4.A Bulk action computation

In this appendix we present more details for computing the Einstein-Hilbert action. As shown in [36] we can write the bulk action as

$$I = -\frac{c}{24\pi}\left[I_{\mathrm{TZ}}[\phi] - A - 4\pi(g-1)(1-\log 4R_0^2)\right] , \tag{4.18}$$

where R_0 is a normalization parameter corresponding to the size of the sphere on which the partition function evaluates to one. As in [36] we set $R_0 = c = 1$, and so the action for a particular non-handlebody solution vanishes. Additionally, the action $I_{\mathrm{TZ}}[\phi]$ is equivalent to the Takhtajan-Zograf action for a scalar field [48]. As shown in [36], if we define R_k to be the radius of C_k, and Δ_k as the distance between the center of C_k and the point $w_\infty^{(k)}$ mapped to ∞ by L_k, the action can be written as

$$I_{TZ}[\phi] = \int_D d^2w \left((\nabla\phi)^2 + e^{2\phi}\right) + \sum_k \left(\int_{C_k} 4\phi\, d\theta_\infty^{(k)} - 4\pi \log\left|R_k^2 - \Delta_k^2\right|\right) . \tag{4.19}$$

We follow the convention of [36] where the orientation of a $d\theta$ element associated with a particular circle is inherited from its orientation as the boundary of D. In practice, this means that almost all of the elements have the opposite orientations one would naively expect.

In all the Schottky domains we consider, there is a symmetry of the plane given by an inversion through the unit circle (∂U). Therefore it will be convenient to reduce (4.19) to integrals only over the part of D inside the unit circle, which we denote as $\tilde{D}$. As

shown in [36] we can use the transformation properties of ϕ to show that

$$\int_D d^2w\,(\nabla\phi)^2 = 2\int_{\tilde{D}} d^2w\,(\nabla\phi)^2 + 4\int_{\partial\tilde{D}} (\phi + \log|w|)\; d\theta\,, \tag{4.20}$$

where the coordinate θ refers to the angle measured from the origin. In practice, the boundary of $\tilde{D}$ will consist of a set of disjoint circles $\{\partial D_i\} = \tilde{D} \cap \{C_k, C_k'\}$ and the boundary of the unit disk U. Furthermore, we can explicitly evaluate the integral of $\log|w|$ over the boundary circles and write (4.20) as

$$\int_D d^2w\,(\nabla\phi)^2 = 2\int_{\tilde{D}} d^2w\,(\nabla\phi)^2 + 4\int_{\partial U}\phi\,d\theta + \sum_i\left[4\int_{\partial D_i}\phi\,d\theta + 4\pi\log\left(1-\frac{R_i^2}{X_i^2}\right)\right], \tag{4.21}$$

where X_i is the distance between the center of ∂D_i and the origin. In all of the domains we consider, X_i is zero only for the unit and not included in the sum. Additionally it was shown in [36] that we can integrate the $(\nabla\phi)^2$ term by parts to get on shell

$$\int_{\tilde{D}} d^2w\,(\nabla\phi)^2 = -\int_{\tilde{D}} d^2w\,\phi\,e^{2\phi} - \int_{\partial U}\phi\,d\theta - \sum_i\int_{\partial D_i}\phi\,d\theta_0^{(i)}\,, \tag{4.22}$$

where $\theta_0^{(i)}$ is the angular coordinate as measured from the center of the boundary circle ∂D_i. Putting everything together, we can then write

$$\int_D d^2w\,(\nabla\phi)^2 = -2\int_{\tilde{D}} d^2w\,\phi\,e^{2\phi} + 2\int_{\partial U}\phi\,d\theta + \sum_i\left[2\int_{\partial D_i}\phi\,(2d\theta - d\theta_0^{(i)}) + 4\pi\log\left(1-\frac{R_i^2}{X_i^2}\right)\right]. \tag{4.23}$$

Next, we can tackle the sum over C_k in the formula (4.19). We make the assumption that neither C_k nor C_k' intersect the unit circle, the case in which they do was worked out in [36]. Note that we can divide the circles into two classes, one in which one of C_k

or $C'_k \subset U$ and one in which $C_k, C'_k \not\subset U$. However, with the additional assumption that there is an inversion symmetry through U, for every pair of circles $C_k, C'_k \not\subset U$ there is a pair of circles $C_{\bar{k}}, C'_{\bar{k}} \subset U$. Additionally, only one from the pair of circles C_k, C'_k enters the above formula, and for each pair there is a freedom in choosing which one to be C_k and C'_k. For each of these pairs we label C_k to be the one inside U. Therefore we can write the sum of integrals over C_k as follows:

$$\sum_k 4\int_{C_k} \phi \, d\theta_\infty^{(k)} = \sum_{k:\, C'_k \not\subset U} 4\int_{C_k} \phi \, d\theta_\infty^{(k)} + \sum_{k:\, C'_k \subset U} 4\left(\int_{C_k} \phi \, d\theta_\infty^{(k)} + \int_{C_{\bar{k}}} \phi \, d\theta_\infty^{(\bar{k})}\right). \quad (4.24)$$

Of the three terms, only the last one involves an integral over a circle not in U, but using the inversion symmetry we can reduce it to an integral over C_k

$$\sum_k 4\int_{C_k} \phi \, d\theta_\infty^{(k)} = \sum_{k:\, C'_k \not\subset U} 4\int_{C_k} \phi \, d\theta_\infty^{(k)} + \sum_{k:\, C'_k \subset U} 4\int_{C_k} \left(\phi \, + (\phi + \log|w|)\frac{d\theta_\infty^{(\bar{k})}}{d\theta_\infty^{(k)}}\right) d\theta_\infty^{(k)} \,. \quad (4.25)$$

As the Jacobian factor and the parameters R_k and D_k can all be computed analytically from the setup of the Schottky domain, the only numeric integration occurs within the domain $\tilde{D}$.

Finally, we note that $A = \int_D e^{2\phi} d^2w$ and so this integration in I_{TZ} cancels the A term in the action. Putting it all together, we have the following on shell action

$$\begin{aligned} I = -\frac{c}{24\pi}\Bigg[& -4\pi(g-1)\log 4 - 2\int_{\tilde{D}} d^2w\, \phi\, e^{2\phi} + 2\int_{\partial U} \phi \, d\theta \\ & + \sum_{k:\, C'_k \not\subset U} \left(2\int_{C_k} \phi\,(2d\theta + 2d\theta_\infty^{(k)} - d\theta_0^{(k)}) + 4\pi \log\frac{1 - R_k^2/X_k^2}{|R_k^2 - \Delta_k^2|}\right) \\ & + \sum_{k:\, C'_k \subset U} \left(2\int_{C_k} \phi\,(2d\theta + 2d\theta_\infty^{(k)} - d\theta_0^{(k)}) + 4\int_{C_k} (\phi + \log|w|)\frac{d\theta_\infty^{(\bar{k})}}{d\theta_\infty^{(k)}} d\theta_\infty^{(k)}\right. \end{aligned}$$

$$+2\int_{C_{k'}}\phi\left(2d\theta-d\theta_0^{(k')}\right)+4\pi\log\frac{(1-R_k^2/X_k^2)(1-R_{k'}^2/X_{k'}^2)}{|R_k^2-\Delta_k^2|\left|R_{\bar{k}}^2-\Delta_{\bar{k}}^2\right|}\Bigg)\Bigg]\,. \tag{4.26}$$

The action written explicitly in this way is very useful because it only involves quantities one can compute analytically and numeric integrations over $\tilde{D}$ and $\partial\tilde{D}$.

In many scenarios one can derive relations such as $d\theta+d\theta_\infty^{(k)}=d\theta_0^{(k)}$ which greatly simplify the above formula. Additionally, one is often able to use reflection symmetries to further reduce the domain of integration. Practically, it is only numerically feasible to compute integrals over $d\theta_0^{(k)}$ and so one can introduce more Jacobian factors to convert all integrals to this form.

Part II

Applications

Chapter 5

Confinement in Inhomogenous Backgrounds

5.1 Introduction

The AdS/CFT correspondence [14, 15, 16] provides elegant geometrizations of many aspects of quantum field theory, including the phenomenon of confinement [22]. In gauge theories, an order parameter for confinement is the expectation value of a "temporal" Wilson loop around a Euclidean time circle:

$$\langle |\mathrm{Tr}(W)| \rangle \equiv \left\langle \frac{1}{N} \mathrm{Tr} \left(\mathcal{P} e^{-\oint A_\tau d\tau} \right) \right\rangle \quad . \tag{5.1}$$

The expectation is of the form $e^{-\beta E_q}$, where E_q is the energy of a probe quark. In a confining phase this energy diverges, and so the expectation value (5.1) vanishes. But a non-zero expectation value requires a finite probe quark energy and implies the theory to be in a deconfined phase [63, 64, 65].

The holographic prescription [66] for computing the expectation value of a Wilson

loop $\mathcal{C}$ involves considering a fundamental string in the bulk which intersects the asymptotically AdS conformal boundary on the curve $\mathcal{C}$ defined by the Wilson loop. Here we identify the (conformal) boundary of the bulk with the gauge theory spacetime. At small bulk string coupling, the semi-classical approximation to the associated worldsheet path integral gives

$$\langle |\mathrm{Tr}(W)| \rangle \simeq e^{-S_{\mathrm{cl}}}, \tag{5.2}$$

where S_{cl} is the classical string action of Euclidean worldsheet. As we focus on the vanishing or non-vanishing of (5.2), we need only determine if any worldsheets have finite action. When there is no bulk worldsheet with boundary $\mathcal{C}$, expression (5.2) vanishes and the theory is confined.

The bulk topology associated with the Euclidean time circle is thus of critical importance. When this circle is non-contractible, there can be no worldsheet with boundary $\mathcal{C}$ having the topology of a disk. Since other topologies are allowed only in special cases[1], it is of great interest to construct asymptotically locally AdS spacetimes with non-contractible Euclidean time circles.

The prototypical example of a bulk geometry dual to a confining vacuum is the AdS-soliton [22, 67]. The solution may be constructed by Wick-rotating the Schwarzschild-AdS black hole and involves an arbitrary constant $b > 0$. In Fefferman-Graham gauge and Euclidean signature the metric may be written

$$ds^2 = \frac{\ell^2}{z^2}\left[dz^2 + \left(1+\frac{z^d}{b^d}\right)^{4/d} d\tau^2 + \left(1+\frac{z^d}{b^d}\right)^{4/d} dx_i dx^i + \alpha_d^2 b^2 \left(1-\frac{z^d}{b^d}\right)^2 \left(1+\frac{z^d}{b^d}\right)^{\frac{4}{d}-2} d\theta^2\right], \tag{5.3}$$

[1]When the bulk has additional boundaries not associated with the original CFT spacetime. Such boundaries typically lie at the end of an infinite throat related to an extreme horizon in the bulk

where $i = 1, \ldots d-2$ and $\alpha_d = \frac{2^{1-2/d}}{d}$. We take θ to be dimensionless and to have b-independent period 2π (as required by regularity at $z = b$). The conformal boundary may be taken to have metric

$$ds^2_{bndy} = d\tau^2 + dx_i dx^i + \alpha_d^2 b^2 \, d\theta^2, \tag{5.4}$$

so that b controls the size of the θ-circle on the boundary.

Below, we generalize this solution by allowing the size of the S^1 – and thus the confinement scale – to vary slowly along the boundary. We work in Euclidean signature, but our results define Lorentz-signature solutions via a trivial Wick rotation of τ, or equivalently by evolving the associated initial data at $t = 0$. We construct the bulk geometries in section 5.2 using an adiabatic expansion. Section 5.3 then extracts predictions for Wilson loops and the stress tensor in the dual gauge theory. Readers most interested in such results may skip directly to this section. Numerical results for interesting coefficients are given for $3 \leq d \leq 8$. The special case $d = 2$ is solved analytically in appendix 5.A and used to check our numerical codes.

5.2 Adiabatically Varying Confining Vacua

In any local theory, one may use a solution with continuous free parameters to build new solutions by promoting constant such parameters to slowly varying functions. The explicit functional form will then require corrections, but these may be found by solving the equations of motion in an adiabatic expansion. In particular, this procedure has been used extensively in the fluid-gravity correspondence [68] to construct holographic duals of conformal fluids near thermal equilibrium; see [69, 70] for reviews. Indeed, because (5.3) is the double-Wick rotation of an AdS-Schwarzschild black hole, our solutions below could

have been constructed as double Wick-rotations of appropriately static and symmetric instances of the fluid-gravity correspondence that satisfy certain regularity conditions. However, we nevertheless find it useful to construct the relevant equations and study regularity directly in terms of coordinates adapted to our symmetries (as opposed to the ingoing Eddington-Finkelstein black hole coordinates of [68, 69, 70]).

To be more explicit, suppose that we begin with a bulk geometry having free parameters $\{c_\alpha\}$. We promote each constant to a slowly varying function by making the replacement $c_\alpha \to c_\alpha(\epsilon x)$ to define a new metric $\tilde{g}^{(0)}_{AB}$. Here ϵ is a dimensionless book-keeping parameter that controls the adiabatic expansion.

Our $\tilde{g}^{(0)}_{AB}$ no longer solves Einstein's equation exactly, but we can use it to construct a solution by considering the ansatz

$$ds^2 = \tilde{g}^{(0)}_{AB}\, dx^A dx^B + \epsilon\, \tilde{g}^{(1)}_{AB}\, dx^A dx^B + \epsilon^2\, \tilde{g}^{(2)}_{AB}\, dx^A dx^B + \cdots . \tag{5.5}$$

Inserting (5.5) into the Einstein equation gives, at each order n, a set of equations for the metric correction $\tilde{g}^{(n)}_{AB}$. In general, at each order n there may also be consistency conditions that impose relations between the c_α and their derivatives. However, no such conditions will arise in the setting studied below.

We will use this method to construct a class of confining geometries which approach the AdS-soliton (5.3) in the limit as $\epsilon \to 0$. Our solutions are constructed in Euclidean signature and have a τ translation symmetry. As a result, they are bulk stationary points of the path integral that computes the vacuum of the dual gauge theory. As in the discussion of [22, 67] we assume this saddle to dominate. Wick rotating to Lorentz signature or evolving initial data from $t = 0$ will then give Lorentz-signature solutions dual to the gauge theory vacua.

5.2.1 Ansatz and boundary conditions

We begin with the AdS-soliton (5.3) and promote b to a slowly varying function of a single spatial coordinate x, i.e. $b \to b(\epsilon x)$. The effect on the boundary metric is to make the size of the S^1 fibers vary with x. Although for simplicity we will allow this size to vary only along a single coordinate direction, we describe at the end of section 5.2.2 below how at order ϵ^2 this seemingly-special case in fact suffices to determine the response to completely general slow variations of b in the $(d-1)$ directions (τ, x^i).

Since the dual CFT will have a ground state on any static spacetime, one expects no restrictions on the functional form of $b(\epsilon x)$. We will verify below that no constraints arise within the adiabatic expansion. A key point will be that adding x-dependence in the above way will allow us to preserve regularity everywhere in the bulk, and in particular at the fixed points of the rotational Killing field ∂_θ.

It will be convenient to let $x = x^1$, $y^1 = \tau$, and $y^i = x^i$ for $i \geq 2$. With these definitions, the boundary coordinates are given by $x^\mu = (\theta, x, y^i)$ where again $i = 1, \ldots, d-2$. Below, we use rotational invariance among the y^i to write $g_{y^i y^j} = g_{yy}\delta_{ij}$.

Working in Fefferman-Graham gauge, we consider solutions of the form

$$ds^2 = \frac{\ell^2}{z^2} g_{AB} dx^A dx^B = \frac{\ell^2}{z^2}\left(g^{(0)}_{AB}\, dx^A dx^B + \epsilon\, g^{(1)}_{AB}\, dx^A dx^B + \epsilon^2\, g^{(2)}_{AB}\, dx^A dx^B + \cdots\right), \tag{5.6}$$

so that in the notation of (5.5) we have $\tilde{g}^{(n)}_{AB} = \frac{\ell^2}{z^2} g^{(n)}_{AB}$. The explicit form of our zeroth order ansatz is

$$\begin{aligned} g^{(0)}_{AB}\, dx^A dx^B = {} & dz^2 + \alpha_d^2 b^2 \left(1 - \frac{z^d}{b^d}\right)^2 \left(1 + \frac{z^d}{b^d}\right)^{\frac{4}{d}-2} d\theta^2 \\ & + \left(1 + \frac{z^d}{b^d}\right)^{4/d} dx^2 + \left(1 + \frac{z^d}{b^d}\right)^{4/d} \sum_i dy^i dy^i. \end{aligned} \tag{5.7}$$

Using the Fefferman-Graham gauge condition $g^{(n)}_{Az} = 0$ for $n \geq 1$ as well as reflection symmetry in both θ and y^i, shows that all $g^{(n)}_{AB}$ remain diagonal. Similarly, only the zz, zx, xx, yy, and $\theta\theta$ components of the Einstein tensor can be non-zero.

We wish to satisfy the vacuum Einstein's equation with a negative cosmological constant:

$$0 = E_{AB} := R_{AB} - \frac{1}{2} R\, g_{AB} + \Lambda\, g_{AB} \quad . \tag{5.8}$$

As in [68], at each order in the adiabatic expansion we have $\frac{d(d+1)}{2}$ equations $E^{(n)}_{\mu\nu} = 0$ involving second derivatives with respect to z; we refer to these equations as dynamical. Here μ, ν range over all boundary coordinates. We also obtain $d+1$ equations involving no more than first derivatives in z, and which we call constraints. The latter divide themselves into $E^{(n)}_{z\mu} = 0$ and $E^{(n)}_{zz} = 0$. Rotational symmetry in the y^i requires $E^{(n)}_{y^i y^j} = E^{(n)}_{yy}\delta_{ij}$, so at each order we have only three distinct dynamical equations $E^{(n)}_{xx}$, $E^{(n)}_{\theta\theta}$, and $E^{(n)}_{yy}$ for the three undetermined metric functions $g^{(n)}_{\theta\theta}, g^{(n)}_{xx}$, and $g^{(n)}_{yy}$. Moreover, each derivative ∂_x adds another factor of ϵ, so the dynamical equations for $g^{(n)}_{AB}$ are ultra-local in the boundary directions. We are left with three coupled second order ordinary differential equations in z.

The dynamical equations require two boundary conditions to fix the solution uniquely. The first is given by fixing the induced metric on the boundary to be given by (5.4) with $b \to b(x)$. The zeroth order ansatz satisfies

$$\lim_{z\to 0} g^{(0)}_{\mu\nu} dx^\mu dx^\nu = dx^2 + \alpha_d^2 b^2 d\theta^2 + dy_i dy^i, \tag{5.9}$$

and so gives the correct boundary metric to all orders. We therefore impose

$$\lim_{z\to 0} g^{(n)}_{\mu\nu} = 0 \tag{5.10}$$

for all $n > 0$.

The second boundary condition is determined by regularity at the fixed points of ∂_θ. This occurs at some $z = \tilde{b}(x)$ where the associated S^1 shrinks to zero size. At zeroth order one finds $\tilde{b} = b$, though there are corrections at higher orders. To impose regularity, it suffices to construct coordinates $R(z, x)$ and $X(z, x)$ such that $g_{\theta\theta}$ vanishes at $R = 0$ and the metric takes the form

$$ds^2 = g_{RR}|_{R=0}\left(dR^2 + R^2 d\theta^2\right) + g_{XX}|_{R=0} dX^2 + g_{YY}|_{R=0} \sum_{i=1}^{d-2} dY^i dY^i + O(R^2) \tag{5.11}$$

where $g_{RR}|_{R=0}, g_{XX}|_{R=0}, g_{YY}|_{R=0}$ are positive (and thus non-vanishing) functions of X.

Expanding the zeroth-order ansatz (5.7) in powers of $z - b(x)$ shows that it satisfies regularity as previously claimed. One may then check that the full ansatz (5.6) satisfies (5.11) to order ϵ^2 with

$$\begin{aligned} z &= (1-R)b - \epsilon^2 \frac{1}{3} 16^{-1/d} b \left(b'^2 + \frac{2}{\alpha_d^2 d^2} \left. \partial_z^2 g^{(2)}_{\theta\theta} \right|_{z=b} \right) + O(\epsilon^4) \\ x &= X + \epsilon\, 16^{-1/d}\, b\, b' \left(R + \frac{1}{2}R^2 - \frac{1}{6}(d-2)R^3 \right) + O(\epsilon^4, R^4), \end{aligned} \tag{5.12}$$

so long as we impose the boundary conditions

$$\begin{aligned} 0 &= \left. g^{(1)}_{\theta\theta} \right|_{z=b} \\ 0 &= \left. \partial_z g^{(1)}_{xx} \right|_{z=b} \\ 0 &= \left. \partial_z g^{(1)}_{yy} \right|_{z=b} \end{aligned}$$

$$
\begin{aligned}
0 &= \partial_z g^{(2)}_{\theta\theta}\Big|_{z=b} - \frac{1}{6} b \left(\alpha_d^2 d^2 b'^2 + 2\, \partial_z^2 g^{(2)}_{\theta\theta}\Big|_{z=b} \right) \\
0 &= 2\, d\, b\, g^{(2)}_{xx}\big|_{z=b} + 2\alpha_d^{-2}\, \partial_z g^{(2)}_{\theta\theta}\Big|_{z=b} - d\, b^2\, \partial_z g^{(2)}_{xx}\big|_{z=b} + 2\, d\, b^2\, b'' \\
0 &= 2\, d\, b\, g^{(2)}_{yy}\big|_{z=b} + 2\alpha_d^{-2}\, \partial_z g^{(2)}_{\theta\theta}\Big|_{z=b} - d\, b^2\, \partial_z g^{(2)}_{yy}\big|_{z=b} - 2\, d\, b\, b'^2 .
\end{aligned} \tag{5.13}
$$

We emphasize that we have chosen the period of θ to remain precisely 2π at all x at each order in ϵ.

5.2.2 Adiabatic solutions

We have now specified two boundary conditions at each order for each of the dynamical variables $g^{(n)}_{xx}, g^{(n)}_{\theta\theta}$, and $g^{(n)}_{yy}$. This is enough to uniquely determine solutions to the dynamical equations $E_{\mu\nu} = 0$ at each order. It turns out that any such solution automatically satisfies the constraints $E_{zA} = 0$ or, equivalently, $E_{RA} = 0$. For $A = \theta, Y^i$ this is clear from the reflection symmetries $\theta \to -\theta$ and $Y^i \to -Y^i$. For $A = X, R$, we proceed by noting that the Bianchi identities $\nabla_A E^{AB}$ imply first order evolution equations for the constraints E^{RA}. Using (5.11), one finds that imposing $E^{\mu\nu} = 0$ requires $E^{RR} = C^{RR}\,(R^{-1} + \dots)$ and $E^{RX} = C^{RX}\,(R^{-1} + \dots)$ where C^{RR}, C^{RX} are constants and the dots $(\dots)$ represent terms that vanish as $R \to 0$. But regularity requires[2] E_{RR}, E_{RX} to be finite at $R = 0$. This sets $C_{RR} = 0 = C_{RX}$, so that the constraints hold identically everywhere in the bulk. It thus suffices to solve the dynamical equations $E_{\mu\nu} = 0$ alone subject to (5.9) and (5.13). At least in the adiabatic expansion, this verifies the expectation that bulk solutions exist for all profiles $b(\epsilon x)$.

Let us now examine in more detail the equations $E^{(n)}_{\mu\nu} = 0$ that result from expanding $E_{\mu\nu}$ in powers of ϵ . In general, the lower order terms $g^{(n)}_{AB}$ in (5.6) lead to sources for the higher order terms. As noted above, each boundary derivative contributes an explicit

[2] A simple argument notes that $\mathrm{Tr}E^2 := E^{AB}E^{CD}g_{DA}g_{BC}$ is a positive definite quadratic form that must be finite at $R = 0$. Explicitly, the leading terms at $R = 0$ are $(g_{RR}E^{RR})^2 + 2g_{RR}g_{XX}(E^{RX})^2$.

power of ϵ. Covariance requires each term in $E_{\mu\nu}$ to contain an even number of such derivatives, so evaluating $E_{\mu\nu}$ on the zeroth-order ansatz (5.7) alone can provide source terms only for $g^{(n)}_{AB}$ with n even.

In particular, there can be no source terms at order ϵ so that the dynamical equations for $g^{(1)}_{AB}$ are homogeneous. Since the boundary conditions (5.9) and (5.13) are also homogeneous at this order, the unique solution is $g^{(1)}_{AB} = 0$.

The story is more interesting at second order. Explicit computation gives the following lengthy dynamical equations:

$$
\begin{aligned}
0 =& 4(d-2)z^{d+2}\left((d+1)b^d + (d-2)z^d\right)b'^2 - 4\,b(d-2)z^{d+2}\left(b^d + z^d\right)b'' \\
&- 4\,b^2(d-4)z^{2d}g^{(2)}_{xx} - 4\,b^2(d-4)(d-2)z^{2d}g^{(2)}_{yy} \\
&+ b^2 z\left(b^d + z^d\right)\left((d-7)z^d - (d-1)b^d\right)\partial_z g^{(2)}_{xx} \\
&+ b^2(d-2)z\left(b^d + z^d\right)\left((d-7)z^d - (d-1)b^d\right)\partial_z g^{(2)}_{yy} \\
&+ b^2 z^2\left(b^d + z^d\right)^2\partial_z^2 g^{(2)}_{xx} + b^2(d-2)z^2\left(b^d + z^d\right)^2\partial_z^2 g^{(2)}_{yy},
\end{aligned}
$$

$$
\begin{aligned}
0 =& 4\,(d-2)z^{d+2}\left(z^d - b^d\right)^3\left(b^{2d} + (d+1)b^d z^d + (d-2)z^{2d}\right)b'^2 \\
&- 4\alpha_d^{-2}\,z^{2d}\left(b^d + z^d\right)^2\left(-(2d^2-5d+4)b^{2d} - 2(3d-4)b^d z^d + (d-4)z^{2d}\right)g^{(2)}_{\theta\theta} \\
&- 4\,b^2(d-2)z^{2d}\left(z^d - b^d\right)^3\left((d+4)b^d + (d-4)z^d\right)g^{(2)}_{yy} \\
&- \alpha_d^{-2} z\left(b^d - z^d\right)\left(b^d + z^d\right)^3\left((d-1)b^{2d} - 2(3d-4)b^d z^d + (d-7)z^{2d}\right)\partial_z g^{(2)}_{\theta\theta} \\
&+ b^2(d-2)z\left(b^d - z^d\right)^2\left(z^{2d} - b^{2d}\right)\left((d-1)b^{2d} + 8b^d z^d + (d-7)z^{2d}\right)\partial_z g^{(2)}_{yy} \\
&+ \alpha_d^{-2} z^2(b^d - z^d)^2(b^d + z^d)^4\partial_z^2 g^{(2)}_{\theta\theta} + b^2(d-2)z^2\left(b^d - z^d\right)^4\left(b^d + z^d\right)^2\partial_z^2 g^{(2)}_{yy},
\end{aligned}
$$

$$
\begin{aligned}
0 =& 4z^{d+2}\left(b^d - z^d\right)^2\left(z^d - b^d\right)\left(d\,b^{2d} + ((d-2)d-6)b^d z^d + (d-3)(d-2)z^{2d}\right)b'^2 \\
&+ 2\,b\,z^2\left(b^d - z^d\right)^3\left(b^d + z^d\right)\left(b^{2d} + 4b^d z^d + (2d-5)z^{2d}\right)b''
\end{aligned}
$$

$$
\begin{aligned}
&- 4\alpha_d^{-2}\, z^{2d} \left(b^d + z^d\right)^2 \left(-(2d^2-5d+4)b^{2d} - 2(3d-4)b^d z^d + (d-4)z^{2d}\right) g^{(2)}_{\theta\theta} \\
&- 4\, b^2 z^{2d} \left(z^d - b^d\right)^3 \left((d+4)b^d + (d-4)z^d\right) g^{(2)}_{xx} \\
&- 4\, b^2 (d-3) z^{2d} \left(z^d - b^d\right)^3 \left((d+4)b^d + (d-4)z^d\right) g^{(2)}_{yy} \\
&- \alpha_d^{-2} z \left(b^d - z^d\right) \left(b^d + z^d\right)^3 \left((d-1)b^{2d} - 2(3d-4)b^d z^d + (d-7)z^{2d}\right) \partial_z g^{(2)}_{\theta\theta} \\
&+ b^2 z \left(b^d - z^d\right)^2 \left(z^{2d} - b^{2d}\right) \left((d-1)b^{2d} + 8\, b^d z^d + (d-7)z^{2d}\right) \partial_z g^{(2)}_{xx} \\
&+ b^2 (d-3) z \left(b^d - z^d\right)^2 \left(z^{2d} - b^{2d}\right) \left((d-1)b^{2d} + 8\, b^d z^d + (d-7)z^{2d}\right) \partial_z g^{(2)}_{yy} \\
&+ \alpha_d^{-2} z^2 \left(b^d - z^d\right)^2 \left(b^d + z^d\right)^4 \partial_z^2 g^{(2)}_{\theta\theta} + b^2 z^2 \left(b^d - z^d\right)^4 \left(b^d + z^d\right)^2 \partial_z^2 g^{(2)}_{xx} \\
&+ b^2 (d-3) z^2 \left(b^d - z^d\right)^4 \left(b^d + z^d\right)^2 \partial_z^2 g^{(2)}_{yy}.
\end{aligned} \tag{5.14}
$$

As a check, we can use (5.14) to analytically compute the asymptotic expansion of $g^{(2)}_{xx}, g^{(2)}_{\theta\theta}, g^{(2)}_{yy}$ in powers of z. Solving (5.14) via the Frobenius method near $z = 0$, for $d \geq 3$ we find

$$
\begin{aligned}
g^{(2)}_{\theta\theta} &= \alpha_d^2 \frac{b\, b''}{d-1} z^2 + c_\theta z^d + O(z^{d+1}), \\
g^{(2)}_{xx} &= \frac{b''}{b\,(d-1)} z^2 + c_x z^d + O(z^{d+1}), \\
g^{(2)}_{yy} &= -\frac{b''}{b\,(d-1)(d-2)} z^2 + c_y z^d + O(z^{d+1}),
\end{aligned} \tag{5.15}
$$

where the coefficients of z^d are determined by the boundary conditions at the horizon.

On the other hand, for any boundary metric $\gamma^{(0)}_{\mu\nu}$, it is known (see e.g. [17]) that for $d \geq 3$ the z^2 coefficient in the expansion of $g_{\mu\nu}$ is given by

$$
\gamma^{(2)}_{\mu\nu} = -\frac{\ell^2}{d-2} \left(\mathcal{R}_{\mu\nu} - \frac{1}{2(d-1)} \mathcal{R} \gamma^{(0)}_{\mu\nu} \right), \tag{5.16}
$$

where $\mathcal{R}_{\mu\nu}$ is the Ricci tensor of $\gamma^{(0)}_{\mu\nu}$. Furthermore, the terms $z^n \gamma^{(n)}_{\mu\nu}$ with $3 \leq n < d$ involve higher numbers of derivatives and so vanish to order ϵ^2 (and similarly for the

$z^d \log z^2$ term for even $d > 2$; for $d = 2$ the $z^2 \log z^2$ term vanishes identically). As the boundary curvature is given by

$$\mathcal{R}_{\theta\theta} = -\epsilon^2 \alpha_d^2 \, b \, b'', \quad \mathcal{R}_{xx} = -\epsilon^2 \, \frac{b''}{b}, \quad \mathcal{R} = -2\,\epsilon^2 \, \frac{b''}{b}, \tag{5.17}$$

we see that (5.16) agrees with (5.15).

While the equations (5.14) are highly coupled, they are also linear and can be solved numerically using the collocation methods described in [32]. By linearity, and dimensional analysis the solutions take the form

$$\begin{aligned} g^{(2)}_{xx}(z,x) &= (b'(x))^2 \, \mathrm{g}^{(b')^2}_{xx}(z/b) + (b(x)b''(x)) \, \mathrm{g}^{(bb'')}_{xx}(z/b), \\ g^{(2)}_{yy}(z,x) &= (b'(x))^2 \, \mathrm{g}^{(b')^2}_{yy}(z/b) + (b(x)b''(x)) \, \mathrm{g}^{(bb'')}_{yy}(z/b), \\ g^{(2)}_{\theta\theta}(z,x) &= \alpha_d^2 \left[(b(x)\, b'(x))^2 \, \mathrm{g}^{(bb')^2}_{\theta\theta}(z/b) + b(x)^3 \, b''(x) \; \mathrm{g}^{(b^3 b'')}_{\theta\theta}(z/b) \right], \end{aligned} \tag{5.18}$$

where the functions $\mathrm{g}^{(b')^2}_{xx}(z/b)$, etc have no further dependence on $b(x)$. Results for these dimensionless coefficient functions are shown in figures 5.1 - 5.3.

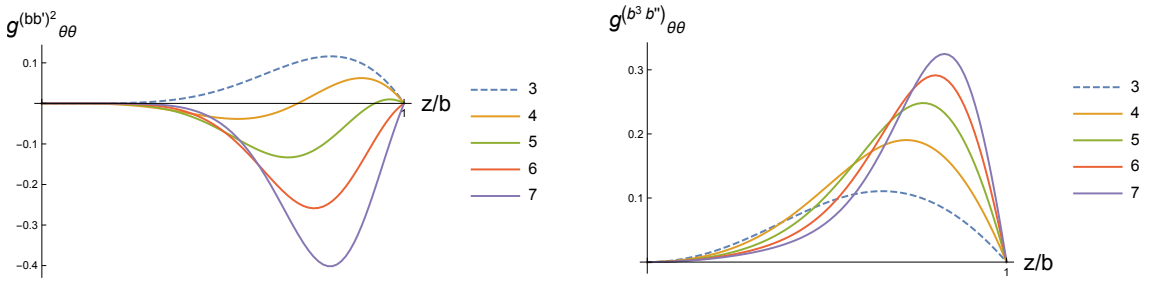

(a) (b)

Figure 5.1: (Color online) Numerical solutions for (a) $\mathrm{g}^{(bb')^2}_{\theta\theta}$ and (b) $\mathrm{g}^{(b^3 b'')}_{\theta\theta}$ as functions of z/b for $d = 3$ to $d = 7$ using the notation (5.18). In each case the left endpoint is the asymptotic boundary $z = 0$ and the right endpoint is the fixed point of ∂_θ (where $g_{\theta\theta} = 0$).

Although we have thus far allowed dependence only on a single coordinate x, the

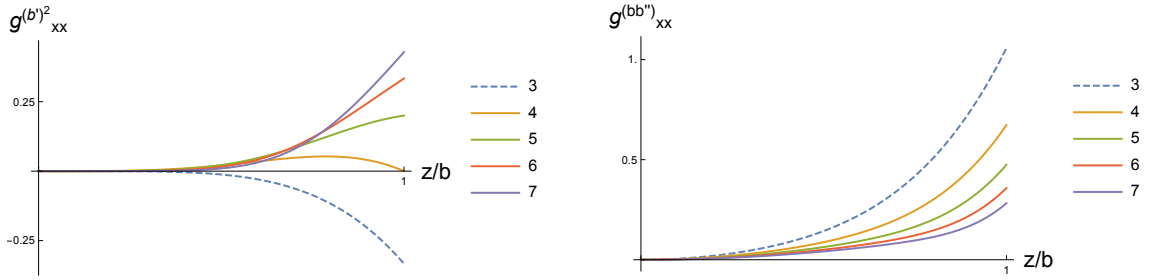

(a) (b)

Figure 5.2: (Color online) Numerical solutions for (a) $\mathrm{g}_{xx}^{(b')^2}$ and (b) $\mathrm{g}_{xx}^{(bb'')}$ for $d = 3$ to $d = 7$ using the notation (5.18). In each case the left endpoint is the asymptotic boundary $z = 0$ and the right endpoint is the fixed point of ∂_θ (where $g_{\theta\theta} = 0$).

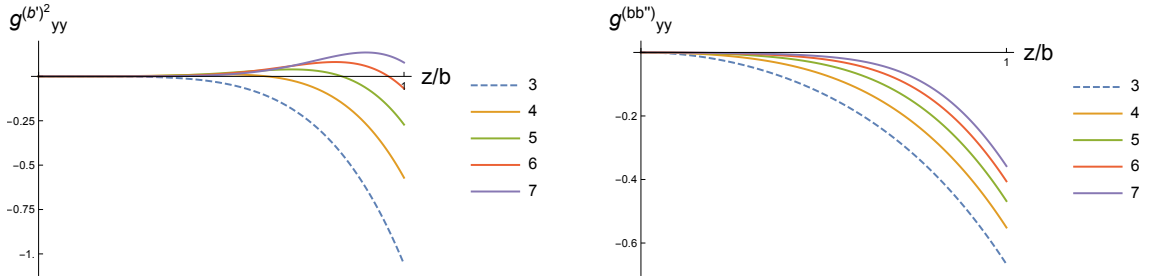

(a) (b)

Figure 5.3: (Color online) Numerical solutions for (a) $\mathrm{g}_{yy}^{(b')^2}$ and (b) $\mathrm{g}_{yy}^{(bb'')}$ for $d = 3$ to $d = 7$ using the notation (5.18). In each case the left endpoint is the asymptotic boundary $z = 0$ and the right endpoint is the fixed point of ∂_θ (where $g_{\theta\theta} = 0$).

results above in fact determine the $O(\epsilon^2)$ response of our system to general slow variations of b in the $(d-1)$ directions (x, y^i). In particular, since the metric at each order ϵ^n and each bulk point (z, x, y^i, θ) is locally determined by the boundary metric at (x, y^i, θ), in computing the response to gradients we are free to simply define x at each such boundary point to run in the direction of any gradient of b, so long as we then take the y^i to label the orthogonal directions. We may then separately consider the response to the matrix of second derivatives of b (the Hessian). Here it is useful to choose coordinates that diagonalize the Hessian. Furthermore, since the $O(\epsilon^2)$ response to second derivatives is linear, it suffices to separately compute the response to each eigenvalue λ_α of the Hessian.

And for studying any particular eigenvalue, we can choose the x coordinate to run in the corresponding direction. As a result, letting α, β run over directions corresponding to eigenvectors of the Hessian and denoting the the second order response to the Hessian of g_{AB} in the direction associated with some particular eigenvalue λ_β by $g^{(2,Hess)}_{\beta\beta}$, we have

$$g^{(2,Hess)}_{\beta\beta} = b\left[\mathfrak{g}^{(bb'')}_{xx}(z/b)\lambda_\beta + \mathfrak{g}^{(bb'')}_{yy}(z/b)\sum_{\alpha\neq\beta}\lambda_\alpha\right] \tag{5.19}$$

in terms of the functions $\mathfrak{g}^{(bb'')}_{xx}(z/b)$, $\mathfrak{g}^{(bb'')}_{yy}(z/b)$ computed above.

5.3 Gauge Theory Implications

We now use the above solutions above to extract physical data about the confining gauge theory. In particular, the quark/anti-quark potential $V(x_q, x_{aq})$ can be studied by computing the expectation value of rectangular Wilson loops extending along e.g. x and $\tau = y^1$. For $\Delta\tau \gg \Delta x = x_q - x_{aq}$, one expects from (5.1) that

$$W(\mathcal{C}) \sim e^{-V(x_q, x_{aq})\,\Delta\tau}. \tag{5.20}$$

Using the holographic prescription (5.2), we see that $V(x_q, x_{aq})$ is proportional to the (renormalized) area of the string world-sheet per unit time $\Delta\tau$. If we further take Δx (and thus also $\Delta\tau$) much larger than the scale b, this renormalized area can be approximated by that of the corresponding rectangle on the hypersurface where $\partial_\theta = 0$; we follow standard practice in referring to this surface as the IR floor. In the coordinate system (5.11), the IR floor lies at $R = 0$. Transforming to Fefferman-Graham coordinates using

(5.12) and taking into account (5.13), it also lies at $z = \tilde{b}$ with

$$\tilde{b} = b - \frac{\epsilon^2}{2}\, b^2\, \alpha_d^{-2}\, \partial_z g^{(2)}_{\theta\theta}\Big|_{z=b} + O(\epsilon^4). \tag{5.21}$$

Here we assume $d \geq 3$ so that there is at least one y direction. The special case $d = 2$ is discussed separately in appendix 5.A, where it is solved analytically and used to check our numerical codes.

We denote by $\mathcal{C}_{floor}$ the corresponding rectangular loop on this IR floor. Since $\tau = y^1$, the loop $\mathcal{C}_{floor}$ has area

$$A_{\mathcal{C}_{floor}} \approx \ell^2 \int dx\, dy^1 \left(\frac{1}{b^2} 16^{1/d} + \frac{\epsilon^2}{2b^2} \left(h^{(2)}_{xx} + h^{(2)}_{yy} \right) \right), \tag{5.22}$$

where $\ell^2 h_{\mu\nu}$ is the induced metric on the IR floor. Similarly, for loops extending along τ and a y direction, we have

$$A_{\mathcal{C}_{floor}} \approx \ell^2 \int dy^2\, dy^1 \left(\frac{1}{b^2} 16^{1/d} + \frac{\epsilon^2}{b^2}\, h^{(2)}_{yy} \right). \tag{5.23}$$

The second order contributions to $h_{\mu\nu}$ are listed in the table in figure 5.4 using notation analogous to (5.18). Here we extend the calculations to $d = 8$ due to an interesting change of sign for $\mathsf{h}^{(b')^2}_{yy}$ between $d = 6$ and $d = 7$.

The factors in parentheses in (5.22), (5.23) describe an effective tension for the gauge-theory flux tube whose stretching between the quark and anti-quark provides the confining potential. Supposing for the moment that we allow b to vary only in spatial directions (x and y^i for $i \geq 2$), the spacetime remains static and any flux tube will tend to orient itself to minimize this effective tension. As described at the end of section 5.2.2, the coefficients above can be used to deduce the $O(\epsilon^2)$ response to general slow variations of b across (x, y^i). The fact that $\mathsf{h}^{(b')^2}_{xx} > \mathsf{h}^{(b')^2}_{yy}$ for all d in the table in figure 5.4 thus

d	$\mathsf{h}_{xx}^{(b')^2}$	$\mathsf{h}_{xx}^{(bb'')}$	$\mathsf{h}_{yy}^{(b')^2}$	$\mathsf{h}_{yy}^{(bb'')}$
3	-0.333	1.06	-1.06	-0.667
4	0.00	0.673	-0.571	-0.551
5	0.200	0.475	-0.272	-0.468
6	0.333	0.358	-0.0688	-0.406
7	0.429	0.282	0.0778	-0.358
8	0.500	0.231	0.189	-0.320

Figure 5.4: The coefficients $\mathsf{h}_{xx}^{(b')^2}$, $\mathsf{h}_{xx}^{(bb'')}$, $\mathsf{h}_{yy}^{(b')^2}$, and $\mathsf{h}_{yy}^{(bb'')}$ for the induced metric on the IR floor for various dimensions. Though we display only a few significant figures, estimating the numerical precision by comparing results for 100 and 150 lattice points suggests that our numerics are accurate to around a part in 10^{20}. We note that $\mathsf{h}_{xx}^{(b')^2}$ agrees with $(d-4)/d$ to the stated precision.

implies that the flux tube tends to orient itself orthogonal to gradients. In the same way, using (5.19) and comparing directions associated with different eigenvalues of the Hessian, one sees that flux tubes also tend to align themselves with the lowest eigenvalue of the Hessian.

Interestingly, the change of sign of $\mathsf{h}_{yy}^{(b')^2}$ between $d = 6$ and $d = 7$ means that a flux tube that succeeds in aligning itself orthogonal to gradients is attracted to strong gradients for $d \leq 6$ but repelled from strong gradients for $d \geq 7$. In all dimensions, flux tubes are repelled by regions where the second derivative along the tube would be large and positive but are attracted to regions where the eigenvalues of the Hessian are large and positive in orthogonal directions.

Another interesting piece of physics concerns the gravitational potential (or redshift) on the IR floor. This is encoded in $h_{\tau\tau} = h_{y^1 y^1} = (\frac{1}{b^2} 2^{4/d} + \epsilon^2 \, h_{yy}^{(2)}) + O(\epsilon^4)$. Again assuming a static spacetime one finds

$$h_{\tau\tau}^{(2)} = \mathsf{h}_{yy}^{(b')^2} |\partial_\mu b|^2 + \mathsf{h}_{yy}^{(bb'')} \mathrm{Tr}\left(b \, \partial_\mu \partial_\nu b\right), \tag{5.24}$$

where $|\partial_\mu b|^2$ and $\mathrm{Tr}\left(\partial_\mu \partial_\nu b\right)$ respectively denote that norm of the gradient of b and the

trace of its Hessian. It is interesting that the table in figure 5.4 shows gradients to lower the potential for $d \leq 6$ but to raise the potential for $d = 7, 8$ (and presumably for higher dimensions as well).

Note that the value of $h_{\tau\tau}$ at an extremum (where $\partial_\mu b = 0$) is unaffected by $\mathsf{h}_{yy}^{(b')^2}$. The fact that $\mathsf{h}_{yy}^{(bb'')} < 0$ in figure 5.4 thus means that the $O(\epsilon^2)$ corrections act to reduce the height of local maximum of $h_{\tau\tau}$ and to reduce the depth of local minima. This should be no surprise, as at this order the response of the system is linear in b'' while on general grounds linear perturbation theory about the AdS soliton should describe the change in $h_{\tau\tau}$ as a smeared version of the boundary perturbation (i.e., given by convolution with some appropriate kernel) over a scale $\sim b$. The point here is that smearing a maximum necessarily reduces its height, while smearing a minimum decreases its depth. Indeed, all adiabatic coefficients associated with b'' can in principle be calculated from the associated linear-response Green's functions.

Finally, we can also compute coefficients for corrections to the boundary stress tensor. Since at order ϵ^2 we may neglect quadratic and higher powers of boundary curvatures, our boundary stress tensor takes the form

$$T_{\mu\nu} = \frac{d\ell^{d-1}}{2\kappa}\gamma_{\mu\nu}^{(d)} + O(\epsilon^4) \tag{5.25}$$

for both odd and even $d \geq 3$. Here $\kappa = 8\pi G_N/\ell^{d-1}$ in terms of the bulk Newton constant G_N and $\gamma_{\mu\nu}^{(n)}$ is the z^n coefficient of the Fefferman-Graham expansion (not to be confused with the $g_{\mu\nu}^{(n)}$ in the adiabatic expansion). We expand the stress tensor as

$$T_{\mu\nu} = T_{\mu\nu}{}^{(0)} + \epsilon\, T_{\mu\nu}{}^{(1)} + \epsilon^2\, T_{\mu\nu}{}^{(2)} + \cdots \tag{5.26}$$

The zeroth order result is standard with

$$\begin{aligned} T^{(0)}_{xx} &= \frac{\ell^{d-1}}{4\pi G_N}\frac{1}{b^d}\,, \\ T^{(0)}_{yy} &= \frac{\ell^{d-1}}{4\pi G_N}\frac{1}{b^d}\,, \\ T^{(0)}_{\theta\theta} &= -\frac{\ell^{d-1}}{4\pi G_N}\frac{\alpha_d^2(d-1)}{b^{d-2}}\,. \end{aligned} \tag{5.27}$$

Since $g^{(1)}_{\mu\nu}$ vanishes, so does $T_{\mu\nu}{}^{(1)}$. The second order contributions can be extracted from the numerical solutions for $g^{(2)}_{\mu\nu}$. The results are summarized in figure 5.5 using the notation

$$\begin{aligned} T^{(2)}_{xx} &= \frac{\ell^{d-1}}{8\pi G}\left[\left(\frac{(b')^2}{b^d}\right)\mathsf{T}^{(b^{-d}b'^2)}_{xx} + \left(\frac{b''}{b^{d-1}}\right)\mathsf{T}^{(b^{-(d-1)}b'')}_{xx}\right], \\ T^{(2)}_{yy} &= \frac{\ell^{d-1}}{8\pi G}\left[\left(\frac{(b')^2}{b^d}\right)\mathsf{T}^{(b^{-d}b'^2)}_{yy} + \left(\frac{b''}{b^{d-1}}\right)\mathsf{T}^{(b^{-(d-1)}b'')}_{yy}\right], \\ T^{(2)}_{\theta\theta} &= \frac{\ell^{d-1}}{8\pi G}\left[\left(\frac{(b')^2}{b^{d-2}}\right)\mathsf{T}^{(b^{-(d-2)}b'^2)}_{\theta\theta} + \left(\frac{b''}{b^{d-3}}\right)\mathsf{T}^{(b^{-(d-3)}b'')}_{\theta\theta}\right]. \end{aligned} \tag{5.28}$$

d	$\mathsf{T}^{(b^{-(d-2)}b'^2)}_{\theta\theta}$	$\mathsf{T}^{(b^{-(d-3)}b'')}_{\theta\theta}$	$\mathsf{T}^{(b^{-d}b'^2)}_{xx}$	$\mathsf{T}^{(b^{-(d-1)}b'')}_{xx}$	$\mathsf{T}^{(b^{-d}b'^2)}_{yy}$	$\mathsf{T}^{(b^{-(d-1)}b'')}_{yy}$
3	0.00	0.00	0.00	0.00	0.00	0.00
4	−0.375	0.250	1.00	0.00	1.00	−1.00
5	−0.844	0.422	2.30	0.00	2.30	−1.53
6	−1.32	0.529	3.78	0.00	3.78	−1.89
7	−1.77	0.591	5.38	0.00	5.38	−2.15
8	−2.19	0.625	7.07	0.00	7.07	−2.36

Figure 5.5: The coefficients of the second order contributions to the boundary stress tensor for $3 \le d \le 8$. Estimating the numerical precision by comparing results for 100 and 150 lattice points suggests that our numerics are accurate to around a part in 10^8. To this accuracy our results satisfy $T^{(b^{-d}b'^2)}_{yy} = -\frac{d-2}{2}T^{(b^{-(d-1)}b'')}_{yy}$ and $T^{(b^{-d}b'^2)}_{xx} = T^{(b^{-d}b'^2)}_{yy}$.

As in our discussion of the potential on the IR floor, the signs of $\mathsf{T}^{(b^{-(d-3)}b'')}_{\theta\theta}$ and $\mathsf{T}^{(b^{-(d-1)}b'')}_{yy}$ are in all cases consistent with the idea that linear response tends to simply

average over a scale of order b. As a result, the $O(\epsilon^2)$ correction to the (negative) energy density of the confining vacuum makes this energy less negative at a local minimum of b but more negative at a local maximum. On the other hand, gradients always make this energy density even more negative when the second derivatives are held fixed.

Of particular interest is the $O(\epsilon^2)$ shift $E^{(2)}$ in the total energy of the vacuum. This is given by integrating $-T^{(2)}_{yy}$ over the boundary at $\tau = 0$. The interesting point here is that first and second derivatives are often related when averaged over this surface. Indeed, imposing either a boundary condition $b \to \textit{constant}$ as $x \to \pm\infty$ or periodic boundary conditions in x, integrating by parts gives

$$\begin{aligned} E^{(2)} &= -\int_{bndy@\tau=0} \sqrt{\sigma}\, T_{yy} \\ &= -\frac{2\pi\ell^{d-1}}{8\pi G}\int dx d^{d-2}y\ \alpha_d b\ \left[\left(\frac{(b')^2}{b^d}\right)\mathsf{T}^{(b^{-d}b'^2)}_{yy} + \left(\frac{b''}{b^{d-1}}\right)\mathsf{T}^{(b^{-(d-1)}b'')}_{yy}\right] \\ &= -\frac{\alpha_d\ell^{d-1}}{4G}\int dx d^{d-2}y \left(\frac{(b')^2}{b^{d-1}}\right)\left[\mathsf{T}^{(b^{-d}b'^2)}_{yy} + (d-2)\mathsf{T}^{(b^{-(d-1)}b'')}_{yy}\right], \end{aligned} \tag{5.29}$$

where $\sqrt{\sigma} = \alpha_d b$ is the volume element on the $\tau = 0$ slice of the boundary. As shown in figure 5.6, the factor in square brackets is negative in all cases. So the net effect of spatial variations is in fact to make $E^{(2)}$ positive, shifting the energy of the confined vacuum toward zero from its negative zeroth-order value.

It would be interesting to perform a similar analysis of the deconfined state. Computing the second order shift in its free energy and comparing with (5.29) would then determine whether the net effect of gradients is to increase the deconfinement temperature T_D at $O(\epsilon^2)$, or to decrease T_D as our results would appear to suggest. Other interesting extensions would be to add additional curvature on the boundary. Note that

d	$\mathsf{E}^{(2)}$
3	0.00
4	−1.00
5	−2.30
6	−3.78
7	−5.38
8	−7.07

Figure 5.6: The coefficient $\mathsf{E}^{(2)} = \mathsf{T}_{yy}^{(b^{-d}b'^2)} + (d-2)\mathsf{T}_{yy}^{(b^{-(d-1)}b'')}$ of the second order contribution to the vacuum energy for $3 \leq d \leq 8$. The numerical precision is as in figure 5.5.

the particularly simple class of boundary metrics of the form

$$ds^2_{bndy} = dx^2 + k^2(\epsilon x) dy_i dy^i + \alpha_d^2 b^2(\epsilon x)\, d\theta^2, \tag{5.30}$$

is related to those studied here by a combination of a conformal transformation and a change of coordinates in the x direction (associated with $dx \to dx/k$), so that the adiabatic coefficients associated with (5.30) can be computed analytically from the results given above.

5.A 2+1 Dimensional Bulk

Due to the lack of local gravitational degrees of freedom in 2+1 dimensions, all complete asymptotically locally AdS spacetimes are diffeomorphic to global AdS_3 (or to a quotient thereof). We can use this fact to analytically perform the $d = 2$ analogue of the construction in section 5.2, which we can then use to check our numerical code. The $d = 2$ version of the Euclidean metric (5.7) is obtained by simply deleting the y^i terms:

$$ds^2 = \frac{\ell^2}{z^2}\left[dz^2 + \frac{b^2}{4}\left(1 - \frac{z^2}{b^2}\right)^2 d\theta^2 + \left(1 + \frac{z^2}{b^2}\right)^2 dx^2\right]. \tag{5.31}$$

The adiabatic expansion proceeds just as in section 5.2. We need only set $d = 2$ in (5.14) to find the dynamical equations

$$\begin{aligned} 0 &= \left(b^2+z^2\right)\left(z\left(b^2+z^2\right)\partial_z^2 g_{xx}^{(2)} - \left(z^2-3b^2\right)\partial_z g_{xx}^{(2)}\right) - 8b^2 z\, g_{xx}^{(2)}, \\ 0 &= \left(b^2-z^2\right)\left(z\left(b^2-z^2\right)\partial_z^2 g_{\theta\theta}^{(2)} + \left(z^2+3b^2\right)\partial_z g_{\theta\theta}^{(2)}\right) + 8b^2 z\; g_{\theta\theta}^{(2)}. \end{aligned} \tag{5.32}$$

We again have the boundary conditions

$$\lim_{z\to 0} z^2 g_{\mu\nu}^{(n)} = 0 \tag{5.33}$$

at the asymptotic boundary, and regularity at fixed points of ∂_θ requires

$$\begin{aligned} 0 &= \partial_z g_{\theta\theta}^{(2)}\Big|_{z=b} - \frac{1}{3}b\left(\frac{b'^2}{2} + \partial_z^2 g_{\theta\theta}^{(2)}\Big|_{z=b}\right) \quad , \\ 0 &= 2\,b\; g_{xx}^{(2)}\big|_{z=b} + 4\;\partial_z g_{\theta\theta}^{(2)}\Big|_{z=b} - \; b^2\;\partial_z g_{xx}^{(2)}\big|_{z=b} + 2\,b^2\,b'' \quad . \end{aligned} \tag{5.34}$$

Solving (5.32), (5.34) yields

$$\begin{aligned} g_{\theta\theta}^{(2)} &= \frac{z^2\left(b^2-z^2\right)b'^2}{8\,b^2} \quad , \\ g_{xx}^{(2)} &= \frac{z^2\left(b^2+z^2\right)\left(2\,b\,b''-b'^2\right)}{2b^4} \quad . \end{aligned} \tag{5.35}$$

Setting $d = 2$ in our numerical code gives solutions to (5.32), (5.34) that agree with (5.35) to one part in 10^{21}.

Chapter 6

Adiabatic Corrections to Holographic Entanglement

6.1 Introduction

Entanglement is a fundamental property of quantum systems. Studying this entanglement can provide insights into the nature of quantum states, and in particular into the scale of their correlations. In the holographic context, entanglement of the dual CFT is of particular interest through its association with the Einstein-Rosen bridges of black holes [21] and perhaps more generally [71, 72, 73] with the emergence of bulk spacetime.

Our goal here is to generalize the analysis of holographic entanglement away from the commonly-considered highly symmetric systems. For $d = 2$ CFTs, much can be done exactly using conformal transformations. This fact lies behind the recent analysis [27] of the CFT states dual to asymptotically-AdS_3 mutli-boundary vacuum wormholes. In particular, it was understood there that such states admit a simple description at high temperatures where the state can be well-approximated by a thermofield double (TFD) over most of the CFT spacetime, perhaps with adiabatic variations from one point to

another. While a full analysis comparable to [27] is difficult in higher dimensions, we show below that computations of entanglement in spatialy-varying holographic TFDs remains tractable in the adiabatic limit.

We also investigate how entanglement in ground states of $(d-1)$-dimensional confining theories is affected by slow variations of the confinement scale. The particular class of confining theories we consider are those given by compactifying a d-dimensional holographic CFT on an S^1 as in [22]. Such CFT ground states are related to the above thermofield doubles, as both are given by cutting open Euclidean path integrals over geometries with $S^1 \times \mathbb{R}^{d-1}$ topology. Roughly speaking, the thermofield double states are given by cutting open the S^1 factor, while ground states of confining theories are given by cutting open a direction of the $\mathbb{R}^{d-1}$. The particular path integrals considered here will involve warped products of the S^1 over $\mathbb{R}^{d-1}$ in which the size b of the S^1 varies slowly. This gives in the first interpretation TFD states in spacetimes with spatially varying redshift, and in the second ground states of confining theories in which the confinement scale varies with position.

Since we are interested in holographic field theories, in all cases we will work directly with the dual gravitational description. Our CFT path integrals are then interpreted as integrals over all $(d+1)$-dimensional asymptotically locally Anti-de Sitter (AlAdS) spacetimes with boundary geometries as above. Section 6.2 begins below by reviewing the Euclidean bulk geometries recently constructed in [30] that are expected to describe the dominant AlAdS saddle points. For simplicity, we allow b to vary only along one Cartesian direction of the $\mathbb{R}^{d-1}$ space. While such solutions can be constructed by Wick rotating the standard fluid-gravity correspondence [68, 69, 70] in the presence of a time-translation Killing field and an appropriate regularity condition at the bifurcation surface, it is more natural to follow [30] and use the $U(1)$ symmetry to develop a related but different expansion based on standard Schwarzschild-like coordinates rather than the

ingoing Eddington-Finkelstein black hole coordinates of [68, 69, 70].

We then proceed to compute holographic entanglement. Section 6.3 pursues the thermofield-double interpretation and computes the effect of varying b on the Ryu-Takayanagi (RT) entropies of slabs of thickness $2L$ that preserve $\mathbb{R}^{d-2}$ Euclidean symmetry on a surface fixed by a reflection of the S^1. We include both the case of slabs contained in a single copy of the CFT and that of pairs of diametrically opposed slabs in each of the two CFTs. We thus also compute the effect of varying b on the mutual information in opposing slabs and on the critical value L_{crit} of L at which the mutual information becomes non-zero. Section 6.4 then studies the effect on RT entropies for analogous slabs with $S^1 \times \mathbb{R}^{d-3}$ symmetry on a surface fixed by reflecting one direction in the $\mathbb{R}^{d-1}$. Here the interesting feature is the effect on the value L_{crit} at which the entangling surface changes topology from connected ($S^1 \times [0,1] \times \mathbb{R}^{d-3}$) to disconnected (two copies of the $(d-1)$-disk). Readers focused on the final results may wish to jump to sections 6.3.3 and 6.4.3 where the phase transitions are discussed. We close with some final discussion in section 6.5. The special case $d = 2$ is treated analytically in appendix 6.A, and we discuss some estimation of the numerical uncertainty in appendix 6.B.

6.2 Preliminaries

We wish to describe holographic entanglement in CFT states defined by path integrals over geometries with topology $S^1 \times \mathbb{R}^{d-1}$ and metrics of the form

$$ds^2_{CFT} = dx^2 + \delta_{ij} dy^i dy^j + \alpha_d^2 b^2(x) d\theta^2 \quad , \tag{6.1}$$

where $\alpha_d = \frac{2^{1-2/d}}{d}$ and $i = 1, \ldots, d-2$. We take θ to have b-independent period 2π. The relevant states are constructed by slicing open the path integral along a co-dimension

one surface that we identify as $\tau = 0$ for some Euclidean time coordinate τ. To have a good translation to Lorentz signature, we require a $\mathbb{Z}_2$ reflection symmetry $\tau \to -\tau$. One natural choice is to take $\tau = \theta$, in which case we in fact slice the path integral along the pair of surfaces $\theta = 0, \theta = \pi$. The result is an entangled state on a pair of CFTs which gives an adiabatic generalization of the well-known thermofield double state. The exact time-translation symmetry means that the state is in thermal equilibrium when viewed from the perspective of either CFT alone. However, after Wick rotation to Lorentz signature the x-dependent metric factor $g_{\theta\theta}$ means that the state lives in a spacetime with x-dependent gravitational redshift. This equilibrium thus requires any local notion of temperature (such as that defined by the inverse Euclidean period) to be x-dependent as well. This interpretation is equally valid in the special case $d = 2$ in which there are no y directions.

For $d \geq 3$, there is a second interpretation given by choosing τ to be some y direction (say, y^1), so that our CFT lives on a spacetime with a compact spatial S^1. States of this theory are constructed by slicing the path integral along $y^1 = 0$. For small b one may Kaluza-Klein reduce on this S^1. And as discussed in [22], one expects the result to exhibit confinement with a scale set by b. So when b varies, one may think of the result as a confining theory with a position-dependent confinement scale.

But with either interpretation, so long as b varies slowly reasoning analogous to that of [22] implies the bulk path gravitational integral with boundary conditions given by (6.1) to be dominated by a Euclidean solution to Einstein's equation in which the S^1 factor pinches off in the bulk; i.e., there will be a Killing field ∂_θ that generates a $U(1)$ isometry with a fixed-point set of topology $\mathbb{R}^{d-1}$.

When the function $b(x)$ varies slowly, the construction of such solutions may be organized in a derivative expansion. Here we write $b = b(\epsilon x)$ for some small parameter ϵ. The details of this expansion were recently described in [30], where it was argued that for

slowly-varying $b(x)$ the solution should be well-approximated by the zero-order ansatz

$$ds^2 = \frac{\ell^2}{z^2}\left[dz^2 + \left(1+\frac{z^d}{b^d}\right)^{4/d}\left(dx^2+\delta_{ij}dy^i dy^j\right) + \alpha_d^2 b^2\left(1-\frac{z^d}{b^d}\right)^2\left(1+\frac{z^d}{b^d}\right)^{\frac{4}{d}-2} d\theta^2\right], \tag{6.2}$$

where we take θ to have period 2π for all profiles $b(x)$. For the case $b = constant$, the ansatz (6.2) gives the metric on the Euclidean planar AdS-Schwarzschild black hole (or, equivalently, on the Euclidean AdS soliton). The full metric is then taken to be of the form

$$ds^2 = \frac{\ell^2}{z^2}\left(g^{(0)}_{AB}\,dx^A dx^B + \epsilon\, g^{(1)}_{AB}\,dx^A dx^B + \epsilon^2\, g^{(2)}_{AB}\,dx^A dx^B + \cdots\right), \tag{6.3}$$

where the corrections $g^{(n)}_{AB}$ are determined by solving Einstein's equation with appropriate boundary conditions at each order in an adiabatic expansion and $x^A = (z, x, y^i, \theta)$ ranges over all bulk coordinates and similarly for x^B. As shown in [30], the $O(\epsilon)$ correction $g^{(1)}_{AB}$ vanishes and, writing $g_{y^i y^j} = g_{yy}\delta_{ij}$, the $O(\epsilon^2)$ correction is of the form

$$\begin{aligned}
g^{(2)}_{xx}(z,x) &= (b'(x))^2\, \mathfrak{g}^{(b')^2}_{xx}(z/b) + (b(x)b''(x))\, \mathfrak{g}^{(bb'')}_{xx}(z/b),\\
g^{(2)}_{yy}(z,x) &= (b'(x))^2\, \mathfrak{g}^{(b')^2}_{yy}(z/b) + (b(x)b''(x))\, \mathfrak{g}^{(bb'')}_{yy}(z/b),\\
g^{(2)}_{\theta\theta}(z,x) &= \alpha_d^2\left[(b(x)\,b'(x))^2\, \mathfrak{g}^{(bb')^2}_{\theta\theta}(z/b) + b(x)^3\, b''(x)\; \mathfrak{g}^{(b^3 b'')}_{\theta\theta}(z/b)\right].
\end{aligned} \tag{6.4}$$

Here the notation makes explicit all dependence on $b(x)$; there can be no further implicit dependence hidden in form of the coefficient functions $\mathfrak{g}^{(b')^2}_{xx}(z/b)$, etc. These coefficient functions were evaluated numerically in [30] with boundary conditions that ensure that the boundary metric remains (5.9) and that the spacetime remains regular at the fixed point set of ∂_θ (with the period of θ taken to be 2π independent of $b(x)$).

Below, we use the results of [30] to calculate $O(\epsilon^2)$ corrections to the holographic entanglement entropy. We also make use of two further results from [30]. The first is that, for $d > 2$, in the adiabatic expansion the Fefferman-Graham representation of our metrics takes the form

$$ds^2_{z\ll b} = \frac{\ell^2}{z^2}\left[dz^2 + \alpha_d^2\left(b^2 + \epsilon^2\frac{b\,b''}{d-1}z^2\right)d\theta^2 + \left(1+\epsilon^2\frac{b''}{b(d-1)}z^2\right)dx^2 + \left(1-\epsilon^2\frac{b''}{b(d-2)(d-1)}z^2\right)dy^i dy_i + O(z^d,\epsilon^4)\right]. \tag{6.5}$$

The special case $d = 2$ is treated in appendix 6.A. The second is that near the fixed point set of ∂_θ the metric takes the form

$$ds^2 = g_{RR}|_{R=0}\left(dR^2 + R^2 d\theta^2\right) + g_{XX}|_{R=0}dX^2 + g_{YY}|_{R=0}\sum_{i=1}^{d-2} dY^i dY^i + O(R^2), \tag{6.6}$$

with $g_{RR}|_{R=0}, g_{XX}|_{R=0}, g_{YY}|_{R=0}$ functions of X alone, in terms of coordinates X, R that satisfy

$$\begin{aligned} z &= (1-R)b - \epsilon^2\,\frac{1}{3}16^{-1/d}b\left(b'^2 + \frac{2}{\alpha_d^2 d^2}\;\partial_z^2 g^{(2)}_{\theta\theta}\Big|_{z=b}\right) + O(\epsilon^3) \\ x &= X + \epsilon\,16^{-1/d}\,b\,b'\left(R + \frac{1}{2}R^2 - \frac{1}{6}(d-2)R^3\right) + O(\epsilon^3, R^4). \end{aligned} \tag{6.7}$$

The key point of (6.6) is that it ensures the desired regularity at $R = 0$ (where $\partial_\theta = 0$). In terms of the Fefferman - Graham coordinates this set is described by $z = \tilde{b}$ where

$$\tilde{b} = b - \frac{\epsilon^2}{2}\,b^2\,\partial_z g^{(2)}_{\theta\theta}\Big|_{z=b}\,. \tag{6.8}$$

This is the black hole horizon for the adiabatic thermofield double interpretation and the IR floor for the confining one.

6.3 Adiabatic Thermofield Doubles

We begin with the adiabatic thermal field double (ATFD) states defined by slicing our CFT path integral along the surfaces $\theta = 0, \theta = \pi$ fixed by the reflection symmetry $\theta \to -\theta$. It is convenient to denote the union of these two surfaces by C_{CFT}. A slight generalization of the Ryu-Takayangi proposal [23, 24] then states that the von Neumann entropy of the CFT in some region $\mathcal{R}_{CFT} \subset C_{CFT}$ can be computed as follows. First, find the dominant saddle for the corresponding bulk path integral. One expects it to be invariant under a corresponding reflection, and that this reflection leaves fixed a co-dimension one surface that we may call C_{bulk}. Now find the minimal-area surface Σ within C_{bulk} that i) intersects the asymptotically AdS boundary on a set corresponding to the boundary $\partial\mathcal{R}_{CFT}$ of $\mathcal{R}_{CFT}$ and ii) is homologous to $\mathcal{R}_{CFT}$ within C_{bulk} [53, 74]. Since the Lewkowycz-Maldacena argument [75] for the Ryu-Takayanagi proposal applies equally well to this generalization, we shall use it freely below[1]. We also note that the above prescription is equivalent to using the the covariant Hubeny-Rangamani-Takayanagi conjecture [43] in the Wick-rotated Lorentz-signature solution[2].

For simplicity, we consider slab-shaped regions $\mathcal{R}_{CFT}$ defined by conditions of the form $|x - x_0| \leq L$, perhaps also restricted to one of the two boundaries ($\theta = 0$ or $\theta = \pi$). The symmetries then reduce the problem of finding the minimal surface to studying curves in the z, x plane, with the area being proportional to the volume of the y directions. For purposes of displaying a finite result we take the y coordinates to range over a torus of finite volume V. Since we are interested in the decompactified limit, we

[1] See [76] for a discussion of the homology constraint in the context of the Lewkowycz-Maldacena argument.

[2] We thank Veronika Hubeny for pointing out that this follows from the maximin construction of [62]. Since the RT surface is minimal on the Cauchy surface C_{bulk}, its area can be no larger than that of the maximin surface. But the time-reversal symmetry means that the RT surface is also an extremal surface in the full spacetime. It can therefore have area no smaller than the maximin surface, as the latter agrees with the area of the smallest extremal surface.

will always assume each cycle of the y-torus to have length much larger than both b and L. In particular, we assume that the dominant bulk saddle will continue to be given by (6.2).

A technical issue is that the area nevertheless remains infinite due to the divergence of the metric (6.2) at $z = 0$. As usual, we must renormalize this quantity in order to present finite results. Thus we define

$$A_{\rm ren} = \lim_{z_0 \to 0} \left(A_{\rm bare}(z_0) + \sum_{\partial\Sigma} A_{\rm ct}(z_0) \right), \tag{6.9}$$

where $A_{\rm bare}(z_0)$ is the area of the part of the surface with $z > z_0$ and where there is one counter-term contribution $A_{\rm ct}(z_0)$ for each boundary of the minimal surface Σ.

The general theory of such divergences is explained in [77], which shows that when the bulk is described by pure Einstein-Hilbert gravity (with no additional matter fields) one may use counter-terms determined by the boundary metric alone[3], though these generally involve both the induced geometry on $\partial\Sigma$, the extrinsic curvature of $\partial\Sigma$ [79, 80], and even derivatives of such extrinsic curvatures [81] in high enough dimensions. See also [82] for a recent discussion of such counter-terms and their relation to [75].

To find a useful explicit form for our $A_{\rm ct}(z_0)$, we first write the area functional as

$$A_{\rm bare} = V\, \ell^{d-1} \int_\lambda \mathcal{A}_{\rm bare} d\lambda \tag{6.10}$$

with

$$\mathcal{A}_{\rm bare} = g_{yy}^{\frac{1}{2}(d-2)} \left(\frac{z'(\lambda)^2}{z(\lambda)^2} + x'(\lambda)^2 g_{xx} \right)^{1/2} \tag{6.11}$$

for any parameter λ along the associated curve in the z, x plane.

[3]Interestingly, this is not true in general; see [78].

Near $z = 0$ it is useful to set $\lambda = z$ and assume an adiabatic expansion of the form

$$x(\lambda) = x^{(0)}(\lambda) + \epsilon\, x^{(1)}(\lambda) + \cdots . \tag{6.12}$$

The behavior of $x^{(0)}$ near $z = 0$ is determined by the minimal surface equation of motion at order ϵ^0. This may be written

$$\begin{aligned} 0 &= \left((d+1)z^d - (d-1)b^d\right) x^{(0)\prime}(z) - (d-1)\left(b^d - z^d\right)\left(1 + z^d/b^d\right)^{4/d}\left(x^{(0)\prime}(z)\right)^3 \\ &+ z\left(b^d + z^d\right) x^{(0)\prime\prime}(z). \end{aligned} \tag{6.13}$$

Equation (6.13) admits a power series solution of the form

$$x^{(0)}(z) = c_0 + c_d z^d + c_{2d} z^{2d} + \cdots \tag{6.14}$$

Indeed, the result takes the form (6.14) in any metric having the same non-zero coefficients in its Fefferman-Graham expansion. Since $g^{(1)}_{AB} = 0$, at order ϵ the ansatz (6.2) continues to give the full metric. Noting that the endpoint conditions $x(z = 0) = x_0 \pm L$ are independent of ϵ then also gives

$$x^{(1)}(z) = \tilde{c}_d z^d + O(z^{d+1}). \tag{6.15}$$

So near $z = 0$ the area density (6.11) becomes

$$\mathcal{A}_{\text{bare}} = \frac{1}{z^{d-1}} + \frac{1}{2}\frac{\epsilon^2}{z^{d-1}}(d-2)g^{(2)}_{yy} + O(z^0, \epsilon^3), \tag{6.16}$$

as any factors $x^{(0)\prime}(z)$ or $x^{(1)}(z)$ are of order z^d and give corrections that vanish as $z \to 0$.

Combining the Fefferman-Graham expansion of the second order metric correction

(6.5) with the results above we find

$$\mathcal{A}_{\rm bare} = \frac{1}{z^{d-1}} - \frac{\epsilon^2}{2(d-1)} \frac{b''}{b} \frac{1}{z^{d-3}} + O(z^0, \epsilon^3), \tag{6.17}$$

so we may choose

$$A_{\rm ct} = V\, \ell^{d-1} \left[-\tfrac{1}{(d-2)} \tfrac{1}{z_0^{d-2}} + \epsilon^2 \tfrac{1}{2\,(d-1)(d-4)} \tfrac{b''}{b} \tfrac{1}{z_0^{d-4}} \right] \qquad d \neq 2, 4 \tag{6.18}$$

There are no explicit $O(\epsilon)$ counter-terms since $g^{(1)}_{AB} = 0$. One may check that this choice of counterterms precisely implements the covariant counterterm prescription of [82] to $O(\epsilon^2)$. Following this prescription, the counterterms in $d = 4$ will include a logarithmic as well as a constant piece, and in $d = 2$ we only have the logarithmic piece. These terms are given by

$$\begin{aligned} A_{\rm ct} &= V\, \ell^3 \left[-\tfrac{1}{2} \tfrac{1}{z_0^2} - \epsilon^2 \tfrac{1}{6} \tfrac{b''}{b} \log(z_0/\ell) + \epsilon^2 \tfrac{1}{12} \tfrac{b''}{b} \right] \quad , && d = 4 \\ A_{\rm ct} &= \ell\, \log(z_0/\ell) \quad , && d = 2 \end{aligned} \tag{6.19}$$

where no factor of V appears in $d = 2$ because there are no y-directions.

For $d = 3$, the second counter-term in (6.19) vanishes; we nevertheless find that including it in the manner explained below improves the convergence of our numerics.

In practice, we find it convenient to renormalize in the following way. Let $\mathcal{A}_{\rm ct} = -\,\partial_{z_0} A_{\rm ct}|_{z_0 = z}$. Then we can write

$$A_{\rm ct} = \int_{z_0}^{z_{\rm max}} \mathcal{A}_{\rm ct}\, dz + A_{\rm ct}|_{z_0 = z_{\rm max}} \tag{6.20}$$

for any z_{max}. In particular, we can take z_{max} to be the maximal value of z on our bulk

extremal surface. The renormalized area (6.9) can then be written

$$\begin{aligned} A_{\rm ren} &= \lim_{z_0 \to 0} \int_{z_0}^{z_{\rm max}} \left(V \, \ell^{d-1} \mathcal{A}_{\rm bare} + \sum_{\partial\Sigma} \mathcal{A}_{\rm ct} \right) dz + \sum_{\partial\Sigma} A_{\rm ct}|_{z_0 = z_{\rm max}} \ , \\ &= \int_0^{z_{\rm max}} \left(V \, \ell^{d-1} \mathcal{A}_{\rm bare} + \sum_{\partial\Sigma} \mathcal{A}_{\rm ct} \right) dz + \sum_{\partial\Sigma} A_{\rm ct}|_{z_0 = z_{\rm max}} \ . \end{aligned} \tag{6.21}$$

The integral in the second line now converges, and is more stable to compute numerically. The price we pay is having to add the constant term involving $z_{\rm max}$. For $d = 3$, we find that including the second (vanishing!) counter-term in (6.19) in this way improves our numerical convergence. This appears to be due to the fact that we perform these integrals by changing variables to integrate over x instead of z, and that the above renormalization removes an (integrable) singularity in the integrand that arises from the associated factor of $z'(x)$.

We are now ready to compute the entropies of our slabs $|x - x_0| \leq L$. For slabs contained in a single boundary, we know on general grounds that the minimal surface will remain close to the conformal boundary when $L \ll b$ while for $L \gg b$ it will track the horizon closely over almost all of the interval $|x - x_0| \leq L$. The transition between these behaviors is smooth. But if we take our slab to contain the regions $|x - x_0| \leq L$ on both the $\theta = 0$ and $\theta = \pi$ boundaries one finds a well-known phase transition [83, 53, 43, 84] when passing from the regime $L \ll b_0$ to the regime $L \gg b$. In the former case, the minimal surface consists of two copies of that found in the single-boundary case. In the latter case the minimal surface again has two connected components, but each component then stretches from $\theta = 0$ to $\theta = \pi$ while remaining localized near $x = x_0 \pm L$. This is the only context in which the minimal surface reaches or passes through the fixed point set of ∂_θ. In each case we find the general solution numerically below and compare it with analytic approximations for $L \ll b$ and $b(\epsilon \, b')^{-1} \gg L \gg b$. We also provide results

for the case $L \gg b(\epsilon\, b')^{-1} \gg b$. The effect on the phase transition itself is analyzed in section 6.3.3.

6.3.1 Entropy on a single boundary

We begin with connected slab-shaped regions $\mathcal{R}_{CFT}$ of width $2L$ lying in a single boundary. For generic values of the parameters, numerical calculations are required to find the extremal surface. But certain limiting behaviors can be studied analytically. We treat these cases first, and then compare the results with numerical studies of the general case. In the rest of this section, we set $x_0 = 0$ without loss of generality.

Analytically tractable limits

Our first special case will be the large L limit, as the fact that the minimal surface closely tracks the horizon in this regime makes it particularly easy to study. To leading order in L, the renormalized area is just the horizon area in the region $|x| \leq L$. Using the induced metric on the horizon found in [30] gives

$$S \;= \tfrac{V\,\ell^{d-1}}{4G} \int_{-L}^{L} dx \left[\tfrac{2^{2-2/d}}{b^{d-1}} + \epsilon^2\, \tfrac{2^{1-6/d}}{b^{d-1}} \left((d-2)\, g^{(2)}_{yy}\Big|_{z=b} + g^{(2)}_{xx}\Big|_{z=b} + b'^2 \right) + O(\epsilon^4) \right] + \ldots, \quad (6.22)$$

where the $\ldots$ represent terms that do not grow with L when b remains bounded.

For L larger than or comparable to $b/(\epsilon\, b')$, nothing more can be said without choosing an explicit function $b(\epsilon x)$. But in the regime $b/(\epsilon\, b') \gg L \gg b$ we may define $b_0 = b(0)$, $b_0' = \partial_x b|_{x=0}$, and $b_0'' = \partial_x^2 b|_{x=0}$ and use the expansion

$$b = b_0 + \epsilon\, x\, b_0' + \frac{1}{2}\epsilon^2\, x^2\, b_0'' + O(\epsilon^3) \quad (6.23)$$

to simplify (6.22). Writing $A_{\rm ren} = A^{(0)}_{\rm ren} + \epsilon^2 A^{(2)}_{\rm ren} + \ldots$, we find

$$A^{(0)}_{\rm ren}\big|_{L\gg b_0} \sim 2^{3-2/d}\frac{V\,\ell^{d-1}}{b_0^{d-1}}L, \quad A^{(2)}_{\rm ren}\big|_{L\gg b_0} \sim \frac{1}{3}2^{2-\frac{2}{d}}(d-1)\frac{V\,\ell^{d-1}}{b_0^{d+1}}\left(d\,{b_0'}^2 - b_0 b_0''\right)L^3, \quad (6.24)$$

where $\sim$ indicates that we have found only the leading behavior for $L \gg b_0$. Here we were able to obtain an analytic expression at order ϵ^2 because the L^3 term comes only from the $O(\epsilon^2)$ term in (6.23) and thus can involve the metric only at order ϵ^0 as given by (6.2).

For $L \ll b_0$ the minimal surfaces will be confined to $z \ll b_0$, so we can estimate their area by truncating the Fefferman - Graham expansion (6.5) for the metric to some order in z. The Fefferman - Graham expansion for $d = 2$ has a non-trivial contribution from the boundary stress tensor at order z^2, so we treat this case separately in appendix 6.A.

Consulting the expansion (6.5), we see that to zeroth order in the adiabatic expansion we have Poincaré AdS_{d+1}. So for $d > 2$ we find

$$A^{(0)}_{\rm ren} = -\frac{2\pi^{\frac{d-1}{2}}}{d-2}\left(\frac{\Gamma\left(\frac{d}{2(d-1)}\right)}{\Gamma\left(\frac{1}{2(d-1)}\right)}\right)^{d-1}\frac{V\,\ell^{d-1}}{L^{d-2}} + O(L^2). \quad (6.25)$$

This leading term reproduces the standard result for slabs in Poincaré AdS_{d+1} as derived in [23].

Since $d\theta = 0$ on the surface of time reflection symmetry, the truncated induced metric (6.5) depends on b only at order ϵ^2 and there can be no $O(\epsilon)$ correction to the minimal surface or its area. And the fact that the zero-order surface is minimal means that there is no correction at order $O(\epsilon^2)$ from the second-order displacement of the surface within the zeroth-order spacetime. Thus the only $O(\epsilon^2)$ contribution comes from evaluating the change in the area along the zeroth-order minimal surface that comes from including the $O(\epsilon^2)$ parts of (6.5). This correction can be computed from the integral representation

of the hypergeometric function found in equation (15.6.3) of [85] and yields

$$A^{(2)}_{\rm ren} = \frac{\pi^{\frac{d}{2}-2}\, {}_2F_1\left(\frac{1}{2}, -\frac{d-4}{2(d-1)}; \frac{d+2}{2(d-1)}; 1\right)}{3(d-4)} \left(\frac{\Gamma\left(\frac{d}{2d-2}\right)}{\Gamma\left(\frac{1}{2d-2}\right)}\right)^{d-4} \frac{b_0''}{b_0} \frac{V\,\ell^{d-1}}{L^{d-4}} + O(L^4)\,, \tag{6.26}$$

for $d > 2, d \neq 4$ and

$$A^{(2)}_{\rm ren} = \left[\frac{1}{18}\left(5 + \log\left[\frac{\pi^3\,\Gamma\left(\frac{2}{3}\right)^6}{4\,\Gamma\left(\frac{1}{6}\right)^6}\right]\right) - \frac{1}{3}\log L\right] \frac{b_0''}{b_0} V\ell^3 + O(L^4) \qquad \text{for } d = 4\,. \tag{6.27}$$

Numerics and comparisons

We now consider general values of $L \ll 1/(\epsilon\, b')$. This allows us to again use (6.23) so that the results can depend only on the parameters b_0, b_0', and b_0''. For $d \neq 2, 4$ we write

$$A_{\rm ren} = \frac{V\,\ell^{d-1}}{b_0^{d-2}} \mathsf{A}(L/b_0), \tag{6.28}$$

where the function form of $\mathsf{A}(L/b_0)$ is determined only by dimensionless combinations of b and its derivatives. For $d = 2$ and $d = 4$ it is useful to subtract the logarithmic dependence on ℓ coming from the regularization scheme (6.19) and write

$$\begin{aligned} A_{\rm ren} &= \ell\, \mathsf{A}(L/b_0) + \ell\, \log(b_0/\ell)\,, & d = 2 \\ A_{\rm ren} &= \frac{V\,\ell^3}{b_0^2} \mathsf{A}(L/b_0) - \epsilon^2\, V\, \ell^3 \frac{1}{6} \frac{b_0''}{b_0}\, \log(b_0/\ell)\,. & d = 4\,. \end{aligned} \tag{6.29}$$

We may then use the adiabatic expansion to write

$$\mathsf{A}(L/b_0) = \mathsf{A}^{(0)}(L/b_0) + \epsilon\, \mathsf{A}^{(1)}(L/b_0) + \epsilon^2\, \mathsf{A}^{(2)}(L/b_0) + O(\epsilon^3)\,. \tag{6.30}$$

Now, the correction $\mathsf{A}^{(1)}(L/b_0)$ would have to be proportional to the first-order adiabatic parameter b_0'/b_0. But the sign of this parameter changes under $x \to -x$ whereas the area must be invariant. So there can be no correction at this order. We thus consider only the second order corrections, which must be linear in the two dimensionless second-order adiabatic parameters $(b_0')^2$ and $b_0\, b_0''$; i.e., we have

$$\mathsf{A}^{(2)}(L/b_0) = (b_0')^2 \mathsf{A}^{(b')^2}(L/b_0) + b_0\, b_0'' \mathsf{A}^{(bb'')}(L/b_0), \tag{6.31}$$

with $\mathsf{A}^{(b'^2)}, \mathsf{A}^{(bb'')}$ having no further dependence on $b(x)$.

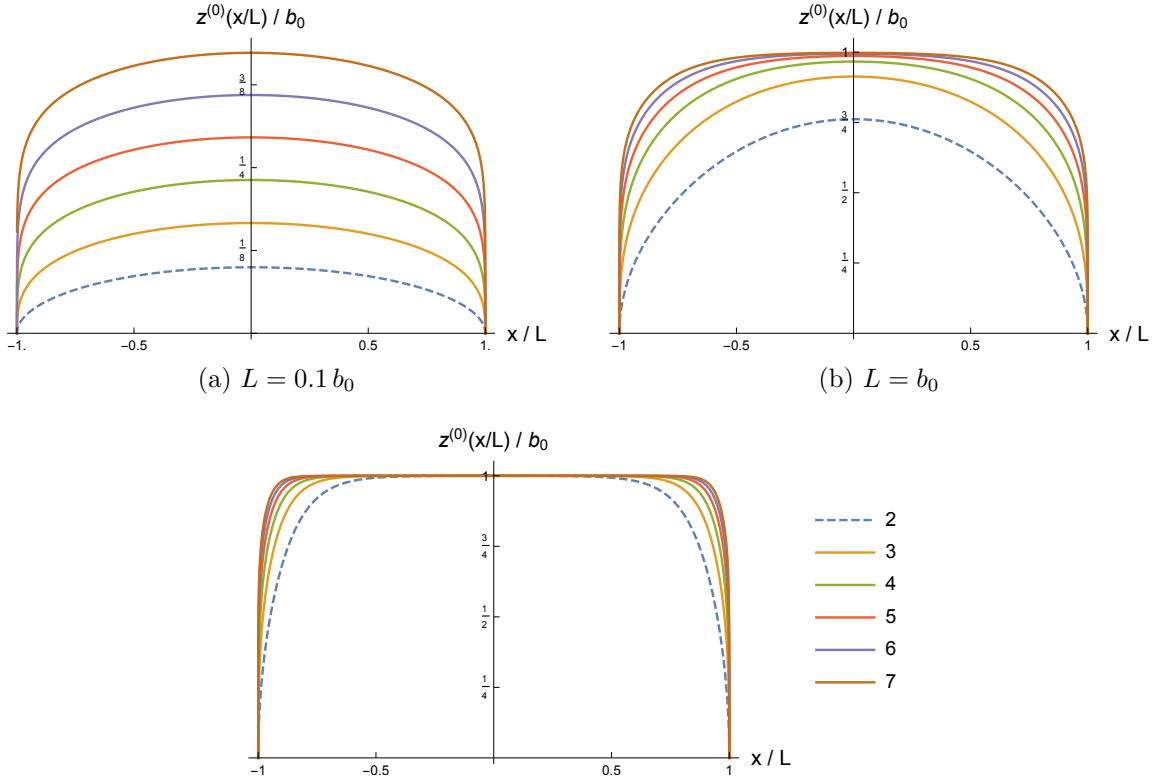

(a) $L = 0.1\, b_0$ (b) $L = b_0$

(c) $L = 5\, b_0$

Figure 6.1: Numerical solutions for $z^{(0)}(x/L)/b_0$ for slabs of width $2L$ on a single boundary with $2 \leq d \leq 7$. As L increases from (a) to (c), the entangling surface quickly approaches the horizon as expected.

Even at order ϵ^0 we require numerics to solve for the surface that extremizes the

area (6.11). We use the Newton-Raphson method outlined in [32]. Figure 6.1 shows the solution for $z^{(0)}(x/L)/b_0$ with $2 \leq d \leq 7$ and various interval sizes. Results for the zeroth order area are shown in figure 6.2.

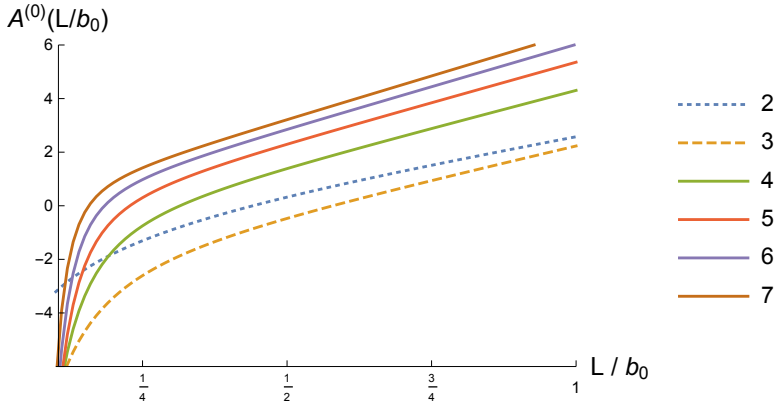

Figure 6.2: The rescaled zeroth order area $\mathsf{A}^{(0)}(L/b_0)$ for slabs of width $2L$ on a single boundary with $2 \leq d \leq 7$. The curves interpolate between a power law proportional to $-(b_0/L)^{d-2}$ for $L \ll b_0$ and linear growth for $L \gg b_0$ where the entangling surface tracks the horizon closely. For $d = 2$ the small L/b_0 behavior is logarithmic.

Computing the second order change in area (6.31) requires only knowledge of the surface to $O(\epsilon)$. This is because the order-zero surface is minimal, so changes in the area computed with with zeroth order metric are quadratic in changes of the surface. The first order equation of motion is complicated, but is straightforward to work out and can be solved numerically by the same techniques as at order ϵ^0. Results for $z^{(1)}(x/L)/(b_0\, b_0')$ are shown in figure 6.3 for various dimensions and interval sizes. The second order correction to the area then follows by summing the following three contributions: the above-mentioned quadratic change in the area computed using the zeroth-order metric due to the shift in the minimal surface at $O(\epsilon)$, the change in the area of the zeroth-order minimal surface due to the inclusion of $O(\epsilon^2)$ terms in the metric, and a cross-term linear in both the $O(\epsilon)$ shift of the surface and the $O(\epsilon)$ correction to the metric. In terms of

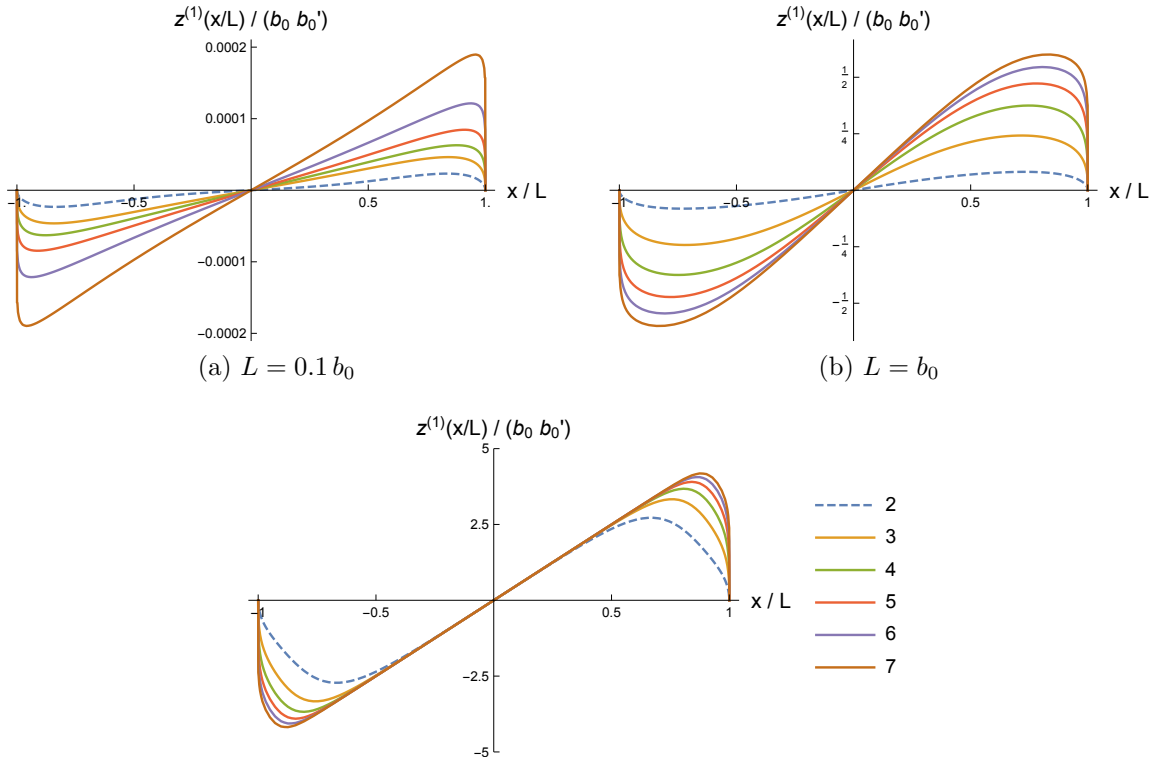

(a) $L = 0.1\, b_0$ (b) $L = b_0$

(c) $L = 5\, b_0$

Figure 6.3: Numerical solutions for $z^{(1)}(x/L)/(b_0\, b_0')$ for slabs of width $2L$ on a single boundary with $2 \leq d \leq 7$. Away from the end points, increasing L causes $z^{(1)}(x/L)$ to approach the first order correction to the horizon location. Since $g^{(1)}_{AB}$ vanishes identically, this correction comes only from expanding $b = b_0 + b_0' x + \ldots$ within the zeroth order ansatz. This correction is thus linear in x, given in this approximation by $z^{(1)}_H(x) = b_0'\, x$.

the densitized area $\mathcal{A}_{\text{ren}}$, this correction takes the form

$$\begin{aligned} A^{(2)}_{\text{ren}} =& \frac{1}{2}\int dx \left[\left(\frac{\partial^2 \mathcal{A}^{(0)}_{\text{ren}}}{\partial z^2} - \frac{d}{dx}\left(\frac{\partial^2 \mathcal{A}^{(0)}_{\text{ren}}}{\partial z\, \partial z'} \right) \right) \Bigg|_{z^{(0)}(x)} \left(z^{(1)}(x) \right)^2 + \frac{\partial^2 \mathcal{A}^{(0)}_{\text{ren}}}{\partial z'^2} \Bigg|_{z^{(0)}(x)} \left(z^{(1)\prime}(x) \right)^2 \right] \\ &+ \int dx \left[\left(\frac{\partial \mathcal{A}^{(1)}_{\text{ren}}}{\partial z} - \frac{d}{dx}\left(\frac{\partial \mathcal{A}^{(1)}_{\text{ren}}}{\partial z'} \right) \right) \Bigg|_{z^{(0)}(x)} z^{(1)}(x) \right] \\ &+ \int dx\, \mathcal{A}^{(2)}_{\text{ren}} \big|_{z^{(0)}(x)} \,, \end{aligned} \tag{6.32}$$

where each line corresponds to one of the above three contributions described above. Numerical results are shown in figure 6.4.

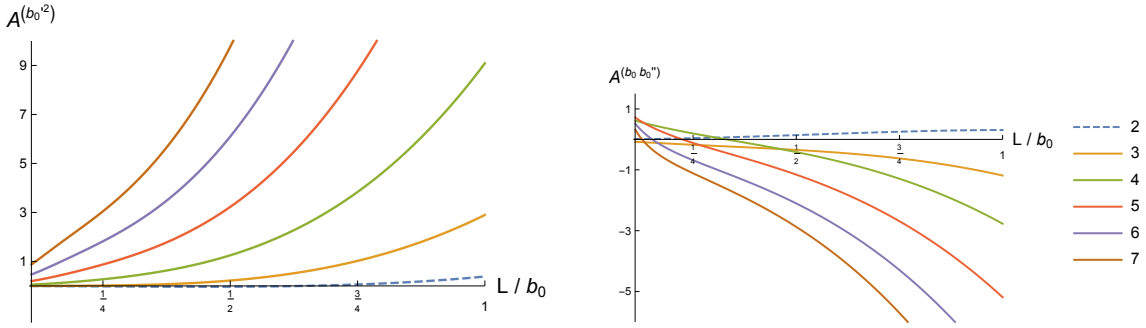

(a) (b)

Figure 6.4: Plots of (a) $\mathsf{A}^{(b_0'^2)}(L/b_0)$ and (b) $\mathsf{A}^{(b_0 b_0'')}(L/b_0)$ for slabs of width $2L$ on a single boundary with $2 \leq d \leq 7$.

As a check on our numerics, we now compare with the analytic expressions of section (6.3.1). We first consider the case $b/(\epsilon\, b') \gg L \gg b_0$. At order ϵ^0 we numerically compute $b_0\, \mathsf{A}^{(0)}/L$ for large L/b_0, while at order ϵ^2 we compute $b_0^3\, \mathsf{A}^{(2)}/L^3$. Results are tabulated in figure 6.5 which shows agreement with (6.24).

d	$b_0\, \mathsf{A}^{(0)}/L$	Pred.	$b_0^3\, \mathsf{A}^{(b_0'^2)}/L^3$	Pred.	$-b_0^3\, \mathsf{A}^{(b_0 b_0'')}/L^3$	Pred.
2	4.000	4.000	1.33	1.33	0.667	0.667
3	5.04	5.04	5.04	5.04	1.68	1.68
4	5.66	5.66	11.3	11.3	2.83	2.83
5	6.06	6.06	20.2	20.2	4.04	4.04
6	6.35	6.35	31.7	31.7	5.29	5.29
7	6.56	6.56	45.9	45.9	6.56	6.56

Figure 6.5: Comparison of the numerically computed $L \gg b_0$ scaling of $\mathsf{A}(L/b_0)$ (left colums) from figure 6.4 with the predictions (Pred., right columns) from (6.24) for $2 \leq d \leq 7$. The numerical precision is at least three significant figures, estimated by comparing results for 100 and 150 lattice points and for fitting intervals $L/b_0 \in [40, 50]$ and $L/b_0 \in [50, 60]$

Turning now to the case $L \ll b_0$, we have verified that the coefficient of $\mathsf{A}^{(2)}$ proportional to $b_0'^2$ vanishes quadratically as $L \ll b_0$, and we may also numerically compute the $b_0\, b_0''$ contribution to $\lim_{L\to 0} L^{d-4}\mathsf{A}^{(2)}$. Our results are tabulated in figure 6.6 and shown

to agree with the analytic results (6.26) and (6.27).

d	$L^{d-2}\,\mathsf{A}^{(0)}$	Pred.	$L^{d-4}\,\mathsf{A}^{(b_0 b_0'')}$	Pred.
3	-0.718	-0.718	-0.729	-0.729
4	-0.0802	-0.0802	$-0.334\,\log L$	$-0.333\,\log L$
5	-0.00864 ± 0.00001	-0.00865	0.0897 ± 0.0020	0.0916
6	-0.000821 ± 0.000002	-0.000822	0.00850 ± 0.00039	0.00885
7	-0.0000684 ± 0.0000002	-0.0000685	0.000834 ± 0.000041	0.000871

Figure 6.6: Comparison of the numerically computed $L \ll b_0$ scaling of $\mathsf{A}(\mathsf{L}/\mathsf{b_0})$ (left colums) from figure 6.4 with the predictions (Pred., right columns) of (6.26), (6.27) for $3 \leq d \leq 7$. The numerical precision (estimated as in figure 6.5) is shown when it falls below three significant figures.

6.3.2 Entropy for pairs of diametrically opposed slabs

We now consider the entropy of a pair of corresponding slabs on opposing boundaries. Both slabs are defined by $|x - x_0| \leq L$, but one lies at $\theta = 0$ while the the other lies at $\theta = \pi$. Without loss of generality we again set $x_0 = 0$ in this section. As in [83, 84], for $L \ll b$ the minimal surface will be simply two copies of the one found in section 6.3.1, so that the mutual information between these two slabs vanishes. But for $L \gg b$ the minimal surface represents a different phase, again having two disconnected pieces but now with each localized near $x = \pm L$. Here the slabs share non-zero mutual information I. In this phase the entropy is independent of L and depends only on the local behavior of $b(x)$ near $x = \pm L$. Note that the contribution from each surface is just the entropy one would compute for a pair of half-spaces, both defined by $x > L$ (or $x < -L$) but on opposite boundaries. For simplicity we thus focus on this 'half-TFD' entropy below. All quantities associated with the half-TFD problem will be marked with hats ($\hat{}$) to distinguish them from the corresponding quantities of section 6.3.1.

As before, computing the area to order ϵ^2 requires only knowledge of the entangling

surface to first order. It thus suffices to write

$$\hat{x}(z) = \hat{x}^{(0)}(z) + \epsilon\, \hat{x}^{(1)}(z) + \cdots , \tag{6.33}$$

At zeroth order the entangling surface relevant to this half-TFD problem lies at precisely $\hat{x}^{(0)}(z) = \pm L$ and extends from one boundary to the other, passing through to the horizon. The total area at this order may be computed analytically and we find

$$\hat{A}^{(0)}_{\text{ren}} = V\, \ell^{d-1} \frac{2^{1-4/d}}{b^{d-2}} \left(\frac{d-4}{d-2}\right) \left(2 - 16^{1/d}\, {}_2F_1\left[\frac{2}{d} - 1, \frac{4}{d}; \frac{2}{d}; -1\right]\right) . \tag{6.34}$$

At first order we proceed numerically, with $\hat{x}^{(1)}(z)$ satisfying the first order equation of motion

$$\begin{aligned} 0 = {} & 2b^4(d-2)b' z^d + \left(b^d + z^d\right)\left(b^d + z^d\right)^{4/d} \partial_z^2 \hat{x}^{(1)} \\ & + \frac{1}{z}\left((d+1)z^d - (d-1)b^d\right)\left(z^d + b^d\right)^{4/d} \partial_z \hat{x}^{(1)} \end{aligned} \tag{6.35}$$

We simplify the analysis by using the symmetry that relates our two boundaries. We thus compute the area for a surface extending from one boundary to the horizon and multiply by 2. The boundary conditions are that $\hat{x} = \pm L$ at $z = 0$ and that $\frac{d\hat{x}}{dR} = 0$ at the horizon $R = 0$, where R is the regular coordinate associated with (6.6). But since it is convenient to work in terms of the original z coordinate, we note that to order ϵ this is equivalent to imposing the boundary condition

$$\hat{x}'(z)\big|_{z=b} = -\frac{\epsilon}{16} b\, b' . \tag{6.36}$$

We solve numerically for the minimal surface in the region $z \in [0, b]$ and simply approximate $\hat{x}(z)$ by $\hat{x} = \pm L$ in the order ϵ^2-sized region $z \in [b, \tilde{b}]$. Numerical solutions for

$\hat{x}^{(1)}(z/b)$ are shown in figure 6.7 for $2 \leq d \leq 7$.

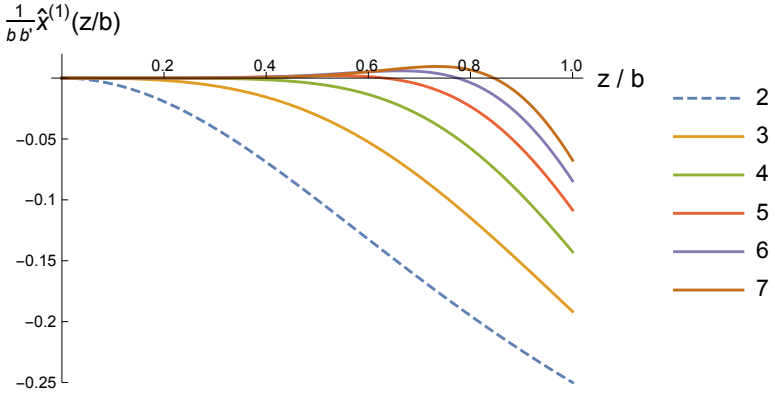

Figure 6.7: Numerical solutions $\frac{\hat{x}^{(1)}(z/b)}{bb'}$ for the half-TFD problem with $2 \leq d \leq 7$, with bb' evaluated at $x = \pm L$. In the large d limit, one may show analytically that this function vanishes everywhere except at the horizon.

The second order area correction now has an additional contribution due to the $O(\epsilon^2)$ shift in the endpoint of the minimal surface. This contribution can be computed analytically and the full second order shift is given by

$$\hat{A}^{(2)}_{\text{ren}} = \tilde{A}^{(2)}_{\text{ren}} + \epsilon^2 \, V \, \ell^{d-1} \frac{2^{\frac{2d-8}{d}}}{d^3 b^{d-3}} \left(2\,d \left({}_2F_1 \left[1, -\frac{2}{d}; \frac{2}{d}; -1 \right] - 3 \right) - \frac{2\sqrt{\pi}\,\Gamma\left(\frac{2}{d}\right)}{\Gamma\left(\frac{1}{2}+\frac{2}{d}\right)} \right) \partial_z g^{(2)}_{tt} \Big|_{z=b} \tag{6.37}$$

where $\tilde{A}^{(2)}_{\text{ren}}$ includes the area of only the part of the surface with $z \leq b$. Note that (6.37) depends on L only through evaluating b (and its derivatives) at $x = \pm L$. We compute (6.37) numerically. Results are displayed in figure 6.8 in terms of dimensionless coefficients defined by

$$\hat{A}^{(2)}_{\text{ren}} = \frac{V\,\ell^{d-1}}{b^{d-2}} \hat{\mathsf{A}}^{(2)}\,, \quad \text{with} \quad \hat{\mathsf{A}}^{(2)} = b'^2 \hat{\mathsf{A}}^{(b'^2)} + b\,b'' \hat{\mathsf{A}}^{(bb'')}\,, d \neq 2, 4. \tag{6.38}$$

Here b, b', b'' are evaluated at $x = \pm L$. For $d = 2, 4$ we use analogous notation but with logarithmic subtractions as in (6.29).

d	$\hat{\mathsf{A}}^{(b'^2)}$	$\hat{\mathsf{A}}^{(b\,b'')}$
2	0.00	0.00
3	0.531	-0.294
4	0.571	0.0716
5	0.815	-0.142
6	1.28	-0.562
7	1.93	-0.845

Figure 6.8: The coefficients $\hat{\mathsf{A}}^{(b'^2)}$ and $\hat{\mathsf{A}}^{(b\,b'')}$ for the half-TFD problem for $2 \leq d \leq 7$. The numerical precision is estimated by comparing results for 100 and 150 lattice points, giving better than one part in 10^{-10}.

6.3.3 Phase transition

We now analyze the transition between the $I = 0$ and $I > 0$ phases for a pair for $|x - x_0| \leq L$ slabs on opposite boundaries. In particular, we compute the effect of inhomogeneities on the critical length L_{crit}.

For this purpose, we should compare twice the area of the entangling surface for a slab $|x| \leq L$ on a single boundary with that of the sum of the surfaces for the half-TFD problems at $x = \pm L$. The phase transition will occur when L is of order b, so at small ϵ we have $L \ll b/(\epsilon b')$ and we may expand $b(\pm L)$ in (6.38) in a Taylor series. At order ϵ^0, the surfaces at $x = \pm L$ have equal area, so we can determine the zeroth order value of L_{crit} by comparing (twice) the numerical value of (6.34) for $b = b_0$ with (twice what is shown in) figure 6.2. Results are displayed in figure 6.9.

As discussed in section 6.3.1, the first order correction to the area of the connected surface vanishes. For the disconnected surfaces, we have a first order correction from expanding (6.38). But this correction is proportional to $x\, b_0'$, so the corresponding contributions cancel between the surfaces at $x = \pm L$; there can be no change in L_{crit} at first order.

At second order, we can write $L_{\rm crit} = L^{(0)}_{\rm crit} + \epsilon^2 L^{(2)}_{\rm crit}$ and solve

$$2A_{\rm ren}(L_{\rm crit}) = \hat{A}_{\rm ren}|_{x=L_c} + \hat{A}_{\rm ren}|_{x=-L_c}. \tag{6.39}$$

Here it is useful to note that Taylor expanding $\hat{A}_{\rm ren}|_{x=\pm L_c}$ and then performing our adiabatic expansion gives

$$\begin{aligned}\hat{A}_{\rm ren}|_{x=L_c} + \hat{A}_{\rm ren}|_{x=-L_c} &= 2\hat{A}_{\rm ren}|_{x=0} + L^2_{\rm crit}\partial_x^2 \hat{A}_{\rm ren}|_{x=0} + \dots \\ &= 2\hat{A}^{(0)}_{ren}|_{x=0} \\ &\quad +\epsilon^2\left(2\hat{A}^{(2)}_{ren}|_{x=0} + \left(L^{(0)}_{\rm crit}\right)^2\left[(b_0')^2\partial_b^2\hat{A}^{(0)}_{ren}|_{x=0} + b_0''\partial_b\hat{A}^{(0)}_{ren}|_{x=0}\right]\right) \\ &\quad +O(\epsilon^4).\end{aligned} \tag{6.40}$$

Solving (6.39) to order ϵ^2 then gives

$$L^{(2)}_{\rm crit} = \frac{\frac{\left(L^{(0)}_{\rm crit}\right)^2}{2}\left((b_0')^2\partial_b^2\hat{A}^{(0)}_{ren}|_{x=0} + b_0''\partial_b\hat{A}^{(0)}_{ren}|_{x=0}\right) + \hat{A}^{(2)}_{ren}|_{x=0} - A^{(2)}(L^{(0)}_{\rm crit})}{\partial_L A^{(0)}_{ren}(L/b_0)\Big|_{L^{(0)}_{\rm crit}}}. \tag{6.41}$$

Figure 6.9 displays numerical results for $2 \le d \le 7$ in terms of the coefficients defined by

$$L^{(2)}_{\rm crit}/b_0 = {b_0'}^2\,\mathsf{L}^{({b_0'}^2)} + b_0 b_0''\,\mathsf{L}^{(b_0 b_0'')}\,. \tag{6.42}$$

In addition, figure 6.10 shows result for the mutual information between the slabs using the notation

$$\begin{aligned}\hat{I} &= \frac{V\,\ell^{d-1}}{b_0^{d-2}}\hat{\mathsf{I}}(L/b_0)\,, \\ \hat{\mathsf{I}}(L/b_0) &= \hat{\mathsf{I}}^{(0)}(L/b_0) + \epsilon^2\left({b_0'}^2\,\hat{\mathsf{I}}^{({b_0'}^2)}(L/b_0) + b_0 b_0''\,\hat{\mathsf{I}}^{(b_0 b_0'')}(L/b_0)\right)\,.\end{aligned} \tag{6.43}$$

d	$L^{(0)}_{\text{crit}}/b_0$	$\mathsf{L}^{(b_0'^2)}$	$\mathsf{L}^{(b_0 b_0'')}$
2	0.441	-0.0285	0.0143
3	0.832	-0.00532 ± 0.00027	0.00111 ± 0.00012
4	0.314	0.0132 ± 0.0004	0.00417 ± 0.00021
5	0.197	0.00305 ± 0.00048	-0.00983 ± 0.00024
6	0.155	0.00300 ± 0.00057	-0.0104 ± 0.0002
7	0.133	0.00405 ± 0.00090	-0.00912 ± 0.00032
8	0.119	0.00872 ± 0.0015	-0.00834 ± 0.00045

Figure 6.9: The coefficients governing L_{crit} to second order. The numerical precision is shown when it falls below three figures when estimated as described in appendix 6.B. The numerical result for $d = 2$ (shown) agrees with analytic predictions from appendix 6.A.

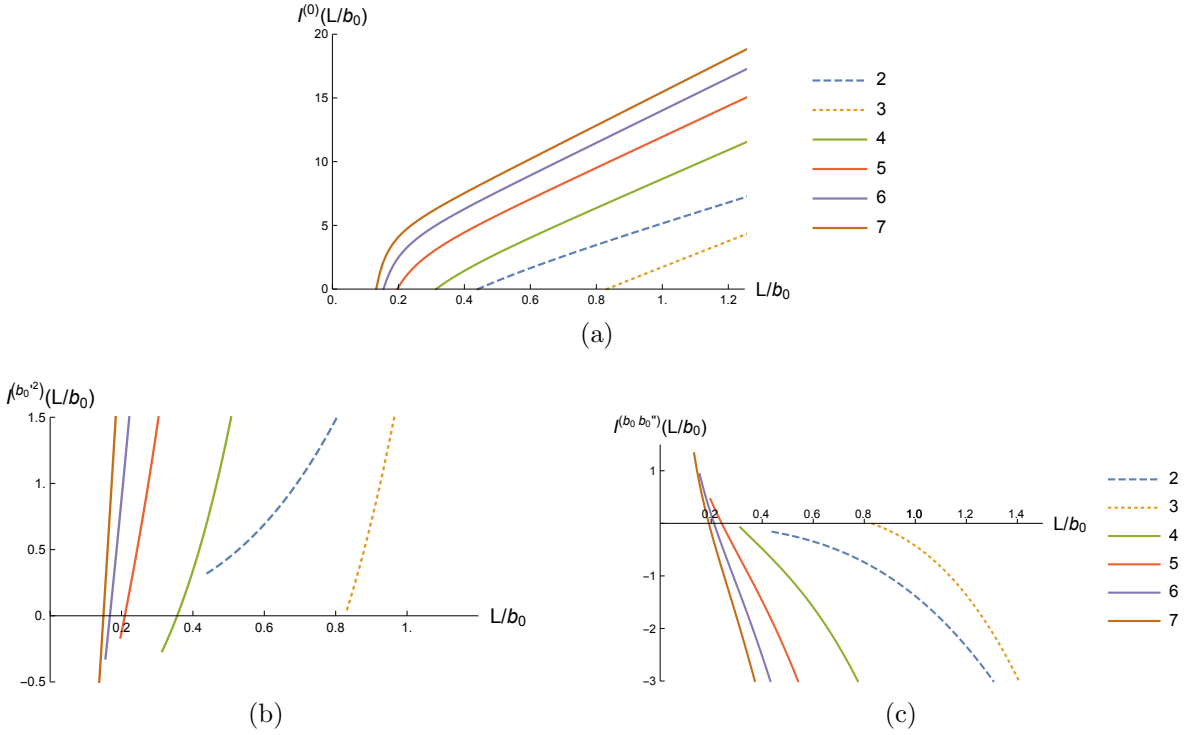

Figure 6.10: The coefficients of $\mathsf{I}(L/b_0)$ for $2 \leq d \leq 7$ to second order. The mutual information vanishes for $L < L_{\text{crit}}$.

We find to second order that $\hat{I}$ has an interesting dependence on dimension. First although $\hat{\mathsf{I}}^{(b_0'^2)}$ is positive for most $L > L_{crit}$, for $d \geq 4$ it becomes slightly negative near L_{crit}. As a result, a non-zero b_0' causes L_{crit} to increase for $d \geq 4$ and decrease for $d = 2, 3$.

The effect of second derivatives depends on dimension as well: a positive b_0'' increases $L_{\rm crit}$ for $2 \leq d \leq 4$ but decreases $L_{\rm crit}$ for $5 \leq d \leq 7$. For $d = 2$ the above behavior is derived analytically in appendix 6.A; it would be interesting to develop an analytic understanding of the higher dimensional results as well. Due to the many interesting features in this data, we take extra care to understand the convergence of our numerics in appendix B.

6.4 States of Confining Theories

We now turn to the second interpretation in which our path integral computes the ground state of a confining gauge theories on the surface $y^1 = 0$. This necessarily restricts our discussion to $d \geq 3$.

We again consider slabs $|x - x_0| \leq L$. As in section 6.3.2, there are two possible phases for the minimal surface. For $L \ll b$ the minimal surface is connected and does not reach $R = 0$. But there is also another local extremum of the area given by a disconnected surface that consists of two disks, each localized near $x - x_0 = \pm L$. At small L the disconnected surface has larger area, though increasing L leads to a phase transition at which the disconnected surface becomes minimal. Interestingly, at still larger values of L the connected extremum becomes singular and ceases to exist. The two phases are shown in figure 6.11 and will be studied in sections 6.4.1 and 6.4.2 below.

The general feature that the entanglement becomes independent of L at large L is to be expected in confining theories, as they have finite correlation lengths. But the sharp phase transition seen here is a feature of large N [86, 87].

Below, we find it useful to write

$$A_{\rm bare} = 2\pi \, \tilde{V} \, \ell^{d-1} \int \mathcal{A}_{\rm bare} \, d\lambda \quad \text{for}$$

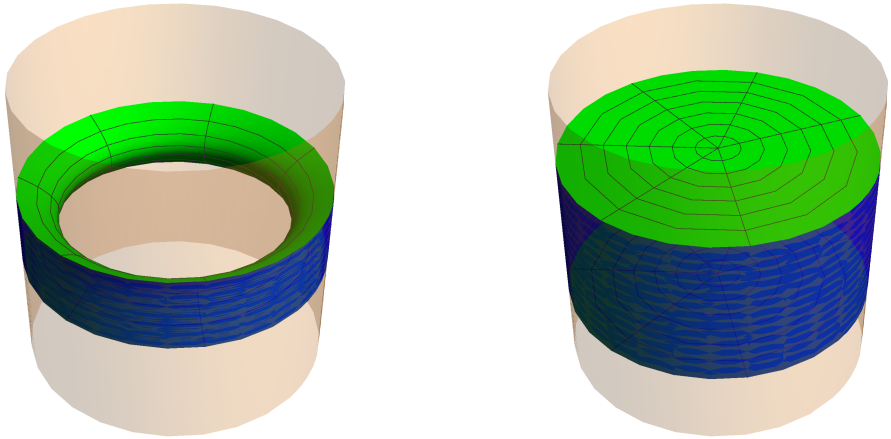

(a) (b)

Figure 6.11: Possible topologies for the extremal surfaces for a strip on the boundary. As shown in (a), for thinner strips the connected surface has minimal area. For thicker strips, the disconnected surface consisting of two disks shown in (b) has minimal area.

$$\mathcal{A}_{\text{bare}} = g_{yy}^{(d-3)/2} g_{\theta\theta}^{1/2} \left(\frac{z'(\lambda)^2}{z(\lambda)^2} + x'(\lambda)^2 \, g_{xx} \right)^{1/2} , \tag{6.44}$$

where $\tilde{V}$ is the volume of a $(d-3)$ torus that we use to regularize the $y^2, \ldots, y^{d-2}$ directions. To compute the entropy, we must as usual find the minimal surface to $O(\epsilon)$. We will also need the explicit counterterms that renormalizing the area functional to second order. The computations are analogous to those in section 6.3, though now the minimal surface equations lead to the asymptotic expansion

$$x(z) = x_B + \frac{\epsilon \, b'}{2\,(d-2)} \, z^2 + c_d \, z^d + O(z^{d+1}, \epsilon^2) \ , \tag{6.45}$$

where x_B is the point of intersection with the boundary. Inserting (6.45) into (6.44) gives

$$\mathcal{A}_{\text{bare}} = \frac{\alpha_d \, b}{z^{d-1}} - \epsilon^2 \, \frac{\alpha_d (d-3)}{2(d-2)^2} \, \frac{b'^2}{b} \, \frac{1}{z^{d-3}} + \epsilon^2 \, \frac{\alpha_d b''}{2(d-1)(d-2)} \frac{1}{z^{d-3}} + O(z^0), \tag{6.46}$$

so for $d > 4$ we may take

$$A_{\rm ct} = 2\pi \tilde{V}\, \alpha_d\, \ell^{d-1} \left[-\frac{1}{(d-2)} \frac{b}{z^{d-2}} + \epsilon^2 \frac{(d-3)}{2(d-2)^2(d-4)} \frac{b'^2}{b} \frac{1}{z^{d-4}} \right. \\ \left. -\epsilon^2 \frac{b''}{2(d-1)(d-2)(d-4)} \frac{1}{z^{d-4}} \right]. \tag{6.47}$$

In lower dimensions we have

$$A_{\rm ct} = 2\pi\, \alpha_d \tilde{V}\, \ell^3 \left[-\frac{1}{2}\frac{b}{z^2} + \epsilon^2 \left(\frac{b''}{12} - \frac{1}{8}\frac{b'^2}{b} \right) \log(z/\ell) + \epsilon^2 \left(-\frac{b''}{24} + \frac{1}{8}\frac{b'^2}{b} \right) \right] \qquad d = 4$$
$$A_{\rm ct} = -2\pi\, \alpha_d\, \ell^2 \frac{b}{z} \qquad\qquad d = 3\,, \tag{6.48}$$

where the counterterms again match the covariant prescription of [82], whose details we have again used to fix the z-independent terms for $d = 4$. We can now compute the area of the minimal surface for the regimes $L \ll b$ and $L \gg b$ and study the phase transition between connected and disconnected topologies. Additionally, without loss of generality we set $x_0 = 0$ for the rest of this section.

6.4.1 Narrow slabs

We begin with the regime $L \ll b$, where the entropy will be given by the connected surface [86, 87]. The computations proceed much as in section 6.3.1, though we are no longer able to obtain analytic results for the second order area in the large and small L limits. Indeed, this phase fails to exist at sufficiently large L, while for the small L limit the first order correction $z^{(1)}(x)$ must be computed numerically even in the approximate geometry (6.5). However, the expansion (6.5) does require the leading small L behavior of $A^{(2)}_{\rm ren}$ to be of order L^{4-d}. As a test of our numerics, we compare below the coefficient of L^{4-d} computed using the full metric against that computed using the truncated metric

(6.5). At zeroth order we can compare against an analytic prediction, as at this order (6.5) is just Poincaré AdS_{d+1} and θ acts just like a y-coordinate with period $2\pi\alpha_d b$. As a result, the area is given by (6.25) with $V = 2\pi\alpha_d\, b\, \tilde{V}$.

As in section 6.3.1, we consider the case $L \ll b/(\epsilon\, b')$ so to order ϵ^2 the inhomogeneities are described by b_0, b_0', and b_0''. We state our numerical results for the connected area in terms of the dimensionless function $\mathsf{A}_\mathsf{c}(L/b_0)$ defined for $d \neq 4$ by

$$A_{\rm ren} = \frac{2\pi\tilde{V}\,\ell^{d-1}}{b_0^{d-3}}\mathsf{A}_\mathsf{c}(L/b_0)\,. \tag{6.49}$$

where the subscript c will denote quantities associated with the connected entangling surface. For $d = 4$ it is useful to explicitly remove the $\log(\ell)$ dependence introduced by our regularization scheme. We therefore write

$$A_{\rm ren} = \frac{2\pi\tilde{V}\,\ell^3}{b_0}\mathsf{A}_\mathsf{c}(L/b_0) + \epsilon^2\, 2\pi\alpha_d\tilde{V}\,\ell^3\left(\frac{b_0''}{12} - \frac{1}{8}\frac{{b_0'}^2}{b_0}\right)\log(\ell/b_0)\,. \tag{6.50}$$

As before, we use the adiabatic expansion to write

$$\begin{aligned}\mathsf{A}_\mathsf{c}(L/b_0) &= \mathsf{A}_\mathsf{c}{}^{(0)}(L/b_0) + \epsilon\,\mathsf{A}_\mathsf{c}{}^{(1)}(L/b_0) + \epsilon^2\,\mathsf{A}_\mathsf{c}{}^{(2)}(L/b_0) + O(\epsilon^3)\\ \text{with}\;\; \mathsf{A}_\mathsf{c}{}^{(2)}(L/b_0) &= (b_0')^2\mathsf{A}_\mathsf{c}^{({b_0'}^2)}(L/b_0) + b_0\, b_0''\mathsf{A}_\mathsf{c}^{(b_0\, b_0'')}(L/b_0)\,,\end{aligned} \tag{6.51}$$

where symmetry under $x \to -x$ again requires the first order correction to vanish. Numerical results are displayed in figure 6.12.

As a check on our numerics, we extract $\lim_{L\to 0} L^{d-2}A_{\rm ren}^{(0)}$ and $\lim_{L\to 0} L^{d-4}A_{\rm ren}^{(2)}$ and compare in figure 6.13 with the same coefficients as determined by approximating the metric to $O(z^2)$ in the Fefferman - Graham expansion (6.5).

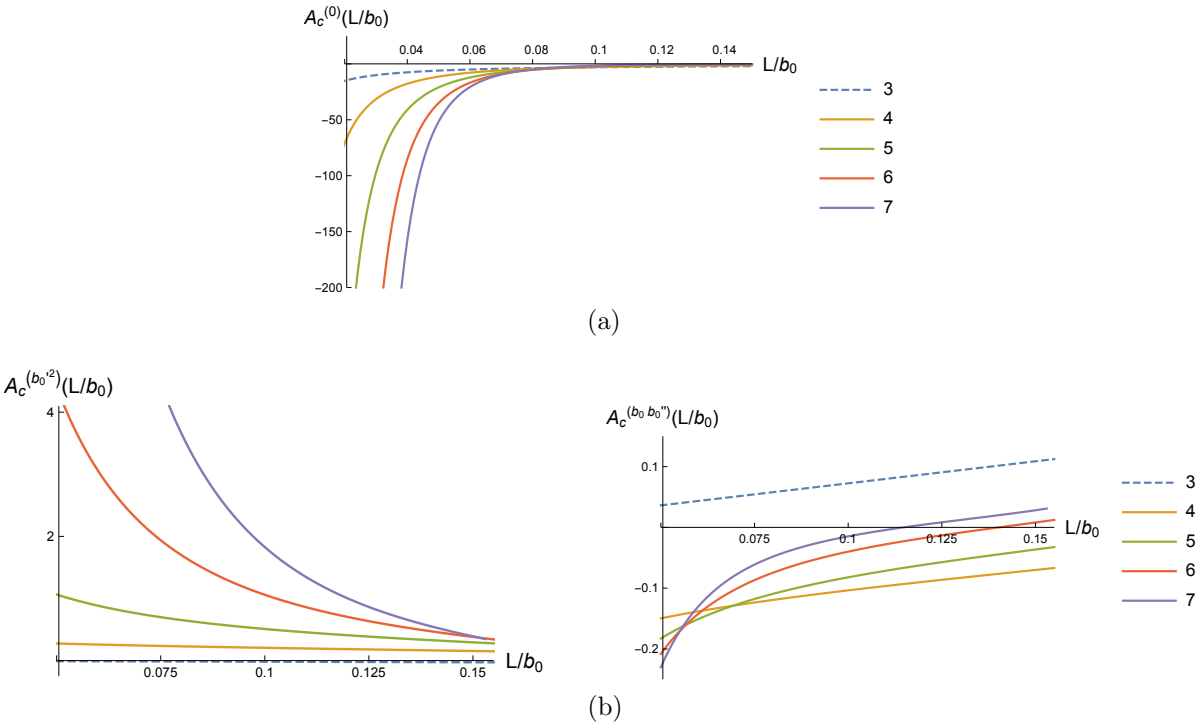

Figure 6.12: Numerical results for $\mathsf{A}_c^{(0)}(L/b_0)$, $\mathsf{A}_c^{(b_0'^2)}(L/b_0)$, and $\mathsf{A}_c^{(b_0 b_0'')}(L/b_0)$ for $3 \leq d \leq 7$.

6.4.2 Wide slabs

For $L \gg b$, the entangling surface is given by two disconnected disks each localized near $x = \pm L$. As in section 6.3.2, the entropy depends on L only through the local behavior of $b(x)$ near $x = \pm L$. Furthermore, the contribution from each surface is just the entropy one would compute for the corresponding half-space $x > L$ or $x < -L$. For simplicity we thus focus below on this notion of 'half space entropy' and choose $\mathcal{R}_{CFT}$ to be the region $x > \pm L$. Note that our geometry ends at $z = \tilde{b}$, with the extremal surface obeying the boundary condition of regularity (6.36).

The detailed computations are much as in section 6.3.2, so we simply display the results. The area of the disconnected surface can be written in terms of the dimensionless functions described in (6.49) and (6.51) after replacing $\mathsf{A_c}(L/b_0)$ with $\mathsf{A_d}$. We compute the zeroth order coefficients analytically, but the second order coefficients require numerics.

d	$\lim_{L\to 0} L^{d-2}\mathsf{A_c}^{(0)}$	Pred.
3	-0.301	-0.301
4	-0.0283	-0.0283
5	-0.00262	-0.00262
6	-0.000218	-0.000217
7	-0.0000161	-0.0000160

(a)

d	$\lim_{L\to 0} L^{d-4}\partial_{(b_0')^2}\mathsf{A_c}^{(2)}$	Approx.
3	-0.186 ± 0.003	-0.186 ± 0.003
4	-0.0828 ± 0.0006	-0.0828 ± 0.0006
5	0.0678 ± 0.0044	0.0678 ± 0.0044
6	0.0189 ± 0.0027	0.0189 ± 0.0027
7	0.00400 ± 0.00077	0.00400 ± 0.00077

(b)

d	$\lim_{L\to 0} L^{d-4}\partial_{b_0\, b_0''}\mathsf{A_c}^{(2)}$	Approx.
3	0.740 ± 0.003	0.740 ± 0.003
4	0.516 ± 0.0008	0.516 ± 0.0008
5	-0.00948 ± 0.00004	-0.00949 ± 0.00004
6	$-(5.70 \pm 0.08) \times 10^{-4}$	$-(5.70 \pm 0.08) \times 10^{-4}$
7	$-(3.49 \pm 0.12) \times 10^{-5}$	$-(3.49 \pm 0.12) \times 10^{-5}$

(c)

Figure 6.13: Comparison of the numerically computed $L \ll b_0$ scaling of $\mathsf{A(L/b_0)}$ for $3 \leq d \leq 7$ from figure 6.12 (left columns) with that determined by truncating (6.5) at order z^2 (right columns, with "Pred." and "Approx." referring to analytic and numerical results respectively). The numerical precision is shown when it falls below three significant figures, estimated by comparing results for 100 and 150 lattice points and for fitting different ranges of L depending on the dimension.

Half-space entropy results for $3 \leq d \leq 7$ are tabulated in figure 6.14 using our by-now standard notation.

6.4.3 Phase transition

Finally, we turn to the effect of adiabatic variations on the critical value L_{crit} at which the dominant phase becomes disconnected. As in section 6.3.3, we do so by comparing the area of the connected surface (figure 6.12) with the area of the disconnected surface

d	$\mathsf{A_d}^{(0)}$	$\mathsf{A_d}^{(b'^2)}$	$\mathsf{A_d}^{(b\,b'')}$
3	-0.667	-0.0882	0.0882
4	-0.354	-0.0424	0.0283
5	-0.232	-0.0875	0.0437
6	-0.167	-0.135	0.0540
7	-0.126	-0.158	0.0527

Figure 6.14: The coefficients $\mathsf{A_d}^{(0)}$, $\mathsf{A_d}^{(b'^2)}$, and $\mathsf{A_d}^{(b\,b'')}$. The numerical precision is around six significant figures, estimated by comparing results for 100 and 150 lattice points.

evaluated at $x = \pm L$ (figure 6.14). Since the phase transition occurs at $L \ll b/(\epsilon b')$, we again expand $b(x)$ in a Taylor's series to compute A_d. The second-order coefficients of of L_{crit} are again given by (6.41) with the replacements $2A_{ren} \to \mathsf{A}_c$, $\hat{A}_{ren} \to \mathsf{A}_d$. We determine $L_{\rm crit}$ numerically to second order, and display these results in figure 6.15 using the notation of (6.42).

d	$L^{(0)}_{\rm crit}/b_0$	$\mathsf{L}^{(b_0'^2)}$	$\mathsf{L}^{(b_0 b_0'')}$
3	0.249	-0.0475 ± 0.0002	0.0116 ± 0.0002
4	0.217	-0.0694	0.287
5	0.191	-0.107 ± 0.004	0.0233
6	0.170	-0.167 ± 0.017	0.0194
7	0.152	-0.237 ± 0.036	0.0157

Figure 6.15: Numerical values of $L_{\rm crit}/b_0$ and the coefficients $\mathsf{L}^{(b_0'^2)}$ and $\mathsf{L}^{(b_0 b_0'')}$ from (6.41) for the RT phase transition for slabs $|x| \leq L$ in our confined ground state with $3 \leq d \leq 7$. The numerical precision is shown when it falls below three figures, estimated by comparing results for 100 and 150 lattice points.

6.5 Discussion

In the above work, we computed the leading (second order) effects of inhomogeneities on the holographic entropy of slab-shaped regions defined by $|x - x_0| \leq L$. We studied thermofield-double states on spacetimes where the redshift changes slowly with position, and the ground states of certain confining theories with corresponding slow changes in

the confinement scale. In each case, we studied the effect on the length scale L_{crit} associated with a Ryu-Takayanagi phase transition. Most of our results were numerical, though the special case $d = 2$ (AdS_3) was treated analytically in appendix 6.A. In higher dimensions, some analytic results were also available in special limits and were used to check our numerics.

For the thermofield double, L_{crit} is a measure of the non-locality of entanglements between opposite CFTs. The second-order coefficients (figure 6.9) governing the response of L_{crit} to inhomogeneities turn out to be numerical small. Some insight as to why is provided by the analytic $d = 2$ treatment of appendix 6.A, which shows these coefficients to be proportional to $(L_{crit}/b)^3$. So the small values of L_{crit}/b lead to even smaller coefficients $\mathsf{L}^{(b_0'^2)}$, $\mathsf{L}^{(b_0 b_0'')}$.

The coefficients shown in figure 6.9 display highly non-trivial structure with respect to the dimension d. For $d \leq 3$, gradients decrease L_{crit}, while they increase L_{crit} for $d \geq 4$. This remains true whether one studies the local response to b_0' or the average change over all x. The former is precisely the sign of $\mathsf{L}^{(b_0'^2)}$ in figure 6.9. But averaging $L^{(2)}_{crit}$ over x allows one to use either periodic boundary conditions or $b \to$ *constant* as $x \to \pm\infty$ to integrate $b^2 b''$ by parts, giving a positive-definite quantity multiplied by $(\mathsf{L}^{(b_0'^2)} - 2\mathsf{L}^{(b_0 b_0'')})$. It turns out that both change sign between $d = 3$ and $d = 4$. Interestingly, it is the large d behavior that corresponds to the naive expectation that that the response is given by averaging $b(x)$ over a scale $|x - x_0| \lesssim b$, as such averaging would decrease L_{crit} near a maximum of $b(x)$ and thus require $\mathsf{L}^{(b_0 b_0'')} < 0$. This is the opposite sign to that found analytically for $d = 2$ in appendix 6.A.

One also notes that the coefficients $\mathsf{L}^{(b_0 b_0'')}$ are not monotonic with d, but appear to have a local minimum near $d = 6$. In contrast, $\mathsf{L}^{(b_0'^2)}$ appears to be monotonic in d but is also highly non-uniform. In particular, while most cases exhibit a clear increase in value with d, the coefficients for $d = 5$ and $d = 6$ are remarkably close. The in-depth analysis

of numerical convergence in appendix 6.B appear to confirm that these features are real and are not just numerical artifacts. It would be useful to have an analytic understanding of these dimension-dependent features; the large d limit may be worth particular study.

In contrast, the response of our confining ground states is both larger and more uniform in d; figure 6.15 shows no changes of signs. It is nevertheless interesting that gradients – either local or averaged – always decrease L_{crit}. This is naturally understood as a corresponding decrease in the length scale characterizing confinement. But comparing our results with [30] challenges this interpretation. For $d \leq 5$, [30] found that the gradients *decrease* the tension of flux tubes aligned in their direction, while the increase of tension one would expect from a decrease in the confinement length scale occurred only for $d \geq 6$. Furthermore, for $d > 3$ it found that gradients always raised the negative energy of the confining ground state – a result naturally associated with a larger confinement length scale. The main conclusion appears to be that confinement is not generally characterized by a single scale, but that changes in different confinement-related phenomenon under small perturbations are often uncorrelated. It would be interesting to develop more analytic understanding of such effects, and also to determine to what extent our results apply to other systems with spatially-varying confinement scale such as those that might be constructed in a condensed matter laboratory.

6.A Adiabatic Thermofield Doubles in 1+1 Dimensions

Holographic 1+1 CFTs have asymptotically AdS_3 bulk duals. Due to the lack of local gravitational degrees of freedom in 2+1 dimensions, all complete asymptotically locally AdS spacetimes are diffeomorphic to global AdS_3 (or to a quotient thereof). This fact

greatly simplifies the associated minimal surfaces, allowing us to compute properties of adiabatic thermofield-double analytically for $d = 2$. We do so here in an attempt to gain insight into our numerical results, and also as a check on our numerics.

For $d = 2$, the zeroth order ansatz (6.2) becomes simply

$$ds^2 = \frac{1}{z^2}\left[dz^2 + b^2\left(1 - \frac{z^2}{b^2}\right)^2 d\theta^2 + \left(1 + \frac{z^2}{b^2}\right)^2 dx^2\right] \quad . \tag{6.52}$$

As shown in appendix A of [30], the second order corrections are

$$\begin{aligned} g^{(2)}_{\theta\theta} &= \frac{z^2\,(b^2 - z^2)\,b'^2}{2\,b^2} \\ g^{(2)}_{xx} &= \frac{z^2\,(b^2 + z^2)\left(2\,b\,b'' - b'^2\right)}{2b^4} \quad . \end{aligned} \tag{6.53}$$

Using (6.8), this places the horizon at

$$z_H = b + \epsilon^2\,\frac{1}{8}\,b\,b'^2 + O(\epsilon^4). \tag{6.54}$$

We can now compute various entropies. Taking $\mathcal{R}_{CFT}$ to be the half space $x > 0$ in the union of the two CFTs, the equation of motion for the first order correction $x^{(1)}(z)$ to the entangling surface reduces to

$$0 = \left(b^2 - 3z^2\right)\,\partial_z x^{(1)}(z) - z\left(b^2 + z^2\right)\partial_z^2 x^{(1)}(z), \tag{6.55}$$

and the boundary conditions become

$$\begin{aligned} x^{(1)}(0) &= 0 \\ x^{(1)}(b) &= -\frac{1}{4}b\,b' \quad . \end{aligned} \tag{6.56}$$

The solution is given by

$$x^{(1)}(z) = -\frac{b\, b'\, z^2}{2\,(b^2+z^2)} \quad . \tag{6.57}$$

Comparing (6.57) to our numerics for $d = 2$ gives agreement to one part in 10^{16}. Turning now to the renormalized entropy, using (6.54) we find that the second order contribution coming from integrating the zeroth order surface over the region $z \in [b, z_H]$ precisely cancels the second order contribution associated with the first-order shift of extremal surface within the zeroth order background. As these were the only possible contributions to this order, in agreement with our numerics we find that the full second order contribution vanishes exactly.

We may also analytically compute the entropy of a strip (analogous to our slabs in higher dimensions). We take the strip to be thin compared to the adiabatic scale ($L \ll b/\epsilon b'$). Solving the equations of motion gives

$$\begin{aligned} z^{(0)}(x) &= b_0 \sqrt{\frac{\cosh\frac{2L}{b_0} - \cosh\frac{2x}{b_0}}{\cosh\frac{2x}{b_0} + \cosh\frac{2L}{b_0}}} \\ z^{(1)}(x) &= b_0' \frac{\left(-2\,(b_0^2 - 2x^2 + 2L^2)\sinh\frac{2x}{b_0}\cosh\frac{2L}{b_0} + 2b_0 x\cosh\frac{4L}{b_0} + b_0\left(b_0\sinh\frac{4x}{b_0} - 2x\cosh\frac{4x}{b_0}\right)\right)}{4\sqrt{\cosh\frac{2L}{b_0} - \cosh\frac{2x}{b_0}}\left(\cosh\frac{2x}{b_0} + \cosh\frac{2L}{b_0}\right)^{3/2}}. \end{aligned} \tag{6.58}$$

The numerically derived surfaces agree with the above to one part in 10^{14} to zeroth order and one part in 10^7 to first order. Computing the entanglement entropy gives

$$\begin{aligned} A_{\text{ren}}^{(0)} &= 2\log\sinh\frac{2L}{b_0} \\ A_{\text{ren}}^{(2)} &= \left(-\frac{L^2}{b_0^2} + \frac{4}{3}\frac{L^3}{b_0^3}\coth\frac{2L}{b_0}\right){b_0'}^2 + \left(\frac{L^2}{b_0^2} - \frac{2}{3}\frac{L^3}{b_0^3}\coth\frac{2L}{b_0}\right)b_0''. \end{aligned} \tag{6.59}$$

Comparing this result to our $d = 2$ numerics shows discrepancies only at the level of one part in 10^4 level for the coefficient of ${b_0'}^2$ and one part in 10^{15} for the coefficient of b_0''.

With these expressions for the area, we can compute the location of the phase transition between vanishing and non-vanishing mutual information to second order. To zeroth order, for the half space entangling surface we have $\hat{\mathsf{A}}^{(0)} = 0$ so from (6.59) $\hat{A}^{(0)}_{\rm ren} = A^{(0)}_{\rm ren}$ gives

$$L^{(0)}_{\rm crit} = \frac{b_0}{2} \sinh^{-1}(1)\,. \tag{6.60}$$

At first order it is manifest that $A^{(1)}_{\rm ren} = 0$. In contrast, keeping in mind the renormalization prescription (6.29), the area of the entangling surface for half space $x < L$ does have a first order correction. But it is canceled by the corresponding correction to the entangling surface for $x > -L$, so the $O(\epsilon)$ correction $L^{(1)}_{\rm crit}$ to L_{crit} vanishes.

However, at second order we find

$$\hat{A}^{(2)}_{\rm ren} = -\frac{\ell}{2}\frac{L^2}{b_0^2}{b_0'}^2 + \frac{\ell}{2}\frac{L^2}{b_0}b_0''\,. \tag{6.61}$$

Comparing with (6.59) and using (6.41) yields

$$L^{(2)}_{\rm crit} = -\frac{b_0}{48} \sinh^{-1}(1)^3 (2{b_0'}^2 - b_0 b_0'')\,. \tag{6.62}$$

This result agrees with the results in figure 6.9 to one part in 10^4.

As a final check on our $d = 2$ results we can solve for the diffeomorphism taking $g^{(0)}_{\mu\nu}$ with constant b_0 to $\tilde{g}^{(0)}_{\mu\nu} := g^{(0)}_{\mu\nu} + \epsilon^2\, g^{(2)}_{\mu\nu}$. Working near $x = 0$, we find that the correct diffeomorphism beomes

$$\tilde{z} = z + \epsilon\, z\, \frac{x\, b_0'}{b_0} + \epsilon^2\, z\, \frac{(2x^2\,(b_0^2 + z^2)\,({b_0'}^2 + b_0\, b_0'') - z^2\, b_0^2\, {b_0'}^2)}{4 b_0^2\,(b_0^2 + z^2)} + O(\epsilon^3)$$

$$\tilde{x} = x + \epsilon \frac{b_0' \left(b_0^2(x^2 - z^2) + x^2 z^2\right)}{2b_0 \left(b_0^2 + z^2\right)} + \epsilon^2 \frac{x \left(b_0^2 \left(x^2 - 3z^2\right) + x^2 z^2\right) \left(b_0'^2 + b_0 b_0''\right)}{6b_0^2 \left(b_0^2 + z^2\right)} + O(\epsilon^3), \tag{6.63}$$

which indeed takes the entangling surfaces of global AdS_3 to (6.58) as desired. One may also check that (6.63) maps the phase transition for $b(x) = constant$ (given by (6.60)) to the value specified by (6.62).

6.B Estimation of Numerical Uncertainty

We have used two distinct methods to estimate the numerical uncertainty of our results. First, for the majority of the tables we merely make a rough estimate by computing a particular coefficient using a variety numerical parameters. We then take the approximate error to be given by the standard deviation of this set. For example for the $L \gg b_0$ scaling of figure 6.5, we compare values calculated using 100 and 150 lattice points and for fitting intervals $L/b_0 \in [40, 50]$ and $L/b_0 \in [50, 60]$. The estimated error is the standard deviation of this four point data set. The value displayed in the table is the mean.

However, as noted in the main text, the values tabulated in figure 6.9 are rather less uniform than one might expect. As a result, we now take extra care to analyze the numerical results reported there. After investigating the possible sources of error by varying the precision of different parts of the computation, we find the dominant error (by far) to come from using a finite number N of lattice points in the interval $[-L, L]$. We now study how our results change with N.

We first compute L_{crit} using $N = [50, 300]$ lattice points in steps of 10. Next, we

approximate the function $\frac{dL_{\text{crit}}}{dN}$ by choosing an appropriate p so that the data

$$D_N = \frac{1}{10}\left[L_{\text{crit}}(N) - L_{\text{crit}}(N+10)\right] N^p \tag{6.64}$$

appears constant to the eye. See figure 6.16 for examples. We then compute the average $\bar{D}$ of D_N over the data set and model our results by

$$\frac{dL_{\text{crit}}(N)}{dN} = \bar{D}\, N^p\,. \tag{6.65}$$

Given (6.65), we can compute $\Delta(N_0) = L_{\text{crit}}(N_0) - L_{\text{crit}}(\infty)$. We have reported the values $\Delta(N_0)$ for $N_0 = 300$ as the numerical uncertainties in figure 6.16. Though we do not fully understand the particular values of p found in this way, we believe this to be a conservative estimate of our errors (especially when D_N clearly decreases). We display $\bar{D}$ as well as the determined value of p for $2 \leq d \leq 8$ in figure 6.17.

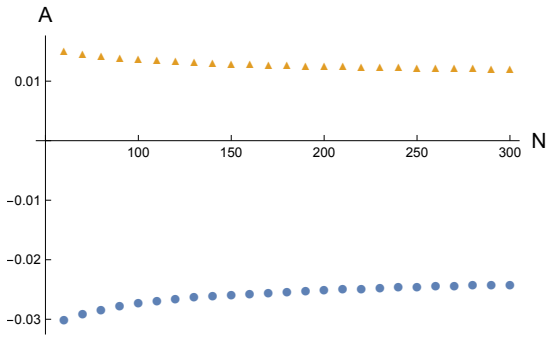

(a) $d = 5$, $p = 7/4$

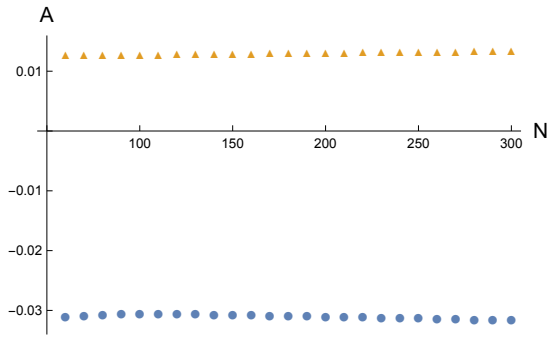

(b) $d = 6$, $p = 7/4$

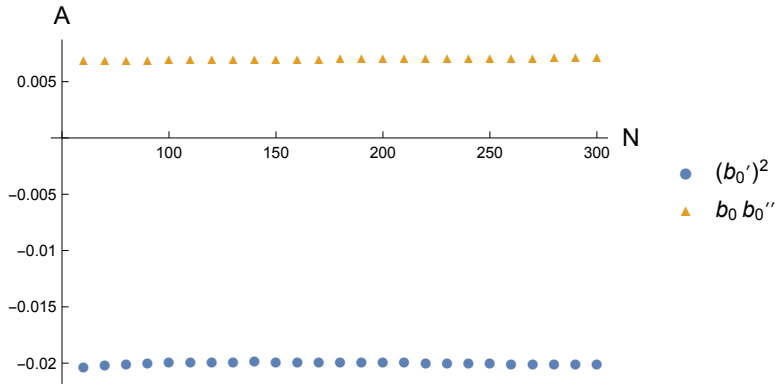

(c) $d = 7$, $p = 13/8$

Figure 6.16: Plots of D_N as defined in (6.64) vs. N with $d = 5, 6, 7$ for the ${b_0'}^2$ and $b_0 b_0''$ coefficients (triangles and disks respectively). We choose p so that the datasets are either flat or slowly approaching zero.

d	$\bar{D}^{({b_0'}^2)}$	$\bar{D}^{(b_0 b_0'')}$	p
2	0.00301	1.94×10^{-8}	2.75
3	−0.0819	0.0365	2
4	−0.0224	0.0116	1.75
5	−0.0256	0.0130	1.75
6	−0.0309	0.0131	1.75
7	−0.0199	0.00710	1.625
8	−0.0128	0.00391	1.5

Figure 6.17: We display the estimated values of $\bar{D}$ for each of the coefficients ${b_0'}^2$ and $b_0 b_0''$ and p for $2 \leq d \leq 8$.

Chapter 7

Outlook

In this dissertation, we explored various classical black hole spacetimes and their role in holography. Black holes are the source of some of the toughest conceptual hurdles toward constructing a theory of quantum gravity; although, as we see through the AdS/CFT correspondence, further study of these objects also provides some guidance for the resolution of their mysteries. In this sense, black holes are an excellent testing ground for exploring quantum gravity.

We considered how black hole states of non-trivial topology might be associated naturally with an operator through holography in chapter 3. In particular, we constructed a class of states by acting on the vacuum with an operator defined in the CFT via a path integral over a torus with two punctures. For finely tuned moduli, one might expect to be able use this operator to add arbitrarily high topology behind the horizon. However, we found the unexpected result that with certain mild restrictions on the operator, the solutions of high topology never dominate the gravitational path integral. Additionally, investigation into the ground state of this operator resulted in a puzzle related to its positivity, signaling a need for better methods of categorizing these semi-classical saddle points.

Next in chapter 4 we explored the allowed subregion entanglement entropies of holographic states. We evaluated a proposal for a set of constraints on these entropies by constructing the gravitational dual of states at the extremum of the allowed values, with the dual states given by multi-boundary wormhole geometries. We were unable to find such states, possibly suggesting that there might be further constraints on the entropies or that a more complicated construction procedure is needed to find these states.

Further, in chapters 5 and 6 we showed how we could use a perturbative expansion about black hole solutions to study various CFT states. We considered the effect of spatial curvature on properties of confinement as well as entanglement in the confining vacuum state. Additionally, we considered a thermal CFT state with a spatially varying local temperature and studied how this temperature gradient changed the entanglement structure of the thermal vacuum. These techniques could also be applied to study the confinement/deconfinement phase transition in similar regimes.

We hope that the main takeaway of this dissertation is that black hole spacetimes have great potential to probe various aspects of quantum gravity. The examples given only represent a fraction of the work that has been done, and also point the direction toward interesting avenues to explore. In particular, in three dimensions one has control over a large class of solutions with non-trivial topology, providing a powerful framework for exploring the significance of these states in the context quantum gravity. As such, in chapter 2 we have provided a pedagogical introduction to the methods used to study these spacetimes, as well as a practical set of tools implemented in a *Mathematica* package.

While we have only skimmed the surface of addressing the issues laid out in the introduction, we have taken some steps toward gaining insights into black holes and quantum gravity. On this subject, holography is an incredibly powerful tool with many active avenues of research. There is plenty of more work to be done!

Bibliography

[1] A. Einstein, *Die grundlage der allgemeinen relativitätstheorie*, Annalen der Physik **49** (1916) 769822.

[2] K. Schwarzschild, *über das gravitations-feld eines massenpunktes nach der einsteinschen theorie*, Sitzungsberichte der Königlich Preussischen Akademie der Wissenschaften zu Berlin **7** (1916) 189196.

[3] R. Penrose, *Gravitational collapse and space-time singularities*, Phys. Rev. Lett. **14** (Jan, 1965) 57–59.

[4] B. Balick and R. L. Brown, *Intense sub-arcsecond structure in the galactic center*, Astrophysical Journal **194** (Dec, 1974) 265–270.

[5] **LIGO Scientific and Virgo** Collaboration, B. P. Abbott et. al., *Observation of gravitational waves from a binary black hole merger*, Phys. Rev. Lett. **116** (Feb, 2016) 061102.

[6] **LIGO Scientific and Virgo** Collaboration, B. P. Abbott et. al., *Gw151226: Observation of gravitational waves from a 22-solar-mass binary black hole coalescence*, Phys. Rev. Lett. **116** (Jun, 2016) 241103.

[7] **LIGO Scientific and Virgo** Collaboration, B. P. Abbott et. al., *Gw170104: Observation of a 50-solar-mass binary black hole coalescence at redshift 0.2*, Phys. Rev. Lett. **118** (Jun, 2017) 221101.

[8] J. M. Bardeen, B. Carter, and S. W. Hawking, *The four laws of black hole mechanics*, Communications in Mathematical Physics **31** (June, 1973) 161–170.

[9] S. W. Hawking, *Black hole explosions*, Nature **248** (1974) 30–31.

[10] J. D. Bekenstein, *Black holes and the second law*, Lett. Nuovo Cim. **4** (1972) 737–740.

[11] J. D. Bekenstein, *Black holes and entropy*, Phys. Rev. **D7** (1973) 2333–2346.

[12] J. D. Bekenstein, *Generalized second law of thermodynamics in black hole physics*, Phys. Rev. **D9** (1974) 3292–3300.

[13] A. Strominger and C. Vafa, *Microscopic origin of the Bekenstein-Hawking entropy*, Phys. Lett. **B379** (1996) 99–104, [hep-th/9601029].

[14] J. M. Maldacena, *The Large N limit of superconformal field theories and supergravity*, Int. J. Theor. Phys. **38** (1999) 1113–1133, [hep-th/9711200]. [Adv. Theor. Math. Phys.2,231(1998)].

[15] S. S. Gubser, I. R. Klebanov, and A. M. Polyakov, *Gauge theory correlators from noncritical string theory*, Phys. Lett. **B428** (1998) 105–114, [hep-th/9802109].

[16] E. Witten, *Anti-de Sitter space and holography*, Adv. Theor. Math. Phys. **2** (1998) 253–291, [hep-th/9802150].

[17] D. Marolf, W. Kelly, and S. Fischetti, *Conserved Charges in Asymptotically (Locally) AdS Spacetimes*, arXiv:1211.6347.

[18] O. Aharony, S. S. Gubser, J. M. Maldacena, H. Ooguri, and Y. Oz, *Large N field theories, string theory and gravity*, Phys. Rept. **323** (2000) 183–386, [hep-th/9905111].

[19] E. D'Hoker and D. Z. Freedman, *Supersymmetric gauge theories and the AdS / CFT correspondence*, in
Strings, Branes and Extra Dimensions: TASI 2001: Proceedings, pp. 3–158, 2002. hep-th/0201253.

[20] J. Polchinski, *Introduction to Gauge/Gravity Duality*, arXiv:1010.6134.

[21] J. M. Maldacena, *Eternal black holes in anti-de Sitter*, JHEP **04** (2003) 021, [hep-th/0106112].

[22] E. Witten, *Anti-de Sitter space, thermal phase transition, and confinement in gauge theories*, Adv. Theor. Math. Phys. **2** (1998) 505–532, [hep-th/9803131].

[23] S. Ryu and T. Takayanagi, *Holographic derivation of entanglement entropy from AdS/CFT*, Phys. Rev. Lett. **96** (2006) 181602, [hep-th/0603001].

[24] S. Ryu and T. Takayanagi, *Aspects of Holographic Entanglement Entropy*, JHEP **08** (2006) 045, [hep-th/0605073].

[25] J. B. Hartle and S. W. Hawking, *Wave function of the universe*, Phys. Rev. D **28** (Dec, 1983) 2960–2975.

[26] V. Balasubramanian, P. Hayden, A. Maloney, D. Marolf, and S. F. Ross, *Multiboundary Wormholes and Holographic Entanglement*, Class. Quant. Grav. **31** (2014) 185015, [arXiv:1406.2663].

[27] D. Marolf, H. Maxfield, A. Peach, and S. F. Ross, *Hot multiboundary wormholes from bipartite entanglement*, Class. Quant. Grav. **32** (2015), no. 21 215006, [arXiv:1506.0412].

[28] D. Marolf and J. Wien, *The Torus Operator in Holography*, arXiv:1708.0304.

[29] D. Marolf, M. Rota, and J. Wien, *Handlebody phases and the polyhedrality of the holographic entropy cone*, JHEP **10** (2017) 069, [arXiv:1705.1073].

[30] D. Marolf and J. Wien, *Holographic confinement in inhomogeneous backgrounds*, JHEP **08** (2016) 015, [arXiv:1605.0280].

[31] D. Marolf and J. Wien, *Adiabatic corrections to holographic entanglement in thermofield doubles and confining ground states*, JHEP **09** (2016) 058, [arXiv:1605.0280].

[32] O. J. C. Dias, J. E. Santos, and B. Way, *Numerical Methods for Finding Stationary Gravitational Solutions*, arXiv:1510.0280.

[33] B. Way, Holographic Applications for Black Holes and Condensed Matter. PhD thesis, University of California, Santa Barbara, 2013.

[34] F.-J. Sayas, *A gentle introduction to the finite element method*, .

[35] E. Süli, *Lecture notes on finite element methods for partial differential equations*, .

[36] H. Maxfield, S. Ross, and B. Way, *Holographic partition functions and phases for higher genus Riemann surfaces*, Class. Quant. Grav. **33** (2016), no. 12 125018, [arXiv:1601.0098].

[37] D. R. Brill, *Multi - black hole geometries in (2+1)-dimensional gravity*, Phys. Rev. **D53** (1996) 4133–4176, [gr-qc/9511022].

[38] S. Aminneborg, I. Bengtsson, D. Brill, S. Holst, and P. Peldan, *Black holes and wormholes in (2+1)-dimensions*, Class. Quant. Grav. **15** (1998) 627–644, [gr-qc/9707036].

[39] K. Skenderis and B. C. van Rees, *Holography and wormholes in 2+1 dimensions*, Commun. Math. Phys. **301** (2011) 583–626, [arXiv:0912.2090].

[40] K. Krasnov, *Holography and Riemann surfaces*, Adv. Theor. Math. Phys. **4** (2000) 929–979, [hep-th/0005106].

[41] K. Krasnov, *Black hole thermodynamics and Riemann surfaces*, Class. Quant. Grav. **20** (2003) 2235–2250, [gr-qc/0302073].

[42] S. W. Hawking and D. N. Page, *Thermodynamics of Black Holes in anti-De Sitter Space*, Commun. Math. Phys. **87** (1983) 577.

[43] V. E. Hubeny, M. Rangamani, and T. Takayanagi, *A Covariant holographic entanglement entropy proposal*, JHEP **07** (2007) 062, [arXiv:0705.0016].

[44] G. J. Galloway, K. Schleich, D. M. Witt, and E. Woolgar, *Topological censorship and higher genus black holes*, Phys. Rev. **D60** (1999) 104039, [gr-qc/9902061].

[45] N. Seiberg and E. Witten, *The D1 / D5 system and singular CFT*, JHEP **04** (1999) 017, [hep-th/9903224].

[46] J. M. Maldacena and L. Maoz, *Wormholes in AdS*, JHEP **02** (2004) 053, [hep-th/0401024].

[47] L. R. Ford, Automorphic functions. Chelsea Pub. Co., 1972.

[48] L. Takhtajan and P. Zograf, *On uniformization of Riemann surfaces and Weyl-Peterson metric on Teichmuller and Schottky spaces*, Math. USSR Sb. **60** (1988), no. 2 297–131.

[49] X. Yin, *On Non-handlebody Instantons in 3D Gravity*, JHEP **09** (2008) 120, [arXiv:0711.2803].

[50] P. Koebe, *Über die uniformisierung der algebraischen kurven ii*, Math. Ann **69** (1910) 1–81.

[51] H. Maxfield, *Entanglement entropy in three dimensional gravity*, JHEP **04** (2015) 031, [arXiv:1412.0687].

[52] M. Headrick and T. Takayanagi, *A holographic proof of the strong subadditivity of entanglement entropy*, arXiv:0704.3719.

[53] M. Headrick, *Entanglement renyi entropies in holographic theories*, arXiv:1006.0047.

[54] V. E. Hubeny, H. Maxfield, M. Rangamani, and E. Tonni, *Holographic entanglement plateaux*, arXiv:1306.4004.

[55] P. Hayden, M. Headrick, and A. Maloney, *Holographic mutual information is monogamous*, arXiv:1107.2940.

[56] M. Rangamani and M. Rota, *Entanglement structures in qubit systems*, arXiv:1505.0369.

[57] P. Hosur, X.-L. Qi, D. A. Roberts, and B. Yoshida, *Chaos in quantum channels*, arXiv:1511.0402.

[58] M. Rota, *Tripartite information of highly entangled states*, arXiv:1512.0375.

[59] N. Bao, S. Nezami, H. Ooguri, B. Stoica, J. Sully, and M. Walter, *The Holographic Entropy Cone*, JHEP **09** (2015) 130, [arXiv:1505.0783].

[60] F. Matús, *Infinitely many information inequalities*, Proc. Int. Symp. Inf. Theory (ISIT) (2007) 41.

[61] P. Hayden, S. Nezami, X.-L. Qi, N. Thomas, M. Walter, and Z. Yang, *Holographic duality from random tensor networks*, JHEP **11** (2016) 009, [arXiv:1601.0169].

[62] A. C. Wall, *Maximin surfaces, and the strong subadditivity of the covariant holographic entanglement entropy*, arXiv:1211.3494.

[63] A. Polyakov, *Compact gauge fields and the infrared catastrophe*, Physics Letters B **59** (1975), no. 1 82 – 84.

[64] A. M. Polyakov, *Thermal Properties of Gauge Fields And Quark Liberation*, Phys. Lett. **72B** (1978) 477.

[65] L. Susskind, *Lattice Models of Quark Confinement At High Temperature*, Phys. Rev. **D20** (1979) 2610.

[66] J. M. Maldacena, *Wilson loops in large N field theories*, Phys. Rev. Lett. **80** (1998) 4859–4862, [hep-th/9803002].

[67] G. T. Horowitz and R. C. Myers, *The AdS/CFT Correspondence and a New Positive Energy Conjecture for General Relativity*, Phys. Rev. **D59** (1998) 026005.

[68] S. Bhattacharyya, V. E. Hubeny, S. Minwalla, and M. Rangamani, *Nonlinear Fluid Dynamics from Gravity*, JHEP **02** (2008) 045, [arXiv:0712.2456].

[69] V. E. Hubeny, S. Minwalla, and M. Rangamani, *The fluid/gravity correspondence*, in Black holes in higher dimensions, pp. 348–383, 2012. arXiv:1107.5780.

[70] M. Rangamani, *Gravity and Hydrodynamics: Lectures on the fluid-gravity correspondence*, Class. Quant. Grav. **26** (2009) 224003, [arXiv:0905.4352].

[71] M. Van Raamsdonk, *Building up spacetime with quantum entanglement*, Gen. Rel. Grav. **42** (2010) 2323–2329, [arXiv:1005.3035]. [Int. J. Mod. Phys.D19,2429(2010)].

[72] B. Czech, J. L. Karczmarek, F. Nogueira, and M. Van Raamsdonk, *Rindler Quantum Gravity*, Class. Quant. Grav. **29** (2012) 235025, [arXiv:1206.1323].

[73] J. Maldacena and L. Susskind, *Cool horizons for entangled black holes*, Fortsch. Phys. **61** (2013) 781–811, [arXiv:1306.0533].

[74] D. V. Fursaev, *Proof of the holographic formula for entanglement entropy*, JHEP **09** (2006) 018, [hep-th/0606184].

[75] A. Lewkowycz and J. Maldacena, *Generalized gravitational entropy*, JHEP **08** (2013) 090, [arXiv:1304.4926].

[76] F. M. Haehl, T. Hartman, D. Marolf, H. Maxfield, and M. Rangamani, *Topological aspects of generalized gravitational entropy*, JHEP **05** (2015) 023, [arXiv:1412.7561].

[77] C. R. Graham and E. Witten, *Conformal anomaly of submanifold observables in AdS / CFT correspondence*, Nucl. Phys. **B546** (1999) 52–64, [hep-th/9901021].

[78] D. Marolf and A. C. Wall, *State-Dependent Divergences in the Entanglement Entropy*, JHEP **10** (2016) 109, [arXiv:1607.0124].

[79] T. Jacobson, G. Kang, and R. C. Myers, *On black hole entropy*, Phys. Rev. **D49** (1994) 6587–6598, [gr-qc/9312023].

[80] X. Dong, *Holographic Entanglement Entropy for General Higher Derivative Gravity*, JHEP **01** (2014) 044, [arXiv:1310.5713].

[81] R.-X. Miao and W.-z. Guo, *Holographic Entanglement Entropy for the Most General Higher Derivative Gravity*, JHEP **08** (2015) 031, [arXiv:1411.5579].

[82] M. Taylor and W. Woodhead, *Renormalized entanglement entropy*, arXiv:1604.0680.

[83] I. A. Morrison and M. M. Roberts, *Mutual information between thermo-field doubles and disconnected holographic boundaries*, JHEP **07** (2013) 081, [arXiv:1211.2887].

[84] T. Hartman and J. Maldacena, *Time Evolution of Entanglement Entropy from Black Hole Interiors*, JHEP **05** (2013) 014, [arXiv:1303.1080].

[85] "NIST Digital Library of Mathematical Functions." http://dlmf.nist.gov/, Release 1.0.10 of 2015-08-07.

[86] I. R. Klebanov, D. Kutasov, and A. Murugan, *Entanglement as a probe of confinement*, Nucl. Phys. **B796** (2008) 274–293, [arXiv:0709.2140].

[87] T. Nishioka and T. Takayanagi, *AdS Bubbles, Entropy and Closed String Tachyons*, JHEP **01** (2007) 090, [hep-th/0611035].